Doctoral theses at NTNU, 2020:330

Feng Wang

Dynamic anti-icing surfaces (DAIS)

Doctoral thesis

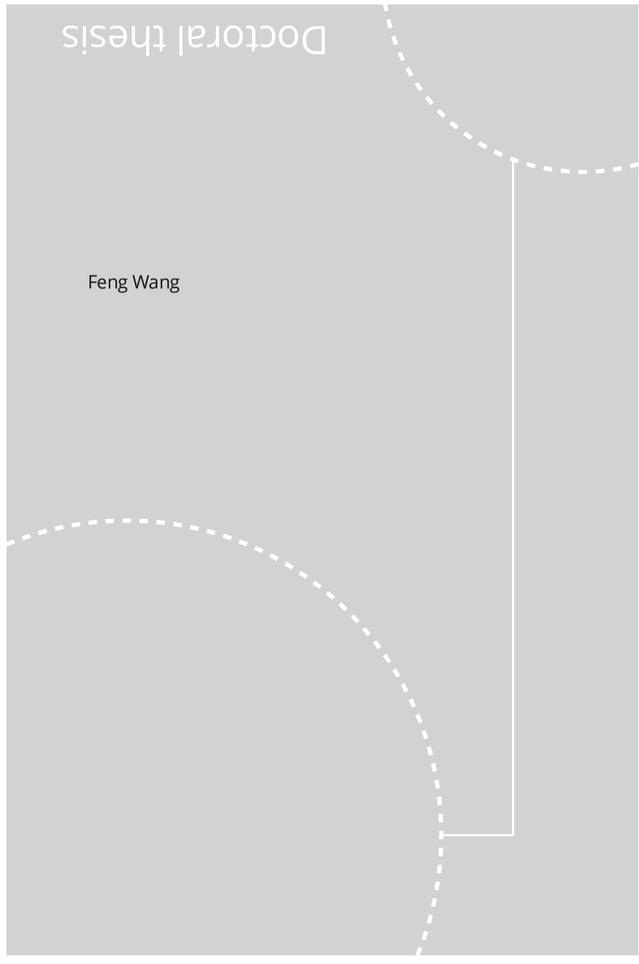

ISBN 978-82-326-5006-4 (printed ver.)
ISBN 978-82-326-5007-1 (electronic ver.)
ISSN 1503-8181

NTNU
Norwegian University of Science and Technology

NTNU
Norwegian University of Science and Technology
Thesis for the Degree of
Philosophiae Doctor
Faculty of Engineering
Department of Structural Engineering

Doctoral theses at NTNU, 2020:330

NTNU
Norwegian University of Science and Technology

Feng Wang

Dynamic anti-icing surfaces (DAIS)

Thesis for the Degree of Philosophiae Doctor

Trondheim, October 2020

Norwegian University of Science and Technology
Faculty of Engineering
Department of Structural Engineering

NTNU
Norwegian University of
Science and Technology

NTNU
Norwegian University of Science and Technology

Thesis for the Degree of Philosophiae Doctor

Faculty of Engineering
Department of Structural Engineering

ISBN 978-82-326-5006-4 (printed ver.)
ISBN 978-82-326-5007-1 (electronic ver.)
ISSN 1503-8181

Doctoral theses at NTNU, 2020:330

Printed by NTNU Grafisk senter

Not everything that can be counted counts, and not everything that counts can be counted.

— Albert Einstein

Preface

This thesis is submitted to the Norwegian University of Science and Technology (NTNU) for partial fulfilment of the requirements for the degree of philosophiae doctor (PhD).

The doctoral work has been conducted in the period between August 2017 and July 2020 under the supervision of **Professor Zhiliang Zhang** and **Professor Jianying He**. The main experimental work was carried out at NTNU Nanolab and NTNU Nanomechanical Lab, Department of Structural Engineering (KT), Faculty of Engineering (IV), NTNU, Trondheim, Norway. The thesis comprises of an introductory section of overviewing chapters of the relevant research field, and 3 appended journal papers (two published and one submitted).

This work is supported by the Research Council of Norway via the Researcher Project - **Towards Design of Super-Low Ice Adhesion Surfaces** (**SLICE**, Project No.: 250990) in the FRINATEK Program and the Norwegian Micro- and Nano-Fabrication Facility (NorFab, Project No.: 245963).

Feng Wang

Trondheim, July 2020

Abstract

Icing is one of the most ubiquitous natural phenomena accompanying human activities. Undesired ice generation and accretion are extremely hazardous to aircrafts, ships, electrical transmission cables, wind turbines, motor vehicles and many others. Combating excessive icing, especially active de-icing, has been costing a huge amount of energy and time annually global-wide. Consequently, designing and deploying material surfaces that can assist the removal of ice have received growing interests. In the recent years, it is witnessed that anti-icing strategies are shifting from being of static nature, namely no change at the ice-substrate contact area after ice formation, to enabling dynamic changes in the chemical/physical states of the ice/substrate/ice-substrate-interface with tailored functions. In contrast to the static anti-icing surfaces with known deficiencies in icing/deicing cycling durability, inapplicability at extremely low temperature, fragility to surface damage and surface degradation, and inadaptability to environment changes, the modern dynamic anti-icing surfaces (DAIS) have intrinsic superiorities in all respects of materials properties and enhanced anti-icing performances, thanks to their integrated dynamic functions. It is expected that a new variety of DAIS will be created in the near future as they are attracting tremendous interests in the research field.

By definition, DAIS are surfaces that possess spontaneous/stimuli-responsible changes of the chemical/physical state of the substrate, ice, or the ice-substrate interface. The currently reported DAIS can be classified into three categories depending on where the dynamic change takes place, namely surfaces with dynamic substrate change, with dynamic interface change, and with dynamic ice change. Built upon the understanding of dynamic anti-icing surfaces, novel anti-icing surfaces can be designed by integrating dynamic behaviors into substrate, ice-substrate interfaces or ice.

Focusing on dynamic substrate change, thermal responsible surfaces that can dynamically change the phase of lubricant with decreasing temperature for enabling durable icephobicity are designed. Generally, maintaining the longevity and durability of slippery liquid infused porous surface (SLIPS) are of great challenge. A novel phase transformable slippery liquid infused porous surface (PTSLIPS) is invented to overcome

the formidable barrier. The underlying mechanism of PTSLIPS relies on the physical property of lubricant that enables transformation from liquid to solid state above water freezing point. Specifically, peanut oil is chosen to infuse into porous PDMS substrates for creating PTSLIPS, which show low ice adhesion strength (4 ~ 22 kPa) as well as excellent durability. For selected samples, the low ice adhesion strength (~ 16 kPa) maintains after 30 icing/de-icing cycles thanks to the solid state of the lubricant, demonstrating extraordinary long-term icephobicity. In addition to the promising low ice adhesion strength and durability, PTSLIPS also suit to various substrates of varied chemical compositions (both hydrophobic and hydrophilic materials) with wide range of porosity and diverse pore morphologies. The PTSLIPS, therefore, provide the possibility of creating anti-icing surfaces by Do-It-Yourself (DIY) manner with porous materials in daily life.

Turning to dynamic change of the icing interface after ice formation to facilitate easy ice removal, liquid layer generators (LLGs) are designed for the first time. The LLGs can release ethanol to and constantly change the ice-substrate interface. As predicted by atomistic modelling and molecular dynamic simulations, interfacial ethanol layers with different thickness can provide dramatic reduction in ice adhesion even at extremely low temperatures. Two types of LLGs, namely LLG 1 by packing ethanol inside substrate and LLG 2 by storing replenishable ethanol below substrate, are fabricated. The interfacial ethanol on both the two LLGs converts the ice-substrate contact from the solid-solid mode to the solid-liquid-solid mode, which results in super low ice adhesion around 1.0 kPa at -18 °C. Attributing to the constant ethanol release and thickening of the interfacial lubricating layer, LLG can overcome the deficiency induced by surface roughness and hydrophilicity, the two well-known critical factors that result in the failure of other icephobic surfaces. The LLG 1 have a lifespan for a maximum of 593 days without ethanol source replenishment. By introducing an interfacial ethanol layer, ice adhesion strength on selected samples with rough surfaces decrease in an unprecedented manner from 709.2 ~ 760.9 to 22.1 ~ 25.2 kPa at a low temperature of -60 °C. The results validate the LLGs as competitive candidates for practical anti-icing applications and provide an unprecedented icephobic solution for extremely low temperatures.

In a summary, by overcoming the limitations of the static nature of the current anti-icing surfaces and focusing on the dynamic properties, novel anti-icing strategies are explored, varying from the dynamic substrate changes to the dynamic interface changes. Based on the different dynamic design principles, two anti-icing surfaces, the phase transformable slippery liquid infused porous surfaces, PTSLIPS, and the liquid layer generators, LLGs, are developed in this PhD work, both of which demonstrate excellent anti-icing performances.

Taking a bird-view on the DAIS, the related state-of-the-art research is also covered in the last appended paper. With the two fabricated surfaces as illustration and the surveyed development of the research, this thesis is intended to serve not only as the PhD concluding milestone but also as helpful reading materials for researchers in the anti-icing field.

Acknowledgements

I would like to express my most sincere gratitude to my supervisors, **Prof. Zhiliang Zhang** and **Prof. Jianying He**. There is an old Chinese saying, "*In ancient times those who wanted to learn would seek out a teacher, one who could propagate the doctrine, impart professional knowledge, and resolve doubts.*" In my way to the doctorate, Prof. Zhang and Prof. He no doubt are the teachers as in the saying and are more than that. It's never been an easy task to accomplish a PhD degree. Yet, I am lucky to reach the destination under the guidance, suggestions and encouragements from Prof. Zhang and Prof. He. The open-minded discussions on scientific issues, the brainstorming meeting for new ideas, the heated arguments on experiment phenomena, the precise derivations to novel mechanisms, the freedom in exploring various research topics, and many more with Prof. Zhang and Prof. He make every step in my PhD study attractive and memorable. It's also from Prof. Zhang and Prof. He that I learn to enjoy the life in Norway, to find out the glamour of research and to balance work and life.

Besides, I would like to offer my particular thanks to **Dr. Senbo Xiao** for his assistance and guidance. Dr. Xiao is always full of passion for life and research. He also shows great patience for every scientific question we discussed. I benefit a lot from his positive and critical attitudes towards science. My special thanks go to **Prof. Bjørn Helge Skallerud** for the always instructive and helpful discussions. I would also like to thank **Prof. Chao Zhong** in ShanghaiTech University for his kind acceptance of my three-month scientific visit and for the help and patient guidance during the stay.

Another saying from Confucius, "*In a party of three, there must be one whom I can learn from.*" One can always learn a lot from people around in daily life. I always believe it is the research team in **the NTNU Nanomechanical Lab** (NML) that makes my PhD work efficient and unimpeded. My grateful thanks are for the friends in NML: Prof. Jianyang Wu, Prof. Helge Kristiansen, Dr. Zhiwei He, Dr. Yi Gong, Dr. Mao Wang, Dr. Kai Zhao, Dr. Haiyang Yu, Dr. Yang Li, Dr. Xiao Wang, Dr. Shengwen Tu, Dr. Yizhi Zhuo, Dr. Sigrid Rønneberg, Dr. Tong Li, Øyvind Othar Aunet Persvik, Bjørn Strøm, Verner Håkonsen, Li Sun, Merete Falck, Ingrid Snustad, Susanne Sandell, Yuequn Fu, Sandra Sæther, Siqi Liu, Prof. Tianle Zhou, Dr. Sakari Pallaspuro, Dr. Zexin Chang,

Junchao Pan, Thorstein Wang, Xu wang, Meichao Lin, Yu Ding and Yuanhao Chang. All of my colleagues in NML have made the past three years in my life colourful, meaningful and impressive. My thanks also go to the friends and colleagues that worked together in the Nanolab and in the ShanghaiTech University: Wenwu Ding, Sihai Luo, Linfeng Lei, Wenjing Zhang, Xiaoyu Jiang and Dr. Mengkui Cui. It is with their help that my research becomes more efficient.

Last but not least, I would like to express my heartful thanks to my parents, my brother and my girlfriend, for all their unconditional love, supports and understandings.

List of Papers

The thesis is organized based on the following three journal papers, which have been published or submitted:

1. **Wang, F.**, Ding, W., He, J., Zhang, Z. Phase transition enabled durable anti-icing surfaces and its DIY design. *Chemical Engineering Journal*, 2019, 360, 243-249.
2. **Wang, F.**, Xiao, S., Zhuo, Y., Ding, W., He, J., Zhang, Z. Liquid layer generators for excellent icephobicity at extremely low temperatures. *Materials Horizons*, 2019, 6(10), 2063-2072.
3. **Wang, F.**, Xiao, S., Zhuo, Y., He, J., Zhang, Z., Dynamic anti-icing surfaces: emerging field for ice mitigation. *To be submitted*

The other relevant journal papers that are finished in the PhD study but not include in the thesis are listed in the following:

1. **Wang, F.**, Luo, S., Xiao, S., Zhang, W., Zhuo, Y., He, J., Zhang, Z. Enabling phase transition of infused lubricant in porous structure for exceptional oil/water separation. *Journal of Hazardous Materials*, 2020, 390, 122176.
2. **Wang, F.**, Fu, Y., Liu, S., Zhuo, Y., Xiao, S., He, J., Zhang, Z., Exploring the potential of the sacrificial layer in design inorganic anti-icing surfaces. *To be submitted.*

Besides the publications listed above, I have contributed to the following works:

1. Zhuo, Y., **Wang, F.**, Xiao, S., He, J., Zhang, Z. One-step fabrication of bioinspired lubricant-regenerable icephobic slippery liquid-infused porous surfaces. *ACS Omega*, 2018, 3(8), 10139-10144.
2. He, Z., Zhuo, Y., **Wang, F.**, He, J., Zhang, Z. Understanding the role of hollow sub-surface structures in reducing ice adhesion strength. *Soft Matter*, 2019, 15(13), 2905-2910.
3. Zhuo, Y., Li, T., **Wang, F.**, Håkonsen, V., Xiao, S., He, J., Zhang, Z. An ultra-durable icephobic coating by a molecular pulley. *Soft Matter*, 2019, 15(17), 3607-3611.

4. Xiao, S., Skallerud, B. H., **Wang, F.**, Zhang, Z., He, J. Enabling sequential rupture for lowering atomistic ice adhesion. *Nanoscale*, 2019, 11(35), 16262-16269.
5. Zhou, T., Wang, J. W., ... **Wang F.**, He, J. Breathable Nanowood Biofilms as Guiding Layer for Green On-Skin Electronics. *Small*, 2019, 15(31), 1901079.
6. Zhuo, Y., Xiao, S., Håkonsen, V., Li, T., **Wang, F.**, He, J., & Zhang, Z. Ultrafast self-healing and highly transparent coating with mechanically durable icephobicity. *Applied Materials Today*, 2020, 19, 100542.
7. He, Z., Zhuo, Y., **Wang, F.**, He, J., Zhang, Z. Design and preparation of icephobic PDMS-based coatings by introducing an aqueous lubricating layer and macro-crack initiators at the ice-substrate interface. *Progress in Organic Coatings*, 2020, 147, 105737.

Contents

Chapter 1 Introduction

1.1 Project Background

Preventing the formation and accretion of ice on exposed surfaces is of great importance for renewable energy, electrical transmission cables in air, shipping, Arctic operation, and many other applications. In the last decade, significant progress in creating superhydrophobic surfaces has been made. Superhydrophobicity was once believed to be the prerequisite for icephobicity. However, it is now under debate as whether there is an essential correlation between superhydrophobicity and icephobicity. While the understanding in superhydrophobicity is becoming mature, the research on icephobicity has just touched the tip of the iceberg. The majority of the efforts in the literature target delaying ice nucleation by texturing the surface micro- and nanostructures. In this project, we choose a different roadmap to icephobicity, namely, living with ice, but with the lowest possible ice adhesion!

1.2 Objectives of the research

This PhD work is one part of the researcher project - Towards Design of Super-Low Ice Adhesion Surfaces (SLICE), which is financed by the Research Council of Norway via the FRINATEK Program. The objective of the research is to develop multiscale models to maximize the functions of multiscale interface crack initiators.

- Further fundamental understanding of ice-solid adhesion at various length scales.
- Establish multiscale models for predicting ice adhesion strengths.

- generate novel concepts and design principles for engineering weak ice-solid interfaces and achieving super-low ice adhesion.
- develop and demonstrate model materials with super-low ice adhesion.

1.3 Thesis Highlights

The thesis develops a deep understanding on the fundamentals of the emerging DAIS and presents a systematic study on the design principles of the same surfaces. Two kinds of anti-icing surfaces through controlling dynamic performance of substrate and ice-substrate interface are deigned and investigated. The highlights of this thesis are summarised as following:

- A concept called “dynamic anti-icing surfaces” are proposed.
- The dynamic nature means the chemical/physical states of the ice/substrate/ice-substrate-interface can evolve after ice formation.
- The state-of-the-art DAIS are classified.
- Phase transformable slippery liquid infused porous surfaces (PTSLIPS) are designed.
- PTSLIPS show low ice adhesion strength (4.45∼22.43 kPa) as well as excellent durability.
- PTSLIPS indiscriminately adapt to porous substrates with various chemical compositions.
- PTSLIPS also possess self-repairing property that could repair the bulk damage.
- Liquid layer generators (LLGs) that can dynamically release ethanol to ice-substrate interface are designed.
- Atomistic modelling and simulations are employed to explore the excellent lubricating effect of ethanol layer at the ice-solid interface at various temperatures (down to -60 °C).
- Two kinds of LLG, packing ethanol inside the substrate (LLG 1) and storing replenishable ethanol below the substrate (LLG 2) are fabricated.

- LLG 1 can constantly release ethanol for a maximum of 593 days without source replenishment.
- The LLGs exhibited super-low ice adhesion strengths of 1.0 ~ 4.6 kPa and 2.2 ~ 2.8 kPa at -18 °C.
- For selected samples, by introducing an interfacial ethanol layer, the ice adhesion strength on the same surfaces decreased in an unprecedented manner from 709.2 ~ 760.9 kPa to 22.1 ~ 25.2 kPa at a low temperature of -60 °C.

1.4 Thesis Outline

The thesis consists of an introductory section and a collection of six peer-reviewed papers. The introductory contains four chapters. In **Chapter 1**, the project background, objectives and thesis highlights are briefly stated. In **Chapter 2**, a literature review is presented. In **Chapter 3,** the main results that involved in this thesis are summarized. In **Chapter 4**, the conclusions and perspectives are given.

Chapter 2 Literature Review

For a long time, anti-icing surfaces that can mitigate ice problem are desired. Despite the remarkable progress made in surface icephobicity in recent years, there is a major view of static ice-substrate interface projected on the reported anti-icing surfaces. By in-depth monitoring the crucial locations to ice adhesion, namely in the substrate, ice, or the ice-substrate interface, the available anti-icing surfaces are classified by fundamental dynamic principles. The DAIS focus at the dynamic changes of the chemical/physical states of the ice/substrate/ice-substrate-interface for enhancing anti-icing performances, providing a new insight for design novel anti-icing surfaces.

2.1 Introduction

Icing is one of the most common natural phenomena that widely impact human activities. Undesired ice formation and accumulation can introduce numerous severe function and safety problems to aircrafts, power grids, transmission lines, roadways, marine vessels, renewable energy infrastructures, and many others.[1-8]. The traditional methods used for dealing with icing problems, for instance mechanical de-icing, thermal or chemical treatments, are often highly costly and low-efficient[9, 10]. As such, enormous interests have been aroused in deploying surfaces that can control icing and mitigate its related damages. Advanced surfaces with properties like repelling incoming water droplets, delaying ice nucleation, repressing ice growth and weakening ice adhesion are designed for anti-icing purpose[11-14]. From the early lotus-leaf inspired superhydrophobic surfaces fabricated for repelling water droplets and delaying ice nucleation, to the recent omniphobic pitcher-plants-inspired slippery liquid-infused porous surfaces (SLIPSs)

developed for delaying ice nucleation, suppressing frost formation and lowering ice adhesion[11, 12, 15-19, 20-24], there are currently a colourful spectrum of anti-icing surfaces in the literature showing low ice adhesion strength (0.2 ~ 10 kPa) and easy achievable large-scale ice remove capacity[25-27]. It is witnessed that there is a shift in anti-icing surfaces design philosophy from being of static nature, namely no change at the ice-substrate contact area after ice formation, to enabling dynamic changes of the chemical/physical states of the ice/substrate/ice-substrate-interface in order to enhance anti-icing performances. The static anti-icing surfaces functioned to a limited extent, and had deficiencies in icing/deicing cycling durability, inapplicability at extremely low temperature, fragility to surfaces damage and surfaces degradation, and inadaptability to environment changes[16-18, 28-33]. In contrast, the emerging DAIS, thanks to the integrated dynamic properties into the substrate, ice, or the ice-substrate interface, exhibit superior durability, wider temperature tolerability and better environment adaptivity, and are attracting increasing interests[14, 34-39]. This introduction section of this thesis provides a survey and comparison on the static anti-icing surfaces and DAIS. The static anti-icing surfaces contain superhydrophobic surfaces, SLIPSs, interfacial slippage surfaces, and so on. The DAIS include dynamic substrate change, dynamic interface change, and dynamic ice change surfaces.

2.2 Static anti-icing surfaces

Despite the remarkable progress made in surface icephobicity in recent years, the anti-icing surfaces are generally designed from a static perspective, for instance, texturing the surfaces structures, tuning the modulus of substrates, modifying the surfaces energy without considering the property evolution. One of the key characteristics is that the ice-substrate contact area after ice formation is assumed to be constant. The main focus was put on conditions before ice formation not the dynamic changes after icing.

2.2.1 Superhydrophobic surfaces

The lotus-leaf-based superhydrophobic surfaces (SHS) with high contact angles (CAs) and low water adhesion force have received tremendous scientific interest recently[40-43]. The anti-icing performances of SHS have been widely discussed[29, 30, 44-47]. The

icephobicity of SHS includes repelling coming water, delaying ice nucleation and decreasing ice adhesion strength.

Through investigating the icing process of impinging droplets, Mishchenko et al. found the superhydrophobic surfaces can stay ice-free even with temperature down to -25 ~ -30 ℃[11]. The behaviours of single droplets impinging upon the hydrophilic, hydrophobic and superhydrophobic surfaces were recorded. Three states, maximum spreading (r_{max}), maximum retraction (r_{min}) and freezing were compared both on tilted and horizontal surfaces (Fig. 2.1a). It was found that hydrophilic surfaces showed $r_{max} \approx r_{min}$, resulted in large contact area and rapid freezing of water. The droplet impinged onto the smooth hydrophobic surface had $0 < r_{min} < r_{max}$, the droplet could not fully withdraw and freeze on the surface. As a comparison, the droplet on the superhydrophobic surface retracted completely with $r_{min} \approx 0$, hence no ice formed on the surfaces. Therefore, due to the excellent droplets bouncing off performance, the superhydrophobic surfaces can prevent ice formation at very low temperature.

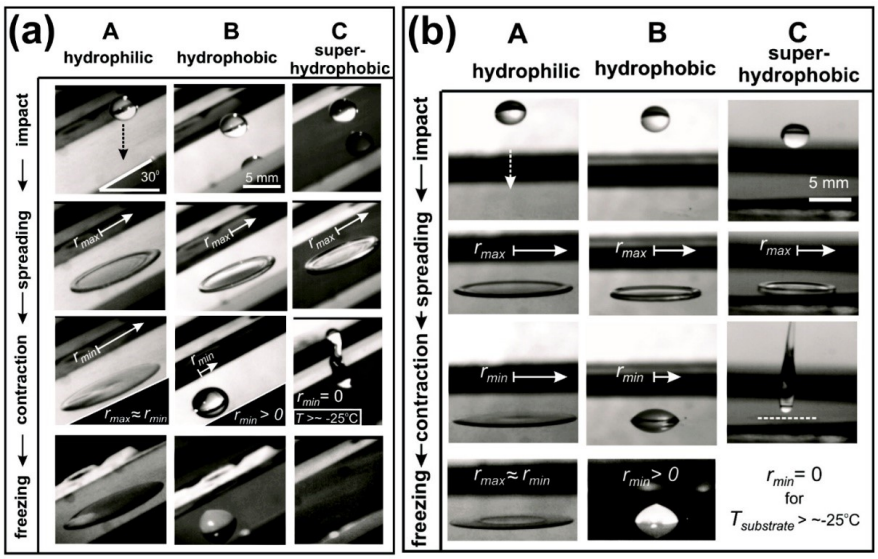

Figure 2.1. Water droplets impinging upon cooled (a) 30° tilted and (b) horizontal surfaces ($T_{substrate}$ < 0 °C) from a 10 cm height[11]. Copyright © 2010 American Chemical Society.

The superhydrophobic surfaces can effectively suppress heterogeneous ice nucleation and delay the freezing of droplets that stand on the surfaces[48-50]. Alizadeh et al. compared

the ice nucleation behaviours on the hydrophilic, hydrophobic and superhydrophobic surfaces. Water droplets were impinged onto the substrates at a velocity of 2.2 m/s, the substrates temperature was fixed at -20 °C. The transient temperature curves showed the heat transfer between the droplet and the substrates (Fig. 2.2). The ice nucleation was closely related to the surface hydrophobicity. The ice freezing happened almost immediately once the droplet was placed onto the surface. While the water droplets on the superhydrophobic surface held much longer time before ice nucleation initiated. The water-substrate interface was the dominant factor that controlled icing. The superhydrophobic surfaces decreased the water-substrate interfacial area and increased the nucleation activation energy, which led to a drastic reduction in the nucleation time (delayed freezing). It was concluded that the superhydrophobic surfaces can effectively delay ice nucleation at very low temperature.

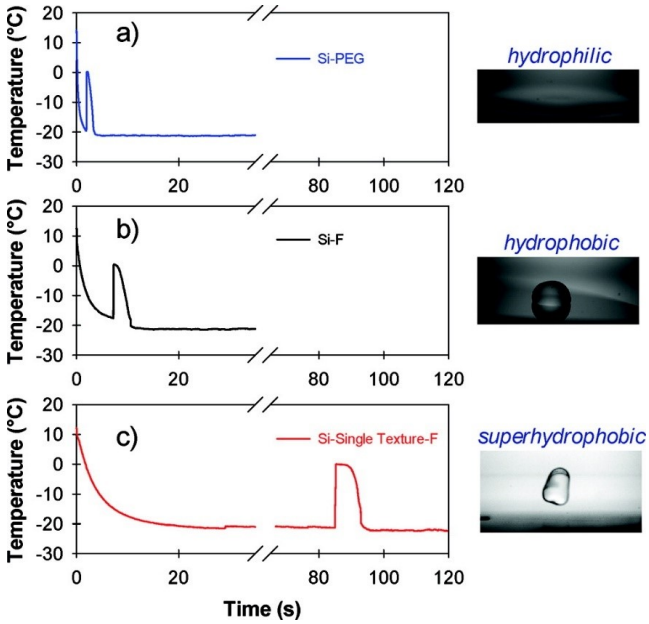

Figure 2.2. Transient temperatures of 4 μL DI water droplet freezing on (a) hydrophilic (b) hydrophobic and (c) Si- superhydrophobic substrates[48]. Copyright © 2012 American Chemical Society.

The ice adhesion strength on the superhydrophobic surfaces were also investigated[18, 28, 29, 51-54]. The superhydrophobic surfaces generally showed low ice adhesion strength at the first test, because of the minimized contact area between ice and the substrates.

However, the surfaces asperities can be easily damaged in the subsequent icing/deicing cycles[18]. The anti-icing performance of the superhydrophobic surfaces decay very fast. It was also found that ice adhesion strength in the humid atmosphere was significantly large for the ice formed in the textured surfaces.

2.2.2 Slippery liquid-infused porous surfaces

The pitcher plant-inspired SLIPSs are created by infiltrating a surface of micro/nano-pores with a lubricating liquid. The lubricant layer atop the substrates enabled the surfaces with excellent repellence to any immiscible materials. Kim et al. firstly investigated the icephobicity of liquid-infused aluminium surfaces[21]. The ice adhesion strength decreased dramatically from more than 800 kPa on Al surfaces to around 16 kPa on SLIPS-coated Al surfaces. As shown in the Fig. 2.3, the frost formation behaviours on the SLIPS-coated Al was significantly different to the untreated Al. With tilt angle of 75°, the condensed droplets on the SLIPS-coated Al slide away easily before freezing and resulted in frost-free surfaces. However, the condensed water on the Al surfaces stay atop and formed ice in short time and resulted in high frost coverage. The extremely low ice adhesion strength on the SLIPSs made them one of the best strategies for design icephobic surfaces. In general, SLIPSs enabled the possibility of self-removal of accreted ice by gravity, wind or vibration. However, the durability of SLIPSs remains as a huge challenge since the lubricant were easily to be exhausted in the practical usage[31, 33, 55].

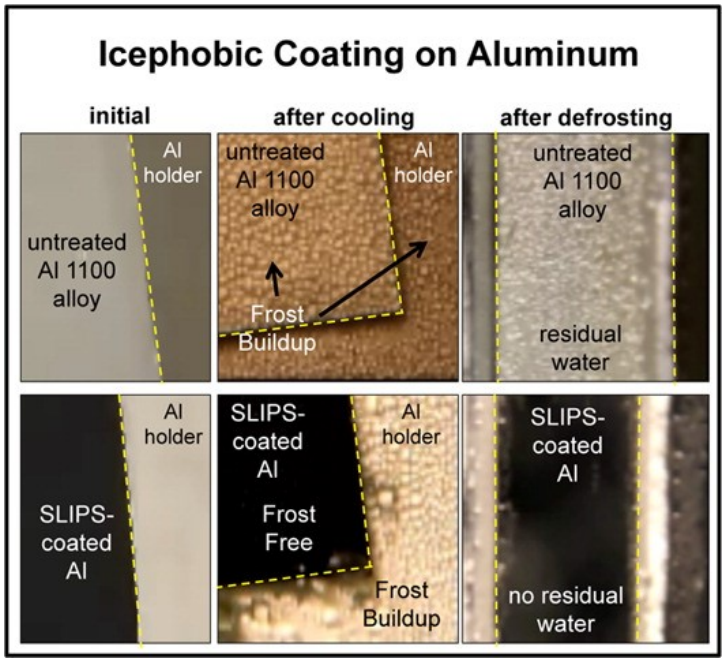

Figure 2.3. The anti-frost performance on the lubricant infused Al surfaces[21]. Copyright © 2012 American Chemical Society.

2.2.3 Interfacial slippage surfaces

Recently, with the purpose of design surfaces with low ice adhesion strength ($\tau_{ice} < 20$ kPa), Golovin et al. fabricated elastomers with interfacial slippage capacity[25-27]. The interfacial slippage surfaces were fabricated through tailoring the cross-link density and altering the no-slip boundary condition. Unlike the lubricating-infused surfaces, there was no visible lubricating oil on the surface, the phase distribution in the interfacial slippage surface was equivalent. Attributing to the interfacial slippage, extremely low ice adhesion strength ($\tau_{ice} < 0.2$ kPa) was achieved. The coatings achieved by this design had homogeneous distributed microstructures, therefore, the surface damage did not affect the icephobicity of the surfaces. In the icing/abrasion tests, the lubricated surfaces lost their icephobicity in short cycles, however, the interfacial slippage surfaces maintained excellent icephobicity as shown in the Fig. 2.4. However, the lubricant introduced for tuning the cross-link density were likely to weaken the mechanical strength of the polymer.

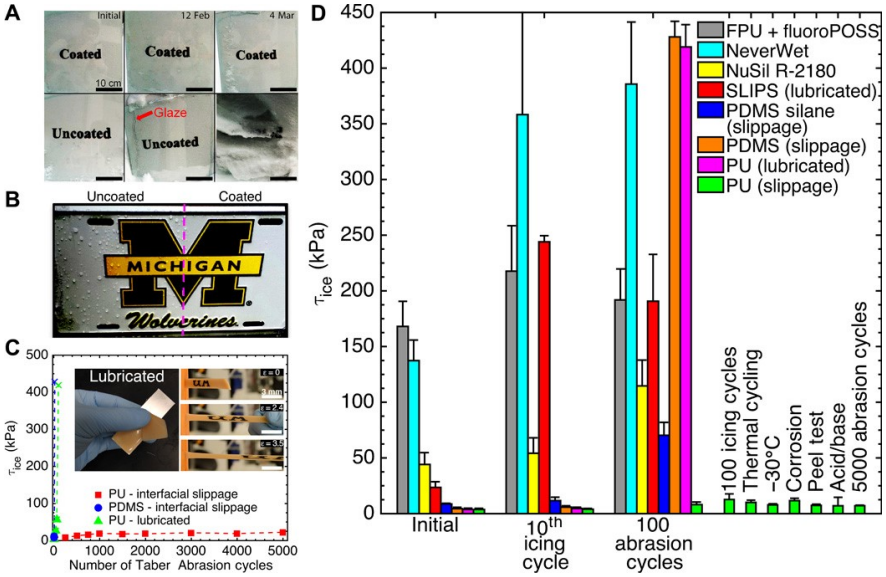

Figure 2.4. The durability of icephobic coatings with interfacial slippage[25]. Copyright © 2016 American Association for the Advancement of Science.

2.3 Dynamic anti-icing surfaces (DAIS)

All the three kinds of anti-icing surfaces introduced above, together with some other anti-icing surfaces represent remarkable progress for icephobic surfaces design. However, the design principles are generally based on the static point view of understandings of the ice-substrate contact regions, that is, no change at the ice-substrate contact area after ice formation. By looking from the viewpoints of dynamic aspects, enabling evolution at the ice-substrate contact regions after ice formation, DAIS can be expected and provides novel insights for anti-icing surfaces design. Focusing on the most relevant ice-substrate interfacial regions (Fig. 2.5a), and their spontaneous/stimuli-responsive changes in chemical/physical states impacting ice adhesion during and after ice formation, for the first time we classify the state-of-the-art DAIS into three categories, namely surfaces with dynamic substrate changes, with dynamic interface changes, and with dynamic ice changes as shown in Fig. 2.5b. Surfaces with dynamic changes in the substrate generally include functional structures that can response to internal and external stimuli, which can modify the substrate properties and enhance anti-icing performances[35, 36, 56-59]. Surfaces with dynamic changes at the ice-substrate

interfaces after ice formation provide the possibility of altering interface interactions for lowering ice adhesion[14, 34, 38, 39, 60-62]. Surfaces with dynamic changes in the ice are able to direct ice growth, propagation and even ice melting, which can mitigate ice accumulation and assist ice remove on the surfaces[13, 37, 63-69]. The following sections detailed these three categories of anti-icing surfaces.

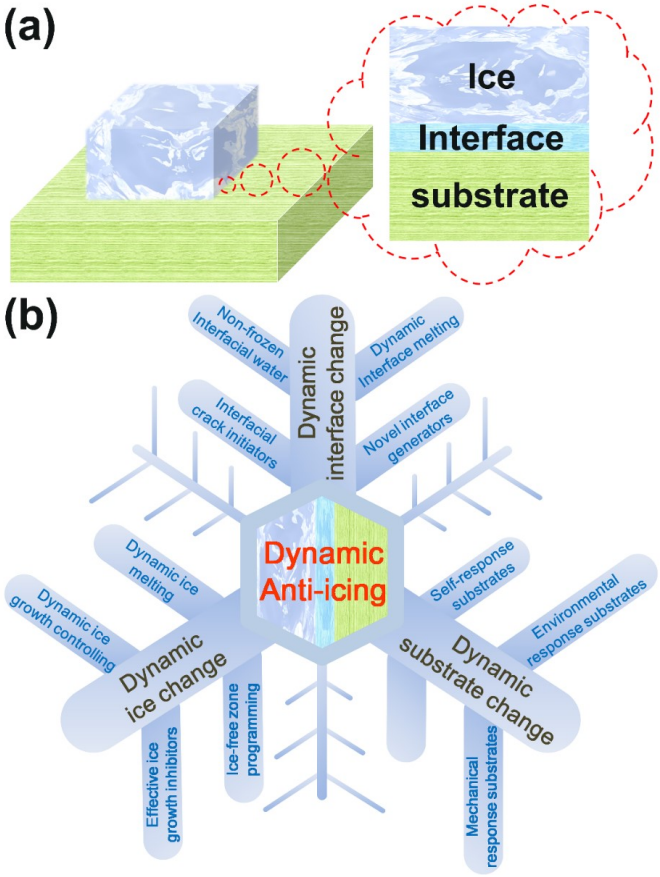

Figure 2.5. DAIS. (a) The three most important regions close to the ice-substrate interface that determine anti-icing performance of a surface. (b) Dynamics anti-icing surfaces targeting the three ice-substrate interfacial regions. The dynamic substrate change includes substrates that can response to the internal/external conditions, namely those by tuning the surface state and affecting the ice formation/adhesion. The dynamic interface change covers the surfaces that can induce dynamic conversion of the chemical/physical states of the ice-substrate interface after ice formation, thus facilitating easy ice removal. The dynamic ice change encompasses the surfaces that can tailor ice growth, propagation or even melt ice for the purpose of mitigating ice accumulation.

2.3.1 DAIS with dynamic substrate change

2.3.1.1 Self-response substrates

Many surfaces exhibit dynamic changes by self-response to their internal forces. Such self-response surfaces widely exist in natural organisms and systems. For instance, earthworms and poison dart frogs have secretion glands under their skin, which release lubricant to form a slippery layer above the skin (Fig. 2.6a)[70, 71]. Surface lubricating is driven by the under-skin disjoining pressure or concentration gradient[57, 72]. The mechanism underlies self-response surfaces has inspired the design of anti-icing surfaces with embedded lubricant in the substrates.

One notable self-response substrate was developed through phase separation as shown in the Fig. 2.6b. The surface lubricant layer was regenerable under the driving force of disjoining pressure originated from the van der Waals interactions at the gel surface[72]. It is intriguing that both the thickness of the lubricant layer and the size of the embedded droplets in this substrate were controllable through polymer crosslinking strength and oil content, which offered a strategy for preparing similar substrates for improving anti-icing performace[56-58, 71, 73-82]. Icephobic surfaces following the same strategy for surface regenerable lubricant layers indeed showed ice adhesion strength below 40 kPa[56], with regenerative lubricating layers after 15 wiping/regenerating tests and long-term ice adhesion strength below 70 kPa. Through a precise deploying of polymer and oil, recently reported novel self-lubricating organogels (SLUGs) displayed extremely low ice adhesion strength of 0.4 kPa[58]. The ice formed on the SLUGs samples with small tilting angles could slide off at -15 ℃, which demonstrated the great potential of self-response substrates in anti-icing.

Beside small liquid oil molecules, solid lubricants were also used in self-response substrates for regenerating surface lubricating layers to assist easy ice removal[57, 76]. For example, alkane embedded in a polymer substrate can diffuse into the surface driven by concentration gradient and the internal stress of the polymer matrix, resulting in a solid alkane layer as shown in Fig. 2.6c. The regenerable solid lubricant alkane had weak interactions with the polymer substrate and served as sacrificial layer in ice removal,

which enable low ice adhesion strength (~ 9 kPa) and good durability in 20 icing/de-icing cycles[57].

Surface damages in practical applications are severely harmful to the icephobicity of anti-icing surfaces, since any possible interlockings between ice and surface voids can greatly enhance ice adhesion. As such, self-response substrates with self-healing functionality were fabricated for anti-icing purposes[35, 36, 73, 83-87]. Such substrates showed significant improvements in mechanical durability because of the ability of self-healing surface damages at sub-zero temperature to maintain smooth topography (Fig. 2.6d). One of the self-healing substrates, Fe-pyridinedicarboxamide-containing PDMS (FePy-PDMS) elastomer, exhibited low ice adhesion strength of ~ 6 kPa and ~ 12 kPa after 50 icing/de-icing cycles[36].

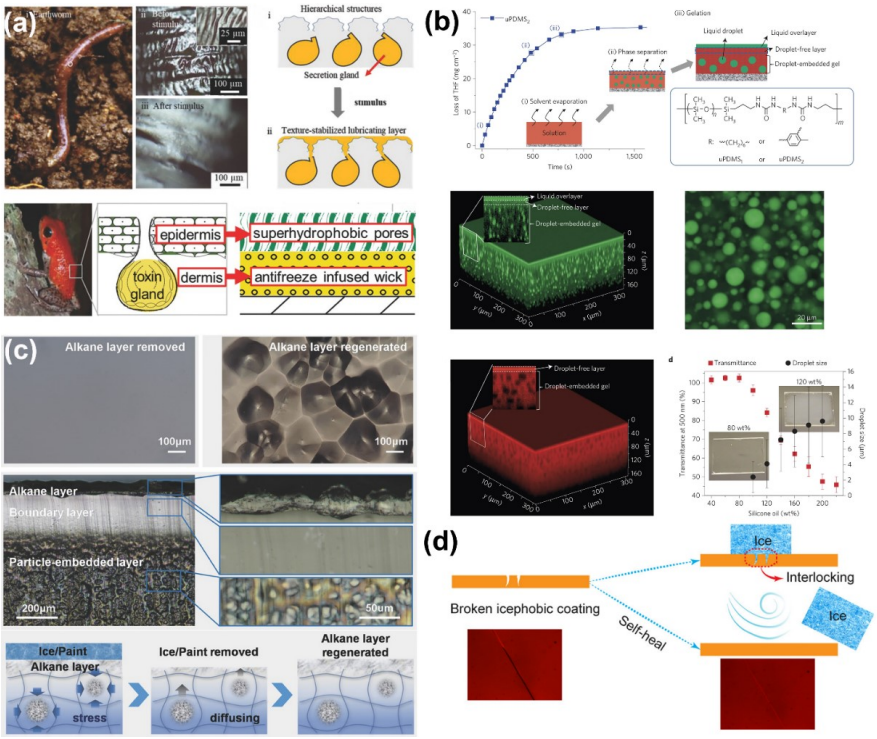

Figure 2.6. Selection of DAIS through self-response substrates. (a) The lubricant regenerable systems in earthworm and poison dart frog[70, 71]. Copyright © 2018 Wiley Publishing Group and 2015 Wiley Publishing Group. (b) The droplet-embedded gel structure, and its secreted surface lubricating film[72]. Copyright © 2015 Nature Publishing Group. (c) The alkane-embedded structure, showing the renderability

of the surface alkane layer, the alkane distribution in the substrate, and the regeneration mechanism of the solid alkane layer[57]. Copyright © 2017 Wiley Publishing Group. (d) The schematic of the self-healing icephobic surface with fabricated samples[36]. Copyright © 2018 American Chemical Society.

2.3.1.2 Environmental response substrates

Many anti-icing surfaces use dynamic substrates that response to the ambient conditions of temperature, magnetic field, light, and so on[35, 59, 88-96]. By integrating temperature sensitive components during fabrication, anti-icing substrates can response to temperature change of the surrounding environment[59, 88]. One of such substrates incorporated a binary liquid mixture (silicon oil and liquid paraffin) into a PDMS network, the resulting reversibly thermo-secreting organogel (RTS-organogel) demonstrated distinct morphologies at different temperature as shown in Fig. 2.7a[59]. The ice adhesion strength on the RTS-organogels were less than 1 kPa at -15 ℃, which can enable sliding of ice cube on the surface samples with small tilting angles. The RTS-organogels were believed to be more durable than the SLUGs, because they could reversibly absorb lubricant into the polymer matrix for replenishing the internal lubricants in storage and against evaporation/contamination.

Liquid lubricants in anti-icing substrates can deplete in limited number of icing/de-icing cycles due to the weak interaction between the lubricant and the base materials, which leads to poor durability. As shown in the Fig. 2.7b, a phase transformable lubricant was used in creating the so-called phase transformable slippery liquid infused porous surfaces (PTSLIPS) recently[35]. Because the lubricant had phase transition point from liquid to solid phase at ~ 3 ℃[35], the durability of the fabricated PTSLIPS was greatly improved, showing a lowest ice adhesion strength of ~ 4 kPa and long-term ice adhesion strength of 16 kPa after 30 icing/de-icing cycles. It is worth noting here that similar phase-change materials (PCMs) were introduced into concrete for anti-icing. During the phase transition upon cooling, the PCMs released substantial latent heat and can hinder ice accumulation in walking pavements[89-91, 97-99].

Magnetic field is relatively less commonly applied in anti-icing practice. However, utilizing magnetic field as stimuli to modulate substrates has been explored, with encouraging results illustrating the potentials of active de-icing technology[92, 93, 95]. The magnetic slippery surfaces (MAGSS) can response to external magnetic field and

generate a volumetric force to suppress water droplets from sinking into the substrate body with bulk oil, which led to small water droplet sliding off angle of 2.5°, as shown in Fig. 2.7c[92]. Remarkably, the MAGSS can maintain its liquid-like phase at low temperature and were highly slippery to ice, showing extremely low ice adhesion strength (~ 2 Pa) without degradation after 60 icing/de-icing cycles.

Light is another important stimulus source for triggering dynamic changes in anti-icing substrates[100-103]. By integrating light-absorbing azobenzene groups into polymer skeleton of the base materials, the so-called UV responsive substrates (UVRS) were able to utilize UV energy for polymer chain conformation conversion[94]. As shown in Fig. 2.7d, the integrated azobenzene groups in the UVRS changed from trans- to cis-conformation under UV light with a wavelength of 365 nm, resulting in slight compress of the whole substrate. The pre-embedded silicon oil in the polymer matrix of the UVRS was released to the substrate surface as a response to the compressive stress, which enabled low ice adhesion strength of 21 kPa and long-termed ice adhesion strength of 47 kPa after 15 icing/de-icing cycles on the UVRS. The light stimuli can also have thermal effects, which further inspired the design of photothermal response substrates[96].

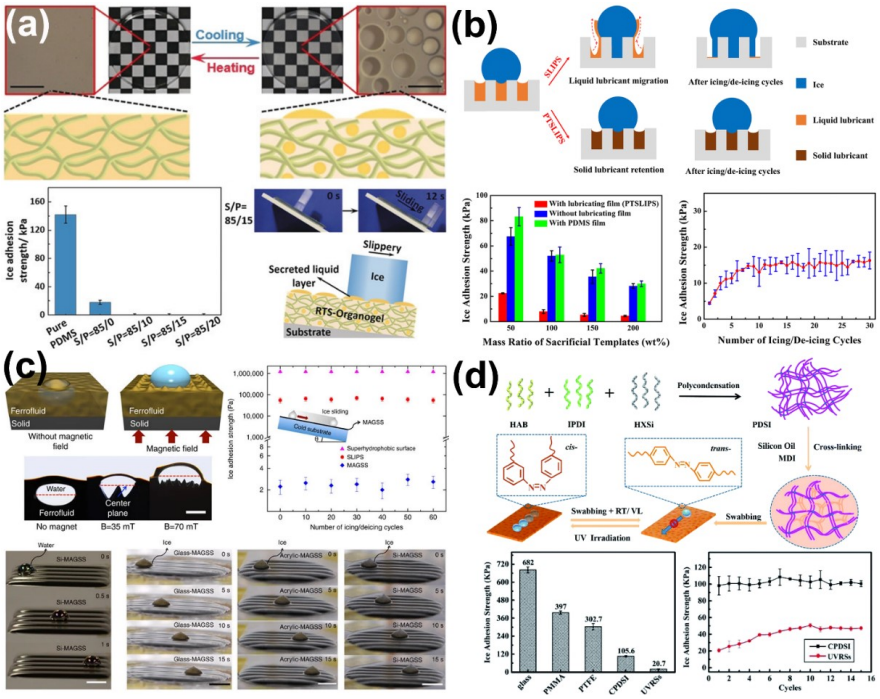

Figure 2.7. Representatives of the DAIS through environmental response substrates. (a) The thermal response lubricant regenerable organogel, showing the droplets secretion at low temperature and reversible droplets absorption at high temperature[59]. Copyright © 2020 Wiley Publishing Group. (b) The phase transformable slippery liquid infused porous surfaces (PTSLIPS)[35]. Copyright © 2019 Elsevier Publishing Group. (c) The magnetic slippery icephobic surfaces[92]. Copyright © 2016 Nature Publishing Group. (d) The UV-responsible substrates (UVRSs)[94]. Copyright © 2020 Royal Society of Chemistry.

2.3.1.3 Mechanical response substrates

Ice removal generally involves stress change on the ice adhered surface. Mechanical response substrates are designed to utilize the stress associated with ice removal to dynamically alter the surface structures in order to achieve low ice adhesion. The surface structures that response to the mechanical force can be both molecular structures in base materials and geometrical patterns above the surfaces[104, 105]. Notably, an ultra-durable icephobic coating was designed by introducing slide-ring crosslinkers, namely molecular pulleys, into PDMS base matrix (Fig. 2.8a)[104]. The slide-ring crosslinkers were not only able to move along the polymer chains under mechanical loading, but also can return to their original state *via* entropic repulsion upon relieving loading[106, 107]. The slide-ring

substrate showed a low ice adhesion of ~ 12 kPa during 20 icing/deicing cycles, and promising ice adhesion strength ~ 22 kPa after 800 abrasion cycles, being one of the most durable elastomers reported so far.

In another report, an interesting fish-scale-like dynamic anti-icing surface prototype was introduced[105]. Because the atomistic interactions ruptured all at once in concurrent rupture mode but incrementally in the sequential rupture mode, opening of the surfaces structure in ice removal featuring the sequential rupture of ice was essential for low ice adhesion. Inspired by the structure topology of fish scales, the fish-scales-like surface was designed by pile arrangement of graphene platelets in atomistic modelling. Under de-icing forces, the graphene platelets dynamically opened up to enabling sequential rupture of ice from the surface (Fig. 2.8b), which led to a ~ 60 % reduction in ice adhesion strength. The theoretical model of fish-scale-like surface was a good starting point of mechanical response structure design for low ice adhesion.

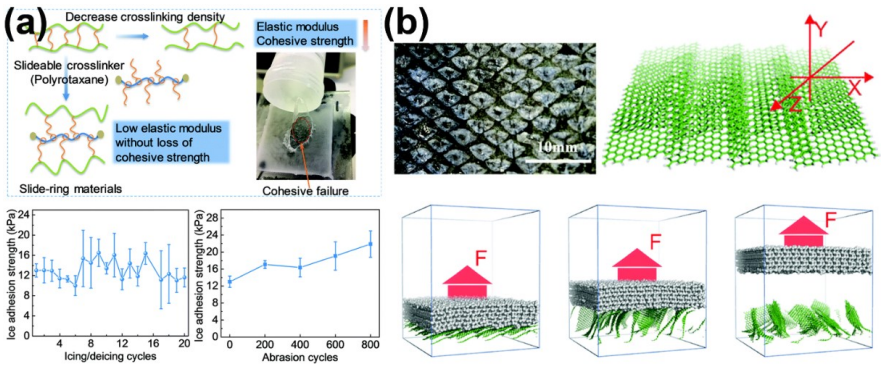

Figure 2.8. Representatives of the DAIS through mechanical response substrates. (a) The slide-ring substrate, showing its molecular mechanism and the enhanced cohesive strength and excellent durability[104]. Copyright © 2019 Royal Society of Chemistry. (b) The fish-scale-like surface, showing sequential rupture of atomistic interactions for lowering atomistic ice adhesion[105]. Copyright © 2019 Royal Society of Chemistry.

2.3.2 DAIS through dynamic interface changes

2.3.2.1 Non-frozen interfacial water

The importance of the ice-substrate interface to ice adhesion is self-evident. It is known that ice is slippery to ice-skating blades, meaning low adhesion strength, due to a surface premelted layer[108]. The premelted liquid or liquid-like aqueous layer exists on the ice surfaces at sub-zero temperature because of regelation or by pressure or friction melting[108-112], which applies not only at ice-vapor but also ice-solid interfaces[113, 114]. As the thickness of the premelted layer at ice-solid interfaces was shown to increase with temperature, utilizing and amplifying the premelted layer for effectively reducing ice adhesion became one of the important strategies of surface icephobicity[115]. Because the premelted layers have thickness at the nanoscale, atomistic simulation and molecular dynamic simulation were employed to investigate their mechanical effects on the nanoscale ice adhesion[116]. As shown in Fig. 2.9a, ice-cube models with premelted interfacial water layers on solid substrates showed negligible ice adhesion stress if compared with ice directly contacted with the solid substrate. Related studies focused on the lubricating effect of the premelted or non-frozen interfacial water layer further supported the potential of utilizing aqueous layer for mitigating icing problems[116-118].

Although interfacial non-frozen water layers were identified at the ice-solid contact interfaces as early as in 2004, intensive experimental explorations on their application in anti-icing came much later[114, 115]. Through rational nano-structuring of solid surfaces for creating an interfacial quasi-liquid layer, ice formation can be delayed for 25 hours at -21 °C[50]. Yet, ice formation is inevitable with long enough icing time. As ice adhesion on certain solid surfaces, such as SiO_2, Si, Au and so on, are too high to any ice removal approach[119, 120], new strategies that could program non-frozen interfacial water on such surfaces for low ice adhesion were in great needs. Using highly hydrated ions were believed to be a good approach for creating quasi-liquid layers (QLL) on solid surfaces, because ions can greatly impact the structure of water and supress ice nucleation[121]. Polyelectrolyte brushes hosting ions were employed to probe the effects of counter ions on ice adhesion (Fig. 2.9b)[122]. It was found that the polyelectrolyte brushes with kosmotropic counterions (G-$SO^{3-}Li^{+}$, G-$SO^{3-}Na^{+}$) had maximum ice adhesion reduction (25 ~ 40 %) comparing to the bare glass (G) at -18 °C, because of the most negative

water structural entropy resulting from strong hydration. In comparison, the polyelectrolyte brushes with chaotropic counterions (G-SO_3^- K^+, G-N^+Cl^-, and G-$N^+SO_4^{2-}$) did not change the ice adhesion, owing to positive water structural entropy of weak hydration[121]. This study provided important reference for integrating counterions for related anti-icing applications[123, 124].

To improve the lubricant effects for extremely low ice adhesion, the thickness of QLL needs to drastically increase. The state-of-the-art liquid-like surfaces, for instance the slippery omniphobic covalently attached liquid surfaces (SOCAL), still exhibited limited thickness of QLL, which restricted ice removal[125-127]. Recently, a non-stick and extremely flexible quasi-liquid surface (QLS) with a coating thickness of 30.1 nm (Fig. 2.9c)[128], which enabled extreme flexibility and quasi-liquid thickness of the surface. The QLS had omniphobic nature with low ice adhesion strength of ~ 26 kPa, and enabled de-icing by air flows (mimicking wind power).

Although the surfaces with quasi-liquid layers are highly favourable for lowering ice adhesion strength, maintaining the durability of the grafted polymer chains on such surfaces exposed to mechanical damages was still challenging. One other difficulty of applying quasi-liquid layers emerges when surfaces roughness scale is larger than the layer thickness. To address these two problems, a robust and durable anti-icing coating fabricated by polymers (polyurethane, PU) with hydrophilic pendant groups was newly reported[119]. The hydrophilic component dimethylolpropionic acid (DMPA) in the coating could absorb water directly from its humid environments or from the contacted ice/snow due to the ion effect (Fig. 2.9d), which resulted in aqueous lubricating layers on the coating surface as long as ice is formed. Surface samples coated by the coating contained 9 wt% DMPA (PU-9) maintained stable and low ice adhesion strength of 27 kPa at temperature as low as -53 °C, and showing almost no change after 30 cycles. It was believed that the coating was adaptable on almost all surfaces including rough ones (Fig. 2.9d, right bottom). The fabrication strategy of the coatings, incorporating hydrophilic pendant groups in soft polymer for aqueous lubricating layer, was thus widely employed in similar studies[38, 62, 120, 129-134].

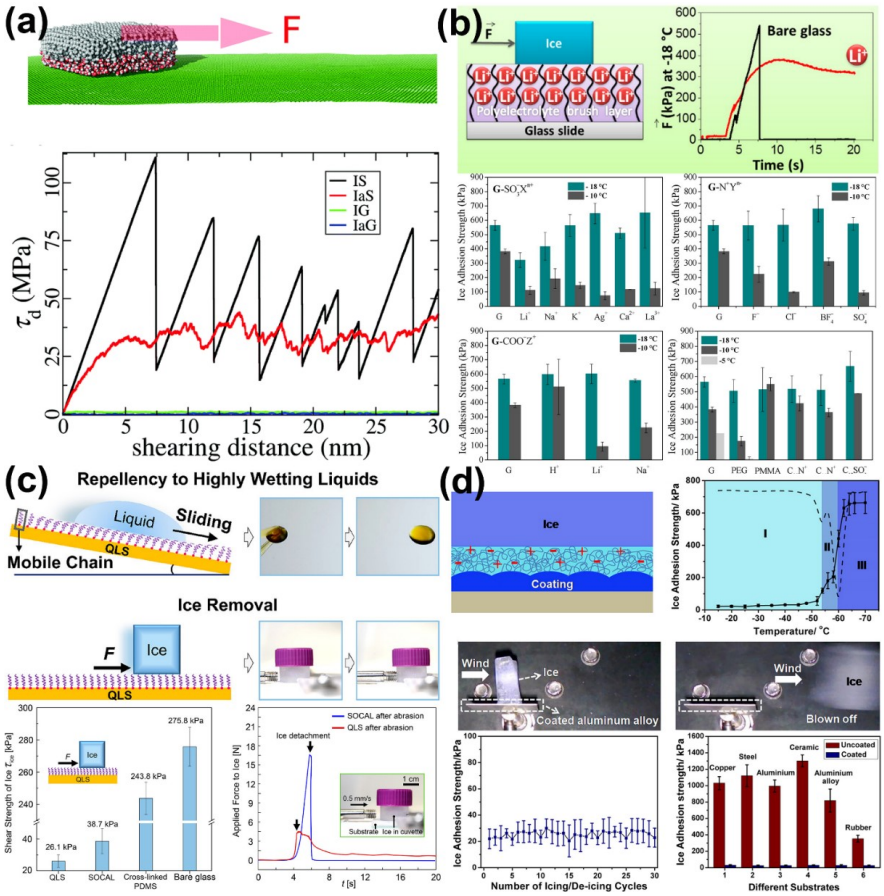

Figure 2.9. Non-frozen interfacial water layer and the representatives of the DAIS. (a) Atomistic modelling and simulation of ice adhesion on different surfaces with/without an interfacial aqueous water layer[116]. Copyright © 2016 Royal Society of Chemistry. (b) The ice adhesion on the bare glass (G) and on polyelectrolyte brush layers comprising of different types of counterions (X^{n+} = Li^+, Na^+, K^+, Ag^+, Ca^{2+}, $C_{16}N^+$, La^{3+}; Y^{n-} = F^-, Cl^-, BF_4^-, $C_{12}SO_3^-$, SO_4^{2-}; and Z^+ = H^+, Li^+, $C_{16}N^+$, Na^+)[122]. Copyright © 2014 American Chemical Society. (c) The liquid repellence and ice removal property of the quasi-liquid surface (QLS)[128]. Copyright © 2020 American Chemical Society. (d) The reduction of the ice adhesion strength by an aqueous lubricating layer[119]. Copyright © 2014 American Chemical Society.

2.3.2.2 Dynamic interface melting

The thickness of aqueous lubricant layers introduced above were generally in nanoscale, varying from a few molecules thickness to tens of nanometer[119, 128]. Interfacial aqueous layer with such thickness range can lead to ice adhesion strength of ~ 20 kPa,

which was good but still beyond the requirement for practical anti-icing application (lower than ~ 12 kPa)[14, 25, 26]. To increase the lubricant effects of aqueous lubricant layer, DAIS that could melt the interfacial ice and create thicker aqueous layer were developed. In the most straightforward manner, the dynamic melting of interfacial ice could be initiated by chemicals (anti-freeze liquid or salts) or thermal energy (magnetic thermal energy, electrothermal energy and photothermal energy) that have long been used in active de-icing techniques for pavement, aircraft, power line systems, and so on[4, 61, 135-146]. In contrast to the high costs and the detrimental environmental impacts of the traditional de-icing methodologies, the recent approaches of introducing active anti-icing agents into passive anti-icing substrates with dynamic change ice-substrate interfaces had shed new light on compromising solutions for ice removal with minimize energy/chemicals input[60, 64, 68, 71, 147].

It is well known that high ice adhesion strength is generally observed on superhydrophobic surfaces if the interlocking happens between ice and the surface hierarchical structure of the surfaces[16-18, 28-30, 148]. Using anti-freeze agents on superhydrophobic surfaces to create liquid interface can provide a practical solution, as demonstrated by a newly fabricated superhydrophobic copper mesh with organogel that can dynamically secrete anti-freeze agents[60]. Specifically, PVA grafted succinic acid (PVA-COOH) on the copper mesh containing anti-freezing agents (mixture of ethylene glycol and water) that were dynamically released at sub-zero temperature to the ice-substrate interface and melted the neighbouring ice. As shown in the Fig. 2.10a, ice adhesion strength of PVA-COOH (0.73 wt%) decreased from ~ 1.3 kPa to < 0.001 kPa by increasing the holding time after ice formation from 1 h to 5 h. For selected samples, the ice cube fallen off automatically after 15 h on the substrate with small tilting angle, showing excellent ice self-removal capacity.

Ionic liquids were also selected as anti-freeze agents for interface melting. Ionic liquids are commonly integrated in ionogels, which are utilized in many fields ranging from solid electrolytes to drug release and to catalysis[149-155]. Ionogel surfaces consisted of ionic liquid and polymer components were introduced for anti-icing, as depicted in Fig. 2.10b[68]. The lubricant layer on the one hand suppressed ice nucleation, on the other hand lowered the ice adhesion to the surfaces. The thickness of interfacial liquid layer

on the ionogel surface increased with holding time, as the ice-substrate interface was dynamically melted as indicated in the Fig. 2.10b, which enabled easy detachment of the frozen droplets. The dynamic process of ice melting at the interface on ionogels was further revealed by atomistic modelling and molecular dynamics simulations, which provided a solid theoretical base for rational design of ionogel-based anti-icing surfaces.

Utilizing thermal energy for interfacial ice melting is another accessible approach for creating non-frozen water lubricating layer. The thermal energy can be generated from the substrate, and then be transferred to melt the interfacial ice, as examples shown in Fig. 2.10c. Multiwalled carbon nanotubes (MWCNT) with superior thermal-conducting property were assembled into a film layer-by-layer through a vacuum-assisted method, which resulted in superhydrophobic surfaces with excellent water repellence and special electrothermal effect for easy ice removal[64]. The temperature of the substrate can be controlled by external voltage without hampering the surface superhydrophobicity. With an input voltage of 30 V, the ice-substrate interface was efficiently melted leading to ice automatically sliding away in 34 seconds.

Using electrothermal surfaces for interfacial ice melting is effective, yet still energy intensive. Nowadays, new surfaces with photothermal effects that harvest solar energy for interfacial ice melting have attracted attentions[37, 146, 156-158]. One eye-catching example of these new surfaces, a so-called photothermal trap, was fabricated recently, which consisted of a trilaminar structure, namely a top solar radiation absorber layer for harvest illumination, a middle thermal spreader layer for lateral heat dispersal, and an insulator layer to minimize heat loss[37]. As shown in the Fig. 2.10d, the frozen droplets started sliding away in 19.8 s with illumination on the substrate with tilting angle 30°. Remarkably, the substrate took a short time of 0.5 s to generate a thin liquid layer after the start of interfacial ice melting. With longer solar illumination time and intensity, DAIS utilizing thermal energy for promoting ice removal not only melt the ice-substrate interfaces but also can melt the whole ice, which will be introduced in the following dynamic ice melting section.

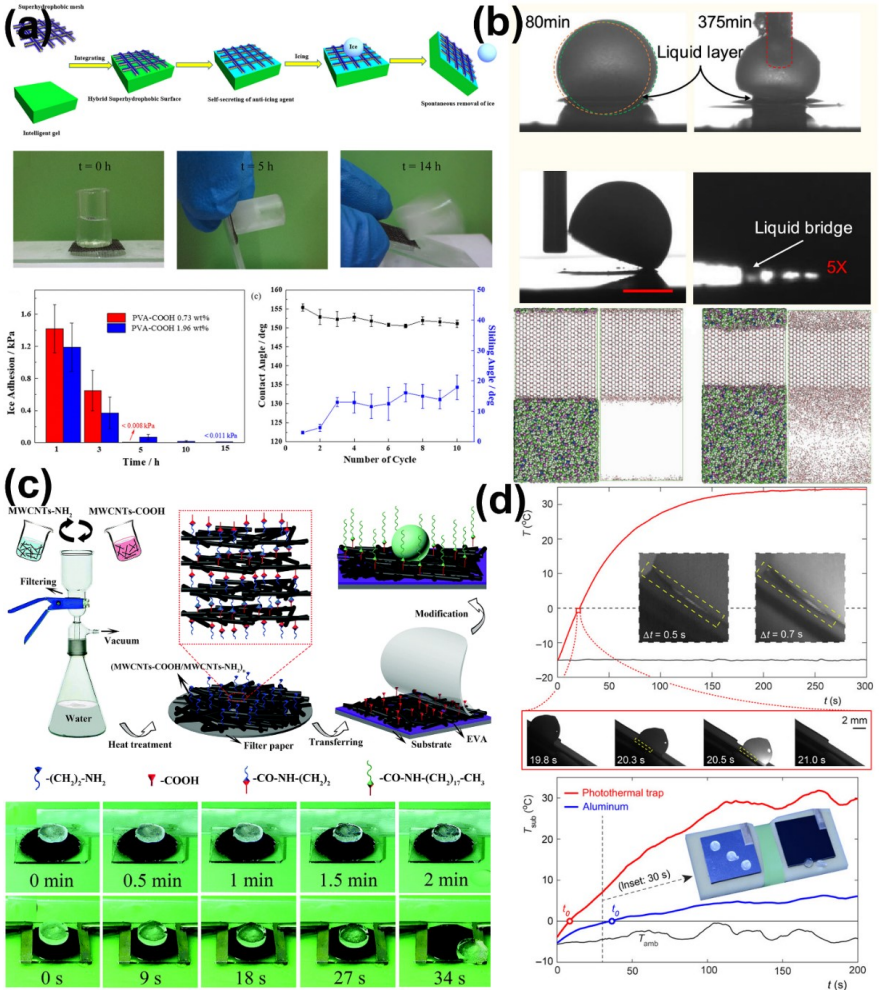

Figure 2.10. Representatives of the DAIS through dynamic interface melting. (a) The hybrid superhydrophobic surfaces that dynamic secrete anti-icing agents[60]. Copyright © 2019 American Chemical Society. (b) The ionogel surfaces using ionic liquid for dynamic anti-icing[68]. Copyright © 2020 American Chemical Society. (c) The superhydrophobic carbon nanotube surfaces with electrothermal effects[64]. Copyright © 2018 Royal Society of Chemistry. (d) The photothermal trap utilizes solar illumination for ice mitigation[37]. Copyright © 2018 American Association for the Advancement of Science.

2.3.2.3 Novel interface generators

The durability, low ice adhesion and extreme-low temperature applicability of anti-icing surfaces are three essential demands for practical applications. It is still challenging

for the current DAIS to meet all the three requirements. As discussed above, substrates that dynamically generate an interfacial aqueous lubricating layer can have improved durability thanks to lubricant regenerability[14, 25, 26]. However, for these anti-icing surfaces there is an exhaustion limit that the anti-freeze agents can secrete. When the concentration gradient of chemicals disappeared, the anti-freeze agent secretion stops, leading to poor durability in icing/de-icing cycles. The anti-icing surfaces with photothermal effects also generally lost their icephobicity at temperature lower than -50 °C. Subsequently, the interfacial aqueous layers tend to freeze at low temperature, which led to a sharp and dramatic increase in ice adhesion strength. For instance, the ice adhesion on substrates with interfacial aqueous layer can increase from ~ 27 kPa to more than 400 kPa at temperature close to -60 °C[119]. For anti-icing at extremely low temperature, such as in environments like in the Arctic area, maintaining low ice adhesion is formidable. Fortunately, a strategy of generating interfacial liquid layer at extremely low temperature and addressing anti-icing in harsh environment was developed recently[34]. Instead of generation pure aqueous layer for lubrication, ethanol was selected as the lubricant at the ice-substrate interface because of its low freezing point of -115 °C, which guaranteed non-frozen lubricating effects at extreme temperature. As verified via the atomistic modelling and molecular dynamic simulation shown in Fig. 2.11a, ethanol layer as thin as 2 nm at the ice-substrate interface can maintain low ice adhesion -60 °C. In comparison, interfacial aqueous layer of the same thickness froze at much high temperature, resulting in loss of lubrication effect. Based on the theoretical study, two liquid layer generators (LLGs) that can dynamically generate ethanol layers at the ice-substrate interfaces were designed (Fig. 2.11b). The first LLG was fabricated by packing ethanol into the substrates, termed LLG-1, which can yield super-low ice adhesion of ~ 1 kPa (samples containing 40 vol% ethanol). Because the ethanol layer was dynamically secreted from the substrate, the LLG-1 had continuous decreases in ice adhesion strength for automatic de-icing. Specifically, ice adhered onto the LLG-1 was detached by gravity in 3 hours in the related experiments. Most remarkably, the LLG-1 was showed to have ethanol secretion lifetime of at least 250 days at -20 °C (Fig. 2.11c). With more ethanol embedded in the substrate, the lifetime of ethanol secretion increased. For example, the LLG-1 sample with 40 vol% ethanol can have a long functioning lifespan of 593 days. In order to further extend the

ethanol exhaustion time, a second LLG (LLG-2) with sub-porous layers was also designed for the possibility of replenishing ethanol in the substrates, which featured the same outperforming anti-icing properties. The LLG-2 strategy was applied on various surfaces, including the contaminated ones with particles and other hydrophilic components. Surprisingly, the contaminated LLG-2 surfaces had super-low ice adhesion strength of ~ 10 kPa, which was expected to further decrease with increasing secreted ethanol layer. The most attractive properties of the LLGs were their unprecedented low ice adhesion strength at extremely low temperature (Fig. 2.11d). By introducing the ethanol lubricating layer at interfaces, the ice adhesion strength on the same surfaces decreased from 709.2 ~ 760.9 to 22.1 ~ 25.2 kPa at -60 °C, which indicats the LLGs as a viable candidate for anti-icing applications at harsh temperature. Thus, the LLGs are the first dynamic substrates that have the potential to meet the above-mentioned three anti-icing requirements intended for realistic applications.

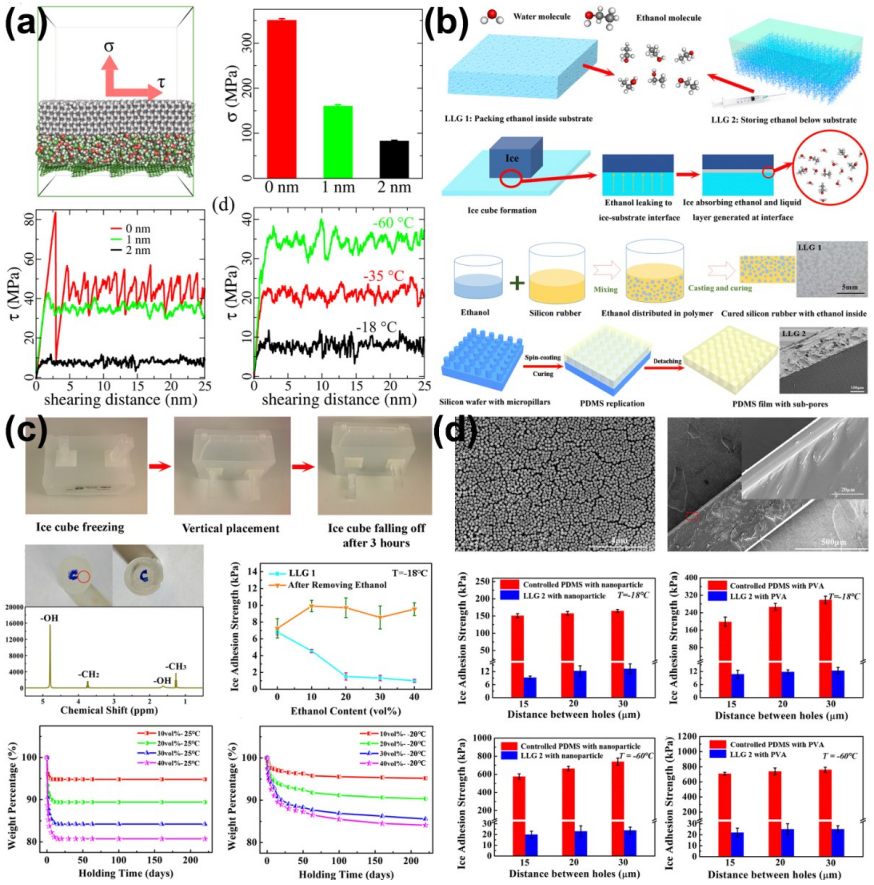

Figure 2.11. Representatives of the DAIS through novel interface generators. (a) Interfacial ethanol layers of different thickness and their effects in reduction ice adhesion strength. (b) The design principles and fabricated samples of the LLGs. (c) The icephobicity and durability of LLG-1. (d) The icephobicity of LLG-2 with various surfaces and under extremely low temperature[34]. Copyright © 2019 Royal Society of Chemistry.

2.3.2.4 Interfacial crack initiators

Dynamic interface change can also be a result of interfacial stress concentration. According to fracture mechanics, ice adhesion strength (τ_c) is governed by $\tau_c = \sqrt{E^* G/\pi a \Lambda}$, where G is the surface energy, E^* is the apparent bulk Young's modulus, a is the length of crack and Λ is a non-dimensional constant. Therefore, generating cracks at the ice-substrate interface is a promising approach for low ice adhesion. Following the fracture mechanics principle, surfaces containing crack initiators at the ice-substrate

interfaces were fabricated, which can enhance crack generation and efficiently reduce ice adhesion[14]. In order to promote the generation of cracks at the ice-substrate interface, three crack initiators on different length scales were identified, namely nanoscale crack initiator (NACI), microscale crack initiator (MICI) and macroscale crack initiator (MACI)[14]. NACI underlies negative and weak affinity of a surface to ice and aids debonding at the ice-substrate interface, which is widely observed in hydrophobic surfaces used for anti-icing[116, 159, 160]. MICI can be taken as the micro-voids under the so-called "Cassie" ice on superhydrophobic surfaces and serve as micro-cracks for ice detachment from the surfaces[28, 54, 161]. Both NACI and MICI have their limitations for achieving super-low ice adhesion (defined as ice adhesion strength lower than 10 kPa)[14]. In contrast, MACI by interface stiffness inhomogeneity is the only crack initiator that can maximize crack size at macroscale length and predominantly facilitate ice removal[14]. As shown by finite element based simulation in Fig. 2.12a, substrates with porous sub-surface structures for MACI consists of significantly larger number of crack initiation sites along the ice-substrate interface than the cases with a homogenous substrate. Correspondingly, PDMS coatings with MACI showed super-low ice adhesion of 5.7 kPa, much lower than their counterparts (Fig. 2.12a).

The novel MACI mechanism enabled by sub-surface structures thus provided a new route for design icephobic surfaces. One low-cost yet effective fabrication strategy of realizing MACI was using sponge structure[162]. As shown in Fig. 2.12b, sugar was used as a sacrificial template for preparing sandwich-like PDMS-based sponge substrates. Because of high porosity, the MACI effect of the sponge-type substrates was greatly enhanced. Furthermore, the elastic modulus of the sponge substrates was intrinsically low. The PDMS sponges thus showed remarkable super-low ice adhesion strength of ~ 0.8 kPa and stable long-term ice adhesion strength of ~ 1 kPa after 25 icing/de-icing cycles.

Stiffness inhomogeneity in the substrate is the key to MACI. Other anti-icing substrates utilizing the surface stiffness inhomogeneity to achieve low ice adhesion can be considered to rely on the same mechanism of MACI. For example, stress-localized surfaces for lowing ice adhesion were developed by surface inhomogeneity programming[39]. Specifically, the stress-localized surface contained two phases, phase I

and phase II, as shown in Fig. 2.12c. The phase I was polymer with relative high elastic modulus, while the phase II was stress-localized materials with low elastic modulus. In such a setup, the phase II served as crack initiator for ice detachment under mechanical loading, which render the stress-localized surface one of the lowest ice adhesion reported so far (in the order of 1 kPa). It is worth noting that the stress-localized surface had excellent mechanical durability thanks to the high elastic modulus of phase I.

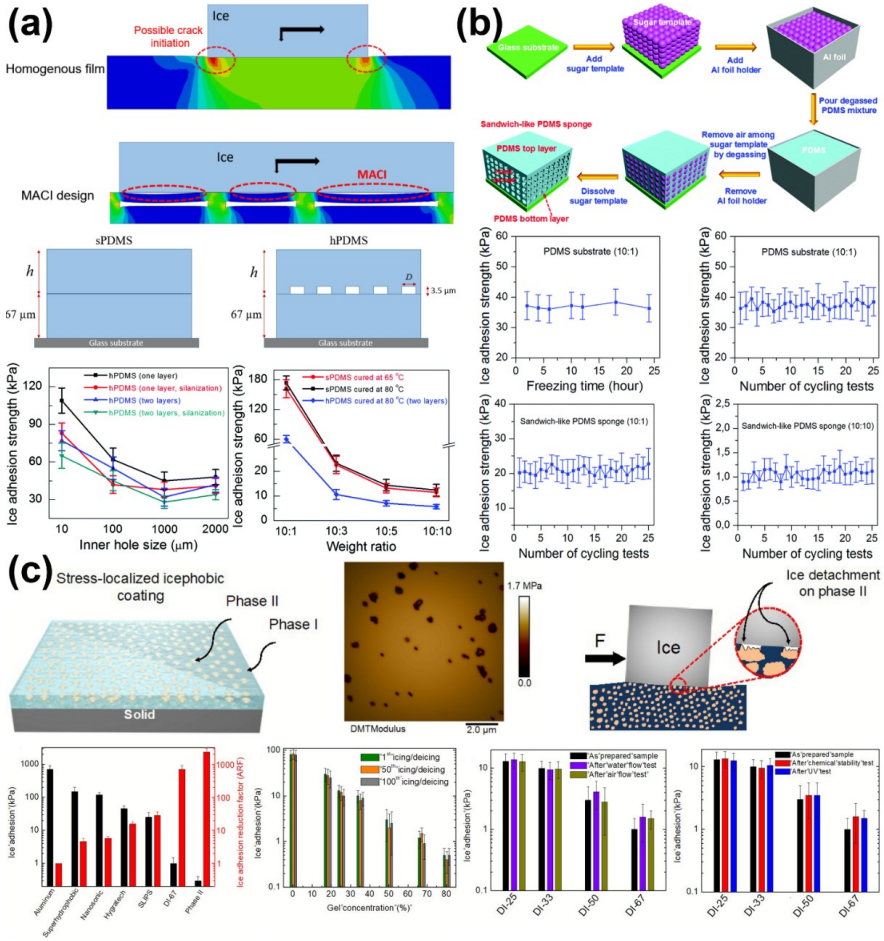

Figure 2.12. Representatives of the DAIS through interfacial crack initiators. (a) The multiscale crack initiators for super-low ice adhesion[14]. Copyright © 2017 Royal Society of Chemistry. (b) The sandwich-like PDMS sponges excellent anti-icing performances[162]. Copyright © 2018 Royal Society of Chemistry. (c) The stress-localized surfaces and their ice adhesion testing results[39]. Copyright © 2019 Royal Society of Chemistry.

2.3.3 DAIS through dynamic ice change

2.3.3.1 Effective ice growth inhibitors

Dynamic anti-icing strategies can also be applied on the ice directly. Natural organisms like insects, fishes and plants utilizing anti-freeze proteins (AFPs) to survive sub-zero temperature are the vivid examples[39, 163, 164]. AFPs can not only suppress freezing-point but also inhibit ice growth and recrystallization[165-169], thanks to their Janus properties. All the AFPs have ice-binding faces (IBFs) and non-ice-binding faces (NIBFs)[170]. In solution, AFPs preferentially bound to any ice crystals with IBFs and leave the NIBF to liquid water, which results in micro-curvatures of ice-water interfaces. Due to the so-called Kevin effect, such curved ice-water interfaces inhibit ice growth[171]. Inspired by the discovery that ice growth was regulated by the AFPs absorption onto the basal/prism planes, novel materials featuring the same property of preferential binding to ice surfaces were discovered, including graphene oxide (GO), oxidized quasi-carbon nitride quantum dots (OQCNs), safranine molecules and so on[66, 172-178]. Although the ice growth in solutions containing these new materials were indeed inhibited, applying the same strategy on the design of anti-icing surfaces is at the early stage of development. AFPs was directly immobilized onto aluminium, which led to delayed frost/ice formation for at least 3 hours, showing significant anti-icing potential[179]. The binding faces of AFPs, IBFs and NIBFs, were screened for freezing-point depression, which indicated only the NIBFs decreased freezing temperature[63]. Despite that the related studies confirmed the potential of AFPs in ant-icing applications, more in-depth investigations are still needed for elucidating their effects on overall surface icephobicity. In outdoor environment, ice nucleation is inevitable due to low temperature, long icing time and surface contaminations. Once ice started to form on exposed surfaces, ice growth/propagation control was believed to be more important to tackle the ice accumulation problem and thus one important focus of anti-icing surface design[180-182].

Phase-switching liquids (PSLs) containing cyclohexane (SCh) were used for inhibiting ice growth, for their property of holding ice melting temperature (T_{mp}) above water freezing point (T_{fp})[183]. When vapor condensed on a solidified PSL surface, the latent heat released during the condensation was trapped in the droplets. The temperature

increases at the solidified cyclohexane (SCh) and air interfaces could attain ≈ 5 °C. The increased temperature thus led to melting of PSL in contacted region (Fig. 2.13a). The best sample showed sustained ice growth delay for more than 96 h. The PSLs infused samples with 10 μm spacing microstructured (SG-10) surfaces can dynamically inhibited the frost propagation for more than 140 min, which was around 7 times longer than lubricant infused surface (LIS).

Counterions at the ice-substrate interface also can inhibit ice growth by dynamic melting[38, 184-186]. Poly([2-(methacryloyloxy)ethyl]trimethylammonium chloride)-Cl (PMETA-Cl) brush was synthesized on silicon wafers, which can accommodate different ions via ion exchange[184]. Brushed with counterions of Cl^-, ClO_4^-, PF_6^-, $TFSI^-$ and PFO^- were investigated, showing hydrophobicity $Cl^- < ClO_4^- < PF_6^- < TFSI^- < PFO^-$. It was suspected the water molecules in the hydrophilic polymer brush (PMETA-Cl and PMETA-ClO_4) moved toward the ice growth fronts when freezing occurred and consequently promoted ice propagation. In contrast, brushes with PF_6^-, $TFSI^-$ and PFO^- counterions and higher hydrophobicity could result in “water depletion regions”, which reduced the freezable water molecules and suppressed ice propagation (Fig. 2.13b).

To understand the mechanisms that control the ice propagation, ice propagation behaviours on polyelectrolyte multilayer (PEM) coated surfaces were investigated[67]. The PEMs are ideal for this purpose, because the outmost layers determine the surface properties and water concentrated only in the outside layer. Two types of PEMS, the Poly(sodium 4-styrenesulfonate)/poly(allylamine hydrochloride) (PSS/PAH) and the PSS/ poly(diallyldimethylammonium chloride) (PSS/PDAD) coatings were fabricated. The PDAD has polyelectrolyte interacting more strongly with water in the outmost layer than that in the PAH. It was found that the ice propagation time on the PSS/PAH was two orders of magnitude longer than on the PSS/PDAD with same number of deposition layers. Counterions and their concentration (Fig. 2.13c) also showed effects on ice inhibiting performance on the PEMs. The results indicated that ice propagation can be inhibited by depressing the water molecules trapped in the outmost layer of polyelectrolyte coatings. More importantly, with silver iodide aqueous droplets (AgI particle, 0.1 μL) placed on the PEMs acting as the artificial ice nuclei, the PSS/PAH

samples were still able to delay ice propagated for 2700 s, demonstrating the robustness and wide applicability of their anti-icing performances.

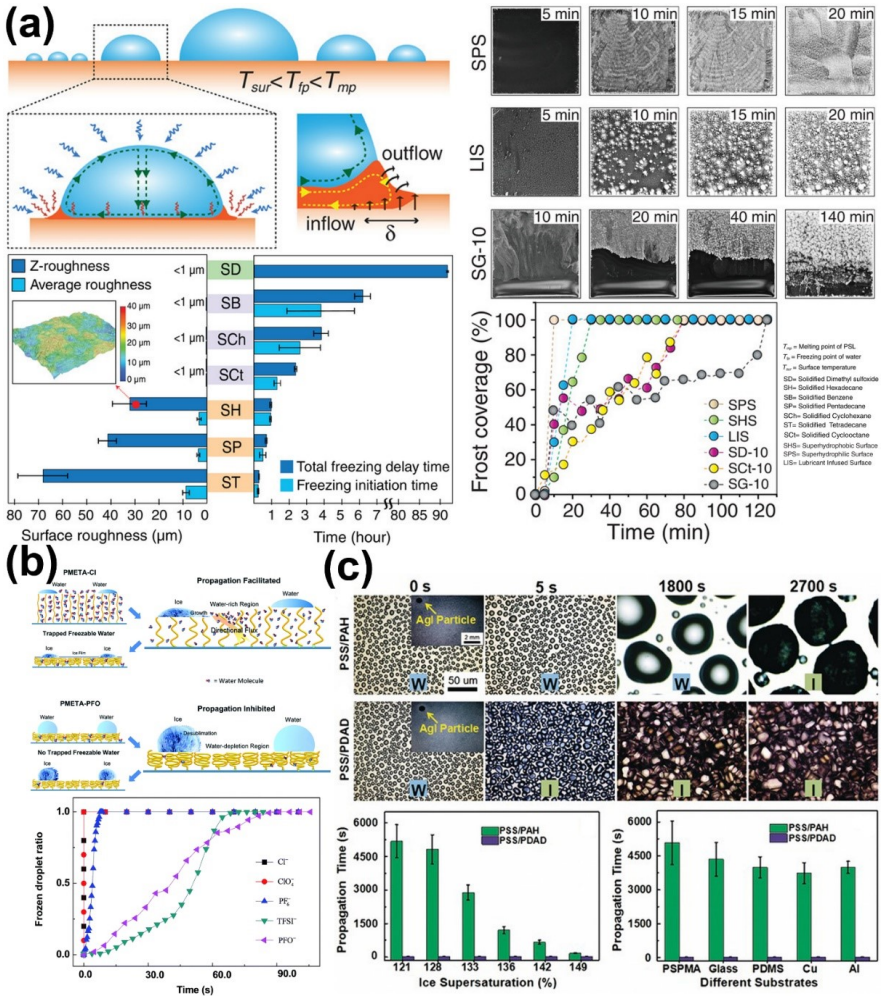

Figure 2.13. Representatives of the DAIS through effective ice growth inhibitors. (a) Phase-switching liquids used for inhibiting ice growth[183]. Copyright © 2019 Wiley Publishing Group. (b) Ion-specific ice propagation on polyelectrolyte brush surfaces[184]. Copyright © 2017 Royal Society of Chemistry. (c) Ice propagation on polyelectrolyte multilayer surfaces, "W" and "I" are denoted as "water" and "ice", respectively[67]. Copyright © 2017 Wiley Publishing Group.

2.3.3.2 Dynamic ice growth controlling

Controlling ice growth on a surface in a defined pattern can also be an effective approach to achieve icephobicity. It was found that water droplets on superhydrophobic surfaces showed spontaneous levitation and trampoline-like bouncing behaviour in a low-pressure environment[187]. Such phenomenon was caused by the overpressure beneath the droplet originated from fast vaporization and the countering surface adhesion restricting the vapor flow. Because strong vaporization led to high degree of cooling on a supercooled droplet, a rapid recalescence freezing was initiated at the free surface[182, 188]. Under the low-pressure and low-humidity conditions, a sudden increase in the vaporization of droplets surfaces resulted in rapid increasing in the overpressure beneath the droplet, which can lead to self-levitation of the droplet if freezing happened, meaning spontaneous-launching of ice. It was expected that this phenomenon can be observed on various surfaces with different textures, as shown in the Fig. 2.14a, suggesting the potential of controlling ice growth for spontaneous ice removal ice.

The freezing-driven ice-removal mechanism was further explored on various surfaces[69]. The successful self-dislodging required free surface of the droplet be solidified first, forming an ice shell on the external surfaces while maintaining the droplet-substrate contacted region remained liquid. As the subsequent freezing phase boundary moved inward in the droplet asymmetrically, the volume of droplet expanded in the solidification and caused mass displacement toward the unsolidified droplet-substrate interface. On non-wetting surfaces with pinned ice-liquid-vapor contact line, the displaced mass had nowhere to spread in the final state of solidification and lifted the droplet upward. This dislodging process was observed on various substrate with a wide range of wettability (from hydrophilic to superhydrophobic) and topography as shown in the Fig. 2.14b.

By controlling the multi-crystal ice growth pattern on the surfaces, another important surface design for novel dynamic ice repellence was also developed recently[13]. By depositing silver iodide (AgI) nanoparticles as ice nucleation active sites on surfaces, ice nucleation can be controlled to occur concurrently. It was found that the ice crystals on a hydrophilic surface (with water contact angle of 14.5°) underwent an along-surface growth (ASG) mode. However, the ice on the hydrophobic surface (with water contact

angle of 107.3°) exhibited an off-surface growth (OSG) mode (Fig. 2.14c). On the smooth surfaces, there is an ASG-to-OSG transition of ice growth mode at surface water contact angle of $\theta = 32.5° \pm 1.9°$. In the OSG mode, the optimal contact area ($A_{contact}$) was only around 10 % of projected area ($A_{project}$). In ice-removal tests, the OSG ice can be easily blown away by a wind breeze with velocity of 5.78 m/s at -3 °C, while the ASG ice remained firmly adhered on the surface.

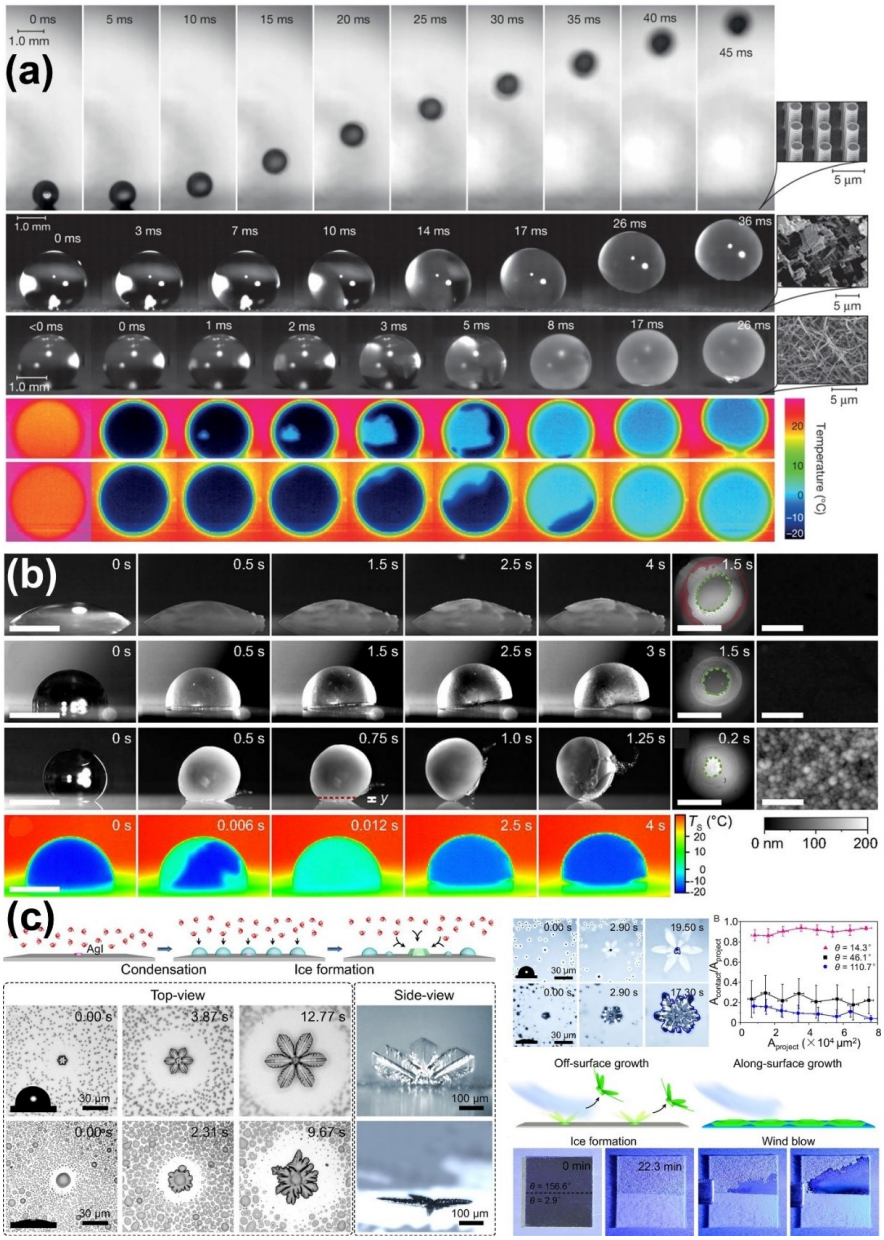

Figure 2.14. Representatives of the DAIS through dynamic ice growth controlling. (a) Spontaneous droplet levitation in freezing from a wide range of surfaces under low-pressure and low humidity conditions[187]. Copyright © 2015 Nature Publishing Group. (b) Self-dislodging behaviour on hydrophilic, hydrophobic and superhydrophobic surfaces[69]. Copyright © 2017 National Academy of Sciences of the

United States of America. (c) Ice growth pattern on surfaces with different wettability and their anti-icing performance[13]. Copyright © 2017 National Academy of Sciences of the United States of America.

2.3.3.3 Ice-free zone programming

As the dynamic ice growth patterns are important for anti-icing, recent investigations further revealed that ice growth on the whole surfaces can be programmed through surfaces chemistry/structure deign[65, 189-191]. On surfaces fabricated by assembling poly(poly(ethylene glycol) methyl ether methacrylate)/polydimethylsiloxane (P(PEGMA)/(PDMS)) Janus particles, ice was found to grow into ice crystals/dendrites in certain regions, leaving other regions dry and clean[189]. The underlying mechanism of the distinct ice growth pattern on the Janus surfaces was elucidated, as depicted in Fig. 2.15a. The icing process on the Janus surfaces followed a unique process. Frist, condensed droplets froze inhomogeneously on the surface. Specifically, ice crystals emerged more likely in the large liquid droplets on the hydrophilic regions of the surface. The frozen droplets then affected the surrounding regions. Instead of freezing, the small droplets on the hydrophobic clusters around the frozen droplets disappeared through evaporation. Then, desublimation effect of vapor to ice assisted the further growth of already frozen droplets into dendrites, which ultimately led to building a dry band around the large frozen dendrites, namely ice-free zones. Because of the ice-free zones and small ice contact area, the Janus surfaces exhibited low ice adhesion strength of 56 kPa.

The guided ice growth pattern on Janus surfaces suggested that surfaces chemistry design could dynamically create ice-free zone. However, the locations of ice-free zones on a surface were mostly random. In a recent report, ordered and large-scale ice-free zones taking up ~ 96 % of the entire surface area were programmed and created on surfaces with patterned polyelectrolyte[190]. On these patterned surfaces, icing was designed to initiate from the polyelectrolyte domains and propagated atop, as shown in Fig. 2.15b, an ice-free zone was generated around. The condensation of vapor into water droplets on the polyelectrolyte released latent heat, which led to significant temperature increase on the substrate close to the frozen droplets. This freezing-driven thermal effect resulted in further water evaporation around the frozen droplets. Because the saturated vapor pressure of water droplets is higher than ice, the newly formed ice was guided to grow exclusively on the patterned polyelectrolyte domains through desublimation[67, 123,

[170, 184]. In contrast, ice growth at the ice-free zone was inhibited. Thus, ice accumulated on the frozen area was accompanied by the consumption of condensed droplets and resulted in the continuous expansion of ice-free zone.

Besides patterning in surface chemistry, micro-structure can also be utilized for programming ice-free zone on surfaces. As shown in the Fig. 2.15c, precisely designed micro-patterned surfaces were used for programming ice growth with an interesting and motivating aim of using ice to fight ice[191]. The unique feature of such surfaces was introducing water into microstripes on the surface. Under cooling, the water stripes on the surface froze firstly, serving as frozen regions. The formation of ice-free and dry area on the surface followed the same process as discussed above, which led to as high as 90 % percent of the total surface area as dry zone (or ice-free zone). Interestingly, it was found that the growth rate of frost on the ice-stripes was one order of magnitude lower than on the smooth solids. In short, the pre-frozen ice pattern not only protected the other region from icing but also slowed down ice propagation.

Natural surfaces like certain tree leaves can also program ice formation in winter[57, 190], namely ice accumulation on convex veins is more significant than flat zones. Inspired by such phenomena, artificial leaves with ice-free regions were designed recently[65]. The micro-textures on the artificial leaves can result in large scale ice-free area without pre-designed water/ice stripes, affecting both water condensation and ice formation on the surface. As water molecules in a supersaturated ambient air diffused more easily to the peaks than to the valleys, the artificial leaves accumulated more and larger droplets on top of its micro-texture, where the freezing of droplets initiated at lower temperature. After ice formation on the peaks of the micro-textures, the low vapor pressure led to the evaporation of droplets from and created stable ice free zone in the valleys as shown in Fig. 2.15d. Combining the experiments and simulation, an important structure parameters α, namely the vertex angle, was proposed to quantitatively correlate to the percentage of ice-free regions and the micro-texture on the surface. The relationship between α and frost coverage were mapped under various ambient humidity, providing significant instructions for constructing ice-free regions through surface structure fabrication.

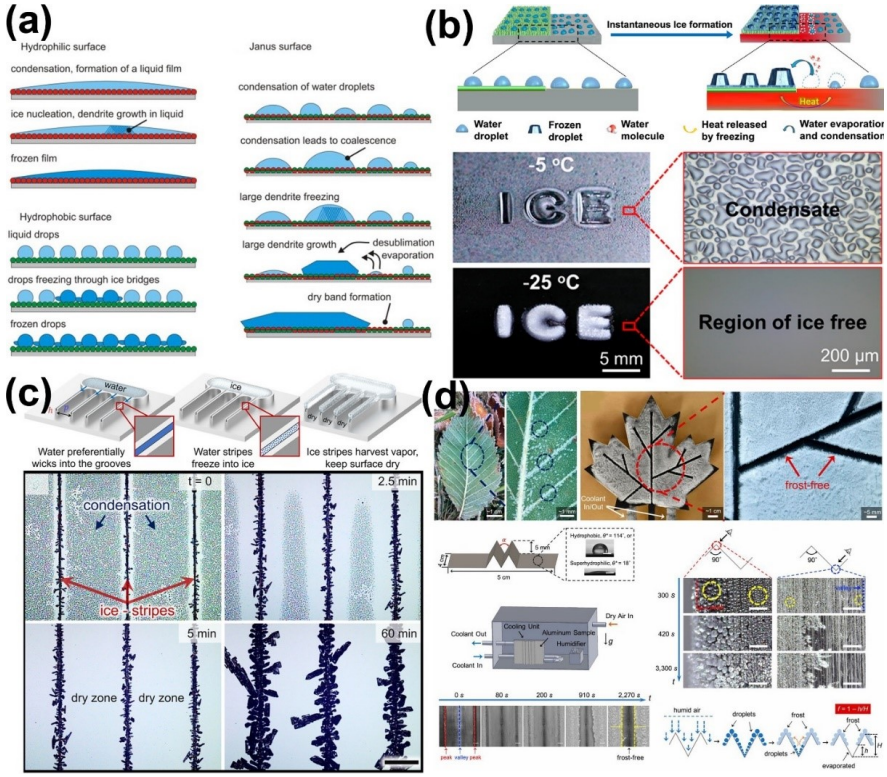

Figure 2.15. Representatives of the DAIS through ice-free zone programming. (a) Ice formation mechanism on rough hydrophilic, hydrophobic, and Janus surfaces[189]. Copyright © 2016 American Chemical Society. (b) Patterned polyelectrolyte coatings for dynamic controlling large scale ice-free region[190]. Copyright © 2020 American Chemical Society. (c) DAIS using microscopic ice patterns[191]. Copyright © 2018 American Chemical Society. (d) Micro-textured surfaces with capacity of dynamic forming ice-free zone[65]. Copyright © 2020 National Academy of Sciences of the United States of America.

2.3.3.3 Dynamic ice melting

Ice melting on anti-icing surfaces is another important aspect of dynamic ice change for avoiding unwanted ice accumulation. The dynamic ice melting surfaces were created by integrating materials with thermal effects, including electrothermal, near infrared photothermal, magnetothermal and solar photothermal effects[147, 192-194].

The use of electrothermal effect for tackling icing problems had a long history. In the last decades, numerous active anti-icing surfaces with additive electrothermal effects were developed, which consumed electrical energy for dynamic ice melting[195-200].

Passive icephobic surfaces, such superhydrophobic and the SLIPS surfaces, can also integrate active thermal effects for anti-icing, as introduced in the dynamic interface melting surfaces section above. By enhancing the power density on such surface, ice can be dynamically and constantly melted at the ice-substrate interface until being fully consumed. Recently, a so-called slippery liquid infused porous electric heating coating (SEHC) was prepared, which contained MWCNTs as electrothermal generators[147]. The SEHC also contained lubricating oil with high thermal conductivity that enabled reduction of ice adhesion strength from 1940 to ~ 58 kPa. The obvious advantage of using SEHC instead of superhydrophobic surface was the thermal conductivity of the lubricant, which was nearly one order of magnitude higher than that of air and thus also higher electrothermal efficiency. The SEHC could melt ice on the surface completely with power density 0.58 W/cm^2, showing significant reduction from 0.65 W/cm^2 on superhydrophobic surfaces (Fig. 2.16a). In another study, the lubricant infused surfaces were integrated with near-infrared photothermal effect for dynamic melting ice[192]. The lubricant infused film (LF) on the surfaces showed much lower ice adhesion strength of ~ 25 kPa than that of surfaces with smooth film (SF, ~ 506 kPa). Surfaces with embedded Fe_3O_4 nanoparticles (0.5 wt%) into the substrate was prepared for melting surface ice. The temperature of such surfaces can increase for more than 50 ℃ in 10 s under irradiation, owing to the excellent near-infrared thermal response of the Fe_3O_4 nanoparticles. In an ice melting test, the ice layer on the surface was melted in 4 s with ambient temperature below -5 ℃ (Fig. 2.16b). The Fe_3O_4 nanoparticles were not only good medium for photothermal generation, but also possessed excellent magnetic-thermal effects. Superhydrophobic coatings containing Fe_3O_4 nanoparticles can dynamically melting ice under magnetic field and sunlamp irradiation (Fig. 2.16c) [193]. Under a magnetic field of 7.8 kW, the hybrid surface containing 50 wt% Fe_3O_4 nanoparticles showed an increase in temperature of ~ 21 ℃ in 25 s. At the meantime, the same surface under sunlamp irradiation (75 W) increased 13 ℃ in 5 min.

The dynamic ice melting surfaces described above by using electric power, near-infrared irradiation and magnetic field were attractive. However, their approaches are partially active and thus can be costly. The photothermal trap surfaces that used solar irradiation energy for ice melting were outstanding candidates and have raised great

interests[37, 146, 156, 157, 194, 201, 202]. Despite the complex design, these novel surfaces introduced in the dynamic interface melting was efficient. For instance, superhydrophobic icephobic surfaces with photothermal effects by using cheap candle soot was newly fabricated[194]. Because of the hierarchical structure and the black color, the candle soot has excellent photothermal conversion efficiency[203-209]. As shown in the Fig. 2.16d, the candle soot coated surfaces possessed combined properties of robust superhydrophobicity and highly efficient light trapping, which enable surface temperature increase of ~ 53 ℃ under 1 sun illumination (1 kW/m^2). In a frost melting test at -30 ℃, the accumulated frost started melt after illuminating 60 s and the surface was free of ice in 720 s, demonstrating superior dynamic ice melting performances.

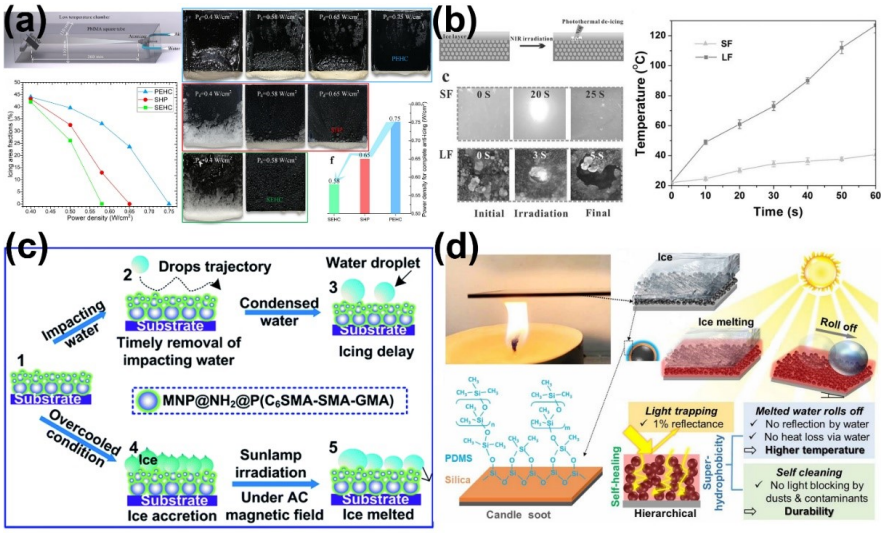

Figure 2.16. Representatives of the DAIS through dynamic ice melting. (a) Dynamic anti-icing performance of SLIPS combined with electrothermal effect[147]. Copyright © 2019 Elsevier Publishing Group. (b) Integrating self-lubrication and near infrared photothermal generation for dynamic ice melting[192]. Copyright © 2015 Wiley Publishing Group. (c) Magnetic particles based superhydrophobic surface for ice melting[193]. Copyright © 2015 Royal Society of Chemistry. (d) Superhydrophobic photothermal icephobic surfaces based on candle soot[194]. Copyright © 2020 National Academy of Sciences of the United States of America.

Chapter 3 Main Results

As the viewpoint in the **Chapter 2**, the state-of-the-art anti-icing surfaces mainly designed based on their static nature, namely no change is considered at the ice-substrate contact area after ice formation. By taking a dynamic look at the chemical/physical states of the ice/substrate/ice-substrate-interface, DAIS are proposed in this thesis. Given the ice formation is inevitable in the practical applications, enabling the dynamic change after ice formation can be a universal solution for a broad range of surfaces. The dynamic principle can be a good route for future anti-icing surfaces design, and can provide a novel avenue towards icephobicity. Based on the dynamic design principle (Fig. 2.5), through tuning the dynamic behaviours at substrate and at the ice-substrate interface, two DAIS are fabricated.

3.1 Phase transformable slippery liquid infused porous surfaces

Firstly, DAIS by enabling dynamic changes at the substrate are explored and designed. Generally, the longevity and durability of slippery liquid infused porous surfaces (SLIPSs) applied for anti-icing purpose are of great challenge. In this work, phase transformable slippery liquid infused porous surfaces (PTSLIPSs) are fabricated to overcome this tough barrier. The underlying mechanism relies on the physical property of lubricant that enables the transformation to solid state before water freezing. Attributing to the dynamic change of lubricant for liquid state to solid state under sub-zero temperature, the lubricants are strongly adhered in the porous structures, enabling the surfaces with excellent lubricant retention in icing/de-icing cycles (Fig. 3.1). the peanut oil infused porous PDMS substrates in this work shows low ice adhesion strength

(4 ~ 22 kPa), For selected samples, low ice adhesion strength around ~16 kPa maintains after 30 icing/de-icing cycles due to the phase transition property of the lubricant (Fig. 3.1). At the same time, thanks to the dynamic phase transition, PTSLIPS suit to various substrates with numerous chemical compositions (both hydrophobic and hydrophilic materials), wide pore size distributions and diverse pore morphologies. PTSLIPS with a variety of ice adhesion strength are demonstrated with substrates (wipers, foams and paper) that can be found easily from household garbage and lab supplies. Therefore, we show the possibility of creating anti-icing surfaces by Do-It-Yourself (DIY) with porous materials in hand. Besides, upon bulk damages, liquid lubricants flow to the damaged area by surface-energy-driven-capillary force in room temperature, thus PTSLIPS can be self-repaired and restore their icephobicity in low temperature. Herein, PTSLIPS provides a widely appliable method for design durable icephobic surfaces by integrating dynamic phase transformable lubricants into SLIPSs.

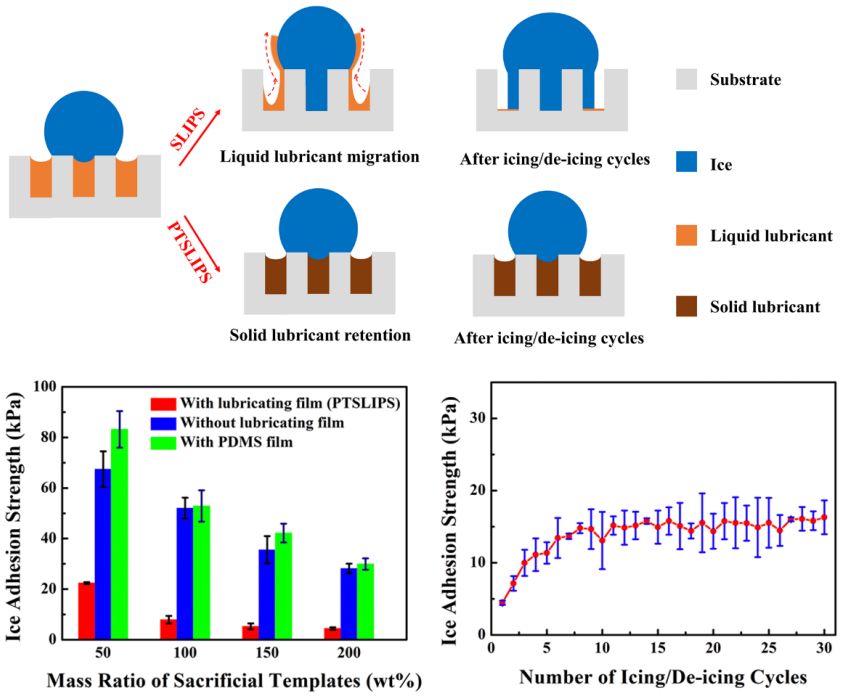

Figure 3.1 The design principle (lubricant retention in icing/de-icing cycles) and the excellent icephobicity of PTSLPS.

3.2 Liquid layer generators

Another work focuses on the dynamic changes at the ice-substrate interface, new icephobic surfaces are fabricated by programming dynamic lubricant layer at the interface. The aim of this work is to fabricate dynamic icephobic surfaces that can combine low ice adhesion strength, excellent durability and extremely low temperature applicability. First, we employee atomistic modelling and simulations to compare the ice adhesion force on substrates with and without a liquid lubricating layer at various temperatures (down to −60 °C) and investigated the reduction in atomistic ice adhesion by substituting the interfacial aqueous layer to a lubricating ethanol layer (Fig. 3.2). The interfacial ethanol layer shows superior icephobicity compared to aqueous layer and maintains icephobicity at extremely low temperatures (−60 °C) in the simulation. On such a theoretical basis, we synthesized ethanol-contained polymers with various roughness levels and chemical components that can release ethanol to the ice-substrate interface, namely, Liquid layer generators (LLGs). Two types of LLG are designed, namely, embedding ethanol in the substrate and storing replenishable ethanol in holding capacities, both exhibit excellent icephobicity with the lowest ice adhesion value of 1.0 kPa observed at −18 °C, which verified the function of the ethanol layer generated by LLG design. Owing to the ability of constant ethanol release and thickening of the interfacial lubricating layers, LLG could overcome the deficiency induced by surface roughness and hydrophilicity - the two critical factors that result in the failure of several other icephobic surfaces. The lifespan of the icephobicity of LLGs was highly encouraging, particularly with replenishable ethanol. Most importantly, LLG effectively functioned at low temperatures, covering the arctic anti-icing requirements, which outperformed other state-of-the-art icephobic surfaces. For select samples, by introducing an interfacial ethanol layer, the ice adhesion strength on the same surfaces decreased in an unprecedented manner from 709.2–760.9 to 22.1–25.2 kPa at a low temperature of −60 °C. All these properties enable LLGs to become a competitive candidate for practical anti-icing applications and provide an icephobic solution for extremely low temperatures in which other earlier published icephobic surfaces fail.

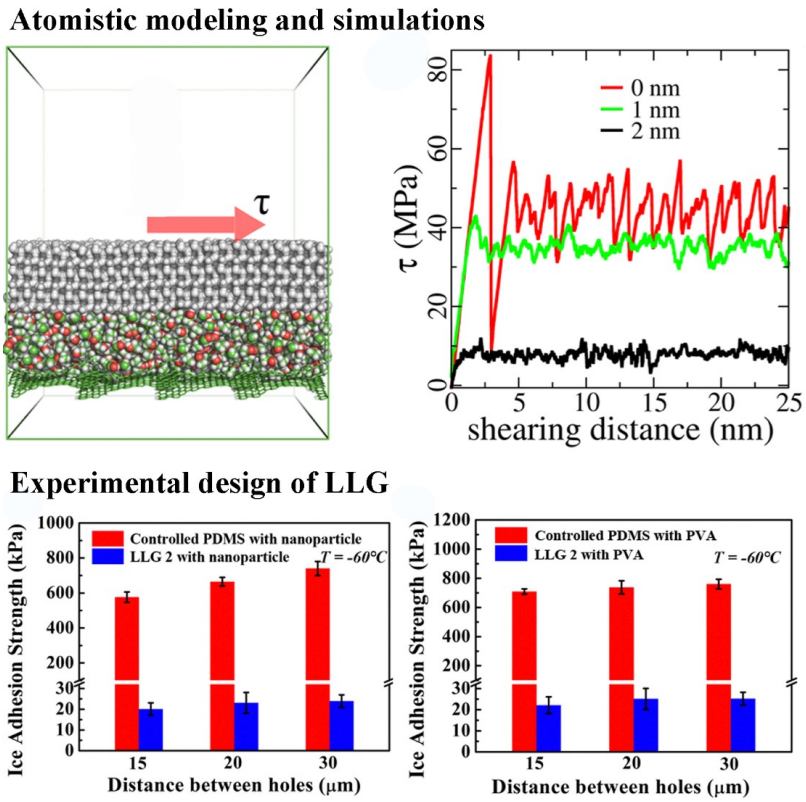

Figure 3.2 The design principle (dynamic ethanol release at the ice-substrate interface) and the excellent icephobicity of LLGs.

Chapter 4 Conclusions and Perspectives

Unwanted icing is one of the major unsolved problems accompanying mankind in the whole civilization history. It is unfortunate that the most common ways utilized today to combat icing are still the traditional de-icing methodologies involved direct mechanical forces, energy-intense thermal treatments or potentially detrimental chemical handling. Despite that the passive anti-icing concept has been proposed for more than a decade, automatic de-icing on application scale or at any industrial technology readiness level is still not available. Nevertheless, there are significant successes in the anti-icing materials related researches, especially on the super-low ice adhesion surfaces that enabling natural forces for effective de-icing. Although challenges such as durability, contamination, extreme temperature and harsh conditions need to be addressed, the upscale of such anti-icing surfaces from laboratory do promise a bright future.

Given the abundant research results on anti-icing materials, the understanding of the icing problem also needs to update. By looking into the evolution of ice-substrate contact region after ice formation, newly design principles can focus on integrating dynamic performance into anti-icing surfaces and enabling enhanced icephobicity. Given the icing is almost inevitably in practice, dynamic programming the ice-substrate contact area after ice formation offers a great potential to solve the icing problem on any surfaces. The DAIS, to some extent, need external energy inputs. Unlike the active de-icing process, attributing to the internal passive icephobicity design, the DAIS generally provides energy-saving alternatives for obtaining ice-free surfaces. Especially the energy from solar illumination, can be an ideal method for dynamic ice removing. Such surfaces still

have relatively low power density or suffer from critical environmental limitation such extremely low temperature, which deserves continuing research effort in the future research. However, the rational structure-property-function relationship in the current DAIS needs more exploring. More theoretical researches on DAIS should be promoted, including atomistic modelling and simulation, and multiscale approaches. Last but not least, to build better design principles from materials choice, structures programming to functions integrating for anti-icing applications.

Bibliography

1. Y. Cao, W. Tan and Z. Wu, Aerospace science and technology, 2018, 75, 353-385.

2. H. Yi, High Voltage Engineering, 2008, 2, 002.

3. X.-l. Jiang, J. Ma, S.-h. Wang, C.-x. SUN and L.-c. SHU, Electric Power, 2005, 38, 27-30.

4. T. Cebeci and F. Kafyeke, Annual review of fluid mechanics, 2003, 35, 11-21.

5. X. Jiang, L. Shu, W. Sima, S. Xie, J. Hu and Z. Zhang, International Journal of Offshore and Polar Engineering, 2004, 14.

6. W. Yu, Y. Lai, W. Bai, X. Zhang, D. S. Zhuang, Q. Li and J. Wang, Cold regions science and technology, 2005, 42, 79-88.

7. A. K. Andersson and L. Chapman, Accident Analysis & Prevention, 2011, 43, 284-289.

8. A. Dehghani-Sanij, S. Dehghani, G. Naterer and Y. Muzychka, Ocean Engineering, 2017, 132, 25-39.

9. J. M. Pinar-Pérez and F. P. G. Márquez, in Renewable Energies, Springer, 2018, pp. 97-109.

10. D. L. Kelting and C. L. Laxon, Review of effects and costs of road de-icing with recommendations for winter road management in the Adirondack Park, Adirondack Watershed Institute., 2010.

11. L. Mishchenko, B. Hatton, V. Bahadur, J. A. Taylor, T. Krupenkin and J. Aizenberg, ACS nano, 2010, 4, 7699-7707.

12. P. Tourkine, M. Le Merrer and D. Quéré, Langmuir, 2009, 25, 7214-7216.

13. J. Liu, C. Zhu, K. Liu, Y. Jiang, Y. Song, J. S. Francisco, X. C. Zeng and J. Wang, Proceedings of the National Academy of Sciences, 2017, 114, 11285-11290.

14. Z. He, S. Xiao, H. Gao, J. He and Z. Zhang, Soft matter, 2017, 13, 6562-6568.

15. S. Kulinich and M. Farzaneh, Langmuir, 2009, 25, 8854-8856.

16. A. J. Meuler, G. H. McKinley and R. E. Cohen, ACS nano, 2010, 4, 7048-7052.

17. S. Jung, M. Dorrestijn, D. Raps, A. Das, C. M. Megaridis and D. Poulikakos, Langmuir, 2011, 27, 3059-3066.

18. S. Kulinich, S. Farhadi, K. Nose and X. Du, Langmuir, 2011, 27, 25-29.

19. A. Gauthier, S. Symon, C. Clanet and D. Quéré, Nature communications, 2015, 6, 1-6.

20. T.-S. Wong, S. H. Kang, S. K. Tang, E. J. Smythe, B. D. Hatton, A. Grinthal and J. Aizenberg, Nature, 2011, 477, 443-447.

21. P. Kim, T.-S. Wong, J. Alvarenga, M. J. Kreder, W. E. Adorno-Martinez and J. Aizenberg, ACS nano, 2012, 6, 6569-6577.

22. P. W. Wilson, W. Lu, H. Xu, P. Kim, M. J. Kreder, J. Alvarenga and J. Aizenberg, Physical Chemistry Chemical Physics, 2013, 15, 581-585.

23. Q. Liu, Y. Yang, M. Huang, Y. Zhou, Y. Liu and X. Liang, Applied Surface Science, 2015, 346, 68-76.

24. S. B. Subramanyam, K. Rykaczewski and K. K. Varanasi, Langmuir, 2013, 29, 13414-13418.

25. K. Golovin, S. P. Kobaku, D. H. Lee, E. T. DiLoreto, J. M. Mabry and A. Tuteja, Science advances, 2016, 2, e1501496.

26. K. Golovin and A. Tuteja, Science advances, 2017, 3, e1701617.

27. K. Golovin, A. Dhyani, M. Thouless and A. Tuteja, Science, 2019, 364, 371-375.

28. K. K. Varanasi, T. Deng, J. D. Smith, M. Hsu and N. Bhate, Applied Physics Letters, 2010, 97, 234102.

29. S. Farhadi, M. Farzaneh and S. Kulinich, Applied Surface Science, 2011, 257, 6264-6269.

30. Y. Wang, J. Xue, Q. Wang, Q. Chen and J. Ding, ACS applied materials & interfaces, 2013, 5, 3370-3381.

31. C. Howell, T. L. Vu, C. P. Johnson, X. Hou, O. Ahanotu, J. Alvarenga, D. C. Leslie, O. Uzun, A. Waterhouse and P. Kim, Chemistry of Materials, 2015, 27, 1792-1800.

32. J. S. Wexler, I. Jacobi and H. A. Stone, Physical review letters, 2015, 114, 168301.

33. K. Rykaczewski, S. Anand, S. B. Subramanyam and K. K. Varanasi, Langmuir, 2013, 29, 5230-5238.

34. F. Wang, S. Xiao, Y. Zhuo, W. Ding, J. He and Z. Zhang, Materials Horizons, 2019, 6, 2063-2072.

35. F. Wang, W. Ding, J. He and Z. Zhang, Chemical Engineering Journal, 2019, 360, 243-249.

36. Y. Zhuo, V. Håkonsen, Z. He, S. Xiao, J. He and Z. Zhang, ACS applied materials & interfaces, 2018, 10, 11972-11978.

37. S. Dash, J. de Ruiter and K. K. Varanasi, Science advances, 2018, 4, eaat0127.

38. Z. He, C. Wu, M. Hua, S. Wu, D. Wu, X. Zhu, J. Wang and X. He, Matter, 2020.

39. P. Irajizad, A. Al-Bayati, B. Eslami, T. Shafquat, M. Nazari, P. Jafari, V. Kashyap, A. Masoudi, D. Araya and H. Ghasemi, Materials Horizons, 2019, 6, 758-766.

40. A. Lafuma and D. Quéré, Nature materials, 2003, 2, 457-460.

41. M. Ma and R. M. Hill, Current opinion in colloid & interface science, 2006, 11, 193-202.

42. Y.-T. Cheng and D. E. Rodak, Applied physics letters, 2005, 86, 144101.

43. T. Verho, C. Bower, P. Andrew, S. Franssila, O. Ikkala and R. H. Ras, Advanced materials, 2011, 23, 673-678.

44. L. Cao, A. K. Jones, V. K. Sikka, J. Wu and D. Gao, Langmuir, 2009, 25, 12444-12448.

45. L. Wang, Q. Gong, S. Zhan, L. Jiang and Y. Zheng, Advanced Materials, 2016, 28, 7729-7735.

46. N. Wang, D. Xiong, Y. Deng, Y. Shi and K. Wang, ACS applied materials & interfaces, 2015, 7, 6260-6272.

47. M. Ruan, W. Li, B. Wang, B. Deng, F. Ma and Z. Yu, Langmuir, 2013, 29, 8482-8491.

48. A. Alizadeh, M. Yamada, R. Li, W. Shang, S. Otta, S. Zhong, L. Ge, A. Dhinojwala, K. R. Conway and V. Bahadur, Langmuir, 2012, 28, 3180-3186.

49. T. M. Schutzius, S. Jung, T. Maitra, P. Eberle, C. Antonini, C. Stamatopoulos and D. Poulikakos, Langmuir, 2015, 31, 4807-4821.

50. P. Eberle, M. K. Tiwari, T. Maitra and D. Poulikakos, Nanoscale, 2014, 6, 4874-4881.

51. S. Kulinich and M. Farzaneh, Applied Surface Science, 2009, 255, 8153-8157.

52. S. Bengaluru Subramanyam, V. Kondrashov, J. r. Rühe and K. K. Varanasi, ACS applied materials & interfaces, 2016, 8, 12583-12587.

53. J. Chen, J. Liu, M. He, K. Li, D. Cui, Q. Zhang, X. Zeng, Y. Zhang, J. Wang and Y. Song, Applied Physics Letters, 2012, 101, 111603.

54. M. Nosonovsky and V. Hejazi, ACS nano, 2012, 6, 8488-8491.

55. J. D. Smith, R. Dhiman, S. Anand, E. Reza-Garduno, R. E. Cohen, G. H. McKinley and K. K. Varanasi, Soft Matter, 2013, 9, 1772-1780.

56. Y. Zhuo, F. Wang, S. Xiao, J. He and Z. Zhang, ACS omega, 2018, 3, 10139-10144.

57. Y. Wang, X. Yao, S. Wu, Q. Li, J. Lv, J. Wang and L. Jiang, Advanced Materials, 2017, 29, 1700865.

58. C. Urata, G. J. Dunderdale, M. W. England and A. Hozumi, Journal of Materials Chemistry A, 2015, 3, 12626-12630.

59. Y. Ru, R. Fang, Z. Gu, L. Jiang and M. Liu, Angewandte Chemie International Edition, 2020, 59, 11876-11880.

60. F. Liu, Z. Wang and Q. Pan, ACS Sustainable Chemistry & Engineering, 2019.

61. F. Giuliani, F. Merusi, G. Polacco, S. Filippi and M. Paci, Construction and Building Materials, 2012, 30, 174-179.

62. D. Chen, M. D. Gelenter, M. Hong, R. E. Cohen and G. H. McKinley, ACS applied materials & interfaces, 2017, 9, 4202-4214.

63. K. Liu, C. Wang, J. Ma, G. Shi, X. Yao, H. Fang, Y. Song and J. Wang, Proceedings of the National Academy of Sciences, 2016, 113, 14739-14744.

64. X. Su, H. Li, X. Lai, Z. Yang, Z. Chen, W. Wu and X. Zeng, Journal of Materials Chemistry A, 2018, 6, 16910-16919.

65. Y. Yao, T. Y. Zhao, C. Machado, E. Feldman, N. A. Patankar and K.-C. Park, Proceedings of the National Academy of Sciences, 2020, 117, 6323-6329.

66. H. Geng, X. Liu, G. Shi, G. Bai, J. Ma, J. Chen, Z. Wu, Y. Song, H. Fang and J. Wang, Angewandte Chemie International Edition, 2017, 56, 997-1001.

67. Y. Jin, Z. He, Q. Guo and J. Wang, Angewandte Chemie International Edition, 2017, 56, 11436-11439.

68. Y. Zhuo, S. Xiao, V. Håkonsen, J. He and Z. Zhang, ACS Materials Letters, 2020.

69. G. Graeber, T. M. Schutzius, H. Eghlidi and D. Poulikakos, Proceedings of the National Academy of Sciences, 2017, 114, 11040-11045.

70. H. Zhao, Q. Sun, X. Deng and J. Cui, Advanced Materials, 2018, 30, 1802141.

71. X. Sun, V. G. Damle, S. Liu and K. Rykaczewski, Advanced Materials Interfaces, 2015, 2, 1400479.

72. J. Cui, D. Daniel, A. Grinthal, K. Lin and J. Aizenberg, Nature materials, 2015, 14, 790-795.

73. G. Chen, S. Liu, Z. Sun, S. Wen, T. Feng and Z. Yue, Progress in Organic Coatings, 2020, 144, 105641.

74. J. H. Kim, M. J. Kim, B. Lee, J. M. Chun, V. Patil and Y.-S. Kim, Applied Surface Science, 2020, 512, 145728.

75. T. Li, Y. Zhuo, V. Håkonsen, S. Rønneberg, J. He and Z. Zhang, Coatings, 2019, 9, 602.

76. A. Sandhu, O. J. Walker, A. Nistal, K. L. Choy and A. J. Clancy, Chemical communications, 2019, 55, 3215-3218.

77. E. Tetteh and E. Loth, Coatings, 2020, 10, 262.

78. Y. Wang, X. Yao, J. Chen, Z. He, J. Liu, Q. Li, J. Wang and L. Jiang, Science China Materials, 2015, 58, 559-565.

79. Y. H. Yeong, A. Milionis, E. Loth and J. Sokhey, Cold Regions Science and Technology, 2018, 148, 29-37.

80. J. Zhang, B. Liu, Y. Tian, F. Wang, Q. Chen, F. Zhang, H. Qian and L. Ma, Coatings, 2020, 10, 119.

81. L. Zhu, J. Xue, Y. Wang, Q. Chen, J. Ding and Q. Wang, ACS applied materials & interfaces, 2013, 5, 4053-4062.

82. X. Zhu, J. Lu, X. Li, B. Wang, Y. Song, X. Miao, Z. Wang and G. Ren, Industrial & Engineering Chemistry Research, 2019, 58, 8148-8153.

83. W. Cui and T. A. Pakkanen, Applied Surface Science, 2020, 504, 144061.

84. T. Ghosh and N. Karak, Journal of colloid and interface science, 2019, 540, 247-257.

85. Y. Li, B. Li, X. Zhao, N. Tian and J. Zhang, ACS applied materials & interfaces, 2018, 10, 39391-39399.

86. J.-F. Su, Y.-D. Guo, X.-M. Xie, X.-L. Zhang, R. Mu, Y.-Y. Wang and Y.-Q. Tan, Construction and Building Materials, 2019, 224, 671-681.

87. Y. Zhuo, S. Xiao, V. Håkonsen, T. Li, F. Wang, J. He and Z. Zhang, Applied Materials Today, 2020, 19, 100542.

88. C. Urata, R. Hönes, T. Sato, H. Kakiuchida, Y. Matsuo and A. Hozumi, Advanced Materials Interfaces, 2019, 6, 1801358.

89. L. C. Liston, Y. Farnam, M. Krafcik, J. Weiss, K. Erk and B. Y. Tao, Applied Thermal Engineering, 2016, 96, 501-507.

90. X. Zhou, G. Kastiukas, C. Lantieri, P. Tataranni, R. Vaiana and C. Sangiorgi, Materials, 2018, 11, 1398.

91. K. Zhu, X. Li, J. Su, H. Li, Y. Zhao and X. Yuan, Polymer Engineering & Science, 2018, 58, 973-979.

92. P. Irajizad, M. Hasnain, N. Farokhnia, S. M. Sajadi and H. Ghasemi, Nature communications, 2016, 7, 1-7.

93. A. Masoudi, P. Irajizad, N. Farokhnia, V. Kashyap and H. Ghasemi, ACS applied materials & interfaces, 2017, 9, 21025-21033.

94. Q. Rao, J. Zhang, X. Zhan, F. Chen and Q. Zhang, Journal of Materials Chemistry A, 2020.

95. R. Wang, S. Hong, X. Huang and H. Liu, Materials Research Express, 2019, 6, 055035.

96. D. Wu, L. Ma, F. Zhang, H. Qian, B. Minhas, Y. Yang, X. Han and D. Zhang, Materials & Design, 2020, 185, 108236.

97. T.-C. Ling and C.-S. Poon, Construction and Building Materials, 2013, 46, 55-62.

98. L. Liston, M. Krafcik, Y. Farnam, B. Tao, K. Erk and J. Weiss, Toward the use of phase change materials (PCM) in concrete pavements: Evaluation of thermal properties of PCM, 2014.

99. A. R. Sakulich and D. P. Bentz, Construction and Building Materials, 2012, 35, 483-490.

100. B. T. Worrell, M. K. McBride, G. B. Lyon, L. M. Cox, C. Wang, S. Mavila, C.-H. Lim, H. M. Coley, C. B. Musgrave and Y. Ding, Nature communications, 2018, 9, 1-7.

101. G. Wang, T. Peng, S. Zhang, J. Wang, X. Wen, H. Yan, L. Hu and L. Wang, RSC Advances, 2015, 5, 28344-28348.

102. W. Xi, H. Peng, A. Aguirre-Soto, C. J. Kloxin, J. W. Stansbury and C. N. Bowman, Macromolecules, 2014, 47, 6159-6165.

103. B. Shang, M. Chen and L. Wu, ACS applied materials & interfaces, 2018, 10, 31777-31783.

104. Y. Zhuo, T. Li, F. Wang, V. Håkonsen, S. Xiao, J. He and Z. Zhang, Soft matter, 2019, 15, 3607-3611.

105. S. Xiao, B. H. Skallerud, F. Wang, Z. Zhang and J. He, Nanoscale, 2019, 11, 16262-16269.

106. S. Choi, T.-w. Kwon, A. Coskun and J. W. Choi, Science, 2017, 357, 279-283.

107. K. Ito, Polymer journal, 2012, 44, 38-41.

108. R. Rosenberg, Physics Today, 2005, 58, 50.

109. M. Faraday, Proceedings of the Royal Society of London, 1860, 440-450.

110. J. T. Bottomley, Journal, 1872.

111. J. Thomson, Proceedings of the Royal Society of London, 1862, 198-204.

112. F. P. Bowden and T. Hughes, Proceedings of the Royal Society of London. Series A. Mathematical and Physical Sciences, 1939, 172, 280-298.

113. G. Malenkov, Journal of Physics: Condensed Matter, 2009, 21, 283101.

114. S. Schöder, H. Reichert, H. Schröder, M. Mezger, J. Okasinski, V. Honkimäki, J. Bilgram and H. Dosch, Physical review letters, 2009, 103, 095502.

115. S. Engemann, H. Reichert, H. Dosch, J. Bilgram, V. Honkimäki and A. Snigirev, Physical review letters, 2004, 92, 205701.

116. S. Xiao, J. He and Z. Zhang, Nanoscale, 2016, 8, 14625-14632.

117. T. Y. Zhao, P. R. Jones and N. A. Patankar, Scientific reports, 2019, 9, 1-12.

118. S. Xiao, J. He and Z. Zhang, Acta Mechanica Solida Sinica, 2017, 30, 224-226.

119. R. Dou, J. Chen, Y. Zhang, X. Wang, D. Cui, Y. Song, L. Jiang and J. Wang, ACS applied materials & interfaces, 2014, 6, 6998-7003.

120. J. Chen, Z. Luo, Q. Fan, J. Lv and J. Wang, Small, 2014, 10, 4693-4699.

121. Y. Marcus, Chemical reviews, 2009, 109, 1346-1370.

122. S. Chernyy, M. Jarn, K. Shimizu, A. Swerin, S. U. Pedersen, K. Daasbjerg, L. Makkonen, P. Claesson and J. Iruthayaraj, ACS applied materials & interfaces, 2014, 6, 6487-6496.

123. Z. He, W. J. Xie, Z. Liu, G. Liu, Z. Wang, Y. Q. Gao and J. Wang, Science advances, 2016, 2, e1600345.

124. B. Liang, G. Zhang, Z. Zhong, Y. Huang and Z. Su, Langmuir, 2018, 35, 1294-1301.

125. S. Wooh and D. Vollmer, Angewandte Chemie International Edition, 2016, 55, 6822-6824.

126. P. Liu, H. Zhang, W. He, H. Li, J. Jiang, M. Liu, H. Sun, M. He, J. Cui and L. Jiang, ACS nano, 2017, 11, 2248-2256.

127. M. Boban, K. Golovin, B. Tobelmann, O. Gupte, J. M. Mabry and A. Tuteja, ACS applied materials & interfaces, 2018, 10, 11406-11413.

128. L. Zhang, Z. Guo, J. Sarma and X. Dai, ACS Applied Materials & Interfaces, 2020, 12, 20084-20095.

129. J. Chen, R. Dou, D. Cui, Q. Zhang, Y. Zhang, F. Xu, X. Zhou, J. Wang, Y. Song and L. Jiang, ACS applied materials & interfaces, 2013, 5, 4026-4030.

130. J. Chen, K. Li, S. Wu, J. Liu, K. Liu and Q. Fan, ACS omega, 2017, 2, 2047-2054.

131. C. Li, X. Li, C. Tao, L. Ren, Y. Zhao, S. Bai and X. Yuan, ACS applied materials & interfaces, 2017, 9, 22959-22969.

132. C. Tao, S. Bai, X. Li, C. Li, L. Ren, Y. Zhao and X. Yuan, Progress in Organic Coatings, 2018, 115, 56-64.

133. Y. Yu, B. Jin, M. I. Jamil, D. Cheng, Q. Zhang, X. Zhan and F. Chen, ACS applied materials & interfaces, 2019, 11, 12838-12845.

134. Z. He, Y. Zhuo, F. Wang, J. He and Z. Zhang, Progress in Organic Coatings, 2020, 147, 105737.

135. F. Li and Z. Wang, Journal of Highway and Transportation Research and Development (English Edition), 2012, 6, 11-17.

136. Z. Liu, M. Xing, S. Chen, R. He and P. Cong, Construction and Building Materials, 2014, 51, 133-140.

137. Z. Liu, S. Chen, R. He, M. Xing, Y. Bai and H. Dou, Journal of Materials in Civil Engineering, 2015, 27, 04014180.

138. Z. Liu, A. Sha, M. Xing and Z. Li, Cold Regions Science and Technology, 2015, 114, 9-14.

139. S. Luo and X. Yang, Construction and Building Materials, 2015, 94, 494-501.

140. O. Xu, S. Han, C. Zhang, Y. Liu, F. Xiao and J. Xu, Construction and Building Materials, 2015, 98, 671-677.

141. M. Zheng, J. Zhou, S. Wu, H. Yuan and J. Meng, Construction and Building Materials, 2015, 84, 277-283.

142. Z. Liu, A. Sha, R. He and M. Xing, Cold Regions Science and Technology, 2016, 129, 104-113.

143. H. Coffman, Journal of the American Helicopter Society, 1987, 32, 34-39.

144. S. K. Thomas, R. P. Cassoni and C. D. MacArthur, Journal of aircraft, 1996, 33, 841-854.

145. J. Laforte, M. Allaire and J. Laflamme, Atmospheric Research, 1998, 46, 143-158.

146. R. Mirzanamadi, C.-E. Hagentoft and P. Johansson, Energies, 2018, 11, 3443.

147. X. Liu, H. Chen, Z. Zhao, Y. Yan and D. Zhang, Surface and Coatings Technology, 2019, 374, 889-896.

148. A. J. Meuler, J. D. Smith, K. K. Varanasi, J. M. Mabry, G. H. McKinley and R. E. Cohen, ACS applied materials & interfaces, 2010, 2, 3100-3110.

149. J. Le Bideau, L. Viau and A. Vioux, Chemical Society Reviews, 2011, 40, 907-925.

150. N. Chen, H. Zhang, L. Li, R. Chen and S. Guo, Advanced Energy Materials, 2018, 8, 1702675.

151. A. Kavanagh, R. Byrne, D. Diamond and K. J. Fraser, Membranes, 2012, 2, 16-39.

152. L. Viau, C. Tourné-Péteilh, J.-M. Devoisselle and A. Vioux, Chemical Communications, 2010, 46, 228-230.

153. M. Kuddushi, N. K. Patel, S. Rajput, O. A. El Seoud, J. P. Mata and N. I. Malek, ChemSystemsChem, 2020.

154. S. J. Craythorne, K. Anderson, F. Lorenzini, C. McCausland, E. F. Smith, P. Licence, A. C. Marr and P. C. Marr, Chemistry–A European Journal, 2009, 15, 7094-7100.

155. F. Shi, Q. Zhang, D. Li and Y. Deng, Chemistry–A European Journal, 2005, 11, 5279-5288.

156. E. Mitridis, T. M. Schutzius, A. Sicher, C. U. Hail, H. Eghlidi and D. Poulikakos, ACS nano, 2018, 12, 7009-7017.

157. C. Wu, H. Geng, S. Tan, H. Wang, J. Lv, Z. He and J. Wang, Materials Horizons, 2020, DOI: 10.1039/D0MH00636J.

158. S. Wu, Y. Du, Y. Alsaid, D. Wu, M. Hua, Y. Yan, B. Yao, Y. Ma, X. Zhu and X. He, Proceedings of the National Academy of Sciences, 2020, 117, 11240-11246.

159. I. A. Ryzhkin and V. F. Petrenko, The Journal of Physical Chemistry B, 1997, 101, 6267-6270.

160. V. F. Petrenko and S. Peng, Canadian journal of physics, 2003, 81, 387-393.

161. V. Hejazi, K. Sobolev and M. Nosonovsky, Scientific reports, 2013, 3, 2194.

162. Z. He, Y. Zhuo, J. He and Z. Zhang, Soft Matter, 2018, 14, 4846-4851.

163. A. L. DeVries and D. E. Wohlschlag, Science, 1969, 163, 1073-1075.

164. T. Sun, F.-H. Lin, R. L. Campbell, J. S. Allingham and P. L. Davies, Science, 2014, 343, 795-798.

165. J. A. Raymond and A. L. DeVries, Proceedings of the National Academy of Sciences, 1977, 74, 2589-2593.

166. C. A. Knight, Nature, 2000, 406, 249-251.

167. J. Xu, R. Jing, X. Ren and G. Gao, Journal of Materials Chemistry A, 2020, 8, 9373-9381.

168. P. L. Davies, Trends in biochemical sciences, 2014, 39, 548-555.

169. L. A. Graham and P. L. Davies, Science, 2005, 310, 461-461.

170. Z. He, K. Liu and J. Wang, Accounts of chemical research, 2018, 51, 1082-1091.

171. C. Knight, C. Cheng and A. DeVries, Biophysical journal, 1991, 59, 409-418.

172. G. Bai, D. Gao, Z. Liu, X. Zhou and J. Wang, Nature, 2019, 576, 437-441.

173. G. Bai, D. Gao and J. Wang, Carbon, 2017, 124, 415-421.

174. G. Bai, Z. Song, H. Geng, D. Gao, K. Liu, S. Wu, W. Rao, L. Guo and J. Wang, Advanced Materials, 2017, 29, 1606843.

175. C. I. Biggs, T. L. Bailey, B. Graham, C. Stubbs, A. Fayter and M. I. Gibson, Nature communications, 2017, 8, 1-12.

176. C. J. Capicciotti, R. S. Mancini, T. R. Turner, T. Koyama, M. G. Alteen, M. Doshi, T. Inada, J. P. Acker and R. N. Ben, ACS omega, 2016, 1, 656-662.

177. R. Drori, C. Li, C. Hu, P. Raiteri, A. L. Rohl, M. D. Ward and B. Kahr, Journal of the American Chemical Society, 2016, 138, 13396-13401.

178. O. Mizrahy, M. Bar-Dolev, S. Guy and I. Braslavsky, PloS one, 2013, 8.

179. Y. Gwak, J.-i. Park, M. Kim, H. S. Kim, M. J. Kwon, S. J. Oh, Y.-P. Kim and E. Jin, Scientific reports, 2015, 5, 12019.

180. M. J. Kreder, J. Alvarenga, P. Kim and J. Aizenberg, Nature Reviews Materials, 2016, 1, 1-15.

181. Q. Hao, Y. Pang, Y. Zhao, J. Zhang, J. Feng and S. Yao, Langmuir, 2014, 30, 15416-15422.

182. S. Jung, M. K. Tiwari and D. Poulikakos, Proceedings of the National Academy of Sciences, 2012, 109, 16073-16078.

183. R. Chatterjee, D. Beysens and S. Anand, Advanced Materials, 2019, 31, 1807812.

184. Z. Liu, Z. He, J. Lv, Y. Jin, S. Wu, G. Liu, F. Zhou and J. Wang, RSC advances, 2017, 7, 840-844.

185. Q. Guo, Z. He, Y. Jin, S. Zhang, S. Wu, G. Bai, H. Xue, Z. Liu, S. Jin and L. Zhao, Langmuir, 2018, 34, 11986-11991.

186. X. Xu, V. V. Jerca and R. Hoogenboom, Chem, 2020, 6, 820-822.

187. T. M. Schutzius, S. Jung, T. Maitra, G. Graeber, M. Köhme and D. Poulikakos, Nature, 2015, 527, 82-85.

188. S. Jung, M. K. Tiwari, N. V. Doan and D. Poulikakos, Nature communications, 2012, 3, 1-8.

189. A. Kirillova, L. Ionov, I. V. Roisman and A. Synytska, Chemistry of Materials, 2016, 28, 6995-7005.

190. Y. Jin, C. Wu, Y. Yang, J. Wu, Z. He and J. Wang, ACS Nano, 2020, 14, 5000-5007.

191. S. F. Ahmadi, S. Nath, G. J. Iliff, B. R. Srijanto, C. P. Collier, P. Yue and J. B. Boreyko, ACS applied materials & interfaces, 2018, 10, 32874-32884.

192. X. Yin, Y. Zhang, D. Wang, Z. Liu, Y. Liu, X. Pei, B. Yu and F. Zhou, Advanced Functional Materials, 2015, 25, 4237-4245.

193. T. Cheng, R. He, Q. Zhang, X. Zhan and F. Chen, Journal of Materials Chemistry A, 2015, 3, 21637-21646.

194. S. Wu, Y. Du, Y. Alsaid, D. Wu, M. Hua, Y. Yan, B. Yao, Y. Ma, X. Zhu and X. He, Proceedings of the National Academy of Sciences, 2020, DOI: 10.1073/pnas.2001972117, 202001972.

195. M. Mohseni and A. Amirfazli, Cold Regions Science and Technology, 2013, 87, 47-58.

196. B. G. Falzon, P. Robinson, S. Frenz and B. Gilbert, Composites Part A: Applied Science and Manufacturing, 2015, 68, 323-335.

197. A. Shinkafi and C. Lawson, International Journal of Mechanical, Aerospace, Industrial and Mechatronics Engineering, 2014, 8, 1069-1076.

198. Z. Zhao, H. Chen, X. Liu, H. Liu and D. Zhang, Surface and Coatings Technology, 2018, 349, 340-346.

199. X. Yao, S. C. Hawkins and B. G. Falzon, Carbon, 2018, 136, 130-138.

200. Z. Zhang, B. Chen, C. Lu, H. Wu, H. Wu, S. Jiang and G. Chai, Composite Structures, 2017, 180, 933-943.

201. G. Jiang, L. Chen, S. Zhang and H. Huang, ACS applied materials & interfaces, 2018, 10, 36505-36511.

202. L. Ma, J. Wang, F. Zhao, D. Wu, Y. Huang, D. Zhang, Z. Zhang, W. Fu, X. Li and Y. Fan, Composites Science and Technology, 2019, 181, 107696.

203. X. Deng, L. Mammen, H.-J. Butt and D. Vollmer, Science, 2012, 335, 67-70.

204. K. Seo and M. Kim, Carbon, 2014, 68, 583-596.

205. L. Xiao, W. Zeng, G. Liao, C. Yi and Z. Xu, ACS Applied Nano Materials, 2018, 1, 1204-1211.

206. R. Iqbal, B. Majhy and A. Sen, ACS applied materials & interfaces, 2017, 9, 31170-31180.

207. J. Li, Z. Zhao, D. Li, H. Tian, F. Zha, H. Feng and L. Guo, Nanoscale, 2017, 9, 13610-13617.

208. B. N. Sahoo and B. Kandasubramanian, Materials Chemistry and Physics, 2014, 148, 134-142.

209. M. I. Jamil, X. Zhan, F. Chen, D. Cheng and Q. Zhang, ACS applied materials & interfaces, 2019, 11, 31532-31542.

Appendix A Appended Papers

A.1 Paper 1

Phase transition enabled durable anti-icing surfaces and its DIY design

Authors: Feng Wang, Wenwu Ding, Jianying He and Zhiliang Zhang

Chemical Engineering Journal, 2019, 360, 243-249

Paper 1

Chemical Engineering Journal 360 (2019) 243–249

Contents lists available at ScienceDirect

Chemical Engineering Journal

journal homepage: www.elsevier.com/locate/cej

Phase transition enabled durable anti-icing surfaces and its DIY design

Feng Wang[a], Wenwu Ding[b], Jianying He[a,*], Zhiliang Zhang[a,*]

[a] NTNU Nanomechanical Lab, Department of Structural Engineering, Norwegian University of Science and Technology (NTNU), Trondheim 7491, Norway
[b] Department of Energy and Process Engineering, Norwegian University of Science and Technology (NTNU), Trondheim 7491, Norway

HIGHLIGHTS

- Phase transformable slippery liquid infused porous surfaces (PTSLIPS) were introduced.
- PTSLIPS showed low ice adhesion strength (4.45 – 22.43 kPa) as well as excellent durability.
- PTSLIPS indiscriminately adapt to porous substrates with various chemical compositions.
- PTSLIPS also possessed self-repairing property that could repair the bulk damage.

GRAPHICAL ABSTRACT

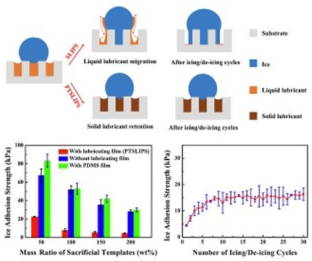

ARTICLE INFO

Keywords:
Phase transformable lubricant
Anti-icing
Ice adhesion strength
Peanut oil
DIY

ABSTRACT

Generally, the longevity and durability of slippery liquid infused porous surfaces (SLIPS) applied for anti-icing purpose are of great challenge. In this work, phase transformable slippery liquid infused porous surfaces (PTSLIPS) are fabricated to overcome this tough barrier. The underlying mechanism relies on the physical property of lubricant that enables the transformation to solid state before water freezing. Peanut oil infused porous PDMS substrates show low ice adhesion strength (4 – 22 kPa) as well as excellent durability. For selected samples, low ice adhesion strength around – 16 kPa maintains after 30 icing/de-icing cycles due to the phase transition property of the lubricant. In addition to the promising ice adhesion strength and durability, PTSLIPS also suit to various substrates with numerous chemical compositions (both hydrophobic and hydrophilic materials), wide pore size distributions and diverse pore morphologies. PTSLIPS with a variety of ice adhesion strength are demonstrated with substrates (wipers, foams and paper) that can be found easily from household garbage and lab supplies. Therefore, we show the possibility of creating anti-icing surfaces by Do-It-Yourself (DIY) with porous materials in hand. The PTSLIPS also possess self-repairing property with excellent physical damage resistance, and scratches on PTSLIPS have minor effects on their ice adhesion strength.

1. Introduction

Ice formation and accretion can cause huge problems for aircrafts, ships, electrical transmission cables, wind turbines, motor vehicles et al. [1–7]. It demands a significant amount of energy and time to clear the ice away once formed [8]. Consequently, designing and deploying material surfaces that can assist the removal of ice have received growing interests. The lotus-leaf-based superhydrophobic surfaces inspired the design of surfaces for prevention of ice formation [9–17]. Superhydrophobic surfaces that can delay ice formation down to −25 °C to −30 °C have been reported [11]. However, the drawbacks of superhydrophobic surfaces for anti-icing have also been revealed [8,12,13,18–20]. In a humid atmosphere, superhydrophobic

* Corresponding authors.
E-mail addresses: jianying.he@ntnu.no (J. He), zhiliang.zhang@ntnu.no (Z. Zhang).

https://doi.org/10.1016/j.cej.2018.11.224
Received 28 August 2018; Received in revised form 17 October 2018; Accepted 29 November 2018
Available online 30 November 2018
1385-8947/

surfaces have even higher freezing rate than smooth surfaces [13] and the condensation of water in the rough structure may lead to very large ice adhesion strength [8,12,14,19]. In addition, because of the low abrasive resistance, superhydrophobic surfaces experience gradual damage during icing and/or de-icing cycles and show low durability [14,21,22].

Recently, the pitcher-plants-inspired slippery liquid-infused porous surfaces (SLIPS) [23] with exceptional icephobicity have been designed [24]. These surfaces show positive effects in delaying frost formation [24,25] and lowering ice adhesion strength (~10–150 kPa) [24,26–28]. In general, SLIPS enable the possibility of self-removal of accreted ice by gravity, wind or vibration [29–31]. Unfortunately, the lubricating layers in SLIPS can be easily carried away by water droplets [32–34] or replaced by ice [35], which result in remarkable degrading in anti-icing performance after few icing/de-icing cycles. Therefore, keeping longevity and durability of the SLIPS is of great challenge for the practical applications of these icephobic surfaces. Some strategies have been developed to improve the durability of SLIPS, such as carefully selecting lubricants and using favorable surface chemistry [36], incorporating nanostructures or increasing texture density [27,37], crosslinking polymer networks into SLIPS [38]. However, the improvements are still limited, and the complex design of surface chemistry or structure in these methods restrict their applications. Thus, new strategies are needed to achieve practical longevity and large scope applications of SLIPS [39].

There are two important principles in designing SLIPS for anti-icing application: 1) the surface should have favorable nano/microstructure for the adhesion and retention of infiltrated lubricant, 2) the chemical affinity between the lubricant and surface should be superior to that between water and the surface [23,24]. To meet these criteria, the surfaces are carefully fabricated with appropriate roughness and subsequent hydrophobic treatment [24,25,36]. In fact, both principles relate to durability of surface. The nano/microstructure are essential for capturing lubricant liquid inside the pores and slowing down the rate of lubricant run off. The strong chemical affinity between surface and lubricant can prevent water from replacing the lubricant liquid and extend the repellent time of SLIPS. So far all the design for improving the durability of SLIPS follow the two principles mentioned above.

In this work, we report synthetic 'phase transformable slippery liquid infused porous surfaces' (PTSLIPS) – that the liquid lubricant converts into solid phase in cold environment before water freezing. The phase transition of lubricant widely expands the potentials of SLIPS. At room temperature (~25 °C), the lubricant is liquid and the surface can be designed with omniphobility through the guidelines shown in Tak-Sing et al.'s report [23]. Once the temperature decreases to below zero degree, the lubricant turns to solid state and more durable anti-icing surface can be obtained. Furthermore, the solid lubricant can retain in pores with various size and morphologies. The solid lubricant can also survive from water replacement when hydrophilic substrates are used. Another important advantage is the environmental friendliness. Comparing with silicon oil and perfluorinated lubricant that commonly used in anti-icing SLIPS [24,27,38], the phase transformable lubricant (peanut oil in this work) which can degrade in natural environment is a safer and cheaper choice.

In summary, we show that PTSLIPS possesses low ice adhesion strength and excellent durability, prevents lubricant loss for various pore sizes regardless of morphologies, suits to numerous porous substrates (both hydrophobic and hydrophilic surfaces), self-repairs and retains low ice adhesion strength after mechanical damage. The PTSLIPS are environmentally friendly that maximize the scope of applications. In addition, we demonstrate that anti-icing PTSLIPS are possible to be designed at home with porous materials in hand.

2. Experimental process

2.1. Methods summary

The porous polydimethylsiloxane (PDMS) substrates were fabricated by a sacrificial templates method. PDMS prepolymer (Sylgard 184, Dow Corning) and curing agent were mixed in a weight ratio of 10:1. Sacrificial templates made of sodium chloride powders from Sigma-Aldrich were added into the mixture with mass ratios of 50, 100, 150 and 200 wt%, respectively. The final mixtures were degassed in a vacuum chamber and then placed under 120 °C for 30 min to obtain cured PDMS. Porous PDMS substrates were successfully fabricated by dissolving sodium chloride in water bath under 70 °C for 72 h. The thickness of porous PDMS was controlled as 0.9 mm by the volume of mixtures used. After immersing the porous PDMS into lubricant for 48 h and wiping out visible oil on the surfaces, PTSLIPSs were obtained. The phase transformable lubricant used for the experiments was peanut oil (analytical standard, Sigma-Aldrich). Some phase transformable lubricants that can be used were recommended in supplementary Table S1. Other porous substrates like foams, wipers and paper could be easily obtained from household garbage and lab supplies, and compositions were shown in supplementary Fig. S1. The extra lubricant on these porous substrates were removed by sloping samples after oil was infused.

2.2. Characterizations

Surface morphologies were observed by the field emission scanning electron microscope (FEI APREO SEM). All samples were sputter-coated with a 5 nm platinum/palladium layer. The water contact angle was measured by using a CAM 200 contact-angle system (KSV Instruments Ltd., Helsinki, Finland), and repeated for 4 times, where water was supplied via a syringe in or out of sessile droplets (~5 μL). The compositions of the porous foam, wipers and paper were confirmed by FT-IR spectroscopy (Thermo Nicolet Nexus FT-IR spectrometer) combined with production information. Ice adhesion strength was measured by a universal mechanical tester (Instron Model 5944) equipped with lab-built cooling system and chamber, as described in previous studies [40]. A polypropylene centrifuge tube with a 1 mm thick wall and a 20 mm inner diameter was placed onto the coatings. 1.5 mL deionized water was infused into the molds, the samples were placed in freezer with constant temperature of −18 °C for over 3 h (held for 24 h for one time ice adhesion strength test and held for 3 h for cycling test) to ensure complete freezing. Before test, the samples were transferred from the freezer to the cooling chamber of the test machine and stabilized at −18 °C for 30 min. During ice adhesion test, a force probe with 5 mm diameter propelled the tube-encased ice columns at a velocity of 0.01 mm·s^{-1}, and the probe was located close to the tested coating surface (less than 1 mm) to minimize the torque on the ice cylinder. The loading curve was recorded, and the peak value of the shear force was divided by contact area to obtain the ice adhesion strength. Four samples from each composition were measured to obtain the ice adhesion strength.

3. Results and discussion

3.1. Icephobicity of PTSLIPS form PDMS substrates

Porous PDMS were used as substrates to investigate the ice adhesion strength and durability of PTSLIPS. The porosity was controlled among 18~47% through varying the sacrificial templates' amounts (Fig. 1a). The Fig. 1b revealed the morphologies of porous PDMS with and without sacrificial templates. The sacrificial templates had random particle size distribution, thus pores with diameter range from nanoscale to macroscale were observed from both cross section and top surface view of samples. Additionally, the surface of the porous PDMS was not ideally flat and no extra process (such as fluorination to lower the surface energy) was taken on PDMS surface after removing sacrificial templates. In this way we intended to show that PTSLIPS were easily handled on porous substrates without complex processing steps, which was important for the DIY of anti-icing PTSLIPS.

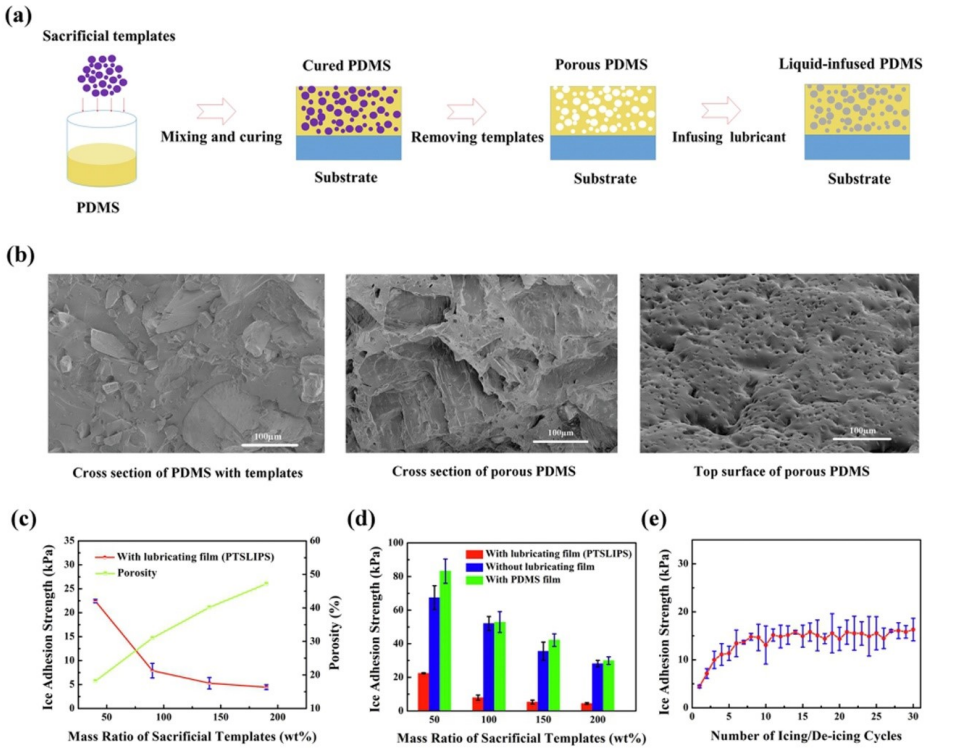

Fig. 1. Design of PTSLIPS with super low ice adhesion strength and excellent durability. (a) Schematics showing the fabrication of porous PDMS through sacrificial templates method and the management of a PTSLIPS by infiltrating a phase transformable lubricant (see Methods Summary). (b) Scanning electron micrographs showing the morphologies of PDMS with 200 wt% mass ratio of sacrificial templates: cross section of cured PDMS before removing templates (left), cross section of porous PDMS after removing templates (center), and top surface of porous PDMS after removing templates (right). (c) Summary of porosity of porous PDMS as a function of mass ratio of sacrificial templates and showing the ice adhesion strength of PTSLIPS along with porosity of PDMS. (d) The comparison of ice adhesion strength among porous PDMS with lubricating film (PTSLIPS), without lubricating film, and with flat PDMS film. (e) Ice adhesion strength of PTSLIPS (from porous PDMS fabricated by 200 wt% sacrificial templates) along with icing/de-icing cycles. (The ice adhesion strength was tested under −18 °C in the whole research).

Referring to ice formation, the PTSLIPS could effectively stop ice front from growing into pores and slow down the rate of lubricant drain, which resulted in low ice adhesion strength and excellent durability. The critical strength (ice adhesion strength) above which the fracture occurs is given by [40,41]

$$\tau = \sqrt{\frac{EG}{\pi a \Lambda}} \quad (1)$$

where E is Young's modulus, G is the surface energy, a is the crack length, and Λ is a non-dimensional constant determined by the geometric configuration of the interface crack [40]. To reduce the ice adhesion strength, efforts on tuning Young's modulus, lowering surface energy, promoting multi-scale crack initiators and increasing crack length have been made [40,42–44]. In this work, low ice adhesion strength (4 ~ 22 kPa) in Fig. 1c was a result from all the three factors, low surface energy, modified Young's modulus, as well as increased crack length originated from the porous PDMS.

To understand the origin of the low ice adhesion strength of the PTSLIPS, we first analyze the ice adhesion strengths of porous PDMS without lubricating film and porous PDMS covered with flat PDMS film (porous PDMS with similar porosity but with smooth surface). As shown in Fig. 1d, the ice adhesion strength decreases with the increase of porosity. With increasing porosity, the apparent Young's modulus decreases, which contributes partly to the reduction of ice adhesion strength in both cases. In addition to lowering apparent Young's modulus, macro-crack initiator (MACI) mechanism could play a role in the ice adhesion of materials with sub-structures (holes) [40]. The porous sub-structures below the surface introduce deformation incompatibility and stiffness inhomogeneity, which maximize the total crack length a and decrease the ice adhesion strength [40,45]. It is interesting to note that the ice adhesion strength of porous PDMS without lubricating film is lower than that of the porous PDMS with flat surface, which indicates that the surface pores were not fully wetted by water and the voids between surface and ice serve as additional stress concentrators (microcracks) [41]. It is known that pure PDMS film displays high ice adhesion strength (~169 kPa) [46]. By introducing phase transformable slippery liquid into porous PDMS, super low ice adhesion (ca. 4 kPa, Fig. 1d) was obtained.

We further studied the durability of PTSLIPS. From the experimental results above, porous PDMS with 47% porosity showed best icephobicity, i.e. lowest ice adhesion strength. Thus, this sample was selected to undergo icing/de-icing cyclic test and the obtained ice adhesion

strength was plotted in Fig. 1e. As expected, the ice adhesion strength increased initially in the first 10 cycles. This was caused by the gradual removal of a residual lubricant film on top of surface [23] together with the removing of ice. The solid lubricant that was trapped in the curved pores was more stable than lubricant on the top of surface and resulted in a constant ice adhesion strength after 10 cycles. The migration of liquid lubricant from the wetting ridge and the surface texture onto ice surface was the main reason for the failure of SLIPS [35]. This migration was driven by capillary force arising by the nucleation of nano-icicle. The liquid lubricant could drain fully from the micro/nano-structures within one or two icing and de-icing cycles. However, the phase transition of lubricant in PTSLIPS solved the problem. The solid lubricant in the pores do not migrate onto ice surface as the liquid lubricant (supplementary Fig. S2). Thus, the drain of lubricant was significantly slowed down. Low ice adhesion strength around ~16 kPa maintained after 30 icing/de-icing cycles, showing an excellent durability. By measuring the weight change of samples before and after cycling test, we found 60 wt% lubricant was still retained in the films after 30 icing/de-icing cycles, which demonstrate oil retention through phase transition and durability of PTSLIPS. To sum up, promising durability was achieved in PTSLIPS. Here we proposed a feasible strategy to prolong the stability of lubricant in the pore through phase transition of lubricant. As a comparison to limited lubricant retention by closely spaced pillars [37], the solid lubricants in freezing atmosphere were more durable and resulted in excellent durability of PTSLIPS.

We also observed that the transition of lubricant from liquid to solid state changed the water contact angle of the surface. The contact angle decreased from 122.54° to 104.43° as lubricant filled pores of porous PDMS, and then further decreased to 86.19° after lubricant transformed into solid state. The detail experiment results and explanation of this change were presented in supplementary Fig. S3.

3.2. Ability of PTSLIPS suits to diverse porous substrates

To enable SLIPS function, chemical affinity of the substrates to the lubricants should be superior to the liquid they want to repel, otherwise the liquid would displace the area of the lubricant and make SLIPS invalid [23]. When extending SLIPS for anti-icing application, it was important that lubricant film survived from water before icing [24]. Otherwise, water occupied the space of lubricant and ice formed in the pores under freezing atmosphere ($T < 0$ °C), which resulted in failure of SLIPS. SLIPS with hydrophilic substrates that had strong chemical affinity with water can easily fail in anti-icing application (Fig. 2). Thus, substrates were always silanized or fluorinated to render the surface hydrophobic and increase the interfacial energy between water and substrate [24,36]. This allowed lubricant to stably adhere to the surface in the presence of water.

In this work, fastening lubricant in the porous structure through phase transition provided an alternative strategy to stabilize lubricant. In the design of PTSLIPS, the surface chemical affinity can be ignored, which significantly extended the choices of substrates (both hydrophobic and hydrophilic surfaces) and simplified manufacture steps. The design mechanism was illustrated in Fig. 2. Once the lubricant transformed into solid state, the water couldn't displace the lubricant and would freeze on the top of lubricating film, which prevented ice forming into pores of hydrophilic substrates. We further demonstrated that by choosing hydrophilic blue wiper (supplementary Fig. S1f showed the mainly compositions of this blue wiper), followed by infusing silicon oil and peanut oil, respectively. They were preplaced in freezer with a temperature of −20 °C, and then water droplets were dripped onto each surface (supplementary Movie S1). Water can easily replace the liquid silicon oil in the pores but cannot replace the solid peanut oil. Water immersed into substrate once dripped onto SLIPS. While the water droplet on PTSLIPS could keep its shape and converted into hemispherical ice. Additionally, as the peanut oil kept in solid state under 3 °C, the oil migration onto ice drop surface caused by capillary force [35] was also prevented (supplementary Fig. S2). In this way, anti-icing materials with excellent durability could be designed not only from hydrophobic substrates but also from hydrophilic substrates.

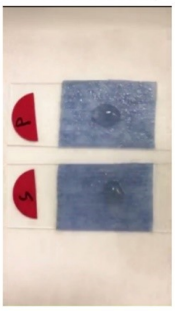

Supplementary Movie S1.

We further demonstrated the PTSLIPS could be easily manufactured from various porous substrates that were familiar in our daily life. Several wipers, foams and paper (supplementary Fig. S1 showed the main compositions of these materials) were taken as substrates to fabricate PTSLIPSs. Low ice adhesion strength ranged from 14 kPa to 28 kPa were achieved from hydrophobic substrates, and much higher ice adhesion strength (217 ~ 280 kPa) was obtained on PTSLIPSs from hydrophilic substrates. This significant difference was due to the interaction between ice and porous skeleton. The interfacial energy between ice and hydrophilic surface was much higher than that of hydrophobic surface, which resulted in stronger ice adhesion [42]. However, the ice adhesion strength of PTSLIPS from hydrophilic surface were significantly lower than reported hydrophilic surface and was comparable with superhydrophobic surface [47]. Thus, this strategy has the potential to achieve appropriate anti-icing property on both hydrophobic and hydrophilic surface. In addition to wide adaptation on substrates with various chemical compositions, PTSLIPS also suited to substrates with wide pore size distributions and pore morphologies (Fig. 3). Generally, carefully designed micro/nanotextured surfaces were essential for retention of the infused lubricating liquids [24,27,28,38]. The liquid lubricants were caught through capillary force, and the force would decrease with pore size increasing [48]. Thus, porous substrates with large pores were inappropriate in the design of SLIPS for liquid lubricants easily ran off. However, in the PTSLIPS, lubricants could remain in the pores once converted to solid phase. Therefore, anti-icing materials could be fabricated through infusing phase transformable lubricants into various porous substrates. Since the strategy in this work broke through the limitation of hydrophobic surface and small pore size in the design of SLIPS, the PTSLIPS could be attractive for people to DIY in home with porous materials in hand.

3.3. The self-repairing characteristic of PTSLIPS

The PTSLIPS also possessed the self-repairing property like SLIPS, moreover PTSLIPS could not only repair the lubricating film on the surface but also the bulk damage (Fig. 4a). For self-repairing the bulk damage, liquid lubricant flew to the damaged area and refilled the voids at first, then phase transition enabled solid lubricant with reasonable strength and repaired the bulk damage. To achieve self-repairing, the pore connectivity in substrate should support for the flowing of lubricant and the lubricant amount at the damage part should be abundant to provide enough mechanical strength. Thus highly porous substrates with excellent pore connectivity were necessary for the design of self-repairing PTSLIPS. PTSLIPS fabricated from

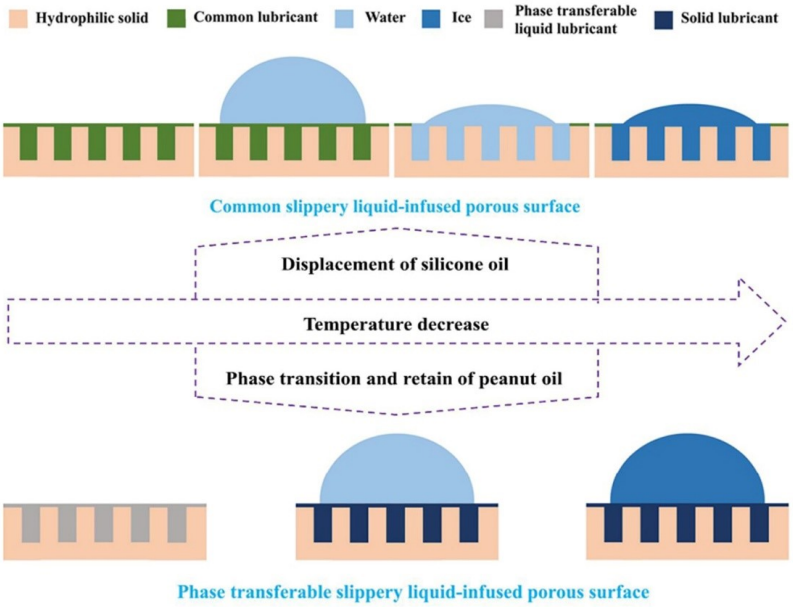

Fig. 2. Schematic illustration of the stability of lubricating films on silicone oil (top) and peanut oil (bottom) infused hydrophilic substrate during freezing process. Schematic side views of state of water droplets and ice.

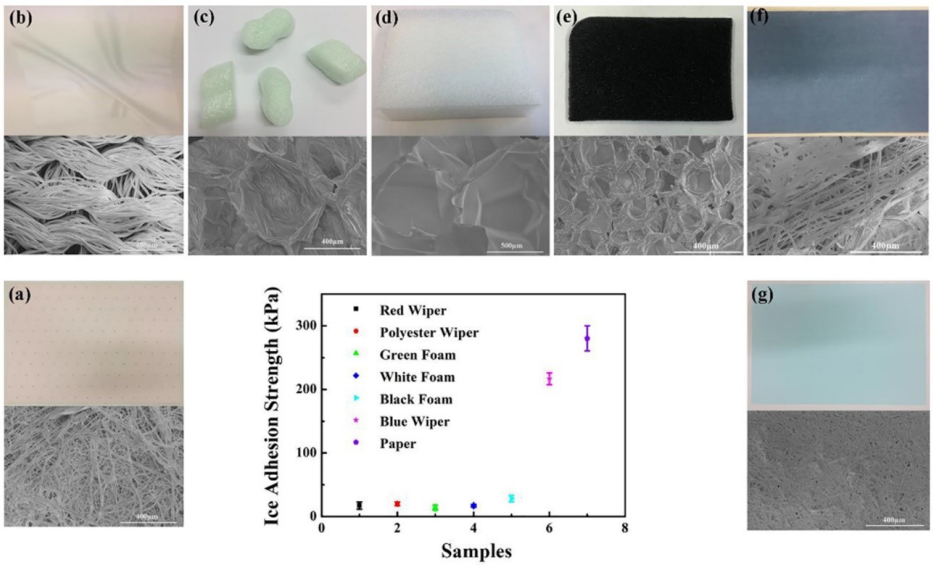

Fig. 3. Feasibility of PTSLIPS from porous substrates with various chemical compositions, pore size distributions and pores morphologies. (a)–(g) Optical images and scanning electron micrographs showing the appearance and structure morphologies of each porous substrate. Ice adhesion strength of samples 1 – 7 derived from substrates of a – g, respectively.

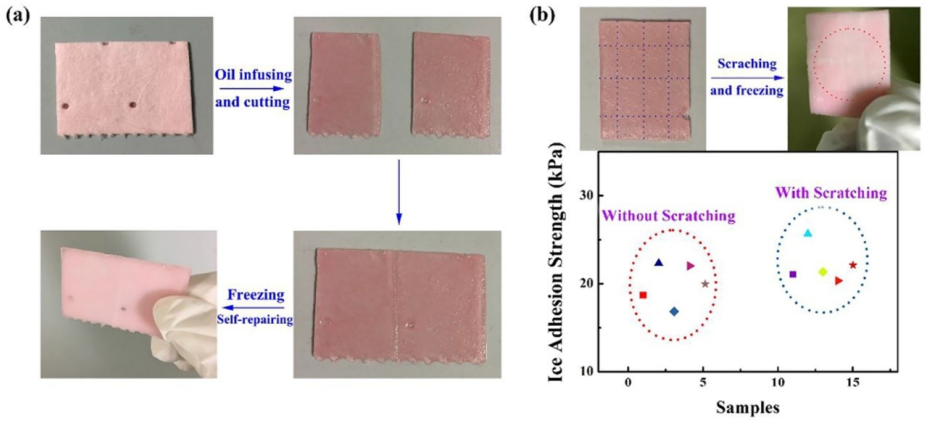

Fig. 4. Self-repairing and mechanical damage resistance of PTSLIPS. (a) Optical images showing the capability of a PTSLIPS to self-repair from physical cut. (b) Ice adhesion strength showing the restoration of icephobicity of a PTSLIPS after mechanical damage. Top panels show the area of scratching (blue dashed lines) and ice adhesion test area (red dashed circle). Bottom panel shows the ice adhesion strength of PTSLIPS with and without scratching. (The freezing temperature was −18 °C for this part).

porous substrate made of polypropylene with porosity ~84% (porous substrates in Fig. 3a) was used to investigate the self-repairing property. The self-repairing of PTSLIPS could be completed through one thawing-freezing process. In Fig. 4a, the bulk healing was finished in 30 min once sample transferred into freezer (with a temperature of −20 °C). Firstly, in temperature above 3 °C, liquid lubricant could flow to the damaged area by surface-energy-driven-capillary force, the physical voids were spontaneously refilled by the lubricant [49]. Then the sample was placed in a freezing atmosphere, which triggered the phase transition of lubricant from liquid to solid. The solid lubricant had stronger intermolecular force and attached reasonable mechanical strength onto the damaged area. The self-repairing characteristic improved the durability of anti-icing materials [46]. PTSLIPS still had excellent anti-icing properties after mechanical damage (Fig. 4b). Ice adhesion strength test was carried out on the surfaces after mechanical scratching. Low ice adhesion strengths (20 ~ 26 kPa) were achieved on the scratched area, which were very similar to the same surfaces without scratching (16 ~ 22 kPa).

4. Conclusion

In summary, this work introduced phase transformable slippery liquid infused porous surfaces (PTSLIPS) with remarkable anti-icing properties. Porous PDMS fabricated through sacrificial template method and infused by peanut oil showed low ice adhesion strength (4 ~ 22 kPa) as well as excellent durability. Since peanut oil kept solid state below 0 °C, the stability of lubricant in porous structure was enhanced in icing/de-icing cycles. For selected samples, low ice adhesion strength around ~16 kPa maintained after 30 icing/de-icing cycles.

The PTSLIPS was further proved to indiscriminately adapt to porous substrates with various chemical compositions. The enhanced retention of solid lubricant in porous structure prevented the lubricant form being replaced by water, therefore avoided ice formation in the pores and lowered down mechanical interlocking between ice and porous structures. The phase transition also made it possible for storing lubricant in pores with wide pore size distributions and various pores morphologies. What mentioned above simplified the fabrication procedure of liquid infused porous surfaces and maximized the substrates (both hydrophobic and hydrophilic materials) used for anti-icing area. The PTSLIPS also possessed self-repairing property that could repair the bulk damage as well as retain low ice adhesion strength after mechanical scratch. Herein, people were able to fabricate anti-icing materials with porous substrates in hand by an easy way.

Acknowledgements

The Research Council of Norway is acknowledged for the support to the FRINATEK project Towards Design of Super-Low Ice Adhesion Surfaces (SLICE, 250990).

Appendix A. Supplementary data

Supplementary data to this article can be found online at https://doi.org/10.1016/j.cej.2018.11.224.

References

[1] A.K. Andersson, L. Chapman, The impact of climate change on winter road maintenance and traffic accidents in West Midlands, UK, Accid. Anal. Prev. 43 (2011) 284–289.
[2] J. Andrey, R. Olley, The relationship between weather and road safety: past and future research directions, Climatol. Bull. 24 (1990) 123–137.
[3] U. Björnstig, J. Björnstig, A. Dahlgren, Slipping on ice and snow—elderly women and young men are typical victims, Accid. Anal. Prev. 29 (1997) 211–215.
[4] J. Shin, T.H. Bond, Surface roughness due to residual ice in the use of low power deicing systems, 31st, Aerospace Sciences Meeting (1993).
[5] R. Gent, N. Dart, J. Cansdale, Aircraft icing, Phil. Trans. R. Soc. Lond. A. 358 (2000) 2873–2911.
[6] J. Marwitz, M. Politovich, B. Bernstein, F. Ralph, P. Neiman, R. Ashenden, J. Bresch, Meteorological conditions associated with the ATR72 aircraft accident near Roselawn, Indiana, on 31, Bull. Am. Meteorol. Soc. 78 (1997) (1994) 41–52.
[7] W. Pike, Extreme warm frontal icing on 25 causes an aircraft accident near Uttoxeter, Meteorol. Appl. 2 (1995) (1994) 273–279.
[8] A.J. Meuler, J.D. Smith, K.K. Varanasi, J.M. Mabry, G.H. McKinley, R.E. Cohen, Relationships between water wettability and ice adhesion, ACS Appl. Mater. Inter. 2 (2010) 3100–3110.
[9] P. Tourkine, M. Le Merrer, D. Quéré, Delayed freezing on water repellent materials, Langmuir 25 (2009) 7214–7216.
[10] S. Kulinich, M. Farzaneh, How wetting hysteresis influences ice adhesion strength on superhydrophobic surfaces, Langmuir 25 (2009) 8854–8856.
[11] L. Mishchenko, B. Hatton, V. Bahadur, J.A. Taylor, T. Krupenkin, J. Aizenberg, Design of ice-free nanostructured surfaces based on repulsion of impacting water droplets, ACS Nano 4 (2010) 7699–7707.
[12] A.J. Meuler, G.H. McKinley, R.E. Cohen, Exploiting topographical texture to impart icephobicity, ACS Nano 4 (2010) 7048–7052.
[13] S. Jung, M. Dorrestijn, D. Raps, A. Das, C.M. Megaridis, D. Poulikakos, Are superhydrophobic surfaces best for icephobicity? Langmuir 27 (2011) 3059–3066.

[14] S. Kulinich, S. Farhadi, K. Nose, X. Du, Superhydrophobic surfaces: are they really ice-repellent? Langmuir 27 (2010) 25–29.
[15] X. Yao, Y. Song, L. Jiang, Applications of bio-inspired special wettable surfaces, Adv. Mater. 23 (2011) 719–734.
[16] J.C. Bird, R. Dhiman, H.-M. Kwon, K.K. Varanasi, Reducing the contact time of a bouncing drop, Nature 503 (2013) 385.
[17] A. Gauthier, S. Symon, C. Clanet, D. Quéré, Water impacting on superhydrophobic macrotextures, Nat. commun. 6 (2015) 8001.
[18] K.A. Wier, T.J. McCarthy, Condensation on ultrahydrophobic surfaces and its effect on droplet mobility: ultrahydrophobic surfaces are not always water repellant, Langmuir 22 (2006) 2433–2436.
[19] K.K. Varanasi, T. Deng, J.D. Smith, M. Hsu, N. Bhate, Frost formation and ice adhesion on superhydrophobic surfaces, Appl. Phys. Lett. 97 (2010) 234102.
[20] Z. He, E.T. Vågenes, C. Delabahan, J. He, Z. Zhang, Room Temperature Characteristics of Polymer-Based Low Ice Adhesion Surfaces, Sci. Rep. 7 (2017) 42181.
[21] S. Farhadi, M. Farzaneh, S. Kulinich, Anti-icing performance of superhydrophobic surfaces, Appl. Surf. Sci. 257 (2011) 6264–6269.
[22] Y. Wang, J. Xue, Q. Wang, Q. Chen, J. Ding, Verification of icephobic/anti-icing properties of a superhydrophobic surface, ACS Appl. Mater. Inter. 5 (2013) 3370–3381.
[23] T.-S. Wong, S.H. Kang, S.K. Tang, E.J. Smythe, B.D. Hatton, A. Grinthal, J. Aizenberg, Bioinspired self-repairing slippery surfaces with pressure-stable omniphobicity, Nature 477 (2011) 443–447.
[24] P. Kim, T.-S. Wong, J. Alvarenga, M.J. Kreder, W.E. Adorno-Martinez, J. Aizenberg, Liquid-infused nanostructured surfaces with extreme anti-ice and anti-frost performance, ACS Nano 6 (2012) 6569–6577.
[25] P.W. Wilson, W. Lu, H. Xu, P. Kim, M.J. Kreder, J. Alvarenga, J. Aizenberg, Inhibition of ice nucleation by slippery liquid-infused porous surfaces (SLIPS), Phys. Chem. Chem. Phys. 15 (2013) 581–585.
[26] Q. Liu, Y. Yang, M. Huang, Y. Zhou, Y. Liu, X. Liang, Durability of a lubricant-infused Electrospray Silicon Rubber surface as an anti-icing coating, Appl. Surf. Sci. 346 (2015) 68–76.
[27] S.B. Subramanyam, K. Rykaczewski, K.K. Varanasi, Ice adhesion on lubricant-impregnated textured surfaces, Langmuir 29 (2013) 13414–13418.
[28] X. Yin, Y. Zhang, D. Wang, Z. Liu, Y. Liu, X. Pei, B. Yu, F. Zhou, Integration of self-lubrication and near-infrared photothermogenesis for excellent anti-icing/deicing performance, Adv. Funct. Mater. 25 (2015) 4237–4245.
[29] M. Susoff, K. Siegmann, C. Pfaffenroth, M. Hirayama, Evaluation of icephobic coatings—screening of different coatings and influence of roughness, Appl. Surf. Sci. 282 (2013) 870–879.
[30] R. Dou, J. Chen, Y. Zhang, X. Wang, D. Cui, Y. Song, L. Jiang, J. Wang, Anti-icing coating with an aqueous lubricating layer, ACS Appl. Mater. Inter. 6 (2014) 6998–7003.
[31] A. Beisswenger, G. Fortin, C. Laforte, Advances in ice adherence and accumulation reduction testing at the anti-icing materials international laboratory (AMIL), Future De-Icing Technologies, Berlin, 2010.
[32] J.D. Smith, R. Dhiman, S. Anand, E. Reza-Garduno, R.E. Cohen, G.H. McKinley, K.K. Varanasi, Droplet mobility on lubricant-impregnated surfaces, Soft Matter 9 (2013) 1772–1780.
[33] C. Howell, T.L. Vu, C.P. Johnson, X. Hou, O. Ahanotu, J. Alvarenga, D.C. Leslie, O. Uzun, A. Waterhouse, P. Kim, Stability of surface-immobilized lubricant interfaces under flow, Chem. Mater. 27 (2015) 1792–1800.
[34] J.S. Wexler, I. Jacobi, H.A. Stone, Shear-driven failure of liquid-infused surfaces, Phys. Rev. Lett. 114 (2015) 168301.
[35] K. Rykaczewski, S. Anand, S.B. Subramanyam, K.K. Varanasi, Mechanism of frost formation on lubricant-impregnated surfaces, Langmuir 29 (2013) 5230–5238.
[36] S. Anand, A.T. Paxson, R. Dhiman, J.D. Smith, K.K. Varanasi, Enhanced condensation on lubricant-impregnated nanotextured surfaces, ACS Nano 6 (2012) 10122–10129.
[37] P. Kim, M.J. Kreder, J. Alvarenga, J. Aizenberg, Hierarchical or not? Effect of the length scale and hierarchy of the surface roughness on omniphobicity of lubricant-infused substrates, Nano Lett. 13 (2013) 1793–1799.
[38] M.J. Coady, M. Wood, G.Q. Wallace, K.E. Nielsen, A.-M. Kietzig, F. Lagugné-Labarthet, P.J. Ragogna, Icephobic behavior of UV-cured polymer networks incorporated into slippery lubricant-infused porous surfaces: improving SLIPS durability, ACS Appl. Mater. Inter. 10 (2018) 2890–2896.
[39] M.J. Kreder, J. Alvarenga, P. Kim, J. Aizenberg, Design of anti-icing surfaces: smooth, textured or slippery? Nat. Rev. Mater. 1 (2016) 15003.
[40] Z. He, S. Xiao, H. Gao, J. He, Z. Zhang, Multiscale crack initiator promoted superlow ice adhesion surfaces, Soft Matter 13 (2017) 6562–6568.
[41] M. Nosonovsky, V. Hejazi, Why superhydrophobic surfaces are not always icephobic, ACS Nano 6 (2012) 8488–8491.
[42] S. Xiao, J. He, Z. Zhang, Nanoscale deicing by molecular dynamics simulation, Nanoscale 8 (2016) 14625–14632.
[43] C. Urata, G.J. Dunderdale, M.W. England, A. Hozumi, Self-lubricating organogels (SLUGs) with exceptional syneresis-induced anti-sticking properties against viscous emulsions and ices, J. Mater. Chem. A 3 (2015) 12626–12630.
[44] K. Golovin, S.P. Kobaku, D.H. Lee, E.T. DiLoreto, J.M. Mabry, A. Tuteja, Designing durable icephobic surfaces, Sci. Adv. 2 (2016) e1501496.
[45] Z. He, Y. Zhuo, J. He, Z. Zhang, Design and preparation of sandwich-like polydimethylsiloxane (PDMS) sponges with super-low ice adhesion, Soft Matter (2018).
[46] Y. Zhuo, V. Håkonsen, Z. He, S. Xiao, J. He, Z. Zhang, Enhancing the Mechanical Durability of Icephobic Surfaces by Introducing Autonomous Self-Healing Function, ACS Appl. Mater. Inter. 10 (2018) 11972–11978.
[47] T. Bharathidasan, S.V. Kumar, M. Bobji, R. Chakradhar, B.J. Basu, Effect of wettability and surface roughness on ice-adhesion strength of hydrophilic, hydrophobic and superhydrophobic surfaces, Appl. Surf. Sci. 314 (2014) 241–250.
[48] H.-J. Butt, M. Kappl, Normal capillary forces, Adv. Colloid. Interface. Sci. 146 (2009) 48–60.
[49] C. Ishino, M. Reyssat, E. Reyssat, K. Okumura, D. Quere, Wicking within forests of micropillars, Europhys. Lett. 79 (2007) 56005.

Supplementary Materials for

Phase transition enabled durable icephobic surfaces and its DIY design

Feng Wang[1], Wenwu Ding[2], Jianying He[1,*], Zhiliang Zhang[1,*]

1. NTNU Nanomechanical Lab, Department of Structural Engineering, Norwegian University of Science and Technology (NTNU), Trondheim 7491, Norway.

2. Department of Energy and Process Engineering, Norwegian University of Science and Technology (NTNU), Trondheim 7491, Norway.

*E-mail: jianying.he@ntnu.no, zhiliang.zhang@ntnu.no

The FT-IR spectra of various porous substrates were displayed in Fig. S1. With the combination of products information, the main compositions of these substrates can be defined, and the wettability can be indicated.

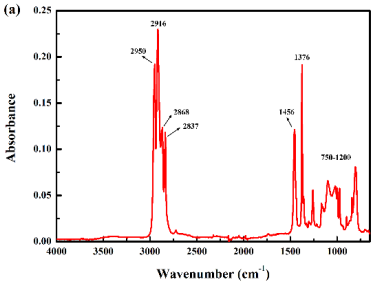

Wave number (cm^{-1})	Assignments
2950	CH_3 asymmetric stretching vibrations
2916	CH_2 asymmetric stretching vibrations
2868	CH_3 symmetric stretching vibrations
2837	CH_2 symmetric stretching vibrations
1456	CH_3 asymmetric deformation vibrations or CH_2 scissoring vibrations
1376	CH_3 symmetric deformation vibrations
750-1200	CH_3 asymmetric rocking, C–H wagging vibrations, C–C asymmetric and symmetric stretching vibrations, CH_2 rocking vibrations and so on

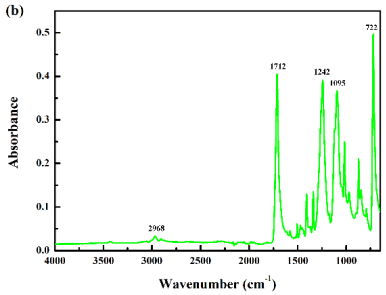

Wave number (cm^{-1})	Assignments
2968	asymmetric C–H stretching
1712	C=O stretching
1242	asymmetric COC stretching
1095	symmetric COC stretching
722	C–H wagging vibrations

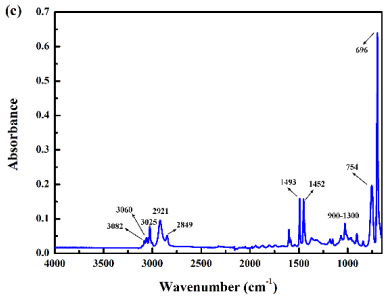

Wave number (cm^{-1})	Assignments
3082, 3060 and 3025	aromatic C-H stretching vibrations
2921	asymmetric stretching vibrations of CH_2
2849	symmetric stretching vibrations of CH_2
1493 and 1452	C-C stretching vibrations in the aromatic ring
900-1300	fingerprint region
754 and 696	C–H wagging vibrations

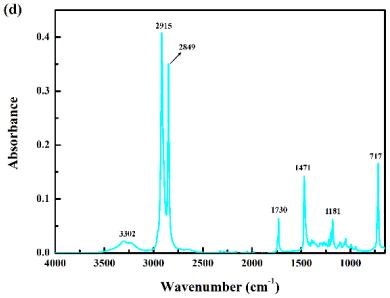

Wave number (cm^{-1})	Assignments
3302	angular deformation of OH
2915	CH_2 asymmetric stretching vibrations
2849	CH_2 symmetric stretching vibrations
1730	C=O (ester) stretching
1471	C-H scissoring vibrations
1181	asymmetric stretching of C-O and CH_2
717	CH_2 rocking vibrations

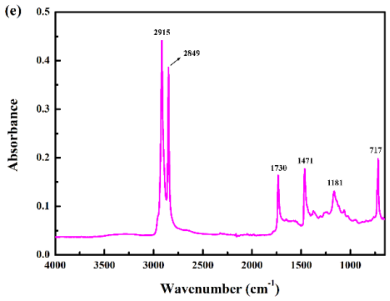

Wave number (cm^{-1})	Assignments
2915	CH_2 asymmetric stretching vibrations
2849	CH_2 symmetric stretching vibrations
1730	C=O (ester) stretching
1471	C-H scissoring vibrations
1181	asymmetric stretching of C-O and CH_2
717	CH_2 rocking vibrations

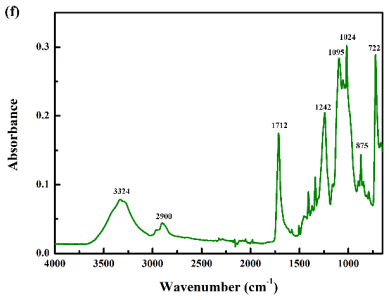

Wave number (cm^{-1})	Assignments
3324	OH stretching
2900	stretching and deformation vibrations of C-H
1712	C=O stretching
1242	asymmetric COC stretching
1095	symmetric COC stretching
1024	stretching of C-O
875	β-glycosidic linkage between glucose units
722	C–H wagging vibrations

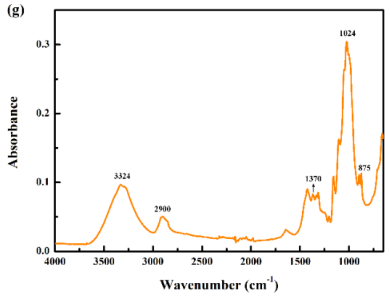

Wave number (cm^{-1})	Assignments
3324	OH stretching
2900 and 1370	stretching and deformation vibrations of C-H
1024	stretching of C-O
875	β-glycosidic linkage between glucose units

Supplementary Figure S1. FT-IR spectra verifying the main compositions of porous substrates. (a) Red wiper is made of polypropylene and is hydrophobic material.[1,2] **(b)** Polyester wiper is made of polyethylene terephthalate and is hydrophobic material.[3,4] **(c)** Green foam is made of polystyrene and is hydrophobic material.[5,6] **(d)** White foam is made of polyvinyl chloride and is hydrophobic material.[7,8] **(e)** Black foam is made of polyvinyl chloride and is hydrophobic material. The band at 3302 cm-1 that shows up in Fig. S1d but not in Fig. S1e mainly result from the different fabrication methods of these two polyvinyl chloride samples. **(f)** Blue wiper is made of 55% cellulose and 45% polyethylene terephthalate, and is hydrophilic material. **(g)** Paper is made of cellulose and is hydrophilic material.[9]

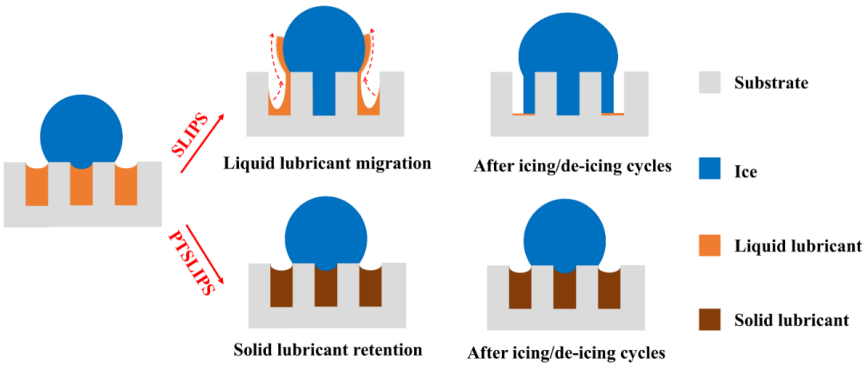

Supplementary Figure S2. Schematic of the state of lubricant in ice/de-icing cycles. Top panels show migration and drain of liquid lubricant during icing/de-icing cycles, while solid lubricant was retained during icing/de-icing cycles in bottom panels, which induces PTSLIPS superior durability.

The change of contact angle can be explained by the model proposed by Cassie and Baxter[10]

$$\cos\theta^* = f_1 \cos\theta_1 + f_2 \cos\theta_2 \qquad (1)$$

where θ^* is the contact angle of the surface, f_1 and f_2 stand for the area fraction of the liquid droplet in contact with the surface part A, and the surface part B, respectively. θ_1 and θ_2 stand for the contact angle of liquid in contact with surface part A and surface part B, respectively. As shown in Fig. S3, contact angle change only depended on the surface part B due to same surface part A (PDMS). The higher wettability of the part B was, the smaller the contact angle was. Generally, the value of water contact angle in air was 180º, since air was considered non-wetting[11]. Fatty acid (main composition of peanut oil, table S1) contained –COOH function groups, thus peanut oil was more wettable than air. Once liquid peanut oil was filled instead of air, contact angle θ^* decreased. The phase change of lubricant further altered the contact angle. The mobility of molecules at surface decreased with lowering temperature, which reduced the total entropy of the surface and thereby increased its free energy, ΔG[12]. The surface free energy could be related with surface tension as equation 2, where G is Gibbs free energy, γ is surface tension and A is surface area[13]. Thus, the surface tension of peanut oil would increase once transformed to solid state.

$$dG = \gamma dA \qquad (2)$$

$$\cos\theta = \frac{\gamma_{SA} - \gamma_{SL}}{\gamma_{LA}} \qquad (3)$$

Based on the definition of contact angle (equation 3)[10], where θ is the contact angle, γ_{SA} is the solid-air interfacial tension, γ_{SL} is the solid-liquid interfacial tension, and γ_{LA} is the liquid-air interfacial tension. The phase transition resulted in greater increase of γ_{SA} than γ_{SL}. The γ_{LA} was regarded as unchanged, and thus θ would decrease. Thus, the wettability gradually increased as surface part B changed from air to liquid lubricant and then to solid lubricant.

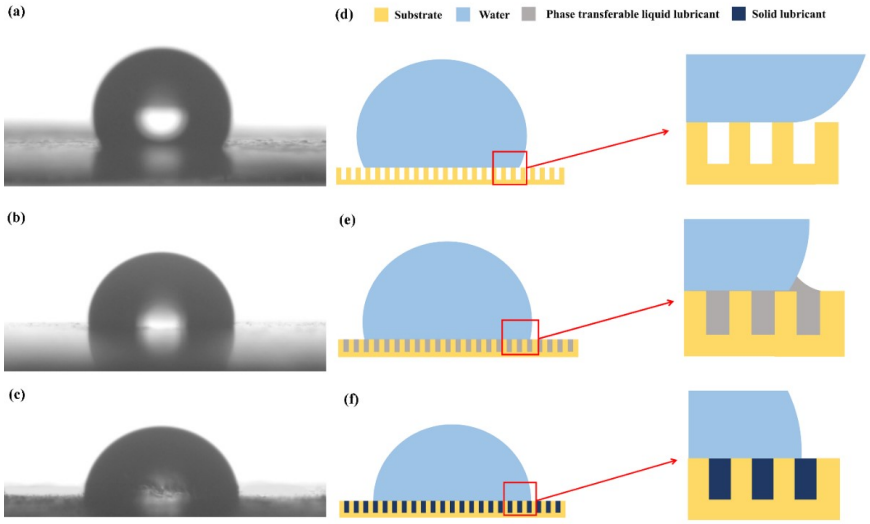

Supplementary Figure S3. Water contact angle of the porous PDMS, liquid lubricant infused porous PDMS, and solid lubricant infused porous PDMS. (a) ~ (c) Experiment results of contact angle (The volume of water droplet used was 5 μL), the contact angles were 122.54º, 104.43º and 86.19º, respectively. The samples (a) and (b) were tested in room temperature, sample (c) was tested at 0℃ after peanut oil converted into solid state. The substrate was porous PDMS fabricated by 200 wt% sacrificial templates. **(d) ~ (f)** Schematics showing the models of wetting for the three different samples.

The design concept of PTSLIPS is that the lubricants used can transform into solid state above 0℃. Table 1 shows melting point of a batch of oils. Both animal fat and vegetable oils have higher melting points than commercial silicone oil and fluorinated synthetic oils. The compositions reveal that lubricants from fatty acids (mainly mixtures of saturated fatty acids and unsaturated fatty acids) are promising choices for manufacturing PTSLIPS. Additionally, these animal fat and vegetable oils are environmentally friendly choices. We further recommend the lubricants to be liquid at room temperature, thus simplifying the infusing process [14]. Therefore, the oils with melting points between 0~30℃ can be good choices. Here is a summary of animal fat, vegetable oil and some frequently used lubricants.

Supplementary Table S1. Summary of animal fat, vegetable oil and some frequently used silicone oil or fluorinated lubricants.

Lubricant	Setting point (℃)	Monounsaturated fatty acid (wt%)	Polyunsaturated fatty acid (wt%)	Saturated fatty acid (wt%)
Mutton tallow	51.5[15]	30.34[16]	1.61[16]	68.05[16]
Beef tallow	47.87[17]	38.26[16]	6.59[16]	55.15[16]
Chicken fat	43.19[17]	49.26[16]	18.26[16]	32.48[16]
Lard	41[18]	42.62[16]	17.29[16]	39.02[16]
Palm oil	35[18]	40.17[19]	9.92[19]	49.91[19]
Cocoa butter	34[18]	33.60[20]	2.68[20]	62.92[20]
Babassu oil	28.9[21]	10[22]	--	90[22]
Coconut oil	2518	623	323	9123
Palm kernel oil	24[18]	15.3[24]	2.3[24]	82[24]
Peanut oil	3[18]	55.7[25]	28.7[25]	15.6[25]
Cotton seed oil	-1	16.2[26]	55.2326	28.5726
Tung oil	-2.5[18]	4.0[27]	90.5[27]	5.5[27]
Olive oil	-6[18]	73[28]	10[28]	16.6[28]
Rapeseed oil	-10[18]	60.37[29]	32.07[29]	6.37[29]
Soybean oil	-16[18]	22.2[28]	60.6[28]	15.7[28]
Sunflower oil	-17[18]	33.8[28]	56.5[28]	8.9[28]
Castor oil	-18[18]	92.4[30]	5.2[30]	2.3[30]
Linseed oil	-24[18]	17.7[28]	73.5[28]	8.8[28]
Silicone oil 5cSt	-54.99	--	--	--
Silicone oil 10cSt	-55	--	--	--
Silicone oil 20cSt	-55	--	--	--
Silicone oil 50cSt	-55	--	--	--
Silicone oil 100cSt	-55	--	--	--
Silicone oil 350cSt	-55	--	--	--
Silicone oil 500cSt	-55	--	--	--
Silicone oil 1000cSt	-55	--	--	--
Silicone oil 10000cSt	-55	--	--	--

Silicone oil 30000cSt	-55	--	--	--
Silicone oil 100000cSt	-55	--	--	--
Medical grade silicone oils	-50.7 ~ -36.9[31]	--	--	--
Krytox 100	-70	--	--	--
Krytox 101	-70	--	--	--
Krytox 102	-63	--	--	--
Krytox 103	-60	--	--	--
Krytox 104	-51	--	--	--
Krytox 105	-36	--	--	--
Krytox 106	-36	--	--	--
Krytox 107	-30	--	--	--
FC-40	-57	--	--	--
FC-43	-50	--	--	--
FC-70	-25	--	--	--
FC-72	-90	--	--	--
FC-770	-127	--	--	--
FC-3283	-50	--	--	--
FC-3284	-73	--	--	--
DC702	< -20	--	--	--
DC704	-35	--	--	--
DC705	-10	--	--	--

Note: 1. These are a brief summary form reference. The melting points and fatty acid composition may have slight difference depend on manufacturers. 2. The melting points of silicon oil 5 ~ 100000 cSt are obtained from the product information on Sigma-Aldrich. The melting points of medical grade silicone oils are evaluated from the endotherm in DSC curves that related to the melting of silicon oil. 3. The commercial Krytox 100 ~ 107 show oil pour point instead of melting point form the product information. 4. The commercial FC-40 ~ 3284 shows oil pour point instead of melting point form the product information. 5. The commercial DC702 ~ 705 also shows oil pour point instead of melting point form the product information.

Supplementary Movie S1. Comparison of the stability and displacement of lubricating films on silicone oil (s) and peanut oil (p) infused hydrophilic substrate.

References

1 Sciarratta, V., Vohrer, U., Hegemann, D., Müller, M. & Oehr, C. Plasma functionalization of polypropylene with acrylic acid. *Surface and Coatings Technology* **174**, 805-810 (2003).

2 Socrates, G. *Infrared and Raman characteristic group frequencies: tables and charts*. (John Wiley & Sons, 2001).

3 Tobin, M. C. The infrared spectra of polymers. II. The infrared spectra of polyethylene terephthalate. *The Journal of Physical Chemistry* **61**, 1392-1400 (1957).

4 Strain, I. *et al.* Electrospinning of recycled PET to generate tough mesomorphic fibre membranes for smoke filtration. *Journal of Materials Chemistry A* **3**, 1632-1640 (2015).

5 Painter, P., Sobkowiak, M. & Park, Y. Vibrational relaxation in atactic polystyrene: An infrared spectroscopic study. *Macromolecules* **40**, 1730-1737 (2007).

6 Olmos, D., Martin, E. & Gonzalez-Benito, J. New molecular-scale information on polystyrene dynamics in PS and PS–BaTiO 3 composites from FTIR spectroscopy. *Physical Chemistry Chemical Physics* **16**, 24339-24349 (2014).

7 Bueno-Ferrer, C., Garrigós, M. & Jiménez, A. Characterization and thermal stability of poly (vinyl chloride) plasticized with epoxidized soybean oil for food packaging. *Polymer degradation and stability* **95**, 2207-2212 (2010).

8 Da Silva, M. A., Vieira, M. G. A., Maçumoto, A. C. G. & Beppu, M. M. Polyvinylchloride (PVC) and natural rubber films plasticized with a natural polymeric plasticizer obtained through polyesterification of rice fatty acid. *Polymer Testing* **30**, 478-484 (2011).

9 Abderrahim, B. *et al.* Kinetic thermal degradation of cellulose, polybutylene succinate and a green composite: comparative study. *World Journal of Environmental Engineering* **3**, 95 (2015).

10 Cassie, A. & Baxter, S. Wettability of porous surfaces. *Transactions of the Faraday society* **40**, 546-551 (1944).

11 Lafuma, A. & Quéré, D. Superhydrophobic states. *Nature materials* **2**, 457 (2003).

12 Moeini, F., Hemmati-Sarapardeh, A., Ghazanfari, M.-H., Masihi, M. & Ayatollahi, S. Toward mechanistic understanding of heavy crude oil/brine interfacial tension: The roles of salinity, temperature and pressure. *Fluid phase equilibria* **375**, 191-200 (2014).

13 Gibbs, J. W. *The Collected Works of J. Willard Gibbs-Volume 1: Thermodynamics*. (Yale University Press, 1945).

14 Wong, T.-S. *et al.* Bioinspired self-repairing slippery surfaces with pressure-stable omniphobicity. *Nature* **477**, 443-447 (2011).

15 List, G., Steidley, K., Neff, W. & Snowder, G. Physical properties of mutton tallow. *Grasas y aceites* **54**, 113-115 (2003).

16 Nizar, N. N. A., Marikkar, J. M. N. & Hashim, D. M. Differentiation of lard, chicken fat, beef fat and mutton fat by GCMS and EA-IRMS techniques. *Journal of oleo science* **62**, 459-464 (2013).

17 Wei, C., Fu, J., Liu, D., Zhang, Z. & Liu, G. Functional properties of chicken fat-based shortenings: Effects of based oils and emulsifiers. *International Journal of Food Properties* **20**, S3277-S3288 (2017).

18 Melting points of oils *The Engineering ToolBox* (2008).

19 Man, Y. C., Haryati, T., Ghazali, H. & Asbi, B. Composition and thermal profile of crude palm oil and its products. *Journal of the American Oil Chemists' Society* **76**, 237-242 (1999).

20 Lipp, M. *et al.* Composition of genuine cocoa butter and cocoa butter equivalents. *Journal of Food Composition and analysis* **14**, 399-408 (2001).

21 Talbot, G. *Specialty Oils and Fats in Food and Nutrition: Properties, Processing and Applications*. (Woodhead Publishing, 2015).

22 Alencar, J., Alves, P. & Craveiro, A. Pyrolysis of tropical vegetable oils. *Journal of Agricultural and Food Chemistry* **31**, 1268-1270 (1983).

23 Katragadda, H. R., Fullana, A., Sidhu, S. & Carbonell-Barrachina, Á. A. Emissions of volatile aldehydes from heated cooking oils. *Food Chemistry* **120**, 59-65 (2010).

24 Ang, C. Y., Liu, K. & Huang, Y.-W. *Asian foods: Science and technology*. (CRC Press, 1999).

25 Ramos, M. J., Fernández, C. M., Casas, A., Rodríguez, L. & Pérez, Á. Influence of fatty acid composition of raw materials on biodiesel properties. *Bioresource technology* **100**, 261-268 (2009).

26 Azcan, N. & Danisman, A. Alkali catalyzed transesterification of cottonseed oil by microwave irradiation. *Fuel* **86**, 2639-2644 (2007).

27 Axtell, B. L. & Fairman, R. *Minor oil crops. Part I-Edible oils. Part II-Non-edible oils. Part III-Essential oils*. (1992).

28 Kamal-Eldin, A. & Andersson, R. A multivariate study of the correlation between tocopherol content and fatty acid composition in vegetable oils. *Journal of the American Oil Chemists' Society* **74**, 375-380 (1997).

29 Gustafsson, I. B., Haglund, Å. & Johansson, L. The taste of dietary fat based on rapeseed oil was superior to that based on sunflower oil when used for frying and baking. *Journal of the Science of Food and Agriculture* **62**, 273-281 (1993).

30 Ndiaye, P. *et al.* Phase behavior of soybean oil, castor oil and their fatty acid ethyl esters in carbon dioxide at high pressures. *The Journal of supercritical fluids* **37**, 29-37 (2006).

31 Martín-Gil, J. *et al.* Thermal behaviour of medical grade silicone oils. *Journal of analytical and applied pyrolysis* **42**, 151-158 (1997).

A.2 Paper 2

Liquid layer generators for excellent icephobicity at extremely low temperatures

Authors: Feng Wang, Senbo Xiao, Yizhi Zhuo, Wenwu Ding, Jianying He, and Zhiliang Zhang

Materials Horizons, 2019, 6, 2063-2072

Paper 2

Materials Horizons

COMMUNICATION

View Article Online
View Journal | View Issue

Cite this: *Mater. Horiz.*, 2019, 6, 2063

Received 3rd June 2019,
Accepted 1st July 2019

DOI: 10.1039/c9mh00859d

rsc.li/materials-horizons

Liquid layer generators for excellent icephobicity at extremely low temperatures†

Feng Wang, [a] Senbo Xiao, [a] Yizhi Zhuo, [a] Wenwu Ding, [b] Jianying He *[a] and Zhiliang Zhang *[a]

Promising progress in the field of icephobicity has been made in the recent years. However, a majority of the reported icephobic surfaces rely on static mechanisms, and they maintain low ice adhesion on surfaces at extreme temperatures (as low as −60 °C), which is highly challenging. Dynamic anti-icing surfaces, which can melt ice or change the ice–substrate interfaces from the solid to liquid phase after the formation of ice, serve as a viable alternative. In this study, liquid layer generators (LLGs), which can release ethanol to the ice–solid interface and convert the ice–substrate contact from the solid–solid mode to the solid–liquid–solid mode, were introduced. Excellent icephobicity on surfaces with an ethanol lubricating layer was found to withstand extremely low temperatures (−60 °C), which was proven by both molecular dynamics simulations and experiments. Two prototypes of LLGs, one by packing ethanol inside and the other by storing replenishable ethanol below the substrate, were fabricated. These LLGs could constantly release ethanol for a maximum of 593 days without source replenishment. Both these prototypes exhibited super-low ice adhesion strengths of 1.0–4.6 kPa and 2.2–2.8 kPa at −18 °C. For select samples, by introducing an interfacial ethanol layer, the ice adhesion strength on the same surfaces decreased in an unprecedented manner from 709.2–760.9 kPa to 22.1–25.2 kPa at a low temperature of −60 °C.

New concepts

State-of-the-art icephobic surfaces mainly rely on static solid–solid ice–substrate contact that fails at low temperatures with a threshold of around −50 °C. A new strategy for anti-icing at such low temperatures is required. Dynamic anti-icing surfaces, which can melt ice or change the ice–substrate interfaces from the solid to liquid phase after the formation of ice, serve as a viable alternative. In this study, durable polymeric materials, termed as liquid layer generators (LLGs), were designed and fabricated to target the achievement of low ice adhesion strengths at unprecedented low temperatures. These LLGs could constantly release interfacial ethanol for a maximum of 593 days, which dynamically converted the ice contact from a firm solid–solid mode to a weak solid–liquid–solid mode, thereby demonstrating super-low ice adhesion strength of ~1 kPa. By introducing a porous layer below the substrate, the interfacial liquid layer could be controlled by replenishable ethanol. The LLG could also overcome the problems of surface roughness and hydrophilicity that fail other icephobic surfaces. At extremely low temperatures of −60 °C, these LLGs maintained low ice adhesion strengths (22.1–25.2 kPa), exhibiting encouraging potential for practical arctic anti-icing applications.

Introduction

Unwanted ice formation and accretion is a common threat to road safety, aircrafts, electrical transmission cables, wind turbines, and many other devices,[1–3] which requires a tremendous amount of energy input for traditional deicing.[4] Consequently, designing and deploying materials and surfaces that can assist in the removal of ice have received growing interests.[5] In the recent years, four main classes of anti-icing/icephobic surfaces have been developed. First, the lotus-leaf effect has inspired superhydrophobic surfaces that can delay or prevent ice formation.[6,7] Unfortunately, such superhydrophobic surfaces can result in higher water-freezing rates than that in smooth surfaces in a highly humid environment,[8] and its hierarchical surface structure can enable mechanical interlocking with strong ice adhesion.[9,10] Second, lubricant-infused surfaces can repel incoming water and lower ice adhesion strength.[11,12] For such types of icephobic surfaces, the depletion of the lubricants remains an unresolved problem, particularly in icing/deicing cycles.[13,14] Third, interfacial slippage surfaces can imbibe oil into silicon elastomers and show low ice adhesion strength.[15–17] However, the swelling of a polymer in oil may degrade the mechanical durability of such a composite. Finally, macrocrack initiators (MACI) and stress localization promote the development

[a] NTNU Nanomechanical Lab, Department of Structural Engineering, Norwegian University of Science and Technology (NTNU), Richard Birkelands vei 1A, Trondheim 7491, Norway. E-mail: jianying.he@ntnu.no, zhiliang.zhang@ntnu.no
[b] Department of Energy and Process Engineering, Norwegian University of Science and Technology (NTNU), Kolbjørn Hejes v 1B, Trondheim 7491, Norway

† Electronic supplementary information (ESI) available. See DOI: 10.1039/c9mh00859d

of surfaces that can facilitate crack generation through stiffness inhomogeneity and deformation incompatibility as well as achieve super-low ice adhesion strength without the use of any surface additives.[18,19] Such MACI surfaces can be combined with other mechanisms to further reduce ice adhesion. Notably, other new strategies for anti-icing have emerged, particularly those that involve ice growth and patterns into the design of surface icephobicity.[20–22]

The surfaces discussed above can be generally categorized as static anti-icing surfaces, implying that there is no dynamic change in the chemical/physical states of the ice–substrate interfaces on these surfaces after ice formation. In contrast, emerging dynamic anti-icing strategies focus on melting or altering the solid ice–substrate interfaces.[23,24] One interesting example of these new dynamic anti-icing surfaces is the photothermal trap approach that utilizes solar illumination or near-infrared irradiation for the rapid melting of accumulated ice.[23] Another notable dynamic anti-icing surface contains polymers with hydrophilic pendant groups that can absorb water from ice and generate an aqueous lubricating layer at the interface.[21] These dynamic anti-icing surfaces hold the potential of gradually converting firm solid–solid ice–substrate contacts to a weak solid–liquid–solid characteristic, and they could maintain icephobicity in a broader temperature range.[24] For instance, a photothermal trap can result in a temperature rise as high as 33 °C,[23] and an aqueous lubricating layer shows great icephobicity before −53 °C.[24]

The ice adhesion strength on dynamic anti-icing surfaces with an aqueous lubrication layer was reported to be ~27 kPa,[24] which await optimization to achieve practical passive anti-icing application levels (lower than ~12 kPa).[18,25] The icephobicity of the dynamic anti-icing surface critically relies on generating an interfacial aqueous layer. When this crucial interfacial liquid layer freezes at lower temperatures (for example, close to −60 °C), the ice adhesion strength can sharply increase to higher than 400 kPa.[24] Therefore, the ability of dynamic anti-icing surfaces to maintain icephobicity in an arctic environment with extremely lower temperatures (−60 °C or even lower) is still a formidable challenge.

The aim of this work is to fabricate dynamic icephobic surfaces that can function at extremely low temperatures. We focus on fabricating a coating, termed as a liquid layer generator (LLG), which can release ethanol at the ice–solid interface for generating a lubricating effect and yielding low ice adhesion strength. First, we used atomistic modeling and simulations to compare the ice adhesion force on substrates with and without a liquid lubricating layer at various temperatures (down to −60 °C) and investigated the reduction in atomistic ice adhesion by substituting the interfacial aqueous layer to a lubricating ethanol layer. On such a theoretical basis, we synthesized ethanol-contained polymers with various roughness levels and chemical components that can release ethanol to the ice–substrate interface, namely, generating an interfacial liquid layer. The fabricated LLGs were found to function at −60 °C with worthwhile icephobicity and significant lifespan. Our combined theoretical and experimental studies contribute toward the understanding of the novel dynamic anti-icing field. LLGs can provide a path to facilitate anti-icing applications in unprecedented low temperatures.

Materials and methods

Atomistic modeling and molecular dynamics (MD) simulations

Atomistic modeling and MD simulations were employed to investigate the lubricating effect of an ethanol layer of various thicknesses at different temperatures. For the sake of simplicity, graphene platelets (dimensions: 2.3 nm × 2.3 nm) were used to fabricate a carbon-based surface, as shown in Fig. S1 (ESI†). These graphene platelets were stacked on top of each other at an equilibrium distance of ~0.6 nm at each edge and extended to a periodic area of 10.4 nm × 10.4 nm. Ice (thickness: 2 nm), with and without ethanol layers of 1 and 2 nm, was then modeled on the substrate, as shown in the photographs of the example system in Fig. S1a and S2 (ESI†). A simulation system with an interfacial aqueous layer (thickness: 2 nm) was also built for comparing the lubricating effect, as shown in Fig. S3(a) (ESI†). The water molecules used the TIP4P/ice model in this system. The OPLS force field was used for the graphene platelets and ethanol layer, and the TIP4P/ice model was used for modeling ice in all the MD simulations.[26,27] The MD package, GROMACS 5.0.7, was employed to perform all the simulations.[28] All the systems were equilibrated for 50 ns before subjected to ice adhesion and shearing simulations. In all the MD simulations, the time step used was 2 fs. The cutoff for nonbonded interaction was 1 nm. The graphene platelets were completely fixed at their position, providing a solid surface. The ice was maintained at a temperature of −93 °C, which is similar to a former study.[29] The ethanol layers were maintained at various temperatures of −18, −35, and −60 °C in different simulations. The same simulation parameters were applied to the system with an aqueous lubricating layer for comparing the lubricating effect at these three temperatures. The Nosé–Hoover temperature coupling method was employed in the simulations,[30,31] where the coupling constant was 0.4 ps. In order to determine the ice adhesion strength and shearing stress, the pulling force was subjected to the center of mass (COM) of the ice, which is similar to that done in earlier studies.[29,32] For determining the vertical ice adhesion strength, the force constant of the pulling harmonic potential was 500 kJ mol^{-1} nm^{-2}. Because of the limited space for horizontal shearing in the periodic simulation box, the harmonic potential was maintained at 2000 kJ mol^{-1} nm^{-2}. The pulling speed for all the deicing simulations was 0.5 m s^{-1}. The ice adhesion strength was calculated using the maximal force for vertical pulling normalized by the surface cross-section area, namely, $\sigma = f_{max}/A$, while the ice shearing stress was obtained by the shearing force normalized by the surface cross-section area, namely, $\tau = f_{shear}/A$.

Fabrication of LLGs with ethanol inside the substrates

We used the silicon rubber Ecoflex™ 00-50 (Smooth-On, Inc.) as the matrix material. The silicon rubber was added in two steps. Silicon rubber part A was first mixed with absolute ethanol

(Sigma-Aldrich) by mechanical stirring for 3 min. Part B was immediately added, and the entire mixture was stirred for another 3 min. The ethanol contents in the mixture were 10, 20, 30, and 40 vol%. The final mixtures were cast into plastic molds and cured at room temperature. After 3 h, LLG 1 was fabricated at various ethanol contents. The ethanol droplets initially trapped in the silicon rubber were spherical, as shown in Fig. S4 (ESI†), where the diameter ranged from 0.37 to 0.47 mm depending on the ethanol content (Fig. S5, ESI†). Ethanol droplets were formed in the silicone rubber curing process, which mostly resulted from the exclusion of the ethanol molecules by the cured polymer chains. The ethanol droplets were, therefore, firmly imprisoned in the polymer matrix at the initial state of LLG 1.

Fabrication of LLGs with capacity below the substrates for replenishable ethanol

Firstly, 4 inch silicon wafers were successively cleaned with ethanol, acetone, and isopropanol. Then, mr-DWL 5 (micro resist technology GmbH) was spin-coated on the silicon wafer at 2000 rpm for 30 s, followed by prebaking at 50 and 90 °C (5 min for each process). The silicon wafer with mr-DWL5 was exposed to MLA150 (Maskless Photolithography, Heidelberg Instruments), followed by post-baking at 50 and 90 °C (5 min for each process). After developing in mr-Dev 600 (micro resist technology GmbH) for ~35 min and hard-baking at 150 °C for 15 min, the silicon wafer with pillars of uniform sizes were fabricated. The patterned area was controlled to dimensions of 5 cm × 5 cm for all the wafers. The distance between the pillars varied from 5 μm to 30 μm, as shown in Fig. 4a–c and Fig. S8 (ESI†).

The silicon wafers with pillars were silanized with trichloro-(1*H*,1*H*,2*H*,2*H*-perfluoroocty)silane (Sigma-Aldrich) in a vacuum chamber for 8 h for facilitating peeling off of the polydimethylsiloxane (PDMS). PDMS prepolymer (Sylgard 184, Dow Corning) and curing agent were mixed in a weight ratio of 10 : 1 and stirred for 5 min. The mixtures were degassed in a vacuum chamber for 30 min to remove air bubbles. The liquid was poured onto the patterned silicon wafer and held for 5 min and then spin-coated (WS-400B-6NPP-LITE/AS, Laurell Technologies) for 1 min at a speed of 500 rpm to obtain the PDMS film (thickness: 420 μm). After curing at 60 °C for 3 h, the PDMS films with subholes were carefully peeled off from the silicon substrates. The films were transferred to glass and prepared for the ice adhesion tests. To finalize LLG 2, ethanol was filled into the subpores using an injector.

Silica nanoparticles and poly(vinyl alcohol) (PVA) were used as surface modifiers for the PDMS surfaces. SiO_2 was synthesized through a facile method. Firstly, 5 ml ammonium hydroxide (28%, Sigma-Aldrich), 95 ml absolute ethanol (>99.8%, Sigma-Aldrich), and 5 ml deionized water were mixed and stirred in a three-necked flask for 10 min. Secondly, the mixture was heated to 60 °C and then 3 ml tetraethyl orthosilicate (TEOS, >99.8%, Sigma-Aldrich) was added. Finally, after stirring for another 12 h, the ethanoic suspension of silica nanoparticles (particle size: ~222.7 nm) were obtained (particle size distribution is shown in Fig. S9, ESI†). The as-prepared suspension was dripped onto PDMS surfaces and spin-coated for 30 s at a speed of 800 rpm, which was repeated five times. PVA (fully hydrolyzed, Sigma-Aldrich) was dissolved in water at 100 °C to obtain a clear solution of 3 wt%. The as-prepared solution was dripped onto PDMS surfaces and spin-coated for 30 s at a speed of 800 rpm, which was also repeated five times. The modified films were heated at 60 °C for 3 h to finalize the treating of PDMS films. To obtain LLG, ethanol was filled into the subpores using an injector.

Characterizations

The chemical structures of the liquid layer at the ice–substrate interface were examined by NMR (Bruker Avance III 400 MHz). The surface morphologies were observed by a field-emission scanning electron microscope (FEI APREO SEM). All the samples were sputter-coated with a 5 nm gold layer. Microscopic photographs of the silicon wafers with different patterns were taken by a DIC microscope (Zeiss AxioScope A1 for reflected light BF-DIC/POL, Carl Zeiss). The surface morphology of the coatings was recorded by atomic force microscopy (AFM, Veeco Metrology) using PeakForce Quantitative NanoMechanics. The ice adhesion strength was measured by a universal mechanical tester (Instron Model 5944) equipped with lab-built cooling system and chamber, as described in earlier studies.[18] A polypropylene centrifuge tube with a 1 mm-thick wall and an inner diameter of 20 mm was placed onto the coatings. Further, 1.5 ml deionized water was infused into each mold, and the samples were placed in a freezer at a constant temperature of −18 °C for 3 h to ensure complete freezing. Before the testing, the samples were transferred from the freezer to the cooling chamber of the test machine. For testing at −18 °C, the samples were stabilized in the cooling chamber of the test machine at −18 °C for 10 min before testing. For the test at −60 °C, the samples were stabilized in the cooling chamber of the test machine at −60 °C for 1 h to ensure total cooling before testing. During the ice adhesion test, a force probe (diameter: 5 mm) propelled the tube-encased ice columns at a velocity of 0.01 mm s^{-1}, and the probe was located close to the tested coating surface (less than 1 mm) to minimize the torque on the ice cylinders. The loading curve was recorded, and the peak value of the shear force was divided by the contact area to obtain the ice adhesion strength. Four samples from each composition were measured to obtain the mean ice adhesion strength.

Results and discussion

Lubricating effect of a nanoscale interfacial ethanol layer

The purpose of atomistic modeling and simulations was to verify the lubricating effect of the ethanol layer at the ice–solid interface at various temperatures. Simulation systems with and without the interfacial ethanol layers on a model carbon-based substrate were built for this purpose, as shown in Fig. 1 and Fig. S1, S2 (ESI†). Pulling force was utilized to determine the atomistic ice adhesion strength in the systems (details in the Methods section).

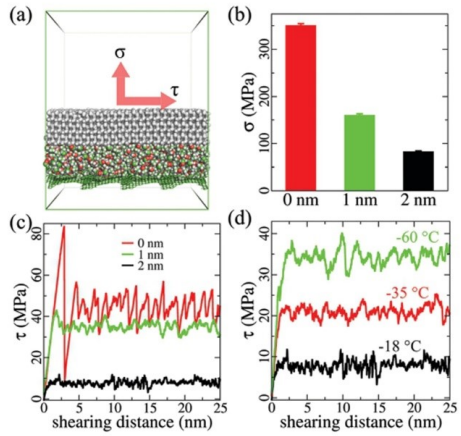

Fig. 1 A thin lubricating ethanol layer for reducing ice adhesion strength. (a) Atomistic model of an ethanol lubricating layer at the ice–solid interface. The ice is shown in white and the carbon-based substrate is shown in green. Periodic boundary of the system is shown in green. Directions of pulling and shearing forces applied on the ice to determine ice adhesion (σ) and shearing (τ) stresses are indicated by red arrows. (b) σ values on the same substrate with ethanol layers of 0, 1, and 2 nm in thickness. (c) τ values with ethanol layers of 0, 1, and 2 nm in thickness at −18 °C. (d) τ values on a 2 nm-thick ethanol layer at various temperatures.

A layer of lubricating ethanol can indeed considerably reduce the atomistic ice adhesion strength (σ) and shearing stress (τ). As shown in Fig. 1a, the ice adhesion strength can be defined as the highest stress needed to vertically detach the ice from the substrate, while the shearing stress was monitored in the horizontal shearing process using the shearing force normalized by the surface area. Without an ethanol layer, the ice adhesion strength obtained in 5 independent simulations was 351 ± 4 MPa. In comparison, a sandwiched ethanol layer of 1 nm reduced the ice adhesion strength down to 160 ± 3 MPa, showing a drastic reduction of ≥50%. When the thickness of the ethanol layer was 2 nm, the ice adhesion strength was further reduced to 83 ± 2 MPa, which was a reduction of ~50%. This result not only confirmed the icephobic potential of the lubricating ethanol layer and its thickness effect, but also showed that the accumulation of ethanol (from 1 to 2 nm) at the ice–solid interface was highly beneficial for deicing operations.

The lubricating effect of the ethanol layer was also significant, and it reduced the ice shearing stress as the layer thickness increased at extremely low temperatures. As shown in Fig. 1c, without a lubricating layer, the ice shearing stress profile was in a typical stick–slip pattern, which is similar to that used in earlier studies,[33,34] showing initial stress peak values exceeding 85 MPa. Such high peak values reveal that high stress is needed to initiate ice cracking during deicing processes. In comparison, an interfacial ethanol layer (thickness: 1 nm) can effectively smoothen the shearing stress profile and yield an average shearing stress value of 34.5 ± 4.5 MPa at −18 °C. When the ethanol layer thickness was 2 nm, the ice shearing stress further reduced to 7.8 ± 1.4 MPa. The lubricating effects of the ethanol layer were maintained even at lower temperatures, as shown in Fig. 1d. When the temperature decreased from −18 to −38 °C, the ice shearing stress obtained with the 2 nm-thick ethanol layer increased to 20.6 ± 2.7 MPa. At extremely low temperatures of −60 °C, the ice shearing stress further increased to 33.2 ± 4.8 MPa. All the ice shearing stress profiles obtained at various temperatures showed smoothening effects of the ethanol layer, and average values lower than the peak values of shearing ice without an ethanol layer, which suggested that generating an ethanol layer at the ice–solid interface could facilitate deicing at low temperatures. The lubricating effect of an ethanol layer outperformed that of an aqueous layer. As shown in Fig. S3 (ESI†), the ice shearing stress values for a 2 nm-thick aqueous layer were much higher than those for an equivalent ethanol layer, as shown in Fig. 1d, at −18 and −38 °C. The aqueous layer lost its lubricating effect completely at −60 °C, confirming the results from an earlier study regarding the deficiency of aqueous layers at low temperatures in anti-icing applications.[24] It should be noted that the loading rate used in the simulations is orders of magnitude higher than those in the experiment, which results in considerably higher absolute ice adhesion strength values.[35] However, the difference in the ice adhesion mechanics is significant under the same simulation parameters and protocol.

Design principles and fabrication of icephobic LLGs

The abovementioned atomistic modeling and simulation results indicate that an ethanol layer with increasing thickness at the ice–substrate interface can considerably reduce the ice adhesion strength. Most importantly, the lubricating effect, and therefore, the surface icephobicity by such an interfacial ethanol layer can function at temperatures as low as −60 °C as ethanol has a low freezing point of −115 °C. The experiments were devoted to designing LLGs that could dynamically accumulate ethanol molecules to form a lubricating layer between the substrate and ice. Two strategies were chosen for fabricating LLGs, as shown in Fig. 2a, namely, (1) packing ethanol inside the substrate (LLG 1) and (2) storing replenishable ethanol below the substrate (LLG 2). For LLG 1, ethanol was directly mixed into the polymer substrate during the synthesis. In contrast, lamellar structures with subpores were created under the substrate for LLG 2, which allowed ethanol to be readily refilled after synthesis.

The icephobic mechanism of the LLG is shown in Fig. 2b. It was essential that LLG could release ethanol to the ice–substrate interface to generate an ethanol layer, as the quasi-liquid/liquid layer was the key for the low ice adhesion strength.[24] By taking into account the fact that ethanol could absorb onto the ice surface for creating the quasi-liquid/liquid layer,[36,37] as well as elastomer membranes were preferential for ethanol permeation,[38,39] silicon rubbers were chosen as the matrix material for fabricating the two LLG substrates. It is evident that with such a design principle and material selection, ethanol molecules inside or below the LLG could dynamically

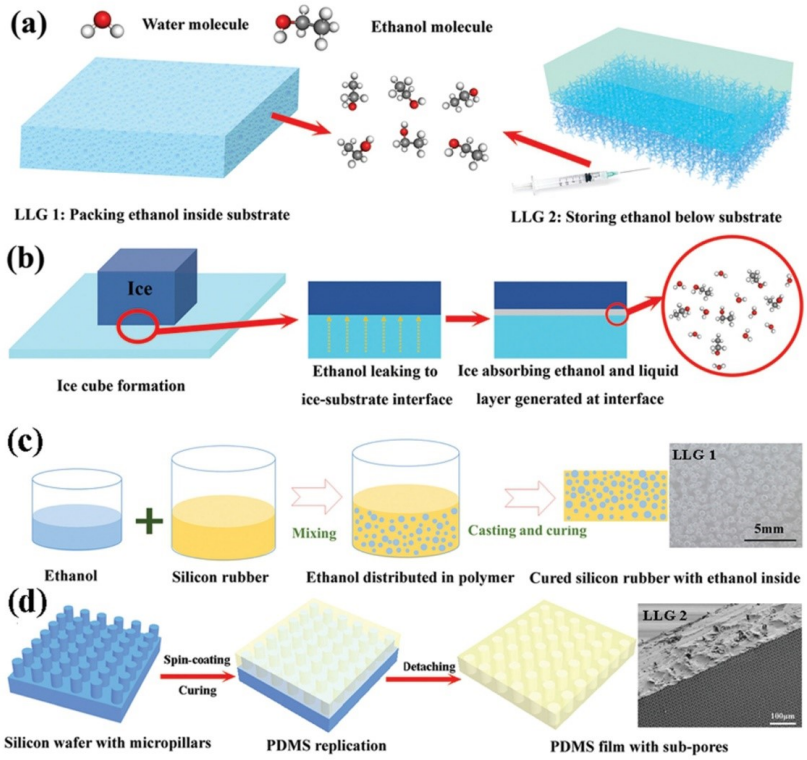

Fig. 2 Schematic illustration of the strategies of generating a liquid layer at the ice–substrate interface. (a) Two strategies to create icephobic LLGs, namely, packing ethanol inside the substrate (left panel) and storing replenishable ethanol below the substrate (right panel). (b) Mechanism of generating a liquid ethanol layer at the ice–substrate interface. (c) Fabricating method of LLG 1: mixing ethanol with silicone rubber that can be quickly cured at room temperature, following which ethanol will be packed inside the substrate after curing. Optical image on the right shows the top view of LLG 1 (with 20 vol% ethanol); small bubbles indicate ethanol droplets inside the body. (d) Fabricating method of LLG 2: replica method for producing subpores for ethanol storage below the surface. SEM image on the right shows the side view of LLG 2 (distance between neighboring holes: 15 μm). Well-arranged small holes can be observed on the bottom surface.

permeate through the polymer matrix and reach the ice–substrate interface. It was expected that the accumulated interfacial ethanol would finally create a liquid layer that could convert the ice–substrate contact from a firm solid–solid mode to a weak solid–liquid–solid mode. The fabrication procedures of the two LLGs are shown in Fig. 2c and d; the experimental details are provided in the Materials and methods section. Samples with a series of ethanol contents were fabricated and characterized for two LLGs, and they were subjected to icephobicity investigations.

Icephobicity of LLGs with ethanol inside the substrate

LLG 1 was fabricated through a facile synthesis method, as shown in Fig. 2c. Ethanol with different volume contents (10–40%) was mixed with silicone rubber that could be quickly cured before a significant evaporation of ethanol. The thickness of the substrate was controlled at ~2 mm. The morphology and size distribution of the ethanol droplets in LLG 1 are shown in Fig. S4 and S5 (ESI†). LLG 1 indeed released ethanol to the interface and demonstrated excellent icephobicity. As exemplified by LLG 1 with 20 vol% ethanol, ice cubes on LLG 1 surface spontaneously fell off in 3 h after vertical placement (Fig. 3a). A liquid layer was detected after the ice cubes were detached from LLG 1. As shown in Fig. 3b, visible dyestuff was observed to diffuse on the ice cube peeled off from LLG 1, which confirmed the secretion of ethanol by LLG 1. The liquid layer on the detached ice cube was carefully collected and transferred for investigation *via* ^{1}H NMR spectroscopy. As shown in the lower panel of Fig. 4b, the strong signal at 4.80 ppm resulted from –OH from both ethanol and water, and the signals from $-CH_2$ and $-CH_3$ of ethanol were also clearly detected. Therefore, the results

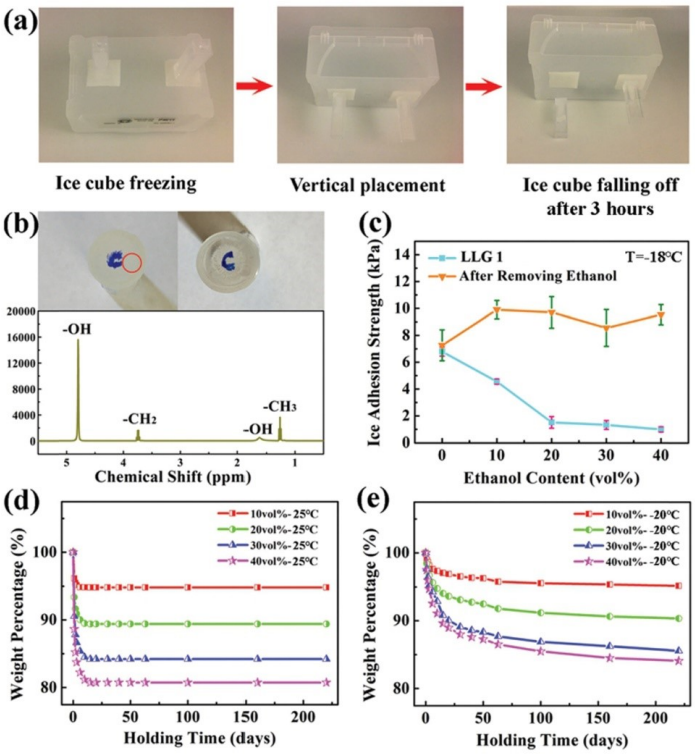

Fig. 3 Icephobicity of LLGs fabricated by packing ethanol inside the substrate. (a) Comparison of ice cube adhesion on LLG 1 surface (left) and the same surface after fully removing the ethanol (right) at −18 °C. (b) Diffusivity of dyestuff on the surfaces of ice cubes that are peeled off from LLG 1 (left) and the one after removing ethanol (right). The ^{1}H NMR spectra (bottom) of the liquid layer on the adhesion side of the ice cube (area marked with a red circle). (c) Comparison of ice adhesion strengths on LLG 1 with various ethanol contents and the same surfaces after ethanol removal at −18 °C. (d) Weight loss of LLG 1 as a function of time at room temperature. (e) Weight loss of the LLGs as a function of time at −20 °C.

from the ^{1}H NMR agreed with the structure of ethanol (CH_3CH_2OH). The ^{1}H NMR spectra confirmed the ethanol component in the liquid layer, which proved the ability of LLG 1 to release ethanol to the ice–substrate interface.

The ice adhesion strength on LLG 1 falls in the super-low region.[18] As shown in Fig. 3c, the ice adhesion strength on LLG 1 ranged from 1.0 to 4.6 kPa, showing a steady decrease with an increase in the content of ethanol in the substrate, all of which were lower than those in the same sample after ethanol exhaustion (8.6–10.0 kPa). It should be noted that the ice adhesion strength on smooth pure silicon rubber was 7.2 kPa, which was lower than that on rough LLG 1 after ethanol exhaustion. Details regarding roughness formation on the LLG 1 surface are shown in Fig. S6 (ESI†). The thicker the interfacial ethanol layer, the lower is the ice adhesion strength, as confirmed by the atomistic modeling results mentioned above. LLG 1 with a higher ethanol content could release more ethanol to the ice–substrate interface, thereby thickening the interfacial liquid layer in the same given time, which accounts for the results shown in Fig. 3c (light blue curve). Such low ice adhesion strength is also lower than the value obtained for pure silicon rubber (detailed comparison and discussion are given in the ESI†). These results again verified the function of the ethanol layer in enhancing the icephobicity of the surfaces.

The ethanol release rate underlies the icephobic durability of the LLG samples, and therefore, the lifespan of LLGs. In order to evaluate the time needed for fully exhausting ethanol from the samples, the mass weights of LLG 1 at room temperature and at −20 °C were determined as a function of holding time after synthesis. At room temperature, ethanol in LLG 1 would completely run out in 15 days, as shown in Fig. 3d. The weight loss of LLG 1 was lower than the initial ethanol content. This was because the curing process of LLG 1 took 3 h. During this time, a certain amount of ethanol evaporated, which was not taken into

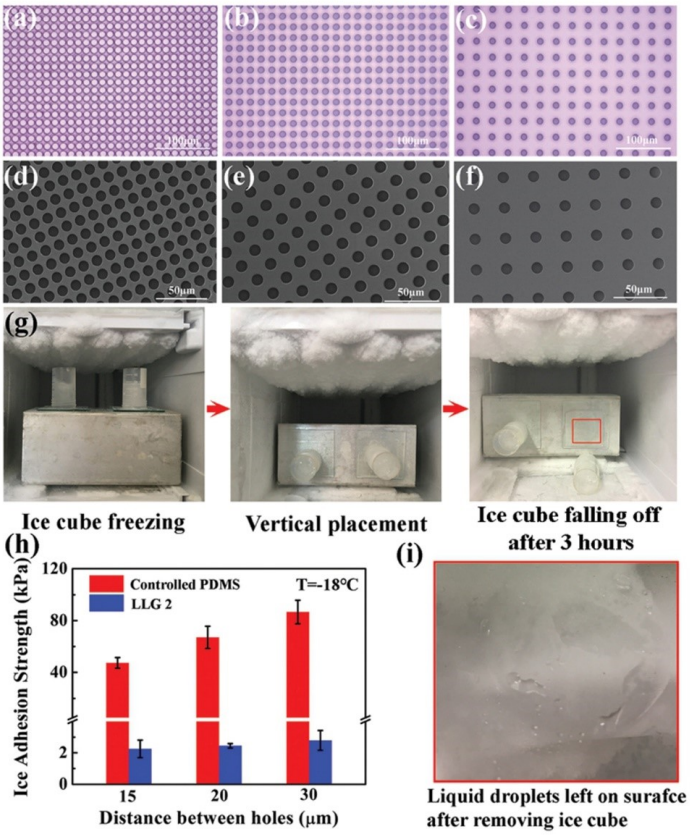

Fig. 4 Icephobicity of LLGs with replenishable ethanol capacity. (a–c) Optical images showing silicon wafers with pillars of different densities; distance between neighboring pillars were 15, 20, and 30 μm, respectively. (d–f) SEM images showing the hole morphologies of PDMS films fabricated on the silicon wafer in (a–c), respectively. (g) Comparison of ice adhesion on the sample without infusing ethanol (left) and LLG surface (right) at a temperature of −18 °C. Distance between holes is 20 μm in both the samples. (h) Ice adhesion strength on the sample without ethanol (controlled PDMS) and LLG 2 with various hole densities obtained at −18 °C. (i) Liquid droplets on the surface of LLG (area marked with a red rectangle in (g)) after removing the ice cube.

account in the details shown in Fig. 3d. Surprisingly, the release of ethanol from LLG 1 maintained at −20 °C could still be observed to be steady even after 250 days (Fig. S7, ESI†). The release of ethanol molecules to the ice–solid interface was a spontaneous thermodynamics process. Because the freezing temperature of ethanol was extremely low, this spontaneous release could occur within a wide temperature range. There were multiple determinants of the ethanol release rate, including diffusion efficiency of ethanol in the polymer, vapor pressure, temperature, their coupling, and other factors.[38] The lower the temperature, the poorer is the ethanol release efficiency and longer is the LLG lifetime. The dynamics of ethanol release from LLG 1 were analyzed, as shown in Fig. S7 (ESI†) (with a detailed discussion). The icephobic lifetime of LLG 1 was expected to be ≥250 days at a temperature of −20 °C, and it was even longer at lower temperatures. In particular, LLG 1 with 40 vol% ethanol was predicted to have a long lifespan of up to 593 days (Fig. S7, ESI†). It was, therefore, reasonable to anticipate long-term icephobicity of the LLGs at lower temperatures as long as the interfacial ethanol layer was not frozen.

Icephobicity of LLGs with replenishable ethanol below the substrate

LLG 1 effectively proved the ability of releasing ethanol to the ice–substrate interface, thereby achieving excellent icephobicity. By embedding a fixed amount of ethanol inside the substrate, LLG 1 suffered from icephobicity depletion with the exhaustion

of ethanol, despite the observed lifetime of ≥250 days. Therefore, LLG 2 was designed to extend the durability along with capacity for easily replenishing ethanol, namely, creating a lamellar structure with a porous layer below the substrate, as shown in Fig. 2d. For the sake of mechanical robustness, PDMS with the same silicone base as that of silicon rubber was made for LLG 2, as it is one of the most common options for fabricating icephobic coatings.[17–19,40–42] In particular, silicon wafers with pillars were used as templates for molding PDMS; an example is shown in Fig. S8 (ESI†). All the pillars have a fixed radius of 5 μm, with an interpillar distance varying from 15 to 30 μm, as shown in Fig. 4a–c, which led to complementing holes in the substrate for holding the replenishing ethanol (Fig. 4d–f).

LLG 2 with ethanol replenishing capacity exhibited equally low ice adhesion strength. As shown in Fig. 4g, the ice cube on LLG 2 spontaneously fell off in 3 h at a temperature of −18 °C, while its counterpart was firmly adhered on the sample without storing ethanol in the holes. The ice adhesion strength obtained on LLG 2 with different hole density fell in the range of 2.2–2.8 kPa, as shown in Fig. 4h, which significantly decreased as compared to the same surface without an ethanol layer (47.3–86.7 kPa). After the detachment of the ice cube from the LLGs, visible liquid droplets were detected on the surface (Fig. 4i), which revealed the same mechanism of LLG as that shown in Fig. 2b. With the holes in the substrate and ethanol replenishing capacity, the extended durability of LLGs was expected, which could guarantee long-term practical anti-icing applications.

Further verification and extremely low temperature applications of LLGs

The icephobic basis of LLGs is to generate a liquid ethanol layer at the ice–substrate interface, as well as converting the ice

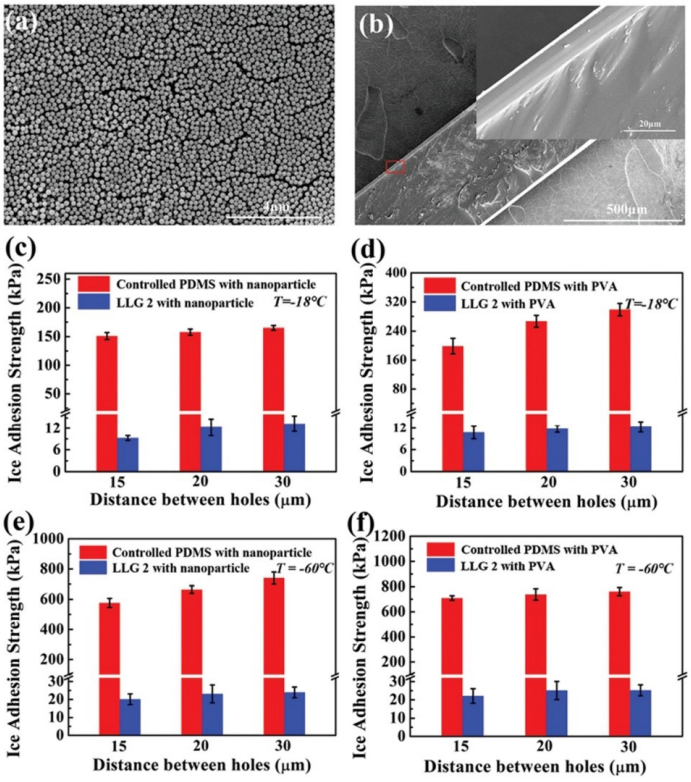

Fig. 5 Icephobicity of LLG 2 with coated nanoparticles and hydrophilic PVA. (a) SEM images showing a homogenous nanoparticle coating on the LLGs. (b) SEM images of the cross-section of PVA-coated LLG 2. Inset shows the corresponding area highlighted by the red rectangle. (c and d) Comparison of ice adhesion strengths on LLG 2 coated with nanoparticles and PVA at −18 °C. (e and f) Comparison of ice adhesion strengths on LLG 2 coated with nanoparticles and PVA at −60 °C.

contact from a strong solid–solid mode to a weak solid–liquid–solid mode. As long as ethanol continues to release from the substrates, surface roughness (possibly impurity) and chemistry would not hamper the functionality of LLGs. LLG 2 was chosen to further verify the icephobicity of LLGs with altered surface roughness and chemistry. SiO_2 nanoparticles and hydrophilic PVA were used to coat the intrinsically hydrophobic PDMS on LLG 2 for separately altering the surface roughness and hydrophobicity. The nanoparticles had a mean diameter of 222.7 nm, with the size distribution shown in Fig. S9 (ESI†). This led to the surface topography of treated LLG 2, as shown in Fig. 5a. The PVA coating on LLG 2 had a thickness of 10 μm, as shown in Fig. 5b. The roughness values of LLG 2 with and without surface treatment were investigated, as shown in Fig. S10 (ESI†).

Notably, the ice adhesion strength on the treated surfaces showed encouraging results. By introducing roughness and hydrophilicity into the PDMS samples, the ice adhesion strength was significantly raised from 47.3–86.7 (Fig. 4h) to 151.0–164.9 (Fig. 5c) and 198.6–298.7 (Fig. 5d) kPa, respectively. Such results were also in agreement with earlier studies in which an increase in surface roughness and hydrophilicity led to higher ice adhesion strengths.[8,18,43] By infusing ethanol into subholes, after 3 h, the icephobicity of the treated surface was restored. As shown in Fig. 5c and d, the ice adhesion strength on LLG 2 coated with nanoparticles and PVA drastically decreased to 9.3–13.3 and 10.8–12.4 kPa, respectively. The nanostructures and coatings on the LLG surfaces can hinder the lubricant release rate.[44] The ethanol release efficiency at the ice–solid interfaces was temperature-dependent, *i.e.*, faster release at higher temperatures. These results suggest that the LLG effectively functioned on surfaces with different chemical components (both hydrophobic and hydrophilic surfaces) and on surfaces with different morphologies (both smooth and rough surfaces), demonstrating anti-icing potential for different application conditions.

It is well known that both properties of ice, namely, its adherence to surfaces and its interaction, obviously changed as the temperature decreased, which led to a significant increase in the ice adhesion strength.[45] It was observed that the ice adhesion strength roughly increased by two orders of magnitude, from ~55 to ~1156 kPa, as the temperature decreased from −15 to −30 °C.[46] The LLG could benefit from the low freezing point of ethanol, and the interfacial ethanol layer could maintain the solid–liquid–solid ice contact at very low temperatures. As shown in the simulation results in Fig. 1c, d and Fig. S3 (ESI†), the lubricating effect induced by ethanol could still act at a temperature of −60 °C. The ice adhesion test at such a low temperature was also carried out. Strikingly, the ice adhesion strength on LLG 2 was maintained at a low value at −60 °C. As shown in Fig. 5e and f, after maintaining for 4 h (3 h at −18 °C and 1 h at −60 °C), both nanoparticle- and PVA-coated PDMS samples demonstrated high ice adhesion strengths of 576.1–740.2 and 709.2–760.9 kPa, respectively, while the corresponding LLGs showed low ice adhesion strengths of 20.1–23.9 and 22.1–25.2 kPa. It should be noted that the lower ice adhesion on LLGs could be expected for longer holding times, as more ethanol and a thicker interfacial liquid layer could be generated by the LLGs. As compared to earlier experimental studies where a sharp increase in ice adhesion strength could be observed at −53 °C,[24] the approach using LLGs was an outstanding dynamics icephobic/anti-icing strategy. Furthermore, considering the low freezing point of ethanol of −114.1 °C, as well as the vast coexisting space of liquid ethanol and ice/water (lowest to −124 °C observed in experiments), as shown in the phase diagram in Fig. S10 (ESI†),[47–49] the liquid layer created by LLGs can function in a broader temperature range, including extremely cold arctic environments.

Conclusion

In summary, this work introduced the LLG, which dynamically secreted a lubricating ethanol layer at the ice–solid interface after ice formation, yielding low ice adhesion strength. Firstly, atomistic modeling and simulations were employed to depict the ice adhesion reduction effect of ethanol layers with different thicknesses at the ice–solid interface at various temperatures. Then, the fabrication of LLGs and ice adhesion test experiments of LLGs were carried out. Both the LLG prototypes, namely, embedding ethanol in the substrate and storing replenishable ethanol in holding capacities, exhibit excellent icephobicity with the lowest ice adhesion value of 1.0 kPa observed at −18 °C, which verified the function of the ethanol layer generated by LLG design. Owing to the ability of constant ethanol release and thickening of the interfacial lubricating layers, LLG could overcome the deficiency induced by surface roughness and hydrophilicity—the two critical factors that result in the failure of several other icephobic surfaces. The lifespan of the icephobicity of LLGs was highly encouraging, particularly with replenishable ethanol. Most importantly, LLG effectively functioned at low temperatures, covering the arctic anti-icing requirements, which outperformed other state-of-the-art icephobic surfaces. For select samples, by introducing an interfacial ethanol layer, the ice adhesion strength on the same surfaces decreased in an unprecedented manner from 709.2–760.9 to 22.1–25.2 kPa at a low temperature of −60 °C. All these properties enable LLGs to become a competitive candidate for practical anti-icing applications and provide an icephobic solution for extremely low temperatures in which other earlier published icephobic surfaces fail.

Conflicts of interest

There are no conflicts to declare.

Acknowledgements

The Research Council of Norway is acknowledged for the support to the FRINATEK project Towards Design of Super-Low Ice Adhesion Surfaces (SLICE, 250990), and the PETROMAKS 2 project Durable Arctic Icephobic Materials (AIM, 255507). The computational resources were provided by the Norwegian Metacenter for Computational Science (NOTUR NN9110 and NN9391K).

References

1 A. K. Andersson and L. Chapman, *Accid. Anal. Prev.*, 2011, **43**, 284–289.
2 R. W. Gent, N. P. Dart and J. T. Cansdale, *Philos. Trans. R. Soc., A*, 2000, **358**, 2873–2911.
3 U. Björnstig, *et al.*, *Accid. Anal. Prev.*, 1997, **29**, 211–215.
4 J. L. Laforte, *et al.*, *Atmos. Res.*, 1998, **46**, 143–158.
5 M. J. Kreder, *et al.*, *Nat. Rev. Mater.*, 2016, **1**, 15003.
6 J. C. Bird, R. Dhiman, H. M. Kwon and K. K. Varanasi, *Nature*, 2013, **503**, 385.
7 A. J. Meuler, *et al.*, *ACS Nano*, 2010, **4**, 7048–7052.
8 S. Jung, *et al.*, *Langmuir*, 2011, **27**, 3059–3066.
9 A. J. Meuler, *et al.*, *ACS Appl. Mater. Interfaces*, 2010, **2**, 3100–3110.
10 K. K. Varanasi, *et al.*, *Appl. Phys. Lett.*, 2010, **97**, 234102.
11 T. S. Wong, *et al.*, *Nature*, 2011, **477**, 443–447.
12 P. Kim, *et al.*, *ACS Nano*, 2012, **6**, 6569–6577.
13 J. S. Wexler, *et al.*, *Phys. Rev. Lett.*, 2015, **114**, 168301.
14 K. Rykaczewski, *et al.*, *Langmuir*, 2013, **29**, 5230–5238.
15 K. Golovin, *et al.*, *Sci. Adv.*, 2016, **2**, 1501496.
16 C. Urata, *et al.*, *J. Mater. Chem. A*, 2015, **3**, 12626–12630.
17 K. Golovin, *et al.*, *Science*, 2019, **364**, 371–375.
18 Z. He, *et al.*, *Soft Matter*, 2017, **13**, 6562–6568.
19 P. Irajizad and A. Al-Bayati, *et al.*, *Mater. Horiz.*, 2019, **6**, 758–766.
20 J. Liu, C. Zhu and K. Liu, *et al.*, *Proc. Natl. Acad. Sci. U. S. A.*, 2017, **114**, 11285–11290.
21 S. F. Ahmadi, S. Nath and G. J. Iliff, *et al.*, *ACS Appl. Mater. Interfaces*, 2018, **10**, 32874–32884.
22 C. Lin, G. Corem and O. Godsi, *et al.*, *J. Am. Chem. Soc.*, 2018, **140**, 15804–15811.
23 S. Dash, *et al.*, *Sci. Adv.*, 2018, **4**, 0127.
24 R. Dou, *et al.*, *ACS Appl. Mater. Interfaces*, 2014, **6**, 6998–7003.
25 K. Golovin, *et al.*, *Sci. Adv.*, 2017, **3**, 1701617.
26 W. L. Jorgensen, *et al.*, *J. Am. Chem. Soc.*, 1996, **118**, 11225–11236.
27 J. L. F. Abascal, *et al.*, *J. Chem. Phys.*, 2005, **122**, 234511.
28 M. J. Abraham, *et al.*, *SoftwareX*, 2015, **1**, 19–25.
29 S. Xiao, *et al.*, *Nanoscale*, 2016, **8**, 14625–14632.
30 S. Nosé, *J. Chem. Phys.*, 1984, **81**, 511–519.
31 W. G. Hoover, *Phys. Rev. A: At., Mol., Opt. Phys.*, 1985, **31**, 1695.
32 S. Xiao, *et al.*, *Phys. Chem. Chem. Phys.*, 2018, **20**, 24759–24767.
33 M. Beeman, *et al.*, *J. Geophys. Res.: Solid Earth*, 1988, **93**, 7625–7633.
34 J. R. Blackford, *et al.*, *Faraday Discuss.*, 2012, **156**, 243–254.
35 S. Xiao, W. Stacklies and M. Cetinkaya, *et al.*, *Biophys. J.*, 2009, **96**, 3997–4005.
36 C. Thierfelder, *et al.*, *Phys. Rev. B: Condens. Matter Mater. Phys.*, 2007, **76**, 195426.
37 J. P. D. Abbatt, *et al.*, *Environ. Res. Lett.*, 2008, **3**, 045008.
38 H. O. Karlsson, *et al.*, *J. Membr. Sci.*, 1993, **76**, 121–146.
39 L. Li, Z. Xiao and S. Tan, *et al.*, *J. Membr. Sci.*, 2004, **243**, 177–187.
40 F. Wang, *et al.*, *Chem. Eng. J.*, 2019, **360**, 243–249.
41 Y. Zhuo, *et al.*, *ACS Appl. Mater. Interfaces*, 2018, **10**, 11972–11978.
42 Y. Zhuo, *et al.*, *ACS Omega*, 2018, **3**, 10139–10144.
43 V. F. Petrenko, *et al.*, *Can. J. Phys.*, 2003, **81**, 387–393.
44 D. J. Preston, Y. Song and Z. Lu, *et al.*, *ACS Appl. Mater. Interfaces*, 2017, **9**, 42383–42392.
45 H. H. G. Jellinek, *Can. J. Phys.*, 1962, **40**, 1294–1309.
46 J. Chen, *et al.*, *ACS Appl. Mater. Interfaces*, 2013, **5**, 4026–4030.
47 R. Anderson, *et al.*, *J. Phys. Chem. C*, 2009, **113**, 12602–12607.
48 P. Boutron, *et al.*, *J. Phys. Chem.*, 1978, **68**, 5032–5041.
49 A. D. Potts, *et al.*, *J. Phys. Chem.*, 1965, **69**, 996–1000.

Supplementary Materials for

Liquid layer generator for excellent icephobicity at extremely low temperature

Feng Wang[a], Senbo Xiao[a], Yizhi Zhuo[a], Wenwu Ding[b], Jianying He[a,*], Zhiliang Zhang[a,*]

a. NTNU Nanomechanical Lab, Department of Structural Engineering, Norwegian University of Science and Technology (NTNU), Trondheim 7491, Norway.

b. Department of Energy and Process Engineering, Norwegian University of Science and Technology (NTNU), Trondheim 7491, Norway.

*E-mail: jianying.he@ntnu.no, zhiliang.zhang@ntnu.no

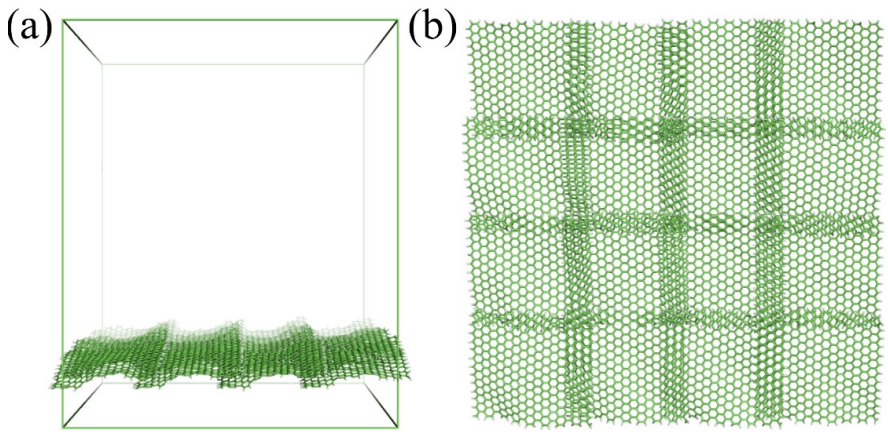

Supplementary Figure S1 | Side (a) and top (b) views of the carbon-based substrate consisting of graphene platelets. The graphene platelets had a uniform size of 2.3 nm × 2.3 nm, and were periodically fixed at equilibrium positions with an overlapping margin of 0.6 nm.

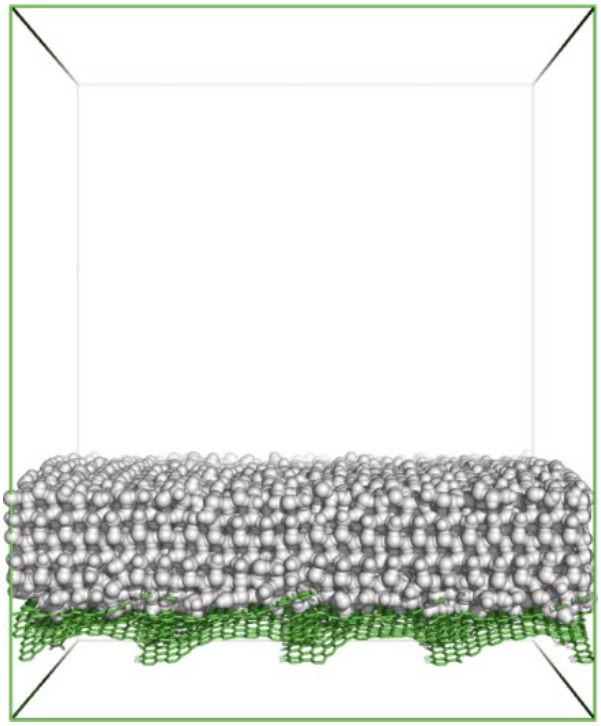

Supplementary Figure S2 | Simulation system of ice directly contacts with substrate without any interfacial lubricating layer.

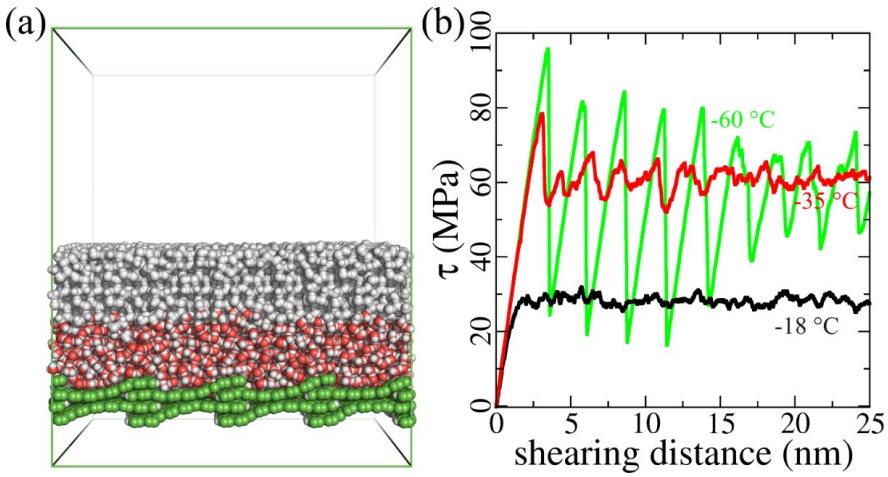

Supplementary Figure S3 | Lubricating effect of an interfacial water layer of 2 nm at varied temperature. (a) The all-atom simulation system. **(b)** Shearing stress, τ, profiles of ice at temperature of -18˚C, -35 ˚C and -60 ˚C, showing an increase pattern of average τ and losing of lubricating effect with decrease of temperature.

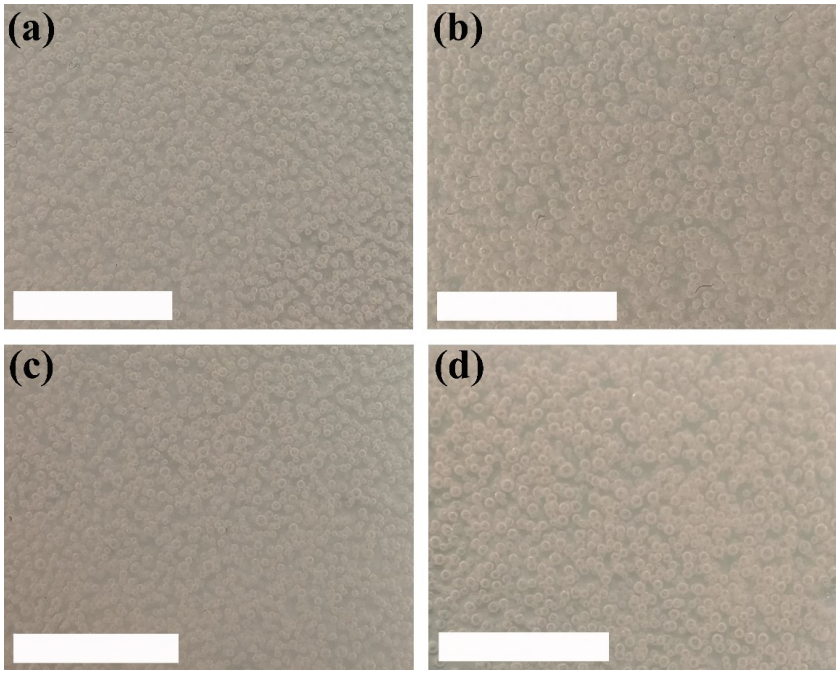

Supplementary Figure S4 | Optical images showing ethanol droplets in the LLG 1. (a) ~ (d) The samples with ethanol volume content of 10 %, 20 %, 30 % and 40 %, respectively. The droplets size shows a trend of increase with increasing ethanol content. The scale bar is 1mm in all images.

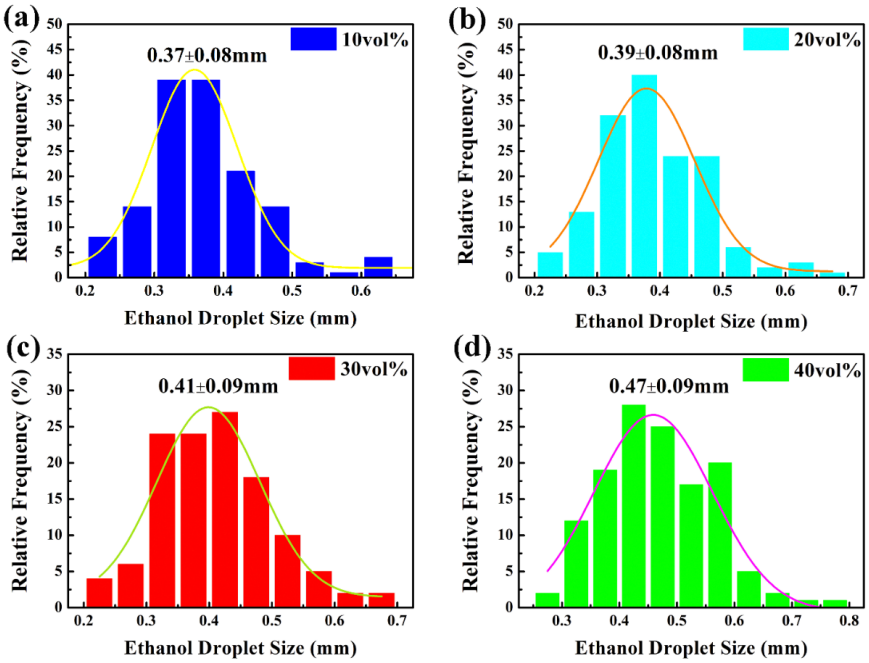

Supplementary Figure S5 | Size distribution of ethanol droplets in the LLG 1. The distribution was close to unimodal Gaussian distribution in all samples. With increasing ethanol content in the polymer, the droplet size increased.

The ice adhesion strength on the ethanol-exhausted sample was higher than that on the pure silicon rubber, which can be explained by the classic ice adhesion theory[1, 2]

$$\tau = \sqrt{\frac{EG}{\pi a \Lambda}} \qquad (1)$$

where E is Young's modulus of the substrate, G is the surface energy, a is the crack length, and Λ is a non-dimensional constant determined by the geometric configuration of the interface cracks. Pores were left in the substrates after the removal of ethanol droplets, which reduced Young's modulus and also acted as macro-crack initiators which could increase the crack length[3]. Both favored weakening ice adhesion strength. Yet importantly, in the curing process of LLG 1, the evaporation of ethanol droplets in the substrate introduced a significant increase in the surface roughness, as schematic shown in Fig. S6, which caused physical ice interlocking with the substrate. Obviously, interlocking outperformed the combining effect of lowering substrate apparent modulus and increased cracking initiators in the dry LLG 1[4]. Thus, the ethanol-exhausted samples shew higher ice adhesion strength.

However, the comparison among the ethanol-exhausted samples was more complex. With increasing ethanol content in LLG 1, obviously, the average pore size increase (Fig. S4 and Fig. S5). Firstly, the Young's modulus would decrease with increasing ethanol content consequently. Secondly, the macro-crack initiators effect was enhanced, which resulted in crack length improvement with increasing ethanol content. Both of them favored low ice adhesion strength along ethanol content[1], which counteract with the effect of increased surface roughness resulted from higher ethanol content (Fig. S6). Because it was hard to quantitatively determine and control which factors to be outperforming in the LLG samples with varied ethanol content, there is no clear trend observed in the ice adhesion results.

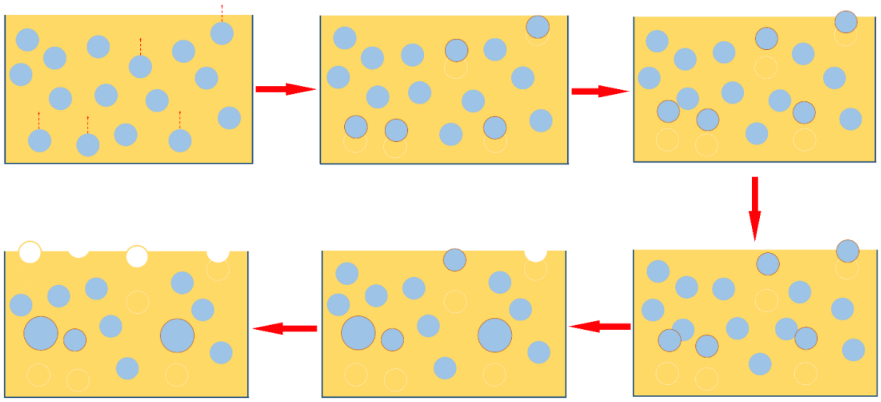

Supplementary Figure S6 | Schematic showing the formation process of the roughness on the LLG 1 surface. The ethanol droplets in the liquid polymer were initially in a metastable phase in the mixture. In the curing process, the ethanol droplets were able to coalesce with their neighbours and float to the surface, then released to the ambient. As the viscosity of the polymer increased with the on-going curing process, the remaining ethanol droplets on the surface created pores that contributed to the roughness of the surface. The surface roughness was proportional to the ethanol content.

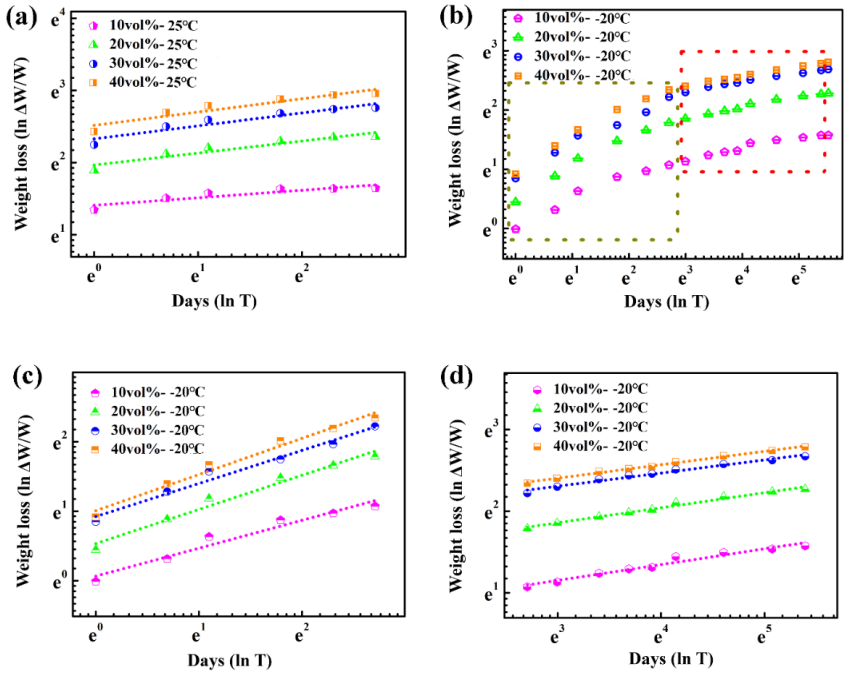

Supplementary Figure S7 | Weight loss of LLGs under different temperature. (a) Weight loss of LLGs at room temperature as a function of time. **(b)** Weight loss of LLGs at -20 °C as a function of time. **(c)** and **(d)** were the fitting curves of the points from left and right part of **(b).** The dot lines in all plots were the fitting curves.

The weight loss of the LLGs showed a linear relationship with time in the logarithm graphs. The relationship below was used to fit the weight loss data in the graphs:

$$\ln\frac{\Delta W}{W} = a + b\ln T \qquad (1)$$

where ΔW is the accumulated weight reduction of the LLGs, W is the initial weight of LLGs, and T ($T \geqslant 1$) is the holding time after fabrication. The constants a and b are determined by ethanol content, temperature, pressure and other ambient factors. The values of a and b for different samples are given in Table 1.

There were two mechanisms causing the weight loss of LLGs, namely active secretion and passive diffusion. The ethanol molecules that were randomly trapped between the silicon rubber can be secreted by the polymer chains in a fast manner, while ethanol droplets sealed in the polymer body can only leak slowly by passive diffusion. As exemplified by data obtained under -20 °C, two sets of constants a and b were needed for

fitting the first and the second half of the data points (Fig. S7b). In the first stage of leaking, less than 15 days depicted by Fig. S7c, both active secretion and passive diffusion were functioning at the same time. Thus, higher ethanol leaking rates were detected, with higher value of b (samples 5 to 8 in Table 1). After 15 days and with the exhaustion of active secretion shown in Fig. S6d, the passive diffusion of ethanol dominated resulting in lower leaking rates (samples 9 to 12 in Table 1). The value of *b* among each series (1 ~ 4, 5 ~ 8, and 9 ~ 12) with different ethanol content was close, which meant similar leaking rate for silicon rubber with different ethanol content under the same temperature.

The constant *a* denotes the initial weight loss and correlates with the ethanol content in the LLG sample series (1 ~ 4, 5 ~ 8, and 9 ~ 12). The values of *a* were higher in Fig. S7a than Fig. S7c, which meant *a* was also proportional to the ambient temperature. It should be noted that the *a* in the Fig. S7c was not comparable with Fig. S7a and Fig. S7c for the different starting time.

By combining the final weight loss in Fig. S7a and the equation (1), we could calculate the lifespan of LLG 1 with various ethanol content. The experimental results in Fig. S7b at 250 day shew the weight of sample with 10 vol% ethanol no more decrease, which agree well with the number in Table 2. Thus, we could reasonably believe the LLG 1 with 40 vol% ethanol could continuously release ethanol for around 593 days.

It should be noted that the weight loss of ethanol in LLG 1 was not perfectly matched with the initial volume ration of the ethanol in the samples. The reason was that the weight was measured after silicon elastomer cured, not including the amount that had evaporated in the 3-hours long curing process of the LLG samples.

Table 1 | The number of a and b for different LLG 1 samples.

Samples	Ethanol content (vol%)	Temperature (°C)	Days	a	b
1	10	25	1 ~ 15	2.517	0.184
2	20	25	1 ~ 15	2.330	0.180
3	30	25	1 ~ 15	1.966	0.167
4	40	25	1 ~ 15	1.408	0.105
5	10	-20	1 ~ 15	1.008	0.519
6	20	-20	1 ~ 15	0.923	0.476
7	30	-20	1 ~ 15	0.535	0.491
8	40	-20	1 ~ 15	0.067	0.401
9	10	-20	15 ~ 220	1.911	0.164
10	20	-20	15~ 220	1.821	0.161
11	30	-20	15 ~ 220	1.303	0.184
12	40	-20	15 ~ 220	0.573	0.193

Table 2 | The calculated lifespans of LLG 1 under -20 ℃.

Samples	Ethanol content (vol%)	Temperature (℃)	Lifespan (days)
1	10	-20	258
2	20	-20	310
3	30	-20	339
4	40	-20	593

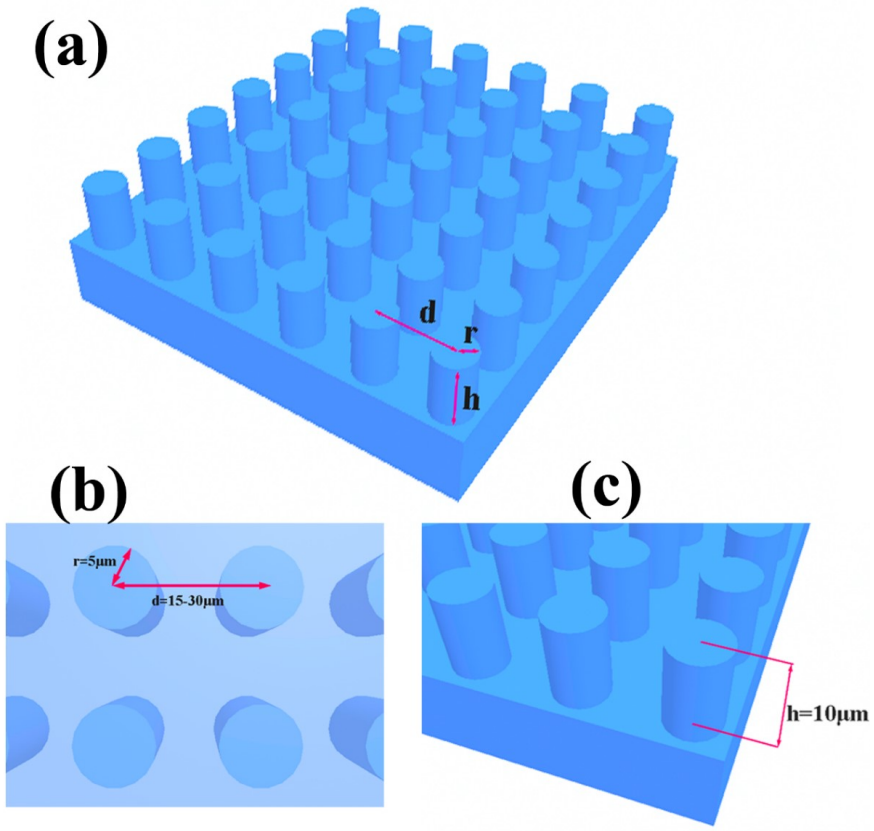

Supplementary Figure S8 | Schematic illustration of the detailed geometry of the pillars on the silicon wafer. r was the radius of pillar, **h** was the height of pillar, and **d** was the centre distance between adjacent pillars. The value of **d** varied from 15 μm to 30 μm. **(a)** the top view of the pillars. **(b)** the side view of the pillars.

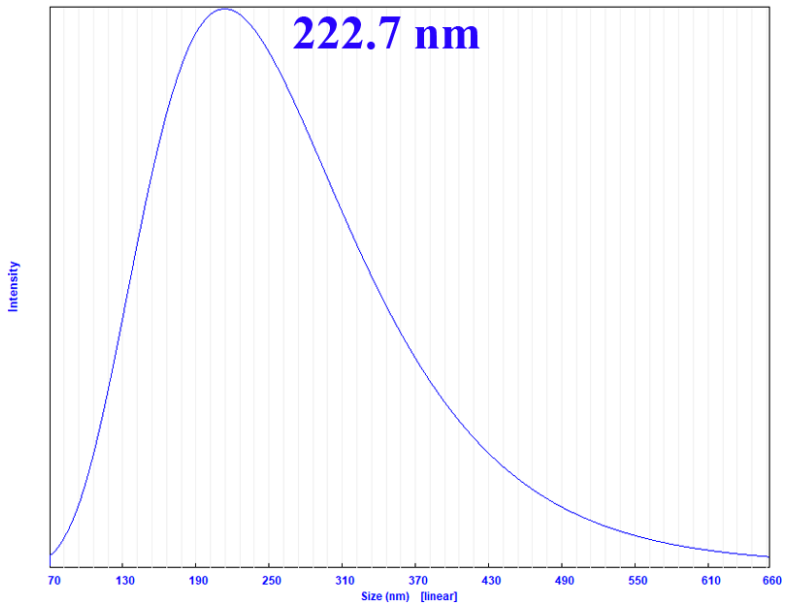

Supplementary Figure S9 | Diameter distribution of SiO_2 particles synthesized in this work. The particle size was in a unimodal distribution, with a mean size of 222.7 nm.

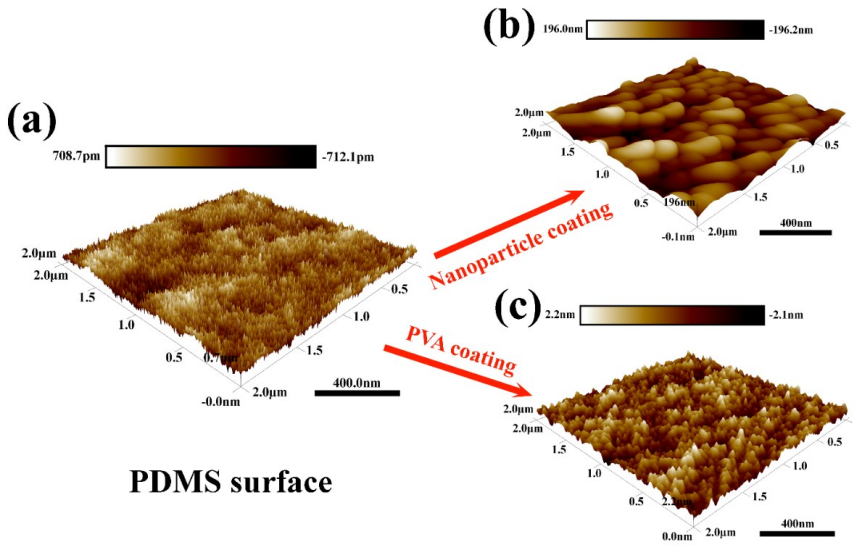

Supplementary Figure S10 | The AFM images showing the roughness of LLG 2 with and without surface treatment. (a) Roughness of PDMS surface as prepared. **(b)** Roughness of PDMS surface after treating with SiO_2 nanoparticles. **(c)** Roughness of PDMS surface after treating with PVA.

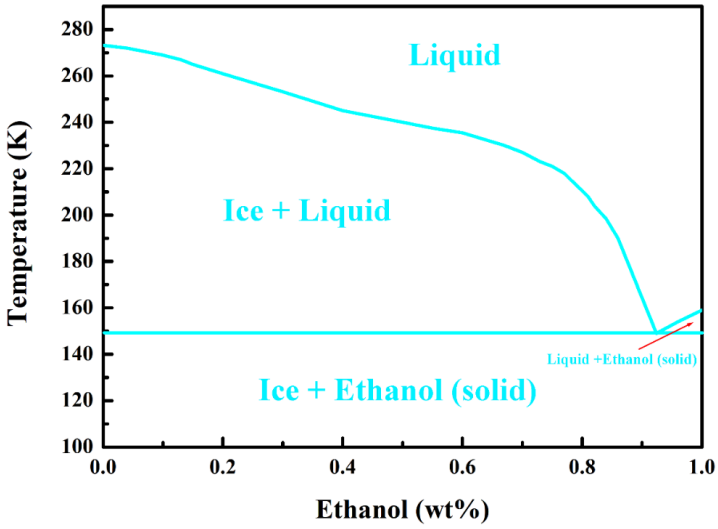

Supplementary Figure S11 | The phase diagram for the EtOH-H_2O system. The phase diagram of the EtOH-H_2O was a good supplement that help to explain why ethanol (or mixture of ethanol and water) could be a better lubricant layer compared to aqueous lubricant layer at low temperature[5-7]. The liquid phase contained both ethanol and water in the figure. Pure ethanol has less hydrogen bonds per unit volume than pure water. With addition of ethanol into water, the hydrogen bonds density in the liquid phase reduced, which finally resulted in lower ice adhesion strength in the one hand. In the second hand, the mixture solution of ethanol and water could effectively lower the freezing point of the liquid layer, maximally as low as 149 K, which maintains lubricating effect to ice in a broad temperature range. Thus, LLG own high icephobic potential that can function well at extremely low temperature.

References

1. Z. He, S. Xiao, H. Gao, J. He and Z. Zhang, *Soft matter*, 2017, **13**, 6562-6568.
2. M. Nosonovsky and V. Hejazi, *ACS nano*, 2012, **6**, 8488-8491.
3. Z. He, Y. Zhuo, J. He and Z. Zhang, *Soft Matter*, 2018.
4. J. Chen, J. Liu, M. He, K. Li, D. Cui, Q. Zhang, X. Zeng, Y. Zhang, J. Wang and Y. Song, *Applied Physics Letters*, 2012, **101**, 111603.
5. R. Anderson, A. Chapoy, H. Haghighi and B. Tohidi, *The Journal of Physical Chemistry C*, 2009, **113**, 12602-12607.
6. A. Potts and D. Davidson, *The Journal of Physical Chemistry*, 1965, **69**, 996-1000.
7. P. Boutron and A. Kaufmann, *The Journal of Chemical Physics*, 1978, **68**, 5032-5041.

A.3 Paper 3

Dynamic anti-icing surfaces: emerging field for ice mitigation

Authors: Feng Wang, Yizhi Zhuo, Senbo Xiao, Jianying He and Zhiliang Zhang

To be submitted 2020

Paper 3

Dynamic anti-icing surfaces: emerging field for ice mitigation

Feng Wang, Yizhi Zhuo, Senbo Xiao*, Jianying He*, Zhiliang Zhang*

NTNU Nanomechanical Lab, Department of Structural Engineering, Norwegian University of Science and Technology (NTNU), Trondheim 7491, Norway.

Corresponding Author

*E-mail: senbo.xiao@ntnu.no; jianying.he@ntnu.no; zhiliang.zhang@ntnu.no

Abstract

Despite the remarkable progress made in surface icephobicity in recent years, there is a major view of static ice-substrate interface projected on the reported anti-icing surfaces. Practically, the ice-substrate interface and its nearby regions, either the structure or properties, alters with time, temperature or external stimuli. It is only possible to understand the dynamic properties of the icing interface first, and then shed light on anti-icing surface design to meet challenges of harsh conditions including extremely low temperature and/or long working time. This article surveyed the state-of-the-art anti-icing surfaces and dissect their dynamic spontaneous/stimuli-responsible changes of the chemical/physical states. By in-depth monitoring the crucial locations to ice adhesion, namely in the substrate, ice, or the ice-substrate interface, the available anti-icing surfaces are for the first time classified by fundamentals dynamic principles. The recent works in the preparation of dynamic anti-icing surfaces, their potentials in practical applications, and the challenges confronted are summarized and discussed, aiming for a thorough review of the promising dynamic anti-icing surfaces, as well as guiding its future designs and applications.

Keywords*: surface icephobicity, icephobic materials, dynamic anti-icing, low ice adhesion*

Introduction

Icing is one of the most common natural phenomena that widely impact human activities. Undesired ice formation and accumulation can introduce numerous severe function and safety problems to aircrafts, power grids, transmission lines, roadways, marine vessels, renewable energy infrastructures, and many others.[1-8]. The traditional

methods used for dealing with icing problems, for instance mechanical de-icing, thermal or chemical treatments, are often highly costly and low-efficient[9, 10]. As such, enormous interests have been aroused in deploying surfaces that can control icing and mitigate its related damages. Advanced surfaces with properties like repelling incoming water droplets, delaying ice nucleation, repressing ice growth and weakening ice adhesion are designed for anti-icing purpose[11-14]. From the early lotus-leaf inspired superhydrophobic surfaces fabricated for repelling water droplets and delaying ice nucleation to the recent omniphobic pitcher-plants-inspired slippery liquid-infused porous surfaces (SLIPSs) developed for delaying ice nucleation, suppressing frost formation and lowering ice adhesion[11, 12, 15-19, 20-24], there are currently a colorful spectrum of anti-icing surfaces reported in the literature showing great potentials of practical low ice adhesion strength (0.2 ~ 10 kPa) and easy achievable large-scale ice remove capacity[25-27]. It is witnessed that there is a shift in anti-icing surfaces design philosophy from being of static nature, namely no change at the ice-substrate contact area after ice formation, to enabling dynamic changes of the chemical/physical states of the ice/substrate/ice-substrate-interface in order to enhance anti-icing performances. The static anti-icing surfaces functioned to a limited extent, and had deficiencies in icing/deicing cycling durability, inapplicability at extremely low temperature, fragility to surfaces damage and surfaces degradation, and inadaptability to environment changes[16-18, 28-33]. In contrast, the emerging dynamic anti-icing surfaces, thanks to the integrated dynamic properties into the substrate, ice, or the ice-substrate interface, exhibit superior durability, wider temperature tolerability and better environment adaptivity, and are attracting increasing interests[14, 34-39].

This review aims to provide a thorough survey on the newest development of dynamic anti-icing surfaces. Focusing on the most relevant ice-substrate interfacial regions (Fig. 1a), and their spontaneous/stimuli-responsive changes in chemical/physical states impacting ice adhesion during and after ice formation, for the first time we classify the state-of-the-art dynamic anti-icing surfaces are classified in to three categories, namely surfaces with dynamic substrate changes, with dynamic interface changes, and with dynamic ice changes as shown in Fig. 1b. Surfaces with dynamic changes in the substrate generally include functional structures that can response to internal and external stimuli,

which can modify the substrate properties and enhance anti-icing performances[35, 36, 40-43]. Surfaces with dynamic changes at the ice-substrate interfaces after ice formation provide the possibility of altering interface interactions for lowering ice adhesion[14, 34, 38, 39, 44-46]. Surfaces with dynamic changes in the ice are able to direct ice growth, propagation and even ice melting, which can mitigate ice accumulation and assist ice remove on the surfaces[13, 37, 47-53]. The following sections detailed these three categories of anti-icing surfaces.

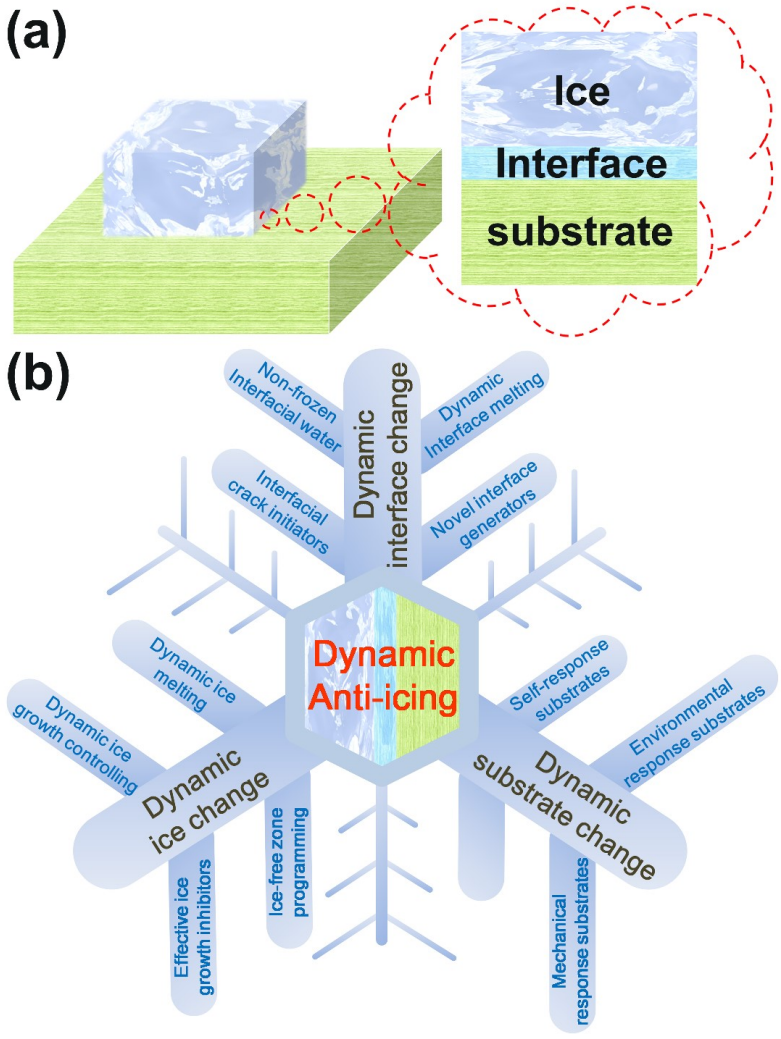

Figure 1. Dynamic anti-icing surfaces. (a) The three most important regions close to the ice-substrate

interface that determine anti-icing performance of a surface. (b) Dynamics anti-icing surfaces targeting the three ice-substrate interfacial regions. The dynamic substrate change includes substrates that can response to the internal/external conditions, namely those by tuning the surface state and affecting the ice formation/adhesion on the top. The dynamic interface change covers the surfaces that can introduce dynamic conversion the chemical/physical states of the ice-substrate interface after ice formation, thus facilitating easy ice removal. The dynamic ice change encompasses the surfaces that can tailor ice growth, propagation or even melt ice for the purpose of mitigating ice accumulation.

1 Dynamic anti-icing surfaces with dynamic substrate changes

1.1 Self-response substrates

Many surfaces exhibit dynamic changes by self-response to their internal forces. Such self-response surfaces widely exit in natural organisms and systems. For instance, earthworms and poison dart frogs have secretion glands under their skin, which release lubricant to form a slippery layer above the skin[54, 55]. Surface lubricating is driven by the under-skin disjoining pressure or concentration gradient[41, 56]. The mechanism underlies self-response surfaces has inspired the design of anti-icing surfaces with embedded lubricant in the substrates.

One notable self-response substrate was developed through phase separation as shown in the Fig. 2b. By first dissolving copolymers of urea and polydimethylsiloxane (uPDMS) and excess silicon oil into tetrahydrofuran (THF) and subsequent evaporation of THF, the resulting crosslinked polymer matrix trapped the excessive silicon oil as internal droplets[56]. Such droplet-embedded gel system by phase separation of micro-scale oil droplet nucleation and the formation was metastable, and was able to secrete a lubricating film on the surface with a spreading factor of $S = \gamma_{ga} - (\gamma_{la} - \gamma_{gl}) > 0$, where γ_{ga}, γ_{la} and γ_{gl} are the gel-air, liquid-air and gel-liquid interfacial tensions, respectively[57]. The surface lubricant layer was regenerable under the driving force of disjoining pressure originated from the van der Waals interactions at the gel surface[56]. It is intriguing that both the thickness of the lubricant layer and the size of the embedded droplets in this substrate were controllable through polymer crosslinking strength and oil content, which offered a strategy for preparing similar substrates for improving anti-icing performace[40-42, 55, 58-67]. Icephobic surfaces following the same strategy for surface regenerable lubricant layers indeed showed ice adhesion strength below 40 kPa[40], with regenerative lubricating layers after 15 wiping/regenerating tests and long-term ice

adhesion strength below 70 kPa. Through a precise deploying of polymer and oil, recently reported novel self-lubricating organogels (SLUGs) displayed extremely low ice adhesion strength of 0.4 kPa[42]. The ice formed on the SLUGs samples with small tilting angles could slide off at -15 °C, which demonstrated the great potential of self-response substrates in anti-icing.

Beside small liquid oil molecules, solid lubricants were also used in self-response substrates for regenerating surface lubricating layers to assist easy ice removal[41, 61]. For example, alkane embedded in a polymer substrate can diffused into the surface driven by concentration gradient and the internal stress of the polymer matrix, resulting in a solid alkane layer as shown in Fig. 2c. The regenerable solid lubricant alkane had weak interactions with the polymer substrate and served as sacrificial layer in ice removal, which enable low ice adhesion strength (~ 9 kPa) and good durability in 20 icing/de-icing cycles[41]. Recently, the perfluoroalkane wax were verified as a good candidate to obtain solid-lubricant regenerable surfaces for anti-icing application[61]. The perfluoroalkane wax regenerating surface demonstrated low ice adhesion strength (~ 20 kPa) and highly environment stability. Comparing to the liquid lubricant layer, solid lubricant layers are mechanically more robust in icing/de-icing cycles.

Surface damages in practical applications are severely harmful to the icephobicity of anti-icing surface, since any possible interlockings between ice and surface voids can greatly enhance ice adhesion to the surface. As such, self-response substrates with self-healing functionality were fabricated for anti-icing purposes[35, 36, 58, 68-71]. Such substrates showed significant improvements in mechanical durability because of the ability of self-healing surface damages at sub-zero temperature to maintain smooth topography (Fig. 2d). One of the self-healing substrates, Fe-pyridinedicarboxamide-containing PDMS (FePy-PDMS) elastomer, exhibited low ice adhesion strength of ~ 6 kPa and ~ 12 kPa after 50 icing/de-icing cycles[36]. In order to increase the self-healing rate for meeting the icing/de-icing cycles, ultrafast self-healing and highly transparent (the coated glass showed light transmittance of 89.1 %) icephobic substrates were prepared by optimizing polymer chain flexibility and concentration of hydrogen bonding, which can restored ~ 80 % of the ultimate tensile strength of the substrate after healing for 45 min at room temperature[72]. The self-healing substrates can be promising candidates for robust anti-icing surfaces in practical environment if the self-healing functionality is further

improved especially at low temperature.

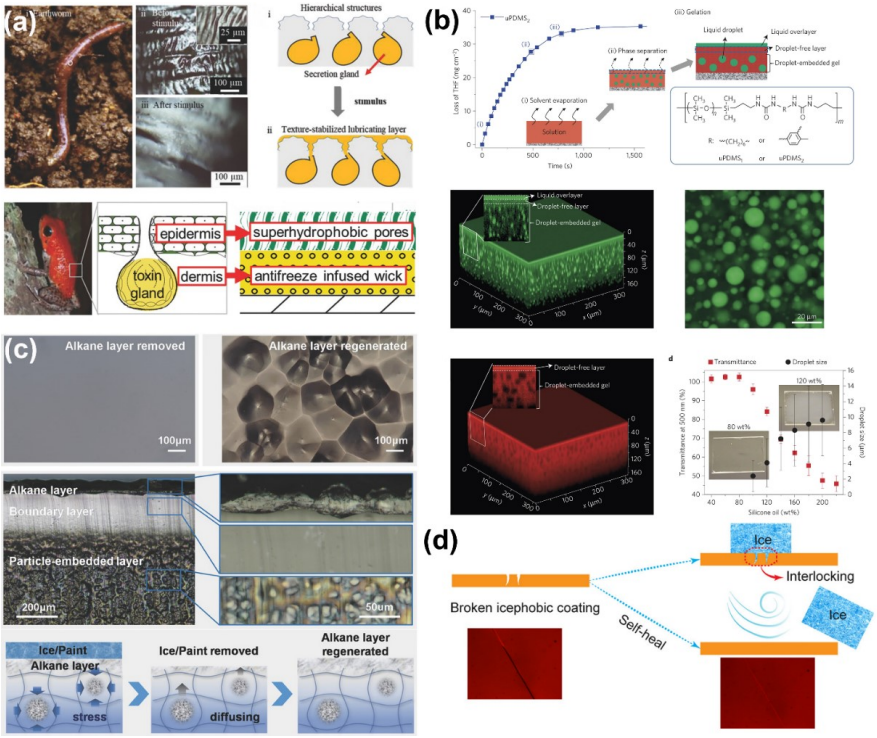

Figure 2. Selection of the dynamic anti-icing surfaces through self-response substrates. (a) The lubricant regenerable systems in earthworm and poison dart frog, and the inspired self-response anti-icing substrates. (b) The droplet-embedded gel structure, and its secreted surface lubricating film. Confocal fluorescence images of the substrate samples visualizing the lubricant film on the substrate surface and the internal distribution of the lubricant droplets. The average size of the individual droplets in the substrates and the light transmittance of samples with different silicone oil contents are given in the right bottom sub-figure. (c) The alkane-embedded structure, showing the renderability of the surface alkane layer, the alkane distribution in the substrate, and the regeneration mechanism of the solid alkane layer. (d) The schematic of the self-healing icephobic surface with fabricated samples. Panels (a) and (c) were adapted with permission from Ref. 41, 54 and 55, Wiley Publishing Group. Panel (b) was adapted with permission from Ref. 56, Nature Publishing Group. Panel (d) was adapted with permission from Ref. 36, American Chemical Society.

1.2 Environmental response substrates

Many anti-icing surfaces use dynamic substrates that response to the ambient conditions of temperature, magnetic field, light, and so on[35, 43, 73-81]. By integrating

temperature sensitive components during fabrication, anti-icing substrates can response to temperature change of the surrounding environment[43, 73]. One of such substrates incorporated a binary liquid mixture (silicon oil and liquid paraffin) into a PDMS network, the resulting reversibly thermo-secreting organogel (RTS-organogel) demonstrated distinct morphologies at different temperature as shown in Fig. 3a[43]. Specifically, the substrate was transparent at high temperature as the internal silicon oil and liquid paraffin were miscible. Upon cooling in icing temperature, the substrate secreted visible oil droplet to its surface owing to the collapse of the polymer matrix and the phase separation of the silicon oil from paraffin. Unlike the liquid layer by propelled by internal force in the SLUGs shown in Fig. 2b, the oil film generated on this substrate was largely driven by temperature. Nevertheless, the lubricating oil film secreted under low temperature was notably beneficial for icephobicity of the surfaces. The ice adhesion strength on the RTS-organogels were less than 1 kPa at -15 ℃, which can enable sliding of ice cube on the surface samples with small tilting angles. The RTS-organogels were believed to be more durable than the SLUGs, because they could reversibly absorb lubricant into the polymer matrix for replenishing the internal lubricants in storage and against evaporation/contamination.

Liquid lubricants in anti-icing substrates can deplete in limited number of icing/de-icing cycles due to the weak interaction between the lubricant and the base materials, which leads to poor durability. Interestingly, special temperature responsive lubricants provide a feasible solution to this issue. As shown in the Fig. 3b, a phase transformable lubricant was used in creating the so-called phase transformable slippery liquid infused porous surfaces (PTSLIPS) recently[35]. Because the lubricant had phase transition point from liquid to solid phase at ~ 3 ℃[35], the durability of the fabricated PTSLIPS was greatly improved, showing a lowest ice adhesion strength of ~ 4 kPa and long-term ice adhesion strength of 16 kPa after 30 icing/de-icing cycles. Although the PTSLIPS can be fabricated using daily accessible materials like foams and common paper, its anti-icing performance was superior than the results observed on other conventional slippery liquid infused porous surfaces used for anti-icing. Because the phase transition point of the lubricant in the PTSLIPS was marginally above water freezing temperature, displaced lubricants on the substrate surface in de-icing can be restored in the subsequent phase

transition cycle of the lubricant at slightly increased temperature, rendering self-healing abilities and promising application potentials. Furthermore, the solid lubricant can also physically prevent water from permeating into the substrate, thus suppressed mechanical interlocking during ice formation on the substrate. It worth noting here that similar phase-change materials (PCMs) were introduced into concrete for anti-icing. During the phase transition upon cooling, the PCMs released substantial latent heat and can hinder ice accumulation in walking pavements[74-76, 82-84].

Magnetic field is relatively less commonly applied in anti-icing practice. However, utilizing magnetic field as stimuli to modulate substrates has been explored, with encouraging results illustrating the potentials of active de-icing technology[77, 78, 80]. The magnetic slippery surfaces (MAGSS) were the successful representatives of this type of anti-icing substrates, which used magnetic fluid (that is, ferrofluid) along with a magnetic field for controlling surface properties as shown in Fig. 3c[77]. The MAGSS can response to external magnetic field and generate a volumetric force to suppress water droplets from sinking into the substrate body with bulk oil, which led to small water droplet sliding off angle of 2.5°. Remarkably, the MAGSS can maintain its liquid-like phase at low temperature and were highly slippery to ice, showing extremely low ice adhesion strength (~2 Pa) without degradation after 60 icing/de-icing cycles.

Light is another important stimuli source for triggering dynamic changes in anti-icing substrates[85-88]. By integrating light-absorbing azobenzene groups into polymer skeleton of the base materials, the so-called UV responsive substrates (UVRS) were able to utilize UV energy for polymer chain conformation conversion[79]. As shown in Fig. 3d, the integrated azobenzene groups in the UVRS changed from trans- to cis-conformation under UV light with a wavelength of 365 nm, resulting in slight compress of the whole substrate. The pre-embedded silicon oil in the polymer matrix of the UVRS was released to the substrate surface as a response to the compressive stress, which enabled low ice adhesion strength of 21 kPa and long-termed ice adhesion strength of 47 kPa after 15 icing/de-icing cycles on the UVRS. The light stimuli also had thermal effects, which further inspired the design of photothermal response substrates. Cocoa oil with low-melting point and efficient photothermal Fe_3O_4 nanoparticles were infused into porous structures together in fabricating lubricant infused surfaces (LIS)[81]. Upon irradiation

with infrared light, the LIS can absorb optical energy via Fe_3O_4 nanoparticles, which led to melting of the internal solid cocoa oil as lubricant for surface slippery liquid. The LIS thus possessed switchable hydrophobic/slippery functionality by turning off/on the light source.

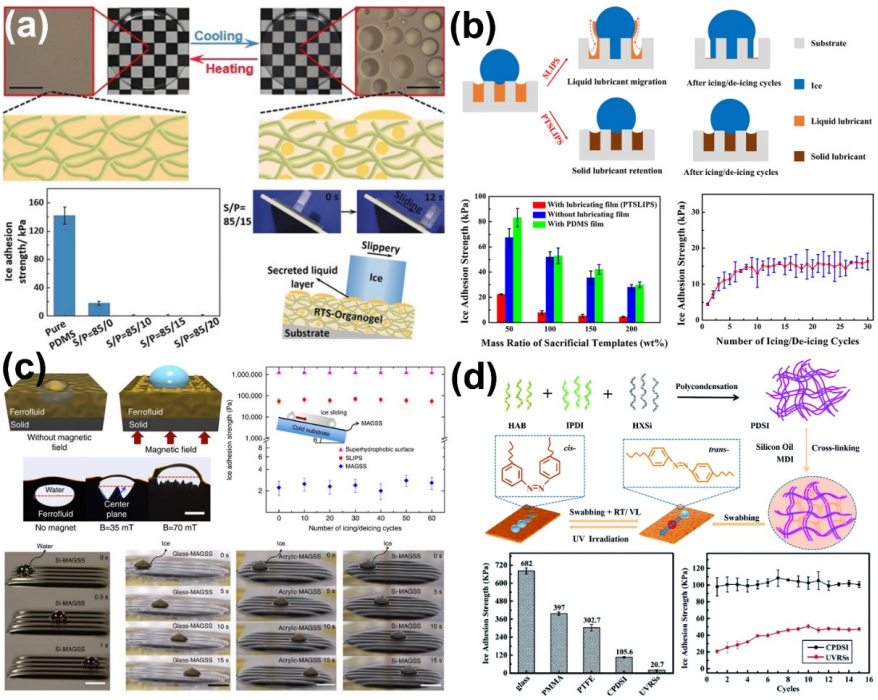

Figure 3. Representatives of the dynamic anti-icing surfaces through environmental response substrates. (a) The thermal response lubricant regenerable organogel, showing the droplets secretion at low temperature and reversible droplets absorption at high temperature. Low ice adhesion enabled small sliding angle of ice on the organogel at -15 ℃ were showed with schematics with corresponding samples (the S/P means the mass ratio of silicone oil and liquid paraffin). (b) The phase transformable slippery liquid infused porous surfaces (PTSLIPS), showing enhanced lubricant durability comparing to slippery liquid infused porous surfaces (SLIPS). (c) The magnetic slippery icephobic surfaces, showing stable water/ice repellency with extremely low adhesion under magnetic field. (d) The UV-responsible substrates (UVRS), showing UV irradiation controlled lubricant release and low ice adhesion strength. Panels (a) adapted with permission from Ref. 43, Wiley Publishing Group. Panel b adapted with permission from Ref. 35, Elsevier Publishing Group. Panel c adapted with permission from Ref. 77, Nature Publishing Group. Panel d adapted with permission from Ref. 79, Royal Society of Chemistry.

1.3 Mechanical response substrates

Ice removal generally involves stress change on the ice adhered surface. Mechanical response substrates are designed to utilize the stress associated with ice removal to dynamically alter the surface structures in order to achieve low ice adhesion. The surface structures that response to the mechanical force can be both molecular structures in base materials and geometrical patterns above the surfaces[89, 90]. Notably, an ultra-durable icephobic coating was designed by introducing slide-ring crosslinkers, namely molecular pulleys, into PDMS base matrix (Fig. 4a)[89]. The slide-ring crosslinkers were not only able to move along the polymer chains under mechanical loading, but also can return to their original state *via* entropic repulsion upon relieving loading[91, 92]. The unique structures in this substrate decreased the elastic modulus of the polymer matrix for low ice adhesion, and at the same time guaranteed excellent cohesive strength for mechanical durability, solving the common deficiency in other low elastic modulus polymer materials used for anti-icing. The slide-ring substrate showed a low ice adhesion of ~12 kPa during 20 icing/deicing cycles, and promising ice adhesion strength ~22 kPa after 800 abrasion cycles, being one of the most durable elastomers reported so far.

In another report, an interesting fish-scale-like dynamic anti-icing surface prototype was introduced[90]. By taking a deep look into sequential and concurrent ice detaching modes from substrates, employing atomistic modeling and molecular dynamics simulations were utilized to reveal mechanisms for lowering ice adhesion at the atomistic interaction level. Because the atomistic interactions ruptured all at once in concurrent rupture mode but incrementally in the sequential rupture mode, opening of the surfaces structure featuring the sequential rupture of ice was essential for low ice adhesion. Inspired by the structure topology of fish scales, the fish-scales-like surface was designed by pile arrangement of graphene platelets in atomistic modeling. Under de-icing forces, the graphene platelets dynamically opened up to enabling sequential rupture of ice from the surface, which led to a ~ 60 % reduction in ice adhesion strength. The theoretical model of fish-scale-like surface was a good starting point of mechanical response structure design for low ice adhesion.

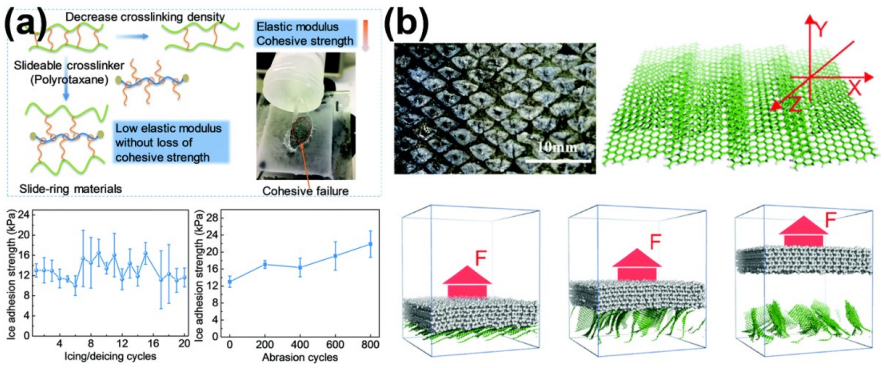

Figure 4. Representatives of the dynamic anti-icing surfaces through mechanical response substrates. (a) The slide-ring substrate, showing its molecular mechanism and the enhanced cohesive strength and excellent durability. (b) The fish-scale-like surface, showing sequential rupture of atomistic interactions for lowering atomistic ice adhesion. Panel (a) and (b) were adapted with permission from Ref. 89 and 90, Royal Society of Chemistry.

2 Dynamic anti-icing surfaces through dynamic interface change

2.1 Non-frozen interfacial water

The importance of the ice-substrate interface to ice adhesion is self-evident. It is known that ice is slippery to ice-skating blades, meaning low adhesion strength, due to a surface premelted layer[93]. The premelted liquid or liquid-like aqueous layer exists on the ice surfaces at subzero temperature because of regelation or by pressure or friction melting[93-97], which applies not only at ice-vapor but also ice-solid interfaces[98, 99]. As the thickness of the premelted layer at ice-solid interfaces was shown to increase with temperature, utilizing and amplifying the premelted layer for effectively reducing ice adhesion became one of the important strategies of surface icephobicity[100]. Because the premelted layers have thickness at the nanoscale, atomistic simulation and molecular dynamic simulation were employed to investigate their mechanical effects on the nanoscale ice adhesion[101]. As shown in Fig. 5a, ice-cube models with premelted interfacial water layers on solid substrates showed negligible ice adhesion stress if compared with ice directly contacted with the solid substrate. The premelted layer converted ice-substrate contact from solid-solid to solid-liquid-solid, which resulted in weak interfaces with disordered and short-term atomistic interactions of van der Waals forces and hydrogen bonds. Related studies focused on the lubricating effect of the

premelted or non-frozen interfacial water layer further supported the potential of utilizing aqueous layer for mitigating icing problems[101-103].

Although interfacial non-frozen water layers were identified at the ice-solid contact interfaces as early as in 2004, intensive experimental explorations on their application in anti-icing came much later[99, 100]. Through rational nano-structuring of solid surfaces for creating an interfacial quasi-liquid layer, ice formation can be delayed for 25 hours at -21 °C[104]. Yet, ice formation is inevitable with long enough icing time. As ice adhesion on certain solid surfaces, such as SiO_2, Si, Au and so on, are too high to any ice removal approach[105, 106], new strategies that could program non-frozen interfacial water on such surfaces for low ice adhesion were in great needs. Using highly hydrated ions were believed to be a good approach for creating quasi-liquid layers (QLL) on solid surfaces, because ions can great impact the structure of water and supress ice nucleation[107]. Polyelectrolyte brushes hosting ions were employed to probe the effects of counter ions on ice adhesion (Fig. 5b)[108]. It was found that the polyelectrolyte brushes with kosmotropic counterions (G-$SO^{3-}Li^{+}$, G-$SO^{3-}Na^{+}$) had maximum ice adhesion reduction (25 ~ 40 %) comparing to the bare glass (G) at -18 °C, because of the most negative water structural entropy resulting from strong hydration. In comparison, the polyelectrolyte brushes with chaotropic counterions (G-$SO_3^- K^+$, G-N^+Cl^-, and G-$N^+SO_4^{2-}$) did not change the ice adhesion, owing to positive water structural entropy of weak hydration[107]. The nature of the polyelectrolyte layer also affected ice adhesion significantly. For instance, brushes with G-$SO_3^-Li^+$ decreased the ice adhesion greatly, which was not observed on samples with G-COO^-Li^+. Such results suggested that kosmotropic counterions incorporated with strongly dissociating polyelectrolyte brush could facilitate easy ice removal. This study provided important reference for integrating counterions for related anti-icing applications[109, 110].

To improve the lubricant effects for extremely low ice adhesion, the thickness of QLL needs to drastically increase. Generally, developing liquid-like surfaces through covalently grafting flexible polymers on flat surfaces was an effective approach. The state-of-the-art liquid-like surfaces, for instance the slippery omniphobic covalently attached liquid surfaces (SOCAL), still exhibited limited thickness of QLL, which restricted sustainable ice removal[111-113]. Recently, a nonstick and extremely flexible

quasi-liquid surface (QLS) with a coating thickness of 30.1 nm (Fig. 5c)[114], which enabled extreme flexibility and quasi-liquid thickness of the surface. The QLS had omniphobic nature of exceptional repellence of water and organic liquids and showed extremely low glass transition temperature (T_g = -125 °C). All the properties enabled low ice adhesion strength of ~ 26 kPa on QLS , and de-icing possibility by air flows (mimicking wind power).

Although the surfaces with quasi-liquid layers are highly favourable for lowering ice adhesion strength, maintaining the durability of the grafted polymer chains on such surfaces exposed to mechanical damages was still challenging. One other difficulty of applying quasi-liquid layers emerges when surfaces roughness scale is larger than the layer thickness. To address these two problems, a robust and durable anti-icing coating fabricated by polymers (polyurethane, PU) with hydrophilic pendant groups was newly reported[105]. The hydrophilic component dimethylolpropionic acid (DMPA) in the coating could absorb water directly from its humid environments or from the contacted ice/snow due to the ion effect (Fig. 5d), which resulted in aqueous lubricating layers on the coating surface as long as ice is formed. Surface samples coated by the coating contained 9 wt% DMPA (PU-9) maintained stable and low ice adhesion strength of 27 kPa at temperature as low as -53 °C. The PU-9 on the coating also exhibited excellent durability during icing/de-icing test, showing almost no change after 30 cycles. It was believed that the coating was adaptable on almost all surfaces including rough ones (Fig. 5d, right bottom). The fabrication strategy of the coatings, incorporating hydrophilic pendant groups in soft polymer for aqueous lubricating layer, was thus widely employed in similar studies[38, 46, 106, 115-120].

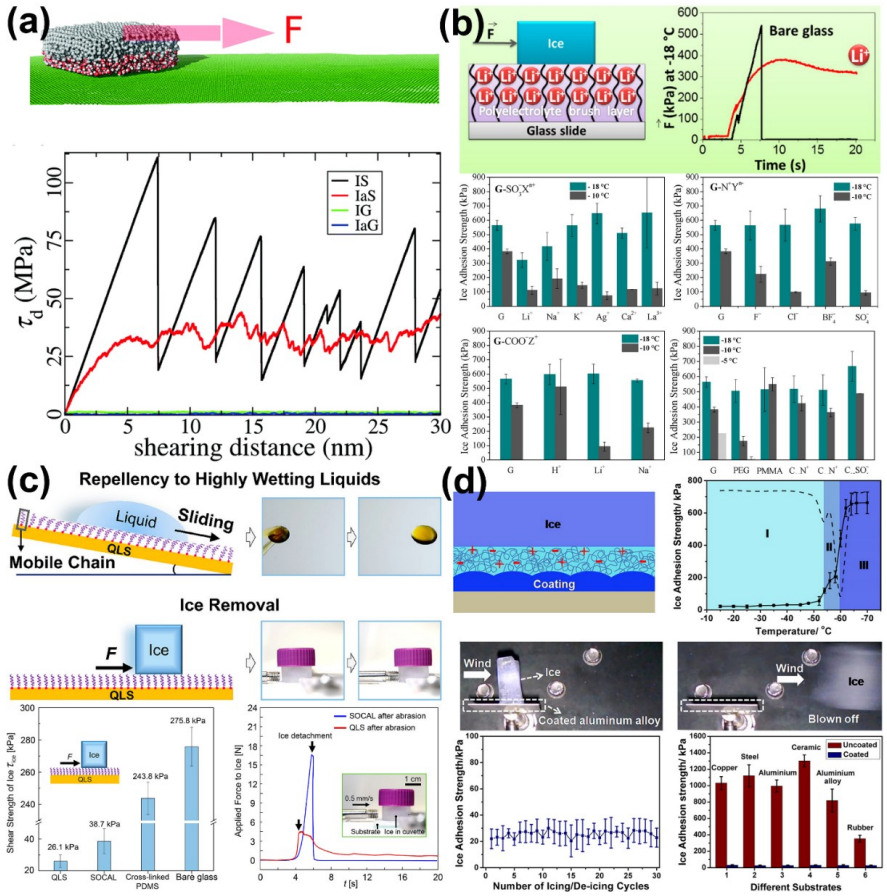

Figure 5. Non-frozen interfacial water layer and the representatives of the dynamic anti-icing surfaces. (a) Atomistic modelling and simulation of ice adhesion on different surfaces with/without an interfacial aqueous water layer. (b) The ice adhesion on the bare glass (G) and on polyelectrolyte brush layers comprising of different types of counterions (X^{n+} = Li^+, Na^+, K^+, Ag^+, Ca^{2+}, $C_{16}N^+$, La^{3+}; Y^{n-} = F^-, Cl^-, BF_4^-, $C_{12}SO_3^-$, SO_4^{2-}; and Z^+ = H^+, Li^+, $C_{16}N^+$, Na^+). (c) The liquid repellency and ice removal property of the quasi-liquid surface (QLS). (d) The reduction of the ice adhesion strength by an aqueous lubricating layer and the anti-icing performance of the coatings. Panels (a) was adapted with permission from Ref. 101, Royal Society of Chemistry. Panel (b), (c) and (d) were adapted with permission from Ref. 107, 114 and 105, American Chemical Society.

2.2 Dynamic interface melting

The thickness of aqueous lubricant layers introduced above were generally in nanoscale, varying from a few molecules thickness to tens of nanometer[105, 114]. Interfacial aqueous layer with such thickness range can lead to ice adhesion strength of ~ 20 kPa, which was good but still beyond the requirement for practical anti-icing application (lower than ~ 12 kPa)[14, 25, 26]. To increase the lubricant effects of aqueous lubricant layer, dynamic anti-icing surfaces that could melt the interfacial ice and create thicker aqueous layer were developed. In the most straightforward manner, the dynamic melting of interfacial ice could be initiated by chemicals (anti-freeze liquid or salts) or thermal energy (magnetic thermal energy, electrothermal energy and photothermal energy) that have long been used in active de-icing techniques for pavement, aircraft, power line systems, and so on[4, 45, 121-132]. In contrast to the high costs and the detrimental environmental impacts of the traditional de-icing methodologies, the recent approaches of introducing the active anti-icing agents into passive anti-icing substrates with dynamic change ice-substrate interfaces had shed new light on compromising solutions for ice removal with minimize energy/chemicals input[44, 48, 52, 55, 133].

It is well known that high ice adhesion strength is generally observed on superhydrophobic surfaces in humid environments, owing to the interlocking between ice and the surface hierarchical structure of the surfaces[16-18, 28-30, 134]. Using anti-freeze agents on superhydrophobic surfaces to create liquid interface can provide a practical solution, as demonstrated by a newly fabricated superhydrophobic copper mesh with organogel that can dynamic secrete anti-freeze agents[44]. Specifically, PVA grafted succinic acid (PVA-COOH) on the copper mesh containing anti-freezing agents (mixture of ethylene glycol and water) that were dynamically released at subzero temperature to the ice-substrate interface and melted the neighbouring ice. With the increasing thickness of the interfacial liquid layer, the ice adhesion strength on the surface deceased correspondingly with time. As shown in the Fig. 6a, ice adhesion strength of PVA-COOH (0.73 wt%) decreased from ~ 1.3 kPa to < 0.001 kPa by increasing the holding time after ice formation from 1 h to 5 h. For selected samples, the ice cube fallen off automatically after 15 h on the substrate with small tilting angle, showing excellent ice self-removal capacity.

Ionic liquids were also selected as anti-freeze agents for interface melting. Ionic liquids are quite commonly integrated in ionogels, which are utilized in many fields ranging from solid electrolytes to drug release and to catalysis[135-141]. Ionogel surfaces consisted of ionic liquid and polymer components were introduced for anti-icing, as depicted in Fig. 6b[52]. In such ionogels, the polymer matrix endowed the substrate with hydrophobicity, and at the same time the embedded ionic liquid can melting the contacting ice at the ice-substrate interface. If water droplet contacting the ionogel instead, the ionic liquid diffused from substrate to the interface and significantly depressed ice/frost formation. In either case, the ionic liquid resulted in an aqueous lubricant layer with high concentration ions at the interface, favoring anti-icing performances. The lubricant layer on the one hand suppressed ice nucleation, on the other hand lowered the ice adhesion to the surfaces. The thickness of interfacial liquid layer on the ionogel surface increased with holding time, as the ice-substrate interface was dynamically melted as indicated in the Fig. 6b, which enabled easy detachment of frozen droplets. Interestingly, the liquid layer can have thickness on macroscale, as visual liquid bridges were observed between the detaching frozen droplets and the surfaces. The dynamic process of ice melting at the interface on ionogels was further revealed by atomistic modeling and molecular dynamics simulations, which provided a solid theoretical base for rational design of ionogel-based anti-icing surfaces.

Utilizing thermal energy for interfacial ice melting is another accessible approach for creating non-frozen water lubricating layer. The thermal energy can be generated from the substrate, and then transferred to melt the interfacial ice, as examples shown in Fig. 6c. Multiwalled carbon nanotubes (MWCNT) with superior thermal-conducting property were assembled into a film layer-by-layer through a vacuum-assisted method, which resulted in superhydrophobic surfaces with excellent water repellence and special electrothermal effect for easy ice removal[48]. The temperature of the substrate can be controlled by external voltage without hampering the surface superhydrophobicity. With an input voltage of 30 V, the ice-substrate interface was efficiently melted leading to ice automatically sliding away in 34 seconds.

Using electrothermal surfaces for interfacial ice melting is effective, yet still energy intensive. Nowadays, new surfaces with photothermal effects that harvest solar energy

for interfacial ice melting have attracted attentions[37, 132, 142-144]. One eye-catching example of these new surfaces, a so-called photothermal trap, was fabricated recently, which consisted of a trilaminar structure, namely a top solar radiation absorber layer for harvest illumination, a middle thermal spreader layer for lateral heat dispersal, and an insulator layer to minimize heat loss[37]. Through this design, the surfaces can efficiently convert solar energy to heat in the substrate. As shown in the Fig. 6d, the frozen droplets started sliding away in 19.8 s with illumination on the substrate with tilting angle 30°. Remarkably, the substrate took a short time of 0.5 s to generate a thin liquid layer after the start of interfacial ice melting. In outdoor ambient anti-icing tests, the substrate also exhibited highly encouraging anti-icing performance, with frozen droplets started sliding away in 30 s in solar illumination intensity of ~ 0.6 kW/m. With longer solar illumination time and intensity, dynamic anti-icing surfaces utilizing thermal energy for promoting ice removal not only melt the ice-substrate interfaces but also can melt the whole ice, which will be introduced in the following dynamic ice melting section.

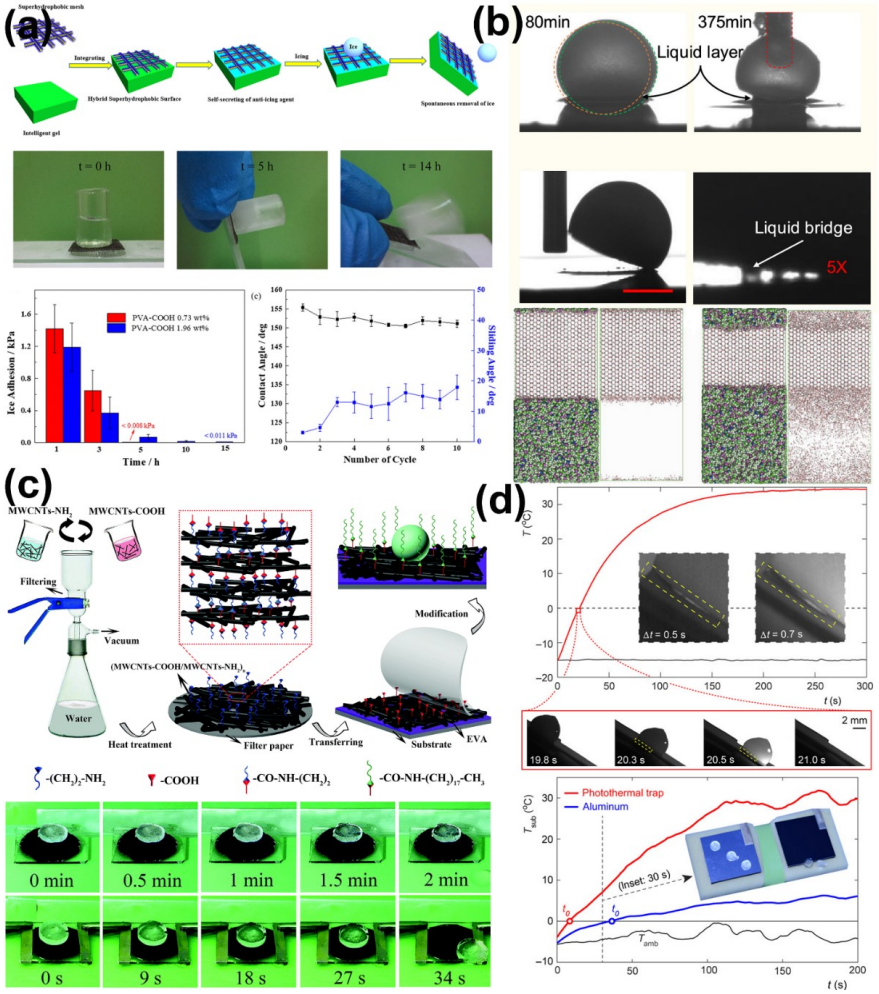

Figure 6. Representatives of the dynamic anti-icing surfaces through dynamic interface melting. (a) The hybrid superhydrophobic surfaces that dynamic secrete anti-icing agents. (b) The ionogel surfaces using ionic liquid for dynamic anti-icing, and their atomistic models of ice melting. (c) The superhydrophobic carbon nanotube surfaces with electrothermal effects. Real-time anti-icing testing experiments were showed in the figure. (d) The photothermal trap utilizes solar illumination for ice mitigation. Panels (a) and (b) were adapted with permission from Ref. 44 and 52, American Chemical Society. Panels (c) was adapted with permission from Ref. 48, Royal Society of Chemistry. Panel (d) was adapted with permission from Ref. 37, Science Publishing Group.

2.3 Novel interface generators

The durability, low ice adhesion and and extreme-low temperature applicability of anti-icing surfaces are three essential demands for practical applications. It is still challenging for the current dynamic anti-icing surfaces to meet all the three requirements. As discussed above, substrates that dynamically generate an interfacial aqueous lubricating layer can have improved durability thanks to lubricant regenerability[14, 25, 26]. However, for these anti-icing surfaces there is an exhaustion limit that the anti-freeze agents can secrete. When the concentration gradient of chemicals disappeared, the anti-freeze agent secretion stopped on these substrates, leading to poor long-term durability in icing/de-icing cycles. The anti-icing surfaces with photothermal effects also generally lost their icephobicity at temperature lower than -50 °C. Subsequently, the interfacial aqueous layers tend to freeze at certain low temperature, which led to a sharp and dramatic increase in ice adhesion strength. For instance, the ice adhesion on substrates with interfacial aqueous layer can increase from ~ 27 kPa to more than 400 kPa at temperature close to -60 °C[105]. For anti-icing at extremely low temperature, such as in environments like in the Arctic area, maintaining low ice adhesion on anti-icing surfaces is formidable. Fortunately, a strategy of generating interfacial liquid layer at extremely low temperature and addressing anti-icing in harsh environment was developed recently[34]. Instead of generation pure aqueous layer for lubrication, ethanol was selected as the lubricant at the ice-substrate interface because of its low freezing point of -115 °C, which guaranteed non-frozen lubricating effects at extreme temperature. As verified via the atomistic modeling and molecular dynamic simulation shown in Fig. 7a, ethanol layer as thin as 2 nm at the ice-substrate interface can maintain low ice adhesion -60 °C. In comparison, interfacial aqueous layer of the same thickness froze at much high temperature, resulting in loss of lubrication effect. Based on the theoretical study, two liquid layer generators (LLGs) that can dynamically generate ethanol layers at the ice-substrate interfaces were designed (Fig. 7b). The first LLG was fabricated by packing ethanol into the substrates, termed LLG-1, which can yield super-low ice adhesion of ~ 1 kPa (samples containing 40 vol% ethanol). Because the ethanol layer was dynamically secreted from the substrate, the LLG-1 had continuous decreases in ice adhesion strength for automatic de-icing. Specifically, ice adhered onto the LLG-1 was detached by gravity

in 3 hours in the related testing experiments. Most remarkably, the LLG-1 was showed to have ethanol secretion lifetime of at least 250 days at -20 °C (Fig. 7c). With more ethanol embedded in the substrate, the lifetime of ethanol secretion increased. For example, the LLG-1 sample with 40 vol% ethanol can have a long functioning lifespan of 593 days. In order to further extend the ethanol exhaustion time, a second LLG (LLG-2) with sub-porous layers was also design for the possibility of replenishing ethanol in the substrates, which featured the same outperforming anti-icing properties. The LLG-2 strategy was applied on various surfaces, including the contaminated ones with particles and other hydrophilic components. Surprisingly, the contaminated LLG-2 surfaces had super-low ice adhesion strength of ~ 10 kPa, which was expected to further decrease with increasing secreted ethanol layer. The most attractive properties of the LLGs were their unprecedented low ice adhesion strength at extremely low temperature (Fig. 7d). By introducing the ethanol lubricating layer at interfaces, the ice adhesion strength on the same surfaces decreased from 709.2 ~ 760.9 to 22.1 ~ 25.2 kPa at -60 °C, which indicats the LLGs as a viable candidate for anti-icing applications at harsh temperature. Thus, the LLGs are the first dynamic substrates that have the potential to meet the above-mentioned three anti-icing requirements intended for realistic applications.

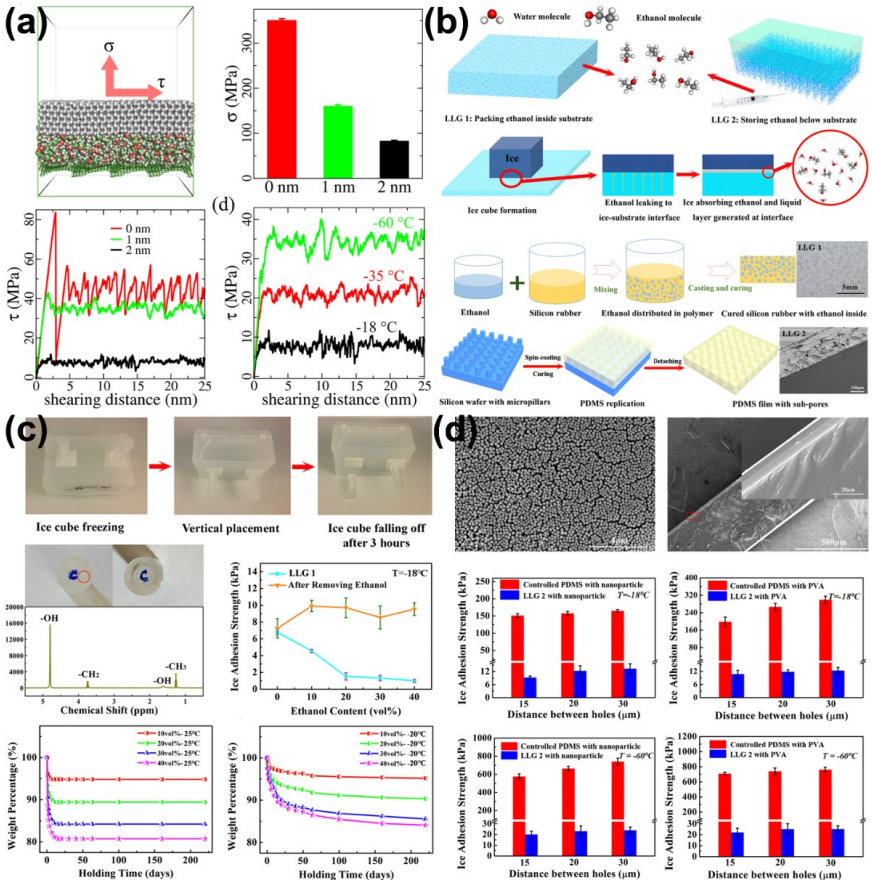

Figure 7. Representatives of the dynamic anti-icing surfaces through novel interface generators. (a) Interfacial ethanol layers of different thickness and their effects in reduction ice adhesion strength. (b) The design principles and fabricated samples of the LLGs. (c) The icephobicity and durability of LLG-1. (d) The icephobicity of LLG-2 with various surfaces and under extremely low temperature. Panels (a-d) were adapted with permission from Ref. 34, Royal Society of Chemistry.

2.4 Interfacial crack initiators

Dynamic interface change can also be a result of interfacial stress concentration. According to fracture mechanics, ice adhesion strength (τ_c) is governed by $\tau_c = \sqrt{E^* G/\pi a \Lambda}$, where G is the surface energy, E^* is the apparent bulk Young's modulus, a is the length of crack and Λ is a non-dimensional constant. Therefore, generating cracks at the ice-substrate interface is a promising approach for low ice adhesion. Following the fracture mechanics principle, surfaces containing crack initiators at the ice-substrate

interfaces were fabricated, which can enhance crack generation and efficiently reduce ice adhesion[14]. In order to promote the generation of cracks at the ice-substrate interface, three crack initiators on different length scales were first identified, namely nanoscale crack initiator (NACI) by surface atomistic and chemistry nature, microscale crack initiator (MICI) by the hierarchical surface structures and macroscale crack initiator (MACI) by interface stiffness inhomogeneity[14]. NACI underlies negative and weak affinity of a surface to ice and aids debonding at the ice-substrate interface, which is widely observed in hydrophobic surfaces used for anti-icing[101, 145, 146]. MICI can be taken as the micro-voids under the so-called "Cassie" ice on superhydrophobic surfaces and serve as micro-cracks for ice detachment from the surfaces[28, 147, 148]. Both NACI and MICI have their limitations for achieving super-low ice adhesion (defined as ice adhesion strength lower than 10 kPa)[14]. In contrast, MACI is the only crack initiator that can maximize crack size at macroscale length at the ice-substrate interfaces and predominantly facilitate easy ice removal[14]. As shown by finite element based simulation in Fig. 8a, porous sub-surface structures for MACI consists of significantly larger number of crack initiation sites along the ice-substrate interface than the cases with a homogenous substrate. Correspondingly, PDMS coatings with MACI showed super-low ice adhesion of 5.7 kPa, much lower than their counterparts, as the coating sketches and results showed in Fig. 8a.

The novel MACI mechanism enabled by sub-surface structures thus provided a new route for design icephobic surfaces. One low-cost yet effective fabrication strategy of realizing MACI was using sponge structure directly[149]. As shown in Fig. 8b, sugar was used as a sacrificial template for preparing sandwich-like PDMS-based sponge substrates. Because of the high porosity, the MACI effect of the sponge-type substrates was greatly enhanced. Furthermore, the elastic modulus of the sponge substrates was intrinsically low, which significantly contributed to the overall surface icephobicity. The PDMS sponges thus showed remarkable super-low ice adhesion strength of ~ 0.8 kPa and stable long-term ice adhesion strength of ~ 1 kPa after 25 icing/de-icing cycles.

Stiffness inhomogeneity in the substrate is the key to MACI. Other anti-icing substrates utilizing the surface stiffness inhomogeneity to achieve low ice adhesion can be considered to rely on the same mechanism of MACI. For example, stress-localized

surfaces for lowing ice adhesion were developed by surface inhomogeneity programming[39]. Specifically, the stress-localized surface contained two phases, phase I and phase II, as shown in Fig. 8c. The phase I was polymer with relative high elastic modulus, while the phase II was stress-localized materials with low elastic modulus. In such a setup, the phase II served as crack initiator, similar to pores in the PDMS-based sponge with MACI, for ice detachment under mechanical loading, which render the stress-localized surface one of the lowest ice adhesion strength reported so far (in the order of 1 kPa). It is worth noting that the stress-localized surface had excellent mechanical durability thanks to the high elastic modulus of phase I. The surfaces with 80 % phase II concentration showed stable long-term ice adhesion strength lower than 1 kPa after 100 icing/de-icing test, which made it a good candidate for applying in practical conditions to reduce ice adhesion on outdoor exposed surfaces.

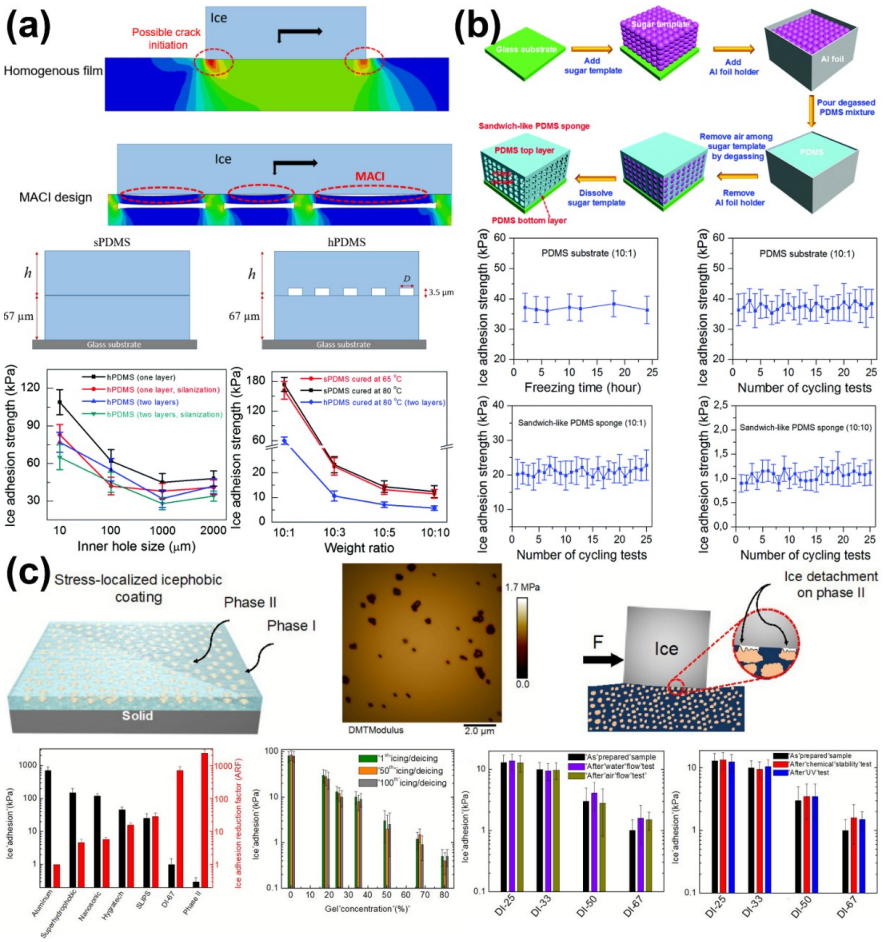

Figure 8. Representatives of the dynamic anti-icing surfaces through interfacial crack initiators. (a) The mechanism of multiscale crack initiator for super-low ice adhesion and their experimental results. (b) The fabrication of sandwich-like PDMS sponges with MACI and the resulting anti-icing performances. (c) The stress-localized surfaces and their ice adhesion testing results. Panels (a), (b) and (c) were adapted with permission from Ref. 14, 149 and 39, Royal Society of Chemistry.

3 Dynamic anti-icing surfaces through dynamic ice change

3.1 Effective ice growth inhibitors

Surface dynamic anti-icing strategies can also be applied on the ice directly. Natural organisms like insects, fishes and plants utilizing anti-freeze proteins (AFPs) to survive subzero temperature are the vivid examples[39, 150, 151]. AFPs can not only suppress freezing-point but also inhibit ice growth and recrystallization[152-156], thanks to their Janus

properties. All the AFPs have ice-binding faces (IBFs) and non-ice-binding faces (NIBFs)[157]. In solution, AFPs preferentially bound to any ice crystals with IBFs and leave the NIBF to liquid water, which results in micro-curvatures of ice-water interfaces. Due to the so-called Kevin effect, such curved ice-water interfaces inhibit ice growth[158]. Inspired by the discovery that ice growth was regulated by the AFPs absorption onto the basal/prism planes, novel materials featuring the same property of preferential binding to ice surfaces were discovered, including graphene oxide (GO), oxidized quasi-carbon nitride quantum dots (OQCNs), safranine molecules and so on[50, 159-165]. Although the ice growth in solutions containing these new materials were indeed inhibited, applying the same strategy on the design of anti-icing surfaces is at the early stage of development. AFPs was directly immobilized onto aluminum, which led to delayed frost/ice formation for at least 3 hours, showing significant anti-icing potential[166]. The binding faces of AFPs, IBFs and NIBFs, were screened for freezing-point depression, which indicated only the NIBFs decreased freezing temperature[47]. Despite that the related studies confirmed the potential of AFPs in ant-icing applications, more in-depth investigations are still needed for elucidating their effects on overall surface icephobicity. In outdoor environment, ice nucleation is inevitable due to low temperature, long icing time and surface contaminations. Once ice started to form on exposed surfaces, ice growth/propagation control was believed to be more important to tackle the ice accumulation problem and thus one important focus of anti-icing surface design[167-169].

Phase-switching liquids (PSLs) containing cyclohexane (SCh) were used for inhibiting ice growth, for their property of holding ice melting temperature (T_{mp}) above water freezing point (T_{fp})[170]. When vapor condensed on a solidified PSL surface, the latent heat released during the condensation was trapped in the droplets. The temperature increases at the solidified cyclohexane (SCh) and air interfaces could attain ≈ 5 °C. (Fig. 9a). The increased temperature thus led to melting of PSL in contacted region. By comparing the freezing initiation time and total freezing delaying time, PSL coated surfaces performed excellently in inhibiting ice growth. The best sample showed sustained ice growth delay for more than 96 h, which was 300 times longer than the superhydrophobic surfaces. The PSLs can also be infused into porous surfaces and form SLIPSs. The infused samples with 10 μm spacing microstructured (SG-10) surfaces can

dynamically inhibited the frost propagation for more than 140 min, which was around 7 times longer than lubricant infused surface (LIS). It should be noted that the reported PSL chemicals, such as benzene, were highly toxic. Other safe and environmentally friendly phase-switching liquids that have melting temperature close to the water freezing point still need to be further explored[35].

Counterions at the ice-substrate interface also can inhibit ice growth by dynamic melting[38, 171-173]. Poly([2-(methacryloyloxy)ethyl]trimethylammonium chloride)-Cl (PMETA-Cl) brush was synthesized on silicon wafers, which can accommodate different ions via ion exchange[171]. Brushed with counterions of Cl^-, ClO_4^-, PF_6^-, $TFSI^-$ and PFO^- were investigated, showing hydrophobicity $Cl^- < ClO_4^- < PF_6^- < TFSI^- < PFO^-$. It was found the ice propagation efficiently on the highly hydrated PMETA-Cl and PMETA-ClO_4 brushes, while much longer time were needed for ice form on brushes with counterions of PF_6^-, $TFSI^-$ and PFO^-. It was suspected the water molecules in the hydrophilic polymer brush (PMETA-Cl and PMETA-ClO_4) moved toward the ice growth fronts when freezing occurred and consequently promoted ice propagation. In contrast, brushes with PF_6^-, $TFSI^-$ and PFO^- counterions and higher hydrophobicity could result in “water depletion regions”, which reduced the freezable water molecules and suppressed ice propagation (Fig. 9b).

To understand the mechanism that control the ice propagation, ice propagation behaviors on polyelectrolyte multilayer (PEM) coated surfaces were investigated[51]. The PEMs are ideal for this purpose, because the outmost layers determine the surface properties and water concentrated only in the outside layer. Two types of PEMS, the Poly(sodium 4-styrenesulfonate)/poly(allylamine hydrochloride) (PSS/PAH) and the PSS/ poly(diallyldimethylammonium chloride) (PSS/PDAD) coatings were fabricated in the research by tuning the compositions of polyelectrolyte pairs during the layer-by-layer deposition. The PDAD has polyelectrolyte interacting more strongly with water in the outmost layer than that in the PAH. It was found that the ice propagation time on the PSS/PAH was two orders of magnitude longer than on the PSS/PDAD with same number of deposition layers. The ice propagation time can be tuned by simply change the composition of the outmost layers, but not by the number of deposition layers. Counterions and their concentration (Fig. 9b) also showed effects on ice inhibiting

performance on the PEMs. The results indicated that ice propagation can be inhibited by depressing the water molecules trapped in the outmost layer of polyelectrolyte coatings. More importantly, the ice growth inhibition properties of PEMs layer in real environment was also investigated in the related studies (Fig. 9c). With silver iodide aqueous droplets (AgI particle, 0.1 μL) placed on the PEMs acting as the artificial ice nuclei, the PSS/PAH samples were still able to delay ice propagated for 2700 s, demonstrating the robustness and wide applicability of their anti-icing performances.

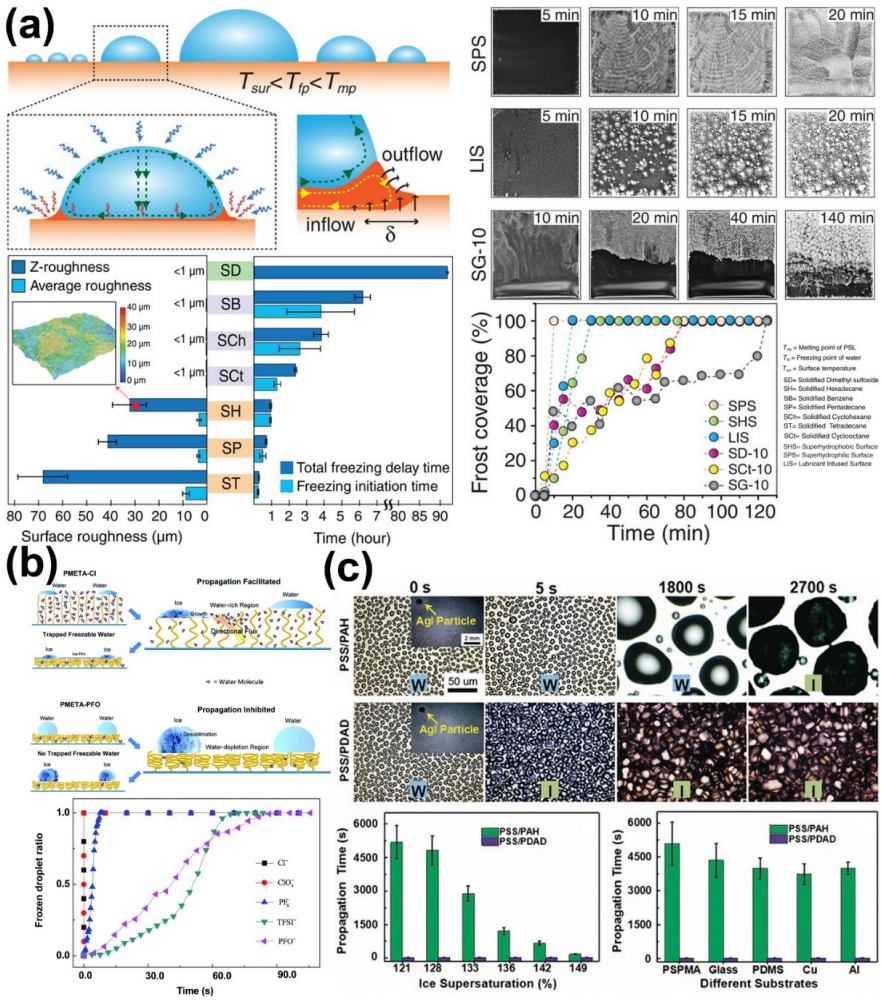

Figure 9. Representatives of the dynamic anti-icing surfaces through effective ice growth inhibitors. (a) Phase-switching liquids used for inhibiting ice growth, and their freezing delaying time. (b) Ion-

specific ice propagation on polyelectrolyte brush surfaces. (c) Ice propagation on polyelectrolyte multilayer surfaces, “W” and “I” are denoted as “water” and “ice”, respectively. Panels (a) was adapted with permission from Ref. 170, Wiley Publishing Group. Panels (b) was adapted with permission from Ref. 171, Royal Society of Chemistry. Panels (c) was adapted with permission from Ref. 51, Wiley Publishing Group.

3.2 Dynamic ice growth controlling

Controlling ice growth on a surface in a defined pattern can also be an effective approach to achieve icephobicity, given that ice formation is unavoidable after growth inhibition for a limited period of time. It was found that water droplets on superhydrophobic surfaces showed spontaneous levitation and trampoline-like bouncing behavior in a low-pressure environment[174]. Such phenomenon was caused by the overpressure beneath the droplet originated from fast vaporization and the countering surface adhesion restricting the vapor flow. Because strong vaporization led to high degree of cooling on a supercooled droplet, a rapid recalescence freezing was initiated at the free surface[169, 175]. The latent heat released in the freezing increased the droplet temperature to the equilibrium freezing temperature (0 °C). Under the low-pressure and low-humidity conditions such as in the condition of the experiment, a sudden increase in the vaporization of droplets surfaces resulted in rapid increasing in the overpressure beneath the droplet, which can lead to self-levitation of the droplet if freezing happened, meaning spontaneous-launching of ice. It was expected that this phenomenon can be observed on various surfaces with different textures, as shown in the Fig. 10a, suggesting the potential of controlling ice growth for spontaneous ice removal ice.

The freezing-driven ice-removal mechanism was further explored on various surfaces[53]. It was found that the key for self-dislodging of frozen droplets lied in the freezing orientating process. Specifically, the successful self-dislodging required free surface of the droplet be solidified first, forming an ice shell on the external surfaces while maintaining the droplet-substrate contacted region remained liquid. As the subsequent freezing phase boundary moved inward in the droplet asymmetrically, the volume of droplet expanded in the solidification and caused mass displacement toward the unsolidified droplet-substrate interface. On non-wetting surfaces with pinned ice-liquid-vapor contact line, the displaced mass had nowhere to spread in the final state of solidification and lifted the droplet upward. This dislodging process was observed on

various substrate with a wide range of wettability (from hydrophilic to superhydrophobic) and topography as shown in the Fig. 10b. Such self-dislodging behavior of frozen droplets provided a universal concept for design ice free surfaces through controlling asymmetric freezing dynamics with inward solidification. Although the above experiments were carried under low pressure, the self-dislodging brought insight into the freezing fundaments and inspired the further development of dynamic icephobic surfaces through controlling ice growth behaviors.

By controlling the multi-crystal ice growth pattern on the surfaces, another important surface design for novel dynamic ice repellency was also developed recently[13]. By depositing silver iodide (AgI) nanoparticles as ice nucleation active sites on surfaces, ice nucleation can be controlled to occur concurrently. It was found that the ice crystals on a hydrophilic surface (with water contact angle of 14.5°) underwent an along surface growth (ASG) mode. However, the ice on the hydrophobic surface (with water contact angle of 107.3°) exhibited an off-surface growth (OSG) mode (Fig. 10c). On the smooth surfaces, there is an ASG-to-OSG transition of ice growth mode at surface water contact angle of θ = 32.5° ± 1.9°. The ASG-to-OSG transition was also observed on porous surfaces at different water contact angle, suggesting the ubiquity of this behavior on various structured surfaces. The growth mode of ice crystals significantly affected the contact area ($A_{contact}$) between ice and its substrate, and subsequently the ice adhesion strength. In the OSG mode, the optimal $A_{contact}$ was only around 10 % of projected area ($A_{project}$). In contrast, the ASG mode resulted in almost full ice contact of the surface project area ($A_{contact}$ /$A_{project}$ ≈ 90%). In ice-removal tests, the OSG ice can be easily blown away by a wind breeze with velocity of 5.78 m/s at -3 °C, while the ASG ice remained firmly adhered on the surface.

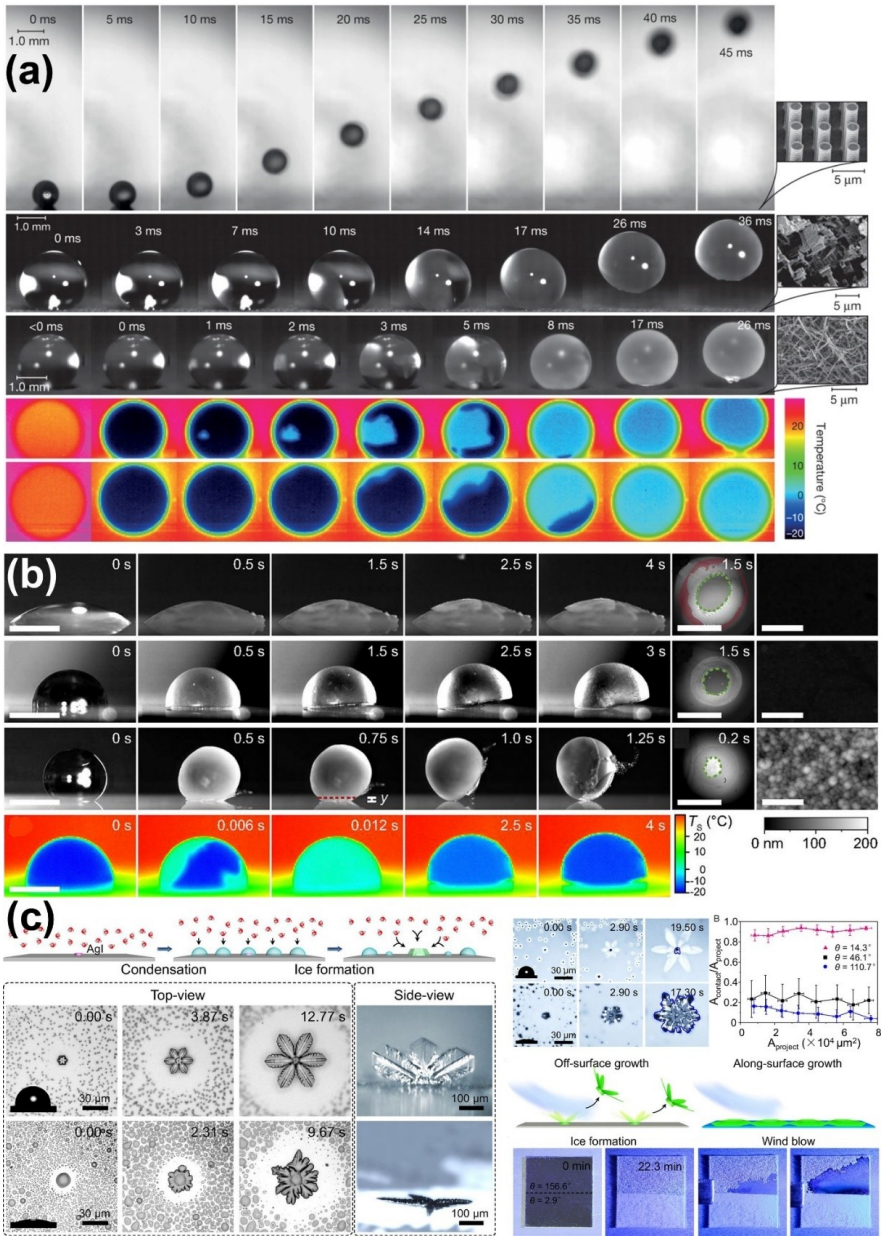

Figure 10. Representatives of the dynamic anti-icing surfaces through dynamic ice growth controlling. (a) Spontaneous droplet levitation in freezing from a wide range of surfaces under low-pressure and low-humidity conditions. (b) Self-dislodging behavior on hydrophilic, hydrophobic and superhydrophobic surfaces. (c) Ice growth pattern on surfaces with different wettability and their anti-icing performance. Panels (a) was adapted with permission from Ref. 174, Nature Publishing Group.

Panels (b) and (c) were adapted with permission from Ref. 53, and 13, National Academy of Sciences of the United States of America.

3.3 Ice-free zone programming

As the dynamic ice growth patterns are important for anti-icing, recent investigations further revealed that ice growth on the whole surfaces can be programmed through surfaces chemistry/structure deign[49, 176-178]. On surfaces fabricated by assembling poly(poly(ethylene glycol) methyl ether methacrylate)/polydimethylsiloxane (P(PEGMA)/(PDMS)) Janus particles, ice was found to grow into ice crystals/dendrites in certain regions, leaving other regions dry and clean[176]. The underlying mechanism of the distinct ice growth pattern on the Janus surfaces was elucidated, as depicted in Fig. 11a. For hydrophilic surface, water condensed into liquid film and formed continues frozen film. While on the hydrophobic surface, water droplets formed instead in condensation, which resulted in frozen droplets and ice bridges. The icing process on the Janus surfaces followed a unique process. Frist, condensed droplets froze inhomogeneously on the surface. Specifically, ice crystals emerged more likely in the large liquid droplets on the hydrophilic regions of the surface. The frozen droplets then affected the surrounding regions. Instead of freezing, the small droplets on the hydrophobic clusters around the frozen droplets disappeared through evaporation. Then, desublimation effect of vapor to ice assisted the further growth of already frozen droplets into dendrites, which ultimately led to building a dry band around the large frozen dendrites, namely ice-free zones. Because of the ice-free zones and small ice contact area, the Janus surfaces exhibited low ice adhesion strength of 56 kPa.

The guided ice growth pattern on Janus surfaces suggested that surfaces chemistry design could dynamically create ice-free zone. However, the locations of ice-free zones on a surface were mostly random. In a recent report, ordered and large scale ice-free zones taking up ~ 96 % of the entire surface area were programmed and created on surfaces with patterned polyelectrolyte[177]. On these patterned surfaces, icing was designed to initiate from the polyelectrolyte domains and propagated atop, as shown in Fig. 11b. The condensation of vapor into water droplets on the polyelectrolyte released latent heat, which led to significant temperature increase atop the substrate close to the frozen droplets. This freezing-driven thermal effect resulted in further water evaporation

around the frozen droplets. Because the saturated vapor pressure of water droplets is higher than ice, the newly formed ice was guided to grow exclusively on the patterned polyelectrolyte domains through desublimation[51, 109, 157, 171]. In contrast, ice growth at the ice-free zone was inhibited. Thus, ice accumulated on the frozen area was accompanied by the consumption of condensed droplets and resulted in the continuous expansion of ice-free zone. It was showed in the experiments that the fraction of ice-free region could be tuned by the grafting density and pattern of polyelectrolyte brushes. By using polyelectrolyte multilayer and polyelectrolyte hydrogel for patterning surfaces, ice-free regions occupying ~ 96 % and ~ 88% of the total surface area can be achieved, respectively.

Besides patterning in surface chemistry, micro-structure can also be utilized for programming ice-free zone on surfaces. As shown in the Fig. 11c, precisely designed micro-patterned surfaces were used for programing ice growth with an interesting and motivating aim of using ice to fight ice[178]. The unique feature of such surfaces was introducing water into microstripes on the surface. Under cooling, the water stripes on the surface froze firstly, serving as frozen regions. The formation of ice-free and dry area on the surface followed the same process as discussed above, which led to as high as 90 % percent of the total surface area as dry-zone (or ice-free zone). Interestingly, it was found that the growth rate of frost on the ice-stripes was one order of magnitude lower than on the smooth solids. In short, the pre-frozen ice pattern not only protected the other region from icing but also slowed down ice propagation.

Natural surfaces like certain tree leaves can also program ice formation in winter[41, 177], namely ice accumulation on convex veins is more significant than flat zones. Inspired by such phenomena, artificial leaves with ice-free regions were designed recently[49]. The micro-textures on the artificial leaves can result in large scale ice-free area without pre-designed water/ice stripes, affecting both water condensation and ice formation on the surface. As water molecules in a supersaturated ambient air diffused more easily to the peaks than to the valleys, the artificial leaves accumulated more and larger droplets on top of its micro-texture, where the freezing of droplets initiated at lower temperature. After ice formation on the peaks of the micro-textures, the low vapor pressure led to the evaporation of droplets from and created stable ice free zone in the valleys as shown in

Fig. 11d. Combining the experiments and simulation, an important structure parameters α, namely the vertex angle, was proposed to quantitatively correlate to the percentage of ice-free regions and the micro-texture on the surface. The relationship between α and frost coverage were mapped under various ambient humidity, providing significant instructions for constructing ice-free regions through surface structure fabrication.

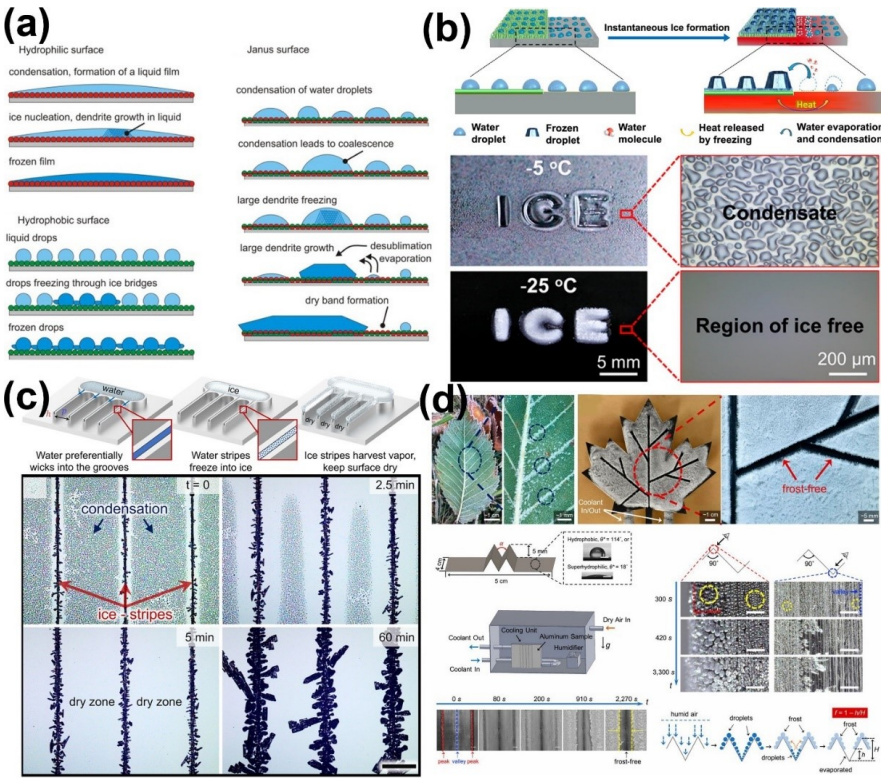

Figure 11. Representatives of the dynamic anti-icing surfaces through ice-free zone programming. (a) Ice formation mechanism on rough hydrophilic, hydrophobic, and Janus surfaces. (b) Patterned polyelectrolyte coatings for dynamic controlling large scale ice-free region. (c) Dynamic anti-icing surfaces using microscopic ice patterns. (d) Micro-textured surfaces with capacity of dynamic forming ice-free zone. Panels (a), (b) and (c) were adapted with permission from Ref. 176, 177 and 178, American Chemical Society. Panels (d) was adapted with permission from Ref. 49, National Academy of Sciences of the United States of America.

3.4 Dynamic ice melting

Ice melting on anti-icing surfaces is another important aspect of dynamic ice change for avoiding unwanted ice accumulation. The dynamic ice melting surfaces were created

by integrating materials with thermal effects, including electrothermal, near-infrared photothermal, magnetothermal and solar photothermal effects[133, 144, 179, 180].

The use of electrothermal effect for tackling icing problems had a long history. In the last decades, numerous active anti-icing surfaces with additive electrothermal effects were developed, which consumed electrical energy for dynamic ice melting[181-186]. Passive icephobic surfaces, such superhydrophobic and the SLIPS surfaces, can also integrate active thermal effects for anti-icing, as introduced in the dynamic interface melting surfaces section above. By enhancing the power density on such surface, ice can be dynamically and constantly melted at the ice-substrate interface until being fully consumed. Recently, a so-called slippery liquid infused porous electric heating coating (SEHC) was prepared, which contained MWCNTs as electrothermal generators[133]. The SEHC also contained lubricating oil with high thermal conductivity that enabled reduction of ice adhesion strength from 1940 to ~ 58 kPa. The obvious advantage of using SEHC instead of superhydrophobic surface was the thermal conductivity of the lubricant, which was nearly one order of magnitude higher than that of air and thus also higher electrothermal efficiency. The SEHC could melt ice on the surface completely with power density 0.58 W/cm^2, showing significant reduction from 0.65 W/cm^2 on superhydrophobic surfaces (Fig. 12a). In another study, the lubricant infused surfaces were integrated with near-infrared photothermal effect for dynamic melting ice[179]. The lubricant infused film (LF) on the surfaces showed much lower ice adhesion strength of ~ 25 kPa than that of surfaces with smooth film (SF, ~ 506 kPa). Surfaces with embedded Fe_3O_4 nanoparticles (0.5 wt%) into the substrate was prepared for melting surface ice. The temperature of such surfaces can increase for more than 50 ℃ in 10 s under irradiation, owing to the excellent near-infrared thermal response of the Fe_3O_4 nanoparticles. In an ice melting test, the ice layer on the surface was melted in 4 s with ambient temperature below -5 ℃ (Fig. 12b). The Fe_3O_4 nanoparticles were not only good medium for photothermal generation, but also possessed excellent magnetic-thermal effects. Superhydrophobic coatings containing Fe_3O_4 nanoparticles can dynamic melting ice under magnetic field and sunlamp irradiation (Fig. 12c) [180]. Under a magnetic field of 7.8 kW, the hybrid surface containing 50 wt% Fe_3O_4 nanoparticles showed an increase in temperature of ~ 21 ℃ in 25 s. At the meantime, the same surface under sunlamp

irradiation (75 W) increased 13 ℃ in 5 min.

The dynamic ice melting surfaces described above by using electric power, near-infrared irradiation and magnetic field were attractive. However, their approaches are partially active and thus can be costly. The photothermal trap surfaces that used solar irradiation energy for ice melting were outstanding candidates and have raised great interests[37, 132, 142-144, 187, 188]. Despite the complex design, these novel surfaces introduced in the dynamic interface melting was efficient. For instance, superhydrophobic icephobic surfaces with photothermal effects by using cheap candle soot was newly fabricated[144]. Because of the hierarchical structure and the black color, the candle soot has excellent photothermal conversion efficiency[189-195]. As shown in the Fig. 12d, the candle soot coated surfaces possessed combined properties of robust superhydrophobicity and highly efficient light trapping, which enable surface temperature increase of ~ 53 ℃ under 1 sun illumination (1 kW/m^2). In a frost melting test at -30 ℃, the accumulated frost started melt after illuminating 60 s and the surface was free of ice in 720 s, demonstrating superior dynamic ice melting performances.

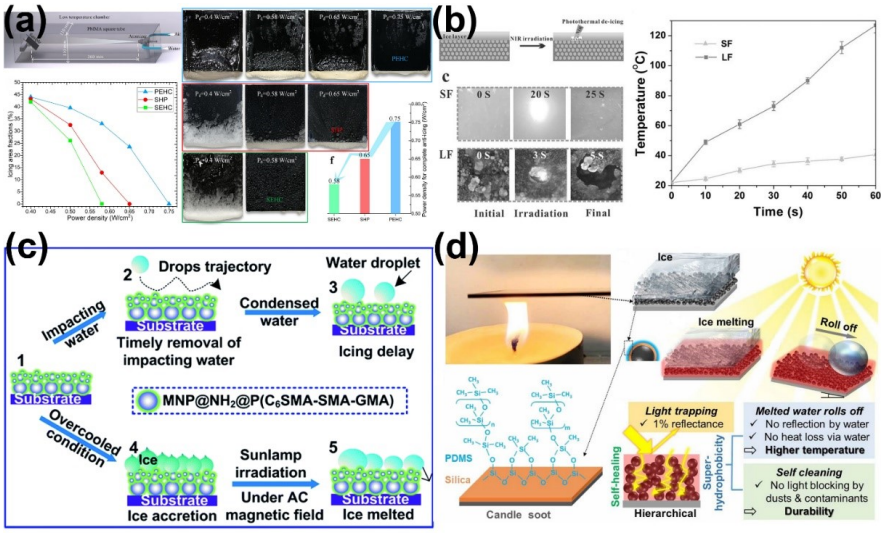

Figure 12. Representatives of the dynamic anti-icing surfaces through dynamic ice melting. (a) Dynamic anti-icing performance of SLIPS combined with electrothermal effect. (b) Integrating self-lubrication and near-infrared photothermal generation for dynamic ice melting. (c) Magnetic particles based superhydrophobic surface for ice melting. (d) Superhydrophobic photothermal icephobic surfaces based on candle soot. Panels (a) was adapted with permission from Ref. 133, Elsevier Publishing Group.

Panels (b) was adapted with permission from Ref. 179, Wiley Publishing Group. Panels (c) was adapted with permission from Ref. 180, Royal Society of Chemistry. Panels (d) was adapted with permission from Ref. 144, National Academy of Sciences of the United States of America.

4. Conclusion perspectives

Unwanted icing is one of the major unsolved problems accompanying mankind in the whole civilization history. It is unfortunate that the most common ways utilized today to combat icing are still the traditional de-icing methodologies involved direct mechanical forces, energy-intense thermal treatments or heavily chemical handling. Despite that the passive anti-icing concept has been proposed for more than a decade, automatic de-icing on application scale or at any industrial technology readiness level is still not available. Nevertheless, there are significant successes in the anti-icing materials related researches, especially on the super-low ice adhesion surfaces that enabling natural forces for effective de-icing. Although challenges such as durability, contamination, extreme temperature and harsh conditions need to be addressed, the up-scale of such anti-icing surfaces from laboratory do promise a bright future. Given the abundant research results on anti-icing materials, the understanding of the icing problem also needs to update. Regarding ice formation on a surface, it is crucial to recognize the dynamic properties of the ice-substrate interface on any surfaces. The dynamic properties can have a long time-span or need to respond to external stimuli to be revealed, which yet can be high beneficial for de-icing. For instance, ice adhesion on the liquid layer generators and other surfaces that secrete interfacial lubricant and constantly decrease to a negligible level with time, provided ample lubricants were embedded in the substrates. As such, automatic de-icing can be realized even in the outdoor environment if the functionality life-time of such surfaces is further enhanced. Several anti-icing surfaces have combined external energy inputs in design. It is fair to say that energy input from solar illumination is most favorable and sustainable choice. Such surfaces still have relatively low power density or suffer from critical environmental limitation such extremely low temperature, which deserves continues research effort in the future research. Last but not least, the rational structure-property-function relationship in the current anti-icing surfaces is missing. It is certainly difficult to establish this relationship given that approaches to realize surface icephobicity vary greatly as well as a wide variety of materials have been selected for surface fabrication. More theoretical researches on dynamic anti-icing surfaces should be

promoted, including atomistic modeling and simulation, and multiscale approaches. Based on the current fast evolving status of anti-icing research, the society can hold an optimistic attitude on unwanted icing and expect practical passive dynamics anti-icing surfaces in a very near future.

Conflicts of interest

There are no conflicts to declare.

Acknowledgements

The Research Council of Norway is acknowledged for the support to the FRINATEK project Towards Design of Super-Low Ice Adhesion Surfaces (SLICE, 250990), and the PETROMAKS 2 project Durable Arctic Icephobic Materials (AIM, 255507).

References

1. Y. Cao, W. Tan and Z. Wu, *Aerospace science and technology*, 2018, **75**, 353-385.
2. H. Yi, *High Voltage Engineering*, 2008, **2**, 002.
3. X.-l. Jiang, J. Ma, S.-h. Wang, C.-x. SUN and L.-c. SHU, *Electric Power*, 2005, **38**, 27-30.
4. T. Cebeci and F. Kafyeke, *Annual review of fluid mechanics*, 2003, **35**, 11-21.
5. X. Jiang, L. Shu, W. Sima, S. Xie, J. Hu and Z. Zhang, *International Journal of Offshore and Polar Engineering*, 2004, **14**.
6. W. Yu, Y. Lai, W. Bai, X. Zhang, D. S. Zhuang, Q. Li and J. Wang, *Cold regions science and technology*, 2005, **42**, 79-88.
7. A. K. Andersson and L. Chapman, *Accident Analysis & Prevention*, 2011, **43**, 284-289.
8. A. Dehghani-Sanij, S. Dehghani, G. Naterer and Y. Muzychka, *Ocean Engineering*, 2017, **132**, 25-39.
9. J. M. Pinar-Pérez and F. P. G. Márquez, in *Renewable Energies*, Springer, 2018, pp. 97-109.
10. D. L. Kelting and C. L. Laxon, *Review of effects and costs of road de-icing with recommendations for winter road management in the Adirondack Park*, Adirondack Watershed Institute., 2010.

11. L. Mishchenko, B. Hatton, V. Bahadur, J. A. Taylor, T. Krupenkin and J. Aizenberg, *ACS nano*, 2010, **4**, 7699-7707.
12. P. Tourkine, M. Le Merrer and D. Quéré, *Langmuir*, 2009, **25**, 7214-7216.
13. J. Liu, C. Zhu, K. Liu, Y. Jiang, Y. Song, J. S. Francisco, X. C. Zeng and J. Wang, *Proceedings of the National Academy of Sciences*, 2017, **114**, 11285-11290.
14. Z. He, S. Xiao, H. Gao, J. He and Z. Zhang, *Soft matter*, 2017, **13**, 6562-6568.
15. S. Kulinich and M. Farzaneh, *Langmuir*, 2009, **25**, 8854-8856.
16. A. J. Meuler, G. H. McKinley and R. E. Cohen, *ACS nano*, 2010, **4**, 7048-7052.
17. S. Jung, M. Dorrestijn, D. Raps, A. Das, C. M. Megaridis and D. Poulikakos, *Langmuir*, 2011, **27**, 3059-3066.
18. S. Kulinich, S. Farhadi, K. Nose and X. Du, *Langmuir*, 2011, **27**, 25-29.
19. A. Gauthier, S. Symon, C. Clanet and D. Quéré, *Nature communications*, 2015, **6**, 1-6.
20. T.-S. Wong, S. H. Kang, S. K. Tang, E. J. Smythe, B. D. Hatton, A. Grinthal and J. Aizenberg, *Nature*, 2011, **477**, 443-447.
21. P. Kim, T.-S. Wong, J. Alvarenga, M. J. Kreder, W. E. Adorno-Martinez and J. Aizenberg, *ACS nano*, 2012, **6**, 6569-6577.
22. P. W. Wilson, W. Lu, H. Xu, P. Kim, M. J. Kreder, J. Alvarenga and J. Aizenberg, *Physical Chemistry Chemical Physics*, 2013, **15**, 581-585.
23. Q. Liu, Y. Yang, M. Huang, Y. Zhou, Y. Liu and X. Liang, *Applied Surface Science*, 2015, **346**, 68-76.
24. S. B. Subramanyam, K. Rykaczewski and K. K. Varanasi, *Langmuir*, 2013, **29**, 13414-13418.
25. K. Golovin, S. P. Kobaku, D. H. Lee, E. T. DiLoreto, J. M. Mabry and A. Tuteja, *Science advances*, 2016, **2**, e1501496.
26. K. Golovin and A. Tuteja, *Science advances*, 2017, **3**, e1701617.
27. K. Golovin, A. Dhyani, M. Thouless and A. Tuteja, *Science*, 2019, **364**, 371-375.
28. K. K. Varanasi, T. Deng, J. D. Smith, M. Hsu and N. Bhate, *Applied Physics Letters*, 2010, **97**, 234102.
29. S. Farhadi, M. Farzaneh and S. Kulinich, *Applied Surface Science*, 2011, **257**, 6264-6269.

30. Y. Wang, J. Xue, Q. Wang, Q. Chen and J. Ding, *ACS applied materials & interfaces*, 2013, **5**, 3370-3381.
31. C. Howell, T. L. Vu, C. P. Johnson, X. Hou, O. Ahanotu, J. Alvarenga, D. C. Leslie, O. Uzun, A. Waterhouse and P. Kim, *Chemistry of Materials*, 2015, **27**, 1792-1800.
32. J. S. Wexler, I. Jacobi and H. A. Stone, *Physical review letters*, 2015, **114**, 168301.
33. K. Rykaczewski, S. Anand, S. B. Subramanyam and K. K. Varanasi, *Langmuir*, 2013, **29**, 5230-5238.
34. F. Wang, S. Xiao, Y. Zhuo, W. Ding, J. He and Z. Zhang, *Materials Horizons*, 2019, **6**, 2063-2072.
35. F. Wang, W. Ding, J. He and Z. Zhang, *Chemical Engineering Journal*, 2019, **360**, 243-249.
36. Y. Zhuo, V. Håkonsen, Z. He, S. Xiao, J. He and Z. Zhang, *ACS applied materials & interfaces*, 2018, **10**, 11972-11978.
37. S. Dash, J. de Ruiter and K. K. Varanasi, *Science advances*, 2018, **4**, eaat0127.
38. Z. He, C. Wu, M. Hua, S. Wu, D. Wu, X. Zhu, J. Wang and X. He, *Matter*, 2020.
39. P. Irajizad, A. Al-Bayati, B. Eslami, T. Shafquat, M. Nazari, P. Jafari, V. Kashyap, A. Masoudi, D. Araya and H. Ghasemi, *Materials Horizons*, 2019, **6**, 758-766.
40. Y. Zhuo, F. Wang, S. Xiao, J. He and Z. Zhang, *ACS omega*, 2018, **3**, 10139-10144.
41. Y. Wang, X. Yao, S. Wu, Q. Li, J. Lv, J. Wang and L. Jiang, *Advanced Materials*, 2017, **29**, 1700865.
42. C. Urata, G. J. Dunderdale, M. W. England and A. Hozumi, *Journal of Materials Chemistry A*, 2015, **3**, 12626-12630.
43. M. Liu, Y. Ru, R. Fang, Z. Gu and L. Jiang, *Angewandte Chemie International Edition*, 2020, **n/a**.
44. F. Liu, Z. Wang and Q. Pan, *ACS Sustainable Chemistry & Engineering*, 2019.
45. F. Giuliani, F. Merusi, G. Polacco, S. Filippi and M. Paci, *Construction and Building Materials*, 2012, **30**, 174-179.
46. D. Chen, M. D. Gelenter, M. Hong, R. E. Cohen and G. H. McKinley, *ACS applied materials & interfaces*, 2017, **9**, 4202-4214.

47. K. Liu, C. Wang, J. Ma, G. Shi, X. Yao, H. Fang, Y. Song and J. Wang, *Proceedings of the National Academy of Sciences*, 2016, **113**, 14739-14744.
48. X. Su, H. Li, X. Lai, Z. Yang, Z. Chen, W. Wu and X. Zeng, *Journal of Materials Chemistry A*, 2018, **6**, 16910-16919.
49. Y. Yao, T. Y. Zhao, C. Machado, E. Feldman, N. A. Patankar and K.-C. Park, *Proceedings of the National Academy of Sciences*, 2020, **117**, 6323-6329.
50. H. Geng, X. Liu, G. Shi, G. Bai, J. Ma, J. Chen, Z. Wu, Y. Song, H. Fang and J. Wang, *Angewandte Chemie International Edition*, 2017, **56**, 997-1001.
51. Y. Jin, Z. He, Q. Guo and J. Wang, *Angewandte Chemie International Edition*, 2017, **56**, 11436-11439.
52. Y. Zhuo, S. Xiao, V. Håkonsen, J. He and Z. Zhang, *ACS Materials Letters*, 2020.
53. G. Graeber, T. M. Schutzius, H. Eghlidi and D. Poulikakos, *Proceedings of the National Academy of Sciences*, 2017, **114**, 11040-11045.
54. H. Zhao, Q. Sun, X. Deng and J. Cui, *Advanced Materials*, 2018, **30**, 1802141.
55. X. Sun, V. G. Damle, S. Liu and K. Rykaczewski, *Advanced Materials Interfaces*, 2015, **2**, 1400479.
56. J. Cui, D. Daniel, A. Grinthal, K. Lin and J. Aizenberg, *Nature materials*, 2015, **14**, 790-795.
57. D. Bonn, J. Eggers, J. Indekeu, J. Meunier and E. Rolley, *Reviews of modern physics*, 2009, **81**, 739.
58. G. Chen, S. Liu, Z. Sun, S. Wen, T. Feng and Z. Yue, *Progress in Organic Coatings*, 2020, **144**, 105641.
59. J. H. Kim, M. J. Kim, B. Lee, J. M. Chun, V. Patil and Y.-S. Kim, *Applied Surface Science*, 2020, **512**, 145728.
60. T. Li, Y. Zhuo, V. Håkonsen, S. Rønneberg, J. He and Z. Zhang, *Coatings*, 2019, **9**, 602.
61. A. Sandhu, O. J. Walker, A. Nistal, K. L. Choy and A. J. Clancy, *Chemical communications*, 2019, **55**, 3215-3218.
62. E. Tetteh and E. Loth, *Coatings*, 2020, **10**, 262.
63. Y. Wang, X. Yao, J. Chen, Z. He, J. Liu, Q. Li, J. Wang and L. Jiang, *Science China Materials*, 2015, **58**, 559-565.

64. Y. H. Yeong, A. Milionis, E. Loth and J. Sokhey, *Cold Regions Science and Technology*, 2018, **148**, 29-37.
65. J. Zhang, B. Liu, Y. Tian, F. Wang, Q. Chen, F. Zhang, H. Qian and L. Ma, *Coatings*, 2020, **10**, 119.
66. L. Zhu, J. Xue, Y. Wang, Q. Chen, J. Ding and Q. Wang, *ACS applied materials & interfaces*, 2013, **5**, 4053-4062.
67. X. Zhu, J. Lu, X. Li, B. Wang, Y. Song, X. Miao, Z. Wang and G. Ren, *Industrial & Engineering Chemistry Research*, 2019, **58**, 8148-8153.
68. W. Cui and T. A. Pakkanen, *Applied Surface Science*, 2020, **504**, 144061.
69. T. Ghosh and N. Karak, *Journal of colloid and interface science*, 2019, **540**, 247-257.
70. Y. Li, B. Li, X. Zhao, N. Tian and J. Zhang, *ACS applied materials & interfaces*, 2018, **10**, 39391-39399.
71. J.-F. Su, Y.-D. Guo, X.-M. Xie, X.-L. Zhang, R. Mu, Y.-Y. Wang and Y.-Q. Tan, *Construction and Building Materials*, 2019, **224**, 671-681.
72. Y. Zhuo, S. Xiao, V. Håkonsen, T. Li, F. Wang, J. He and Z. Zhang, *Applied Materials Today*, 2020, **19**, 100542.
73. C. Urata, R. Hönes, T. Sato, H. Kakiuchida, Y. Matsuo and A. Hozumi, *Advanced Materials Interfaces*, 2019, **6**, 1801358.
74. L. C. Liston, Y. Farnam, M. Krafcik, J. Weiss, K. Erk and B. Y. Tao, *Applied Thermal Engineering*, 2016, **96**, 501-507.
75. X. Zhou, G. Kastiukas, C. Lantieri, P. Tataranni, R. Vaiana and C. Sangiorgi, *Materials*, 2018, **11**, 1398.
76. K. Zhu, X. Li, J. Su, H. Li, Y. Zhao and X. Yuan, *Polymer Engineering & Science*, 2018, **58**, 973-979.
77. P. Irajizad, M. Hasnain, N. Farokhnia, S. M. Sajadi and H. Ghasemi, *Nature communications*, 2016, **7**, 1-7.
78. A. Masoudi, P. Irajizad, N. Farokhnia, V. Kashyap and H. Ghasemi, *ACS applied materials & interfaces*, 2017, **9**, 21025-21033.
79. Q. Rao, J. Zhang, X. Zhan, F. Chen and Q. Zhang, *Journal of Materials Chemistry A*, 2020.

80. R. Wang, S. Hong, X. Huang and H. Liu, *Materials Research Express*, 2019, **6**, 055035.
81. D. Wu, L. Ma, F. Zhang, H. Qian, B. Minhas, Y. Yang, X. Han and D. Zhang, *Materials & Design*, 2020, **185**, 108236.
82. T.-C. Ling and C.-S. Poon, *Construction and Building Materials*, 2013, **46**, 55-62.
83. L. Liston, M. Krafcik, Y. Farnam, B. Tao, K. Erk and J. Weiss, *Toward the use of phase change materials (PCM) in concrete pavements: Evaluation of thermal properties of PCM*, 2014.
84. A. R. Sakulich and D. P. Bentz, *Construction and Building Materials*, 2012, **35**, 483-490.
85. B. T. Worrell, M. K. McBride, G. B. Lyon, L. M. Cox, C. Wang, S. Mavila, C.-H. Lim, H. M. Coley, C. B. Musgrave and Y. Ding, *Nature communications*, 2018, **9**, 1-7.
86. G. Wang, T. Peng, S. Zhang, J. Wang, X. Wen, H. Yan, L. Hu and L. Wang, *RSC Advances*, 2015, **5**, 28344-28348.
87. W. Xi, H. Peng, A. Aguirre-Soto, C. J. Kloxin, J. W. Stansbury and C. N. Bowman, *Macromolecules*, 2014, **47**, 6159-6165.
88. B. Shang, M. Chen and L. Wu, *ACS applied materials & interfaces*, 2018, **10**, 31777-31783.
89. Y. Zhuo, T. Li, F. Wang, V. Håkonsen, S. Xiao, J. He and Z. Zhang, *Soft matter*, 2019, **15**, 3607-3611.
90. S. Xiao, B. H. Skallerud, F. Wang, Z. Zhang and J. He, *Nanoscale*, 2019, **11**, 16262-16269.
91. S. Choi, T.-w. Kwon, A. Coskun and J. W. Choi, *Science*, 2017, **357**, 279-283.
92. K. Ito, *Polymer journal*, 2012, **44**, 38-41.
93. R. Rosenberg, *Physics Today*, 2005, **58**, 50.
94. M. Faraday, *Proceedings of the Royal Society of London*, 1860, 440-450.
95. J. T. Bottomley, *Journal*, 1872.
96. J. Thomson, *Proceedings of the Royal Society of London*, 1862, 198-204.
97. F. P. Bowden and T. Hughes, *Proceedings of the Royal Society of London. Series A. Mathematical and Physical Sciences*, 1939, **172**, 280-298.

98. G. Malenkov, *Journal of Physics: Condensed Matter*, 2009, **21**, 283101.
99. S. Schöder, H. Reichert, H. Schröder, M. Mezger, J. Okasinski, V. Honkimäki, J. Bilgram and H. Dosch, *Physical review letters*, 2009, **103**, 095502.
100. S. Engemann, H. Reichert, H. Dosch, J. Bilgram, V. Honkimäki and A. Snigirev, *Physical review letters*, 2004, **92**, 205701.
101. S. Xiao, J. He and Z. Zhang, *Nanoscale*, 2016, **8**, 14625-14632.
102. T. Y. Zhao, P. R. Jones and N. A. Patankar, *Scientific reports*, 2019, **9**, 1-12.
103. S. Xiao, J. He and Z. Zhang, *Acta Mechanica Solida Sinica*, 2017, **30**, 224-226.
104. P. Eberle, M. K. Tiwari, T. Maitra and D. Poulikakos, *Nanoscale*, 2014, **6**, 4874-4881.
105. R. Dou, J. Chen, Y. Zhang, X. Wang, D. Cui, Y. Song, L. Jiang and J. Wang, *ACS applied materials & interfaces*, 2014, **6**, 6998-7003.
106. J. Chen, Z. Luo, Q. Fan, J. Lv and J. Wang, *Small*, 2014, **10**, 4693-4699.
107. Y. Marcus, *Chemical reviews*, 2009, **109**, 1346-1370.
108. S. Chernyy, M. Jarn, K. Shimizu, A. Swerin, S. U. Pedersen, K. Daasbjerg, L. Makkonen, P. Claesson and J. Iruthayaraj, *ACS applied materials & interfaces*, 2014, **6**, 6487-6496.
109. Z. He, W. J. Xie, Z. Liu, G. Liu, Z. Wang, Y. Q. Gao and J. Wang, *Science advances*, 2016, **2**, e1600345.
110. B. Liang, G. Zhang, Z. Zhong, Y. Huang and Z. Su, *Langmuir*, 2018, **35**, 1294-1301.
111. S. Wooh and D. Vollmer, *Angewandte Chemie International Edition*, 2016, **55**, 6822-6824.
112. P. Liu, H. Zhang, W. He, H. Li, J. Jiang, M. Liu, H. Sun, M. He, J. Cui and L. Jiang, *ACS nano*, 2017, **11**, 2248-2256.
113. M. Boban, K. Golovin, B. Tobelmann, O. Gupte, J. M. Mabry and A. Tuteja, *ACS applied materials & interfaces*, 2018, **10**, 11406-11413.
114. L. Zhang, Z. Guo, J. Sarma and X. Dai, *ACS Applied Materials & Interfaces*, 2020, **12**, 20084-20095.
115. J. Chen, R. Dou, D. Cui, Q. Zhang, Y. Zhang, F. Xu, X. Zhou, J. Wang, Y. Song and L. Jiang, *ACS applied materials & interfaces*, 2013, **5**, 4026-4030.
116. J. Chen, K. Li, S. Wu, J. Liu, K. Liu and Q. Fan, *ACS omega*, 2017, **2**, 2047-2054.

117. C. Li, X. Li, C. Tao, L. Ren, Y. Zhao, S. Bai and X. Yuan, *ACS applied materials & interfaces*, 2017, **9**, 22959-22969.
118. C. Tao, S. Bai, X. Li, C. Li, L. Ren, Y. Zhao and X. Yuan, *Progress in Organic Coatings*, 2018, **115**, 56-64.
119. Y. Yu, B. Jin, M. I. Jamil, D. Cheng, Q. Zhang, X. Zhan and F. Chen, *ACS applied materials & interfaces*, 2019, **11**, 12838-12845.
120. Z. He, Y. Zhuo, F. Wang, J. He and Z. Zhang, *Progress in Organic Coatings*, 2020, **147**, 105737.
121. F. Li and Z. Wang, *Journal of Highway and Transportation Research and Development (English Edition)*, 2012, **6**, 11-17.
122. Z. Liu, M. Xing, S. Chen, R. He and P. Cong, *Construction and Building Materials*, 2014, **51**, 133-140.
123. Z. Liu, S. Chen, R. He, M. Xing, Y. Bai and H. Dou, *Journal of Materials in Civil Engineering*, 2015, **27**, 04014180.
124. Z. Liu, A. Sha, M. Xing and Z. Li, *Cold Regions Science and Technology*, 2015, **114**, 9-14.
125. S. Luo and X. Yang, *Construction and Building Materials*, 2015, **94**, 494-501.
126. O. Xu, S. Han, C. Zhang, Y. Liu, F. Xiao and J. Xu, *Construction and Building Materials*, 2015, **98**, 671-677.
127. M. Zheng, J. Zhou, S. Wu, H. Yuan and J. Meng, *Construction and Building Materials*, 2015, **84**, 277-283.
128. Z. Liu, A. Sha, R. He and M. Xing, *Cold Regions Science and Technology*, 2016, **129**, 104-113.
129. H. Coffman, *Journal of the American Helicopter Society*, 1987, **32**, 34-39.
130. S. K. Thomas, R. P. Cassoni and C. D. MacArthur, *Journal of aircraft*, 1996, **33**, 841-854.
131. J. Laforte, M. Allaire and J. Laflamme, *Atmospheric Research*, 1998, **46**, 143-158.
132. R. Mirzanamadi, C.-E. Hagentoft and P. Johansson, *Energies*, 2018, **11**, 3443.
133. X. Liu, H. Chen, Z. Zhao, Y. Yan and D. Zhang, *Surface and Coatings Technology*, 2019, **374**, 889-896.

134. A. J. Meuler, J. D. Smith, K. K. Varanasi, J. M. Mabry, G. H. McKinley and R. E. Cohen, *ACS applied materials & interfaces*, 2010, **2**, 3100-3110.
135. J. Le Bideau, L. Viau and A. Vioux, *Chemical Society Reviews*, 2011, **40**, 907-925.
136. N. Chen, H. Zhang, L. Li, R. Chen and S. Guo, *Advanced Energy Materials*, 2018, **8**, 1702675.
137. A. Kavanagh, R. Byrne, D. Diamond and K. J. Fraser, *Membranes*, 2012, **2**, 16-39.
138. L. Viau, C. Tourné-Péteilh, J.-M. Devoisselle and A. Vioux, *Chemical Communications*, 2010, **46**, 228-230.
139. M. Kuddushi, N. K. Patel, S. Rajput, O. A. El Seoud, J. P. Mata and N. I. Malek, *ChemSystemsChem*, 2020.
140. S. J. Craythorne, K. Anderson, F. Lorenzini, C. McCausland, E. F. Smith, P. Licence, A. C. Marr and P. C. Marr, *Chemistry–A European Journal*, 2009, **15**, 7094-7100.
141. F. Shi, Q. Zhang, D. Li and Y. Deng, *Chemistry–A European Journal*, 2005, **11**, 5279-5288.
142. E. Mitridis, T. M. Schutzius, A. Sicher, C. U. Hail, H. Eghlidi and D. Poulikakos, *ACS nano*, 2018, **12**, 7009-7017.
143. C. Wu, H. Geng, S. Tan, H. Wang, J. Lv, Z. He and J. Wang, *Materials Horizons*, 2020, DOI: 10.1039/D0MH00636J.
144. S. Wu, Y. Du, Y. Alsaid, D. Wu, M. Hua, Y. Yan, B. Yao, Y. Ma, X. Zhu and X. He, *Proceedings of the National Academy of Sciences*, 2020, DOI: 10.1073/pnas.2001972117, 202001972.
145. I. A. Ryzhkin and V. F. Petrenko, *The Journal of Physical Chemistry B*, 1997, **101**, 6267-6270.
146. V. F. Petrenko and S. Peng, *Canadian journal of physics*, 2003, **81**, 387-393.
147. V. Hejazi, K. Sobolev and M. Nosonovsky, *Scientific reports*, 2013, **3**, 2194.
148. M. Nosonovsky and V. Hejazi, *ACS nano*, 2012, **6**, 8488-8491.
149. Z. He, Y. Zhuo, J. He and Z. Zhang, *Soft Matter*, 2018, **14**, 4846-4851.
150. A. L. DeVries and D. E. Wohlschlag, *Science*, 1969, **163**, 1073-1075.

151. T. Sun, F.-H. Lin, R. L. Campbell, J. S. Allingham and P. L. Davies, *Science*, 2014, **343**, 795-798.
152. J. A. Raymond and A. L. DeVries, *Proceedings of the National Academy of Sciences*, 1977, **74**, 2589-2593.
153. C. A. Knight, *Nature*, 2000, **406**, 249-251.
154. J. Xu, R. Jin, X. Ren and G. Gao, *Journal of Materials Chemistry A*, 2020, DOI: 10.1039/D0TA02370A.
155. P. L. Davies, *Trends in biochemical sciences*, 2014, **39**, 548-555.
156. L. A. Graham and P. L. Davies, *Science*, 2005, **310**, 461-461.
157. Z. He, K. Liu and J. Wang, *Accounts of chemical research*, 2018, **51**, 1082-1091.
158. C. Knight, C. Cheng and A. DeVries, *Biophysical journal*, 1991, **59**, 409-418.
159. G. Bai, D. Gao, Z. Liu, X. Zhou and J. Wang, *Nature*, 2019, **576**, 437-441.
160. G. Bai, D. Gao and J. Wang, *Carbon*, 2017, **124**, 415-421.
161. G. Bai, Z. Song, H. Geng, D. Gao, K. Liu, S. Wu, W. Rao, L. Guo and J. Wang, *Advanced Materials*, 2017, **29**, 1606843.
162. C. I. Biggs, T. L. Bailey, B. Graham, C. Stubbs, A. Fayter and M. I. Gibson, *Nature communications*, 2017, **8**, 1-12.
163. C. J. Capicciotti, R. S. Mancini, T. R. Turner, T. Koyama, M. G. Alteen, M. Doshi, T. Inada, J. P. Acker and R. N. Ben, *ACS omega*, 2016, **1**, 656-662.
164. R. Drori, C. Li, C. Hu, P. Raiteri, A. L. Rohl, M. D. Ward and B. Kahr, *Journal of the American Chemical Society*, 2016, **138**, 13396-13401.
165. O. Mizrahy, M. Bar-Dolev, S. Guy and I. Braslavsky, *PloS one*, 2013, **8**.
166. Y. Gwak, J.-i. Park, M. Kim, H. S. Kim, M. J. Kwon, S. J. Oh, Y.-P. Kim and E. Jin, *Scientific reports*, 2015, **5**, 12019.
167. M. J. Kreder, J. Alvarenga, P. Kim and J. Aizenberg, *Nature Reviews Materials*, 2016, **1**, 1-15.
168. Q. Hao, Y. Pang, Y. Zhao, J. Zhang, J. Feng and S. Yao, *Langmuir*, 2014, **30**, 15416-15422.
169. S. Jung, M. K. Tiwari and D. Poulikakos, *Proceedings of the National Academy of Sciences*, 2012, **109**, 16073-16078.
170. R. Chatterjee, D. Beysens and S. Anand, *Advanced Materials*, 2019, **31**, 1807812.

171. Z. Liu, Z. He, J. Lv, Y. Jin, S. Wu, G. Liu, F. Zhou and J. Wang, *RSC advances*, 2017, **7**, 840-844.
172. Q. Guo, Z. He, Y. Jin, S. Zhang, S. Wu, G. Bai, H. Xue, Z. Liu, S. Jin and L. Zhao, *Langmuir*, 2018, **34**, 11986-11991.
173. X. Xu, V. V. Jerca and R. Hoogenboom, *Chem*, 2020, **6**, 820-822.
174. T. M. Schutzius, S. Jung, T. Maitra, G. Graeber, M. Köhme and D. Poulikakos, *Nature*, 2015, **527**, 82-85.
175. S. Jung, M. K. Tiwari, N. V. Doan and D. Poulikakos, *Nature communications*, 2012, **3**, 1-8.
176. A. Kirillova, L. Ionov, I. V. Roisman and A. Synytska, *Chemistry of Materials*, 2016, **28**, 6995-7005.
177. Y. Jin, C. Wu, Y. Yang, J. Wu, Z. He and J. Wang, *ACS Nano*, 2020, DOI: 10.1021/acsnano.0c01304.
178. S. F. Ahmadi, S. Nath, G. J. Iliff, B. R. Srijanto, C. P. Collier, P. Yue and J. B. Boreyko, *ACS applied materials & interfaces*, 2018, **10**, 32874-32884.
179. X. Yin, Y. Zhang, D. Wang, Z. Liu, Y. Liu, X. Pei, B. Yu and F. Zhou, *Advanced Functional Materials*, 2015, **25**, 4237-4245.
180. T. Cheng, R. He, Q. Zhang, X. Zhan and F. Chen, *Journal of Materials Chemistry A*, 2015, **3**, 21637-21646.
181. M. Mohseni and A. Amirfazli, *Cold Regions Science and Technology*, 2013, **87**, 47-58.
182. B. G. Falzon, P. Robinson, S. Frenz and B. Gilbert, *Composites Part A: Applied Science and Manufacturing*, 2015, **68**, 323-335.
183. A. Shinkafi and C. Lawson, *International Journal of Mechanical, Aerospace, Industrial and Mechatronics Engineering*, 2014, **8**, 1069-1076.
184. Z. Zhao, H. Chen, X. Liu, H. Liu and D. Zhang, *Surface and Coatings Technology*, 2018, **349**, 340-346.
185. X. Yao, S. C. Hawkins and B. G. Falzon, *Carbon*, 2018, **136**, 130-138.
186. Z. Zhang, B. Chen, C. Lu, H. Wu, H. Wu, S. Jiang and G. Chai, *Composite Structures*, 2017, **180**, 933-943.
187. G. Jiang, L. Chen, S. Zhang and H. Huang, *ACS applied materials & interfaces*, 2018, **10**, 36505-36511.

188. L. Ma, J. Wang, F. Zhao, D. Wu, Y. Huang, D. Zhang, Z. Zhang, W. Fu, X. Li and Y. Fan, *Composites Science and Technology*, 2019, **181**, 107696.
189. X. Deng, L. Mammen, H.-J. Butt and D. Vollmer, *Science*, 2012, **335**, 67-70.
190. K. Seo and M. Kim, *Carbon*, 2014, **68**, 583-596.
191. L. Xiao, W. Zeng, G. Liao, C. Yi and Z. Xu, *ACS Applied Nano Materials*, 2018, **1**, 1204-1211.
192. R. Iqbal, B. Majhy and A. Sen, *ACS applied materials & interfaces*, 2017, **9**, 31170-31180.
193. J. Li, Z. Zhao, D. Li, H. Tian, F. Zha, H. Feng and L. Guo, *Nanoscale*, 2017, **9**, 13610-13617.
194. B. N. Sahoo and B. Kandasubramanian, *Materials Chemistry and Physics*, 2014, **148**, 134-142.
195. M. I. Jamil, X. Zhan, F. Chen, D. Cheng and Q. Zhang, *ACS applied materials & interfaces*, 2019, **11**, 31532-31542.

Appendix B

List of previous PhD theses at Department of Structural Engineering

Appendix B

DEPARTMENT OF STRUCTURAL ENGINEERING

NORWEGIAN UNIVERSITY OF SCIENCE AND TECHNOLOGY

N–7491 TRONDHEIM, NORWAY

Telephone: +47 73 59 47 00

"Reliability Analysis of Structural Systems using Nonlinear Finite Element Methods",
C. A. Holm, 1990:23, ISBN 82-7119-178-0.

"Uniform Stratified Flow Interaction with a Submerged Horizontal Cylinder",
Ø. Arntsen, 1990:32, ISBN 82-7119-188-8.

"Large Displacement Analysis of Flexible and Rigid Systems Considering
Displacement-Dependent Loads and Nonlinear Constraints",
K. M. Mathisen, 1990:33, ISBN 82-7119-189-6.

"Solid Mechanics and Material Models including Large Deformations",
E. Levold, 1990:56, ISBN 82-7119-214-0, ISSN 0802-3271.

"Inelastic Deformation Capacity of Flexurally-Loaded Aluminium Alloy Structures",
T. Welo, 1990:62, ISBN 82-7119-220-5, ISSN 0802-3271.

"Visualization of Results from Mechanical Engineering Analysis",
K. Aamnes, 1990:63, ISBN 82-7119-221-3, ISSN 0802-3271.

"Object-Oriented Product Modeling for Structural Design",
S. I. Dale, 1991:6, ISBN 82-7119-258-2, ISSN 0802-3271.

"Parallel Techniques for Solving Finite Element Problems on Transputer Networks",
T. H. Hansen, 1991:19, ISBN 82-7119-273-6, ISSN 0802-3271.

"Statistical Description and Estimation of Ocean Drift Ice Environments",
R. Korsnes, 1991:24, ISBN 82-7119-278-7, ISSN 0802-3271.

“Properties of concrete related to fatigue damage: with emphasis on high strength concrete”,
G. Petkovic, 1991:35, ISBN 82-7119-290-6, ISSN 0802-3271.

"Turbidity Current Modelling",
B. Brørs, 1991:38, ISBN 82-7119-293-0, ISSN 0802-3271.

"Zero-Slump Concrete: Rheology, Degree of Compaction and Strength. Effects of Fillers as Part Cement-Replacement",
C. Sørensen, 1992:8, ISBN 82-7119-357-0, ISSN 0802-3271.

"Nonlinear Analysis of Reinforced Concrete Structures Exposed to Transient Loading",
K. V. Høiseth, 1992:15, ISBN 82-7119-364-3, ISSN 0802-3271.

"Finite Element Formulations and Solution Algorithms for Buckling and Collapse Analysis of Thin Shells",
R. O. Bjærum, 1992:30, ISBN 82-7119-380-5, ISSN 0802-3271.

"Response Statistics of Nonlinear Dynamic Systems",
J. M. Johnsen, 1992:42, ISBN 82-7119-393-7, ISSN 0802-3271.

"Digital Models in Engineering. A Study on why and how engineers build and operate digital models for decisison support",
J. Høyte, 1992:75, ISBN 82-7119-429-1, ISSN 0802-3271.

"Sparse Solution of Finite Element Equations",
A. C. Damhaug, 1992:76, ISBN 82-7119-430-5, ISSN 0802-3271.

"Some Aspects of Floating Ice Related to Sea Surface Operations in the Barents Sea",
S. Løset, 1992:95, ISBN 82-7119-452-6, ISSN 0802-3271.

"Modelling of Cyclic Plasticity with Application to Steel and Aluminium Structures",
O. S. Hopperstad, 1993:7, ISBN 82-7119-461-5, ISSN 0802-3271.

"The Free Formulation: Linear Theory and Extensions with Applications to Tetrahedral Elements
with Rotational Freedoms",
G. Skeie, 1993:17, ISBN 82-7119-472-0, ISSN 0802-3271.

"Høyfast betongs motstand mot piggdekkslitasje. Analyse av resultater fra prøving i Veisliter'n",
T. Tveter, 1993:62, ISBN 82-7119-522-0, ISSN 0802-3271.

"A Nonlinear Finite Element Based on Free Formulation Theory for Analysis of Sandwich Structures",
O. Aamlid, 1993:72, ISBN 82-7119-534-4, ISSN 0802-3271.

"The Effect of Curing Temperature and Silica Fume on Chloride Migration and Pore Structure of High Strength Concrete",
C. J. Hauck, 1993:90, ISBN 82-7119-553-0, ISSN 0802-3271.

"Failure of Concrete under Compressive Strain Gradients",
G. Markeset, 1993:110, ISBN 82-7119-575-1, ISSN 0802-3271.

"An experimental study of internal tidal amphidromes in Vestfjorden",
J. H. Nilsen, 1994:39, ISBN 82-7119-640-5, ISSN 0802-3271.

"Structural analysis of oil wells with emphasis on conductor design",
H. Larsen, 1994:46, ISBN 82-7119-648-0, ISSN 0802-3271.

"Adaptive methods for non-linear finite element analysis of shell structures",
K. M. Okstad, 1994:66, ISBN 82-7119-670-7, ISSN 0802-3271.

"On constitutive modelling in nonlinear analysis of concrete structures",
O. Fyrileiv, 1994:115, ISBN 82-7119-725-8, ISSN 0802-3271.

"Fluctuating wind load and response of a line-like engineering structure with emphasis on motion-induced wind forces",
J. Bogunovic Jakobsen, 1995:62, ISBN 82-7119-809-2, ISSN 0802-3271.

"An experimental study of beam-columns subjected to combined torsion, bending and axial actions",
A. Aalberg, 1995:66, ISBN 82-7119-813-0, ISSN 0802-3271.

"Scaling and cracking in unsealed freeze/thaw testing of Portland cement and silica fume concretes",
S. Jacobsen, 1995:101, ISBN 82-7119-851-3, ISSN 0802-3271.

"Damping of water waves by submerged vegetation. A case study of laminaria hyperborea",
A. M. Dubi, 1995:108, ISBN 82-7119-859-9, ISSN 0802-3271.

"The dynamics of a slope current in the Barents Sea",
Sheng Li, 1995:109, ISBN 82-7119-860-2, ISSN 0802-3271.

"Modellering av delmaterialenes betydning for betongens konsistens",
Ernst Mørtsell, 1996:12, ISBN 82-7119-894-7, ISSN 0802-3271.

"Bending of thin-walled aluminium extrusions",
Birgit Søvik Opheim, 1996:60, ISBN 82-7119-947-1, ISSN 0802-3271.

"Material modelling of aluminium for crashworthiness analysis",
Torodd Berstad, 1996:89, ISBN 82-7119-980-3, ISSN 0802-3271.

"Estimation of structural parameters from response measurements on submerged floating tunnels",
Rolf Magne Larssen, 1996:119, ISBN 82-471-0014-2, ISSN 0802-3271.

“Numerical modelling of plain and reinforced concrete by damage mechanics”,
Mario A. Polanco-Loria, 1997:20, ISBN 82-471-0049-5, ISSN 0802-3271.

“Nonlinear random vibrations - numerical analysis by path integration methods”,
Vibeke Moe, 1997:26, ISBN 82-471-0056-8, ISSN 0802-3271.
“Numerical prediction of vortex-induced vibration by the finite element method”,
Joar Martin Dalheim, 1997:63, ISBN 82-471-0096-7, ISSN 0802-3271.

“Time domain calculations of buffeting response for wind sensitive structures”,
Ketil Aas-Jakobsen, 1997:148, ISBN 82-471-0189-0, ISSN 0802-3271.

"A numerical study of flow about fixed and flexibly mounted circular cylinders",
Trond Stokka Meling, 1998:48, ISBN 82-471-0244-7, ISSN 0802-3271.

“Estimation of chloride penetration into concrete bridges in coastal areas”,
Per Egil Steen, 1998:89, ISBN 82-471-0290-0, ISSN 0802-3271.

“Stress-resultant material models for reinforced concrete plates and shells”,
Jan Arve Øverli, 1998:95, ISBN 82-471-0297-8, ISSN 0802-3271.

“Chloride binding in concrete. Effect of surrounding environment and concrete composition”,
Claus Kenneth Larsen, 1998:101, ISBN 82-471-0337-0, ISSN 0802-3271.

“Rotational capacity of aluminium alloy beams”,
Lars A. Moen, 1999:1, ISBN 82-471-0365-6, ISSN 0802-3271.

“Stretch Bending of Aluminium Extrusions”,
Arild H. Clausen, 1999:29, ISBN 82-471-0396-6, ISSN 0802-3271.

“Aluminium and Steel Beams under Concentrated Loading”,
Tore Tryland, 1999:30, ISBN 82-471-0397-4, ISSN 0802-3271.

"Engineering Models of Elastoplasticity and Fracture for Aluminium Alloys",
Odd-Geir Lademo, 1999:39, ISBN 82-471-0406-7, ISSN 0802-3271.

"Kapasitet og duktilitet av dybelforbindelser i trekonstruksjoner",
Jan Siem, 1999:46, ISBN 82-471-0414-8, ISSN 0802-3271.

“Etablering av distribuert ingeniørarbeid; Teknologiske og organisatoriske erfaringer fra en norsk ingeniørbedrift”,
Lars Line, 1999:52, ISBN 82-471-0420-2, ISSN 0802-3271.

“Estimation of Earthquake-Induced Response”,
Símon Ólafsson, 1999:73, ISBN 82-471-0443-1, ISSN 0802-3271.

“Coastal Concrete Bridges: Moisture State, Chloride Permeability and Aging Effects”
Ragnhild Holen Relling, 1999:74, ISBN 82-471-0445-8, ISSN 0802-3271.

”Capacity Assessment of Titanium Pipes Subjected to Bending and External Pressure”,
Arve Bjørset, 1999:100, ISBN 82-471-0473-3, ISSN 0802-3271.

“Validation of Numerical Collapse Behaviour of Thin-Walled Corrugated Panels”,
Håvar Ilstad, 1999:101, ISBN 82-471-0474-1, ISSN 0802-3271.

“Strength and Ductility of Welded Structures in Aluminium Alloys”,
Miroslaw Matusiak, 1999:113, ISBN 82-471-0487-3, ISSN 0802-3271.

“Thermal Dilation and Autogenous Deformation as Driving Forces to Self-Induced Stresses in High Performance Concrete”,
Øyvind Bjøntegaard, 1999:121, ISBN 82-7984-002-8, ISSN 0802-3271.

“Some Aspects of Ski Base Sliding Friction and Ski Base Structure”,
Dag Anders Moldestad, 1999:137, ISBN 82-7984-019-2, ISSN 0802-3271.

"Electrode reactions and corrosion resistance for steel in mortar and concrete",
Roy Antonsen, 2000:10, ISBN 82-7984-030-3, ISSN 0802-3271.

"Hydro-Physical Conditions in Kelp Forests and the Effect on Wave Damping and Dune Erosion. A case study on Laminaria Hyperborea",
Stig Magnar Løvås, 2000:28, ISBN 82-7984-050-8, ISSN 0802-3271.

"Random Vibration and the Path Integral Method",
Christian Skaug, 2000:39, ISBN 82-7984-061-3, ISSN 0802-3271.

"Buckling and geometrical nonlinear beam-type analyses of timber structures",
Trond Even Eggen, 2000:56, ISBN 82-7984-081-8, ISSN 0802-3271.

”Structural Crashworthiness of Aluminium Foam-Based Components”,
Arve Grønsund Hanssen, 2000:76, ISBN 82-7984-102-4, ISSN 0809-103X.

“Measurements and simulations of the consolidation in first-year sea ice ridges, and some aspects of mechanical behaviour”,
Knut V. Høyland, 2000:94, ISBN 82-7984-121-0, ISSN 0809-103X.

”Kinematics in Regular and Irregular Waves based on a Lagrangian Formulation”,
Svein Helge Gjøsund, 2000-86, ISBN 82-7984-112-1, ISSN 0809-103X.

”Self-Induced Cracking Problems in Hardening Concrete Structures”,
Daniela Bosnjak, 2000-121, ISBN 82-7984-151-2, ISSN 0809-103X.

"Ballistic Penetration and Perforation of Steel Plates",
Tore Børvik, 2000:124, ISBN 82-7984-154-7, ISSN 0809-103X.

"Freeze-Thaw resistance of Concrete. Effect of: Curing Conditions, Moisture Exchange and Materials",
Terje Finnerup Rønning, 2001:14, ISBN 82-7984-165-2, ISSN 0809-103X

"Structural behaviour of post tensioned concrete structures. Flat slab. Slabs on ground",
Steinar Trygstad, 2001:52, ISBN 82-471-5314-9, ISSN 0809-103X.

"Slipforming of Vertical Concrete Structures. Friction between concrete and slipform panel",
Kjell Tore Fosså, 2001:61, ISBN 82-471-5325-4, ISSN 0809-103X.

"Some numerical methods for the simulation of laminar and turbulent incompressible flows",
Jens Holmen, 2002:6, ISBN 82-471-5396-3, ISSN 0809-103X.

“Improved Fatigue Performance of Threaded Drillstring Connections by Cold Rolling”,
Steinar Kristoffersen, 2002:11, ISBN: 82-421-5402-1, ISSN 0809-103X.

"Deformations in Concrete Cantilever Bridges: Observations and Theoretical Modelling",
Peter F. Takâcs, 2002:23, ISBN 82-471-5415-3, ISSN 0809-103X.

"Stiffened aluminium plates subjected to impact loading",
Hilde Giæver Hildrum, 2002:69, ISBN 82-471-5467-6, ISSN 0809-103X.

"Full- and model scale study of wind effects on a medium-rise building in a built up area",
Jónas Thór Snæbjørnsson, 2002:95, ISBN82-471-5495-1, ISSN 0809-103X.

“Evaluation of Concepts for Loading of Hydrocarbons in Ice-infested water”,
Arnor Jensen, 2002:114, ISBN 82-417-5506-0, ISSN 0809-103X.

”Numerical and Physical Modelling of Oil Spreading in Broken Ice”,
Janne K. Økland Gjøsteen, 2002:130, ISBN 82-471-5523-0, ISSN 0809-103X.

”Diagnosis and protection of corroding steel in concrete”,
Franz Pruckner, 20002:140, ISBN 82-471-5555-4, ISSN 0809-103X.

“Tensile and Compressive Creep of Young Concrete: Testing and Modelling”,
Dawood Atrushi, 2003:17, ISBN 82-471-5565-6, ISSN 0809-103X.

“Rheology of Particle Suspensions. Fresh Concrete, Mortar and Cement Paste with Various Types of Lignosulfonates”,
Jon Elvar Wallevik, 2003:18, ISBN 82-471-5566-4, ISSN 0809-103X.

“Oblique Loading of Aluminium Crash Components”,
Aase Reyes, 2003:15, ISBN 82-471-5562-1, ISSN 0809-103X.

“Utilization of Ethiopian Natural Pozzolans”,
Surafel Ketema Desta, 2003:26, ISSN 82-471-5574-5, ISSN:0809-103X.

“Behaviour and strength prediction of reinforced concrete structures with discontinuity regions”, Helge Brå, 2004:11, ISBN 82-471-6222-9, ISSN 1503-8181.

"High-strength steel plates subjected to projectile impact. An experimental and numerical study", Sumita Dey, 2004:38, ISBN 82-471-6282-2 (printed version), ISBN 82-471-6281-4 (electronic version), ISSN 1503-8181.

"Alkali-reactive and inert fillers in concrete. Rheology of fresh mixtures and expansive reactions."
Bård M. Pedersen, 2004:92, ISBN 82-471-6401-9 (printed version), ISBN 82-471-6400-0 (electronic version), ISSN 1503-8181.

"On the Shear Capacity of Steel Girders with Large Web Openings".
Nils Christian Hagen, 2005:9 ISBN 82-471-6878-2 (printed version), ISBN 82-471-6877-4 (electronic version), ISSN 1503-8181.

"Behaviour of aluminium extrusions subjected to axial loading".
Østen Jensen, 2005:7, ISBN 82-471-6873-1 (printed version), ISBN 82-471-6872-3 (electronic version), ISSN 1503-8181.

"Thermal Aspects of corrosion of Steel in Concrete".
Jan-Magnus Østvik, 2005:5, ISBN 82-471-6869-3 (printed version), ISBN 82-471-6868 (electronic version), ISSN 1503-8181.

"Mechanical and adaptive behaviour of bone in relation to hip replacement." A study of bone remodelling and bone grafting.
Sébastien Muller, 2005:34, ISBN 82-471-6933-9 (printed version), ISBN 82-471-6932-0 (electronic version), ISSN 1503-8181.

"Analysis of geometrical nonlinearities with applications to timber structures".
Lars Wollebæk, 2005:74, ISBN 82-471-7050-5 (printed version), ISBN 82-471-7019-1 (electronic version), ISSN 1503-8181.

"Pedestrian induced lateral vibrations of slender footbridges",

Anders Rönnquist, 2005:102, ISBN 82-471-7082-5 (printed version), ISBN 82-471-7081-7 (electronic version), ISSN 1503-8181.

“Initial Strength Development of Fly Ash and Limestone Blended Cements at Various Temperatures Predicted by Ultrasonic Pulse Velocity”,
Tom Ivar Fredvik, 2005:112, ISBN 82-471-7105-8 (printed version), ISBN 82-471-7103-1 (electronic version), ISSN 1503-8181.

“Behaviour and modelling of thin-walled cast components”,
Cato Dørum, 2005:128, ISBN 82-471-7140-6 (printed version), ISBN 82-471-7139-2 (electronic version), ISSN 1503-8181.

“Behaviour and modelling of selfpiercing riveted connections”,
Raffaele Porcaro, 2005:165, ISBN 82-471-7219-4 (printed version), ISBN 82-471-7218-6 (electronic version), ISSN 1503-8181.

”Behaviour and Modelling og Aluminium Plates subjected to Compressive Load”,
Lars Rønning, 2005:154, ISBN 82-471-7169-1 (printed version), ISBN 82-471-7195-3 (electronic version), ISSN 1503-8181.

”Bumper beam-longitudinal system subjected to offset impact loading”,
Satyanarayana Kokkula, 2005:193, ISBN 82-471-7280-1 (printed version), ISBN 82-471-7279-8 (electronic version), ISSN 1503-8181.

“Control of Chloride Penetration into Concrete Structures at Early Age”,
Guofei Liu, 2006:46, ISBN 82-471-7838-9 (printed version), ISBN 82-471-7837-0 (electronic version), ISSN 1503-8181.

“Modelling of Welded Thin-Walled Aluminium Structures”,
Ting Wang, 2006:78, ISBN 82-471-7907-5 (printed version), ISBN 82-471-7906-7 (electronic version), ISSN 1503-8181.

”Time-variant reliability of dynamic systems by importance sampling and probabilistic analysis of ice loads”,
Anna Ivanova Olsen, 2006:139, ISBN 82-471-8041-3 (printed version), ISBN 82-471-8040-5 (electronic version), ISSN 1503-8181.

“Fatigue life prediction of an aluminium alloy automotive component using finite element analysis of surface topography”.
Sigmund Kyrre Ås, 2006:25, ISBN 82-471-7791-9 (printed version), ISBN 82-471-7791-9 (electronic version), ISSN 1503-8181.

”Constitutive models of elastoplasticity and fracture for aluminium alloys under strain path change”,
Dasharatha Achani, 2006:76, ISBN 82-471-7903-2 (printed version), ISBN 82-471-7902-4 (electronic version), ISSN 1503-8181.

“Simulations of 2D dynamic brittle fracture by the Element-free Galerkin method and linear fracture mechanics”,
Tommy Karlsson, 2006:125, ISBN 82-471-8011-1 (printed version), ISBN 82-471-8010-3 (electronic version), ISSN 1503-8181.

“Penetration and Perforation of Granite Targets by Hard Projectiles”,
Chong Chiang Seah, 2006:188, ISBN 82-471-8150-9 (printed version), ISBN 82-471-8149-5 (electronic version), ISSN 1503-8181.

“Deformations, strain capacity and cracking of concrete in plastic and early hardening phases”,
Tor Arne Hammer, 2007:234, ISBN 978-82-471-5191-4 (printed version), ISBN 978-82-471-5207-2 (electronic version), ISSN 1503-8181.

"Crashworthiness of dual-phase high-strength steel: Material and Component behaviour", Venkatapathi Tarigopula, 2007:230, ISBN 82-471-5076-4 (printed version), ISBN 82-471-5093-1 (electronic version), ISSN 1503-8181.

"Fibre reinforcement in load carrying concrete structures",
Åse Lyslo Døssland, 2008:50, ISBN 978-82-471-6910-0 (printed version), ISBN 978-82-471-6924-7 (electronic version), ISSN 1503-8181.

"Low-velocity penetration of aluminium plates",
Frode Grytten, 2008:46, ISBN 978-82-471-6826-4 (printed version), ISBN 978-82-471-6843-1 (electronic version), ISSN 1503-8181.

"Robustness studies of structures subjected to large deformations",
Ørjan Fyllingen, 2008:24, ISBN 978-82-471-6339-9 (printed version), ISBN 978-82-471-6342-9 (electronic version), ISSN 1503-8181.

"Constitutive modelling of morsellised bone",
Knut Birger Lunde, 2008:92, ISBN 978-82-471-7829-4 (printed version), ISBN 978-82-471-7832-4 (electronic version), ISSN 1503-8181.

"Experimental Investigations of Wind Loading on a Suspension Bridge Girder",
Bjørn Isaksen, 2008:131, ISBN 978-82-471-8656-5 (printed version), ISBN 978-82-471-8673-2 (electronic version), ISSN 1503-8181.

"Cracking Risk of Concrete Structures in The Hardening Phase",
Guomin Ji, 2008:198, ISBN 978-82-471-1079-9 (printed version), ISBN 978-82-471-1080-5 (electronic version), ISSN 1503-8181.

"Modelling and numerical analysis of the porcine and human mitral apparatus",
Victorien Emile Prot, 2008:249, ISBN 978-82-471-1192-5 (printed version), ISBN 978-82-471-1193-2 (electronic version), ISSN 1503-8181.

"Strength analysis of net structures",
Heidi Moe, 2009:48, ISBN 978-82-471-1468-1 (printed version), ISBN 978-82-471-1469-8 (electronic version), ISSN1503-8181.

"Numerical analysis of ductile fracture in surface cracked shells",
Espen Berg, 2009:80, ISBN 978-82-471-1537-4 (printed version), ISBN 978-82-471-1538-1 (electronic version), ISSN 1503-8181.

"Subject specific finite element analysis of bone – for evaluation of the healing of a leg lengthening and evaluation of femoral stem design",
Sune Hansborg Pettersen, 2009:99, ISBN 978-82-471-1579-4 (printed version), ISBN 978-82-471-1580-0 (electronic version), ISSN 1503-8181.

"Evaluation of fracture parameters for notched multi-layered structures",
Lingyun Shang, 2009:137, ISBN 978-82-471-1662-3 (printed version), ISBN 978-82-471-1663-0 (electronic version), ISSN 1503-8181.

"Modelling of Dynamic Material Behaviour and Fracture of Aluminium Alloys for Structural Applications"
Yan Chen, 2009:69, ISBN 978-82-471-1515-2 (printed version), ISBN 978-82 471-1516-9 (electronic version), ISSN 1503-8181.

"Nanomechanics of polymer and composite particles"
Jianying He 2009:213, ISBN 978-82-471-1828-3 (printed version), ISBN 978-82-471-1829-0 (electronic version), ISSN 1503-8181.

"Mechanical properties of clear wood from Norway spruce"
Kristian Berbom Dahl 2009:250, ISBN 978-82-471-1911-2 (printed version) ISBN 978-82-471-1912-9 (electronic version), ISSN 1503-8181.

"Modeling of the degradation of TiB_2 mechanical properties by residual stresses and liquid Al penetration along grain boundaries"
Micol Pezzotta 2009:254, ISBN 978-82-471-1923-5 (printed version) ISBN 978-82-471-1924-2 (electronic version) ISSN 1503-8181.

"Effect of welding residual stress on fracture"
Xiabo Ren 2010:77, ISBN 978-82-471-2115-3 (printed version) ISBN 978-82-471-2116-0 (electronic version), ISSN 1503-8181.

"Pan-based carbon fiber as anode material in cathodic protection system for concrete structures"
Mahdi Chini 2010:122, ISBN 978-82-471-2210-5 (printed version) ISBN 978-82-471-2213-6 (electronic version), ISSN 1503-8181.

"Structural Behaviour of deteriorated and retrofitted concrete structures"
Irina Vasililjeva Sæther 2010:171, ISBN 978-82-471-2315-7 (printed version) ISBN 978-82-471-2316-4 (electronic version) ISSN 1503-8181.

"Prediction of local snow loads on roofs"
Vivian Meløysund 2010:247, ISBN 978-82-471-2490-1 (printed version) ISBN 978-82-471-2491-8 (electronic version) ISSN 1503-8181.

"Behaviour and modelling of polymers for crash applications"
Virgile Delhaye 2010:251, ISBN 978-82-471-2501-4 (printed version) ISBN 978-82-471-2502-1 (electronic version) ISSN 1503-8181.
"Blended cement with reducted CO_2 emission – Utilizing the Fly Ash-Limestone Synergy",
Klaartje De Weerdt 2011:32, ISBN 978-82-471-2584-7 (printed version) ISBN 978-82-471-2584-4 (electronic version) ISSN 1503-8181.

"Chloride induced reinforcement corrosion in concrete" Concept of critical chloride content – methods and mechanisms.

Ueli Angst 2011:113, ISBN 978-82-471-2769-9 (printed version) ISBN 978-82-471-2763-6 (electronic version) ISSN 1503-8181.

"A thermo-electric-Mechanical study of the carbon anode and contact interface for Energy savings in the production of aluminium".
Dag Herman Andersen 2011:157, ISBN 978-82-471-2859-6 (printed version) ISBN 978-82-471-2860-2 (electronic version) ISSN 1503-8181.

"Structural Capacity of Anchorage Ties in Masonry Veneer Walls Subjected to Earthquake". The implications of Eurocode 8 and Eurocode 6 on a typical Norwegain veneer wall.
Ahmed Mohamed Yousry Hamed 2011:181, ISBN 978-82-471-2911-1 (printed version) ISBN 978-82-471-2912-8 (electronic ver.) ISSN 1503-8181.

"Work-hardening behaviour in age-hardenable Al-Zn-Mg(-Cu) alloys".
Ida Westermann , 2011:247, ISBN 978-82-471-3056-8 (printed ver.) ISBN 978-82-471-3057-5 (electronic ver.) ISSN 1503-8181.

"Behaviour and modelling of selfpiercing riveted connections using aluminium rivets".
Nguyen-Hieu Hoang, 2011:266, ISBN 978-82-471-3097-1 (printed ver.) ISBN 978-82-471-3099-5 (electronic ver.) ISSN 1503-8181.

"Fibre reinforced concrete".
Sindre Sandbakk, 2011:297, ISBN 978-82-471-3167-1 (printed ver.) ISBN 978-82-471-3168-8 (electronic ver) ISSN 1503:8181.

"Dynamic behaviour of cablesupported bridges subjected to strong natural wind".
Ole Andre Øiseth, 2011:315, ISBN 978-82-471-3209-8 (printed ver.) ISBN 978-82-471-3210-4 (electronic ver.) ISSN 1503-8181.

"Constitutive modeling of solargrade silicon materials"

Julien Cochard, 2011:307, ISBN 978-82-471-3189-3 (printed ver). ISBN 978-82-471-3190-9 (electronic ver.) ISSN 1503-8181.

"Constitutive behavior and fracture of shape memory alloys"
Jim Stian Olsen, 2012:57, ISBN 978-82-471-3382-8 (printed ver.) ISBN 978-82-471-3383-5 (electronic ver.) ISSN 1503-8181.

"Field measurements in mechanical testing using close-range photogrammetry and digital image analysis"
Egil Fagerholt, 2012:95, ISBN 978-82-471-3466-5 (printed ver.) ISBN 978-82-471-3467-2 (electronic ver.) ISSN 1503-8181.

"Towards a better under standing of the ultimate behaviour of lightweight aggregate concrete in compression and bending",
Håvard Nedrelid, 2012:123, ISBN 978-82-471-3527-3 (printed ver.) ISBN 978-82-471-3528-0 (electronic ver.) ISSN 1503-8181.

"Numerical simulations of blood flow in the left side of the heart"
Sigrid Kaarstad Dahl, 2012:135, ISBN 978-82-471-3553-2 (printed ver.) ISBN 978-82-471-3555-6 (electronic ver.) ISSN 1503-8181.

"Moisture induced stresses in glulam"
Vanessa Angst-Nicollier, 2012:139, ISBN 978-82-471-3562-4 (printed ver.) ISBN 978-82-471-3563-1 (electronic ver.) ISSN 1503-8181.

"Biomechanical aspects of distraction osteogensis"
Valentina La Russa, 2012:250, ISBN 978-82-471-3807-6 (printed ver.) ISBN 978-82-471-3808-3 (electronic ver.) ISSN 1503-8181.

"Ductile fracture in dual-phase steel. Theoretical, experimental and numerical study"

Gaute Gruben, 2012:257, ISBN 978-82-471-3822-9 (printed ver.) ISBN 978-82-471-3823-6 (electronic ver.) ISSN 1503-8181.

“Damping in Timber Structures”
Nathalie Labonnote, 2012:263, ISBN 978-82-471-3836-6 (printed ver.) ISBN 978-82-471-3837-3 (electronic ver.) ISSN 1503-8181.

“Biomechanical modeling of fetal veins: The umbilical vein and ductus venosus bifurcation”
Paul Roger Leinan, 2012:299, ISBN 978-82-471-3915-8 (printed ver.) ISBN 978-82-471-3916-5 (electronic ver.) ISSN 1503-8181.

“Large-Deformation behaviour of thermoplastics at various stress states”
Anne Serine Ognedal, 2012:298, ISBN 978-82-471-3913-4 (printed ver.) ISBN 978-82-471-3914-1 (electronic ver.) ISSN 1503-8181.

“Hardening accelerator for fly ash blended cement”
Kien Dinh Hoang, 2012:366, ISBN 978-82-471-4063-5 (printed ver.) ISBN 978-82-471-4064-2 (electronic ver.) ISSN 1503-8181.

“From molecular structure to mechanical properties”
Jianyang Wu, 2013:186, ISBN 978-82-471-4485-5 (printed ver.) ISBN 978-82-471-4486-2 (electronic ver.) ISSN 1503-8181.

“Experimental and numerical study of hybrid concrete structures”
Linn Grepstad Nes, 2013:259, ISBN 978-82-471-4644-6 (printed ver.) ISBN 978-82-471-4645-3 (electronic ver.) ISSN 1503-8181.

“Mechanics of ultra-thin multi crystalline silicon wafers”
Saber Saffar, 2013:199, ISBN 978-82-471-4511-1 (printed ver.) ISBN 978-82-471-4513-5 (electronic ver). ISSN 1503-8181.

“Through process modelling of welded aluminium structures”
Anizahyati Alisibramulisi, 2013:325, ISBN 978-82-471-4788-7 (printed ver.) ISBN 978-82-471-4789-4 (electronic ver.) ISSN 1503-8181.

“Combined blast and fragment loading on steel plates”
Knut Gaarder Rakvåg, 2013:361, ISBN978-82-471-4872-3 (printed ver.) ISBN 978-82-4873-0 (electronic ver.). ISSN 1503-8181.

“Characterization and modelling of the anisotropic behaviour of high-strength aluminium alloy”
Marion Fourmeau, 2014:37, ISBN 978-82-326-0008-3 (printed ver.) ISBN 978-82-326-0009-0 (electronic ver.) ISSN 1503-8181.

“Behaviour of threated steel fasteners at elevated deformation rates”
Henning Fransplass, 2014:65, ISBN 978-82-326-0054-0 (printed ver.) ISBN 978-82-326-0055-7 (electronic ver.) ISSN 1503-8181.

“Sedimentation and Bleeding”
Ya Peng, 2014:89, ISBN 978-82-326-0102-8 (printed ver.) ISBN 978-82-326-0103-5 (electric ver.) ISSN 1503-8181.

“Impact against X65 offshore pipelines”
Martin Kristoffersen, 2014:362, ISBN 978-82-326-0636-8 (printed ver.) ISBN 978-82-326-0637-5 (electronic ver.) ISSN 1503-8181.

“Formability of aluminium alloy subjected to prestrain by rolling”
Dmitry Vysochinskiy, 2014:363,, ISBN 978-82-326-0638-2 (printed ver.) ISBN 978-82-326-0639-9 (electronic ver.) ISSN 1503-8181.

“Experimental and numerical study of Yielding, Work-Hardening and anisotropy in textured AA6xxx alloys using crystal plasticity models”

Mikhail Khadyko, 2015:28, ISBN 978-82-326-0724-2 (printed ver.) ISBN 978-82-326-0725-9 (electronic ver.) ISSN 1503-8181.

"Behaviour and Modelling of AA6xxx Aluminium Alloys Under a Wide Range of Temperatures and Strain Rates"
Vincent Vilamosa, 2015:63, ISBN 978-82-326-0786-0 (printed ver.) ISBN 978-82-326-0787-7 (electronic ver.) ISSN 1503-8181.

"A Probabilistic Approach in Failure Modelling of Aluminium High Pressure Die-Castings"
Octavian Knoll, 2015:137, ISBN 978-82-326-0930-7 (printed ver.) ISBN 978-82-326-0931-4 (electronic ver.) ISSN 1503-8181.

"Ice Abrasion on Marine Concrete Structures"
Egil Møen, 2015:189, ISBN 978-82-326-1034-1 (printed ver.) ISBN 978-82-326-1035-8 (electronic ver.) ISSN 1503-8181.

"Fibre Orientation in Steel-Fibre-Reinforced Concrete"
Giedrius Zirgulis, 2015:229, ISBN 978-82-326-1114-0 (printed ver.) ISBN 978-82-326-1115-7 (electronic ver.) ISSN 1503-8181.

"Effect of spatial variation and possible interference of localised corrosion on the residual capacity of a reinforced concrete beam"
Mohammad Mahdi Kioumarsi, 2015:282, ISBN 978-82-326-1220-8 (printed ver.) ISBN 978-82-1221-5 (electronic ver.) ISSN 1503-8181.

"The role of concrete resistivity in chloride-induced macro-cell corrosion"
Karla Horbostel, 2015:324, ISBN 978-82-326-1304-5 (printed ver.) ISBN 978-82-326-1305-2 (electonic ver.) ISSN 1503-8181.

"Flowable fibre-reinforced concrete for structural applications"

Elena Vidal Sarmiento, 2015-335, ISBN 978-82-326-1324-3 (printed ver.) ISBN 978-82-326-1325-0 (electronic ver.) ISSN 1503-8181.

“Development of chushed sand for concrete production with microproportioning”
Rolands Cepuritis, 2016:19, ISBN 978-82-326-1382-3 (printed ver.) ISBN 978-82-326-1383-0 (electronic ver.) ISSN 1503-8181.

“Withdrawal properties of threaded rods embedded in glued-laminated timer elements”
Haris Stamatopoulos, 2016:48, ISBN 978-82-326-1436-3 (printed ver.) ISBN 978-82-326-1437-0 (electronic ver.) ISSN 1503-8181.

“An Experimental and numerical study of thermoplastics at large deformation”
Marius Andersen, 2016:191, ISBN 978-82-326-1720-3 (printed ver.) ISBN 978-82-326-1721-0 (electronic ver.) ISSN 1503-8181.

“Modeling and Simulation of Ballistic Impact”
Jens Kristian Holmen, 2016:240, ISBN 978-82-326-1818-7 (printed ver). ISBN 978-82-326-1819-4 (electronic ver.) ISSN 1503-8181.

“Early age crack assessment of concrete structures”
Anja B. Estensen Klausen, 2016:256, ISBN 978-82-326-1850-7 (printed ver). ISBN 978-82-326-1851-4 (electronic ver.) ISSN 1503-8181.

“Uncertainty quantification and sensitivity analysis for cardiovascular models”
Vinzenz Gregor Eck, 2016:234, ISBN 978-82-326-1806-4 (printed ver.) ISBN 978-82-326-1807-1 (electronic ver.) ISSN 1503-8181.

“Dynamic behaviour of existing and new railway catenary systems under Norwegain conditions”
Petter Røe Nåvik, 2016:298, ISBN 978-82-326-1935-1 (printed ver.) ISBN 978-82-326-1934-4 (electronic ver.) ISSN 1503-8181.

"Mechanical behaviour of particle-filled elastomers at various temperatures"
Arne Ilseng, 2016-295, ISBN978-82-326-1928-3 (printed ver.) ISBN 978-82-326-1929-0 (electronic ver.) ISSN 1503-8181.

"Nanotechnology for Anti-Icing Application"
Zhiwei He, 2016:348, ISBN 978-82-326-2038-8 (printed ver.) ISBN 978-82-326-2019-5 (electronic ver.) ISSN 1503-8181.

"Conduction Mechanisms in Conductive Adhesives with Metal-Coated Polyer Spheres"
Sigurd Rolland Pettersen, 2016:349, ISBN 978-326-2040-1 (printed ver,) ISBN 978-82-326-2041-8 (electronic ver.) ISSN 1503-8181.

"The interaction between calcium lignosulfonate and cement"
Alessia Colombo, 2017:20, ISBN 978-82-326-2122-4 (printed ver.) ISBN 978-82-326-2123-1 (electronic ver.) ISSN 1503-8181.

"Behaviour and Modelling of Flexible Structures Subjected to Blast Loading"
Vegard Aune, 2017:101, ISBN 978-82-326-2274-0 (printed ver.) ISBN 978-82-326-2275-7 (electronic ver.) ISSN 1503-8181.

"Behaviour of steel connections under quasi-static and impact loading"
Erik Løhre Grimsmo, 2017:159, ISBN 978-82-326-2390-7 (printed ver.) ISBN 978-82-326-2391-4 (electronic ver.) ISSN 1503-8181.

"An experimental and numerical study of cortical bone at he macro and Nano-scale"
Masoud Ramenzanzadehkoldeh,, 2017:208, ISBN 978-82-326-2488-1 (printed ver.) ISBN 978-82-326-2489-8 (electronic ver.) ISSN 1503-8181.

"Optoelectrical Properties of a Novel Organic Semiconductor: 6,13-Dichloropentacene"
Mao Wang, 2017:130, ISBN 978-82-326-2332-7 (printed ver.) ISBN 978-82-326-2333-4) (electronic ver.) ISSN 1503-8181.

"Core-shell structured microgels and their behavior at oil and water interface"
Yi Gong, 2017:182, ISBN 978-82-326-2436-2 (printed. ver.) ISBN 978-82-326-2437-9 (electronic ver.) ISSN 1503-8181.

"Aspects of design of reinforced concrete structures using nonliear finite element analyses"
Morten Engen, 2017:149, ISBN 978-82-326-2370-9 (printed ver.) ISBN 978-82-326-2371-6 (electronic ver.) ISSN 1503-8181.

"Numerical studies on ductile failure of aluminium alloys"
Lars Edvard Dæhli, 2017:284, ISBN 978-82-326-2636-6 (printed ver.) ISBN 978-82-326-2637-3 (electronic ver.) ISSN 1503-8181.

"Modelling and Assessment of Hydrogen Embrittlement in Steels and Nickel Alloys"
Haiyang Yu, 2017:278, ISBN 978-82-326-2624-3 (printed. ver.) ISBN 978-82-326-2625-0 (electronic ver.) ISSN 1503-8181.

"Network arch timber bridges with light timber deck on transverse crossbeams"
Anna Weronika Ostrycharczyk, 2017:318, ISBN 978-82-326-2704-2 (printed ver.) ISBN 978-82-326-2705-9 (electronic ver.) ISSN 1503-8181.

"Splicing of Large Glued Laminated Timber Elements by Use of Long Threated Rods"
Martin Cepelka, 2017:320, ISBN 978-82-326-2708-0 (printed ver.) ISBN 978-82-326-2709-7 (electronic ver.) ISSN 1503-8181.

"Thermomechanical behaviour of semi-crystalline polymers: experiments, modelling and simulation"
Joakim Johnsen, 2017-317, ISBN 978-82-326-2702-8 (printed ver.) ISBN 978-82-326-2703-5 (electronic ver.) ISSN 1503-8181.

"Small-Scale Plasiticity under Hydrogen Environment"
Kai Zhao, 2017:356, ISBN 978-82-326-2782-0 (printed ver.) ISBN 978-82-326-2783-7 (electronic er.) ISSN 1503-8181.

"Risk and Reliability Based Calibration of Structural Design Codes"
Michele Baravalle, 2017:342, ISBN 978-82-326-2752-3 (printed ver,) ISBN 978-82-326-2753-0 (electronic ver.) ISSN 1503-8181.

"Dynamic behaviour of floating bridges exposed to wave excitation"
Knut Andreas Kvåle, 2017:365, ISBN 978-82-326-2800-1 (printed ver.) ISBN 978-82-326-2801-8 (electronic ver.) ISSN 1503-8181.

"Dolomite calcined clay composite cement – hydration and durability"
Alisa Lydia Machner, 2018:39, ISBN 978-82-326-2872-8 (printed ver.). ISBN 978-82-326-2873-5 (electronic ver.) ISSN 1503-8181.

"Modelling of the self-excited forces for bridge decks subjected to random motions: an experimental study"
Bartosz Siedziako, 2018:52, ISBN 978-82-326-2896-4 (printed ver.). ISBN 978-82-326-2897-1 (electronic ver.) ISSN 1503-8181.

"A probabilistic-based methodology for evaluation of timber facade constructions"
Klodian Gradeci, 2018:69, ISBN 978-82-326-2928-2 (printed ver.) ISBN 978-82-326-2929-9 (electronic ver.) ISSN 1503-8181.

"Behaviour and modelling of flow-drill screw connections"
Johan Kolstø Sønstabø, 2018:73, ISBN 978-82-326-2936-7 (printed ver.) ISBN 978-82-326-2937-4 (electronic ver.) ISSN 1503-8181.

"Full-scale investigation of the effects of wind turbulence characteristics on dynamic behavior of long-span cable-supported bridges in complex terrain"

Aksel Fenerci, 2018 100, ISBN 9978-82-326-2990-9 (printed ver.) ISBN 978-82-326-2991-6 (electronic ver.) ISSN 1503-8181.

"Modeling and simulation of the soft palate for improved understanding of the obstructive sleep apnea syndrome"
Hongliang Liu, 2018:101, ISBN 978-82-326-2992-3 (printed ver.) ISBN 978-82-326-2993-0 (electronic ver.) ISSN 1503-8181.

"Long-term extreme response analysis of cable-supported bridges with floating pylons subjected to wind and wave loads".
Yuwang Xu, 2018:229, ISBN 978-82-326-3248-0 (printed ver.) ISBN 978-82-326-3249-7 (electronic ver.) ISSN 1503-8181.

"Reinforcement corrosion in carbonated fly ash concrete"
Andres Belda Revert, 2018:230, ISBN 978-82-326-3250-3 (printed ver.) ISBN 978-82-326-3251-0 (electronic ver.) ISSN 1503-8181.

"Direct finite element method for nonliear earthquake analysis of concrete dams including dam-water-foundation rock interaction"
Arnkjell Løkke, 2018:252, ISBN 978-82-326-3294-7 (printed ver.) ISBN 978-82-326-3295-4 (electronic ver.) ISSN 1503-8181.

"Electromechanical characterization of metal-coated polymer spheres for conductive adhesives"
Molly Strimbeck Bazilchuk, 2018:295, ISBN 978-82-326-3380-7 (printed. ver.) ISBN 978-82-326-3381-4 (electrical ver.) ISSN 1503-8181.

"Determining the tensile properties of Artic materials and modelling their effects on fracture"
Shengwen Tu, 2018:269, ISBN 978-82-326-3328-9 (printed ver.) ISBN 978-82-326-3329-6 (electronic ver.) ISSN 1503-8181.

“Atomistic Insigth into Tranportation of Nanofluid in Ultra-confined Channel”
Xiao Wang, 2018:334, ISBN978-82-326-3456-9 (printed ver.) ISBN 978-82-326-3457-6 (electronic ver.) ISSN 1503-8181.

“An experimental and numerical study of the mechanical behaviour of short glass-fibre reinforced thermoplastics”.
Jens Petter Henrik Holmstrøm, 2019:79, ISBN 978-82-326-3760-7 (printed ver.) ISBN 978-82-326-3761-4 (electronic ver.) ISSN 1503-8181.

“Uncertainty quantification and sensitivity analysis informed modeling of physical systems”
Jacob Sturdy, 2019:115, ISBN 978-82-326-3828-4 (printed ver.) ISBN 978-82-326-3829-1 (electric ver.) ISSN 1503-8181.

“Load model of historic traffic for fatigue life estimation of Norwegian railway bridges”
Gunnstein T. Frøseth, 2019:73, ISBN 978-82-326-3748-5 (printed ver.) ISBN 978-82-326-3749-2 (electronic ver.) ISSN 1503-8181.

“Force identification and response estimation in floating and suspension bridges using measured dynamic response”
Øyvind Wiig Petersen, 2019:88, ISBN 978-82-326-3778-2 (printed ver.) ISBN 978-82-326-377-9 (electronic ver.) ISSN 1503-8181.

“Consistent crack width calculation methods for reinforced concrete elements subjected to 1D and 2D stress states”
Reignard Tan, 2019:147, ISBN 978-82-326-3892-5 (printed ver.) ISBN 978-82-326-3893-2 (electronic ver.) ISSN 1503-8181.

“Nonlinear static and dynamic isogeometric analysis of slender spatial and beam type structures”
Siv Bente Raknes, 2019:181, ISBN 978-82-326-3958-8 (printed ver.) ISBN 978-82-326-3959-5 (electronic ver.) ISSN 1503-8181.

"Experimental study of concrete-ice abrasion and concrete surface topography modification"
Guzel Shamsutdinova, 2019:182, ISBN978-82-326-3960-1 (printed ver.) ISBN 978-82-326-3961-8 (electronic ver.) ISSN 1503-8181.

"Wind forces on bridge decks using state-of-the art FSI methods"
Tore Andreas Helgedagsrud, 2019:180, ISBN 978-82-326-3956-4 (printed ver.) ISBN 978-82-326-3957-1 (electronic ver.) ISSN 1503-8181.

"Numerical Study on Ductile-to-Brittle Transition of Steel and its Behavior under Residual Stresses"
Yang Li, 2019:227, ISBN 978-82-326-4050-8 (printed ver.) ISBN 978-82-326-4015-5 (electronic ver.) ISSN 1503-8181.

"Micromechanical modelling of ductile fracture in aluminium alloys"
Bjørn Håkon Frodal, 2019:253, ISBN 978-82-326-4102-4 (printed ver.) ISBN 978-82-326-4103-1 (electronic ver.) ISSN 1503-8181.

"Monolithic and laminated glass under extreme loading: Experiments, modelling and simulations"
Karoline Osnes, 2019:304, ISBN 978-82-326-4204-5 (printed ver.) ISBN 978-82-326-4205-2 (electronic ver.) ISSN 1503-8181.